



**IN-SITU FTIR STUDIES OF THE PLASMA GLOW
REGION OF CATALYSED NON-THERMAL
PLASMAS**

Thesis submitted by:

ABD HALIM BIN MD ALI

For the degree of Doctor of Philosophy

Newcastle University

School of Engineering

October, 2018

Declaration

I hereby declare that the work in this title entitled “In-situ FTIR studies of the plasma glow region of catalysed non-thermal plasmas” is the result of experiments carried out in the School of Engineering at Newcastle University. No part of this thesis been submitted for a degree or any other qualification at Newcastle University or any other institution.

Abd Halim bin Md Ali

October 2018

Acknowledgment

First and foremost, I would like to thank my advisor, Prof Paul Andrew Christensen for his academic supervision and personal support throughout all my years in Newcastle University. I have been extremely lucky to have a supervisor who cared so much about my work and who responded to my questions and queries so promptly.

Secondly, I would like to thank Majlis Amanah Rakyat (MARA) for the financial supports to study for a PhD, the staff of the Majlis Amanah Rakyat in Kuala Lumpur, Malaysia and London, United Kingdom for their invaluable assistance.

I wish to acknowledge support of the technical staff of the School of Engineering, Newcastle University especially Neville Dickman, Simon Daley and Maggie White who have been very helpful during the course of this work.

A special thanks to all the members of the Christensen Research Group, Dr. Abdullah Al-Abduly, Dr. Supandee Maneelok, Dr. Pierrot Attidekou, Zeinab Mashhadani, Phillip Layford and Ndubuisi Eje for their companionship throughout my studies. This thanks also extended to all my friends in Newcastle especially, Khairul Amalin Abd Rahman, Amirul Busu, Ismail Lukman, Tuan Badrul Hisyam, Faizal Nadzari and Akmal Rahim.

Finally, but by no means least, a very special thanks to my mum, Kasmah Abd Malik and dad, Md Ali Abu for almost unbelievable support. They are the most important people in my world and I dedicated this thesis to them.

Abd Halim bin Md Ali

Newcastle upon Tyne, United Kingdom

October, 2018

List of Publications

- Christensen, P.A., **Abd Halim bin Md Ali**, Mashhadani, Z.T.A.W. et al. *A Direct Fourier Transform Infrared Spectroscopic Comparison of the Plasma- and Thermally-driven Reaction of CO₂ at Macor*. Plasma Chem Plasma Process (2018) 38: 293.
- Christensen, P.A., **Abd Halim bin Md Ali**, Mashhadani, Z.T.A.W. et al. *The production of ketene and C₅O₂ from CO₂, N₂ and CH₄ in a non-thermal plasma catalysed by earth-abundant elements: an in-situ FTIR study*. Plasma Chem Plasma Process (2018) 38: 461.
- Christensen, P.A., Mashhadani, Z.T.A.W., **Abd Halim bin Md Ali** et al. *The production of methane, acetone, “cold” CO and oxygenated species from isopropyl alcohol in a non thermal plasma: an in-situ FTIR study*. Journal of Physical Chemistry A (2018) 122 (17), 4273-4284.
- Christensen, P.A., Mashhadani, Z.T.A.W., **Abd Halim bin Md Ali** et al. *In-situ FTIR studies on the oxidation of isopropyl alcohol over SnO₂ as a function of temperature up to 600 °C and a comparison to the analogous plasma-driven process*. Physical Chemistry Chemical Physics (2018) 20: 9053-9062.

Oral presentations

- In-Situ FTIR studies of the plasma glow region of non-thermal plasma fed with CO₂ in Postgraduate Conference 2016. Newcastle University, UK
- In-situ FTIR Studies of the Non-thermal Plasma Reduction of CO₂ in Postgraduate Conference 2017. Newcastle University, UK.
- The production of ketene and C₅O₂ from CO₂, N₂ and CH₄ in a non-thermal plasma catalysed by earth-abundant elements: an in-situ FTIR study. Unconventional Activation of Catalysts – Fundamental and Applications 2018. IChemE Catalysis Special Interest Group. The University of Manchester, UK.

Abstract

In-situ non-thermal plasma infrared transmission and reflectance cells were designed, fabricated and commissioned in order to study the non-thermal plasma (NTP)-driven reaction of methane, carbon dioxide and dinitrogen. This chemical system was chosen as a model to explore the application of in-situ FTIR spectroscopy to the study of NTP chemistry. As the choice of catalysts for NTP processes has often been made on the basis of those materials active in the analogous thermally-driven processes, the NTP experiments were supported by experiments employing a commercial, diffuse reflectance infrared Fourier transform system utilising a commercial environmental chamber that could be heated to 600°C.

Initial experiments investigated the possible reaction of CO₂ and N₂ in the thermal and plasma systems, the latter providing benchmark data, both quantitative and qualitative, on the NTP reduction of CO₂ to CO. Experiments were also conducted on CH₄ with N₂, followed by studies using CH₄, CO₂ and N₂ as the feed gas. Whilst none of the thermal experiments showed additional species other than the rotationally-excited reactants, wholly unexpected results were obtained in the NTP experiments using CH₄, CO₂ and N₂. Nitrogen was fixed to produce both HCN and acetamide, whilst the chain oxides ketene and C₅O₂ were also produced along with CO and formaldehyde, and a liquid. The results were interpreted in terms of a novel, three-zone model in which the liquid products played an active part in the production of the chain oxides.

SnO₂ and CeO₂ were also investigated with respect to possible catalytic activity, but proved inactive in both the plasma and thermal systems.

Ketenes and their dimers are important reactants that find use in the production of a wide range of chemicals in a diverse range of industries including pigments, pharmaceuticals and agrochemicals and as intermediates for the paper industry. In addition, such chain oxides are known or proposed substrates for radical, nucleophilic addition and cycloaddition chemistry and hence are extremely useful chemical precursors: hence the work reported in this thesis could have significant potential implications for novel chemical synthesis. In addition to terrestrial chemistry, the production of acetamide and the chain oxides could be highly relevant to the study of the interstellar origins of life and prebiotic chemistry.

Table of Contents

	Page
Declaration	i
Acknowledgement	ii
List of Publications	iii
Abstract	iv
Table of Contents	v
List of Figures	xiii
List of Tables	xvii
List of Abbreviations	xix
Chapter 1 Introduction	
1.1. Background.....	1
1.2. CO ₂ and CH ₄ mitigation and valorisation.....	3
1.3. Plasma.....	3
1.4. Non thermal plasma.....	5
1.5. Non thermal plasma reactor used for CO ₂ and CH ₄ conversion.....	5
1.5.1 Dielectric Barrier Discharge.....	5
1.6. The non-thermal plasma conversion of CO ₂ and CH ₄	17
1.7. Infrared Spectroscopy.....	17
1.8. Plasma catalysis.....	19
1.9. Dielectric/catalyst materials and plasma cells to be investigated.....	22
1.10. Project aim and objectives.....	22
1.11. References.....	23
Chapter 2 Experimental	
2.1. Gases, Chemicals and Materials.....	32
2.1.1 Gases.....	32
2.1.2 Chemicals.....	32
2.1.3 Materials.....	32
2.2. The gas delivery system.....	33
2.3. The non-thermal plasma infrared cells.....	34
2.3.1 The non-thermal plasma infrared transmission cell.....	34
2.3.2 The non-thermal plasma infrared reflectance cell.....	38
2.4. The non-thermal plasma FTIR system.....	41

2.5.	The thermal FTIR system.....	43
2.6.	Catalyst preparation.....	47
2.6.1	SnO ₂ synthesis method.....	47
2.6.2	Macor.....	49
2.6.3	Cerium (IV) oxide.....	49
2.7.	Typical in-situ NTP FTIR experiments using the transmission cell.....	50
2.8.	Typical in-situ NTP FTIR analysis procedure.....	52
2.9.	Data manipulation.....	56
2.10.	Material characterisation technique.....	58
2.10.1	X-ray diffraction (XRD).....	58
2.10.2	The thermogravimetric analysis system.....	61
2.11.	References.....	62
Chapter 3	An in-situ study of non-thermal plasma fed with CO₂, and N₂ in plasma- and thermally driven experiments at Macor	
3.1.	Introduction.....	64
3.2.	The plasma-driven reaction of CO ₂ at Macor.....	64
3.2.1	Plasma transmission cell.....	64
3.2.2	Plasma reflectance cell.....	77
3.2.3	The thermally driven reaction of CO ₂ at Macor.....	83
3.3.	Conclusions.....	89
3.4.	References.....	89
Chapter 4	An in-situ FTIR study of non-thermal plasma fed with CO₂, CH₄ and N₂ in plasma and thermally driven experiments at Macor	
4.1.	Introduction.....	92
4.2.	Plasma transmission cell.....	92
4.3.	The spectra collected after 2 minutes.....	99
4.4.	The spectra collected at later times.....	109
4.5.	Thermal plasma.....	121
4.6.	The reaction zones above Macor.....	122
4.7.	Conclusions.....	126
4.8.	References.....	127

Chapter 5	In-situ FTIR studies of non-thermal plasma fed with CO₂, CH₄ and N₂ over SnO₂ and CeO₂ and a comparison to the analogous thermally-driven process	
5.1.	Introduction.....	132
5.2.	The plasmally driven reaction of CO ₂ , CH ₄ and N ₂ at Macor/Ti mesh with SnO ₂	132
5.3.	The thermally driven reaction of CO ₂ , CH ₄ and N ₂ with SnO ₂	137
5.4.	The plasmally driven reaction of CO ₂ , CH ₄ and N ₂ at Macor/Ti mesh with CeO ₂	144
5.5.	The thermally driven reaction of N ₂ with CeO ₂	146
5.5.1	The thermally driven reaction of CO ₂ , CH ₄ and N ₂ with CeO ₂ ..	156
5.6.	Conclusions.....	158
5.7.	References.....	158
Chapter 6	Conclusions and recommendations.....	161
Appendices		
	Appendix 1.....	163
	Appendix 2.....	165
	Appendix 3.....	167
	Appendix 4.....	169

List of Figures

	Page
Chapter 1	
Figure 1.1. Change in average surface temperature reported in Climate Change 2014: Synthesis Report, by Intergovernmental Panel on Climate Change (IPCC).....	2
Figure 1.2. Calculated theoretical thermal conversion (left axis) and corresponding energy efficiency (right axis) as a function of temperature for the reduction of CO ₂ into CO and O ₂	4
Figure 1.3. (a) PBD, (b) VD and (c) SD configurations.....	6
Figure 1.4. A comparison of CO ₂ conversion using three different catalyst in the NTP conversion of CO ₂ at a fixed frequency of 8 kHz.....	12
Figure 1.5. A comparison of CO ₂ and CH ₄ conversion by thermal catalysis, plasma-induced conversion and the combination of plasma and catalysis conversion using 1% Cu- 12% Ni/ γ -Al ₂ O ₃ as the catalyst, 50% CH ₄ + 50% CO ₂ as the feed gas at a total flow rate of 60 cm ³ min ⁻¹ and a temperature of 450 °C.....	13
Figure 1.6. Energy diagram illustrating the working principle of a catalyst.....	14
Figure 1.7. A comparison of CO ₂ and CH ₄ conversion and gaseous products selectivities for catalysis activation only, plasma-induced conversion and plasma catalysis for three different catalyst materials in a DBD reactor at 30 °C and atmospheric pressure.....	15
Figure 1.8. A comparison of CO ₂ and CH ₄ conversion and liquid products selectivities for catalysis activation only, plasma-induced conversion and plasma catalysis for three different catalyst materials in DBD at 30 °C and atmospheric pressure.....	16
Chapter 2	
Figure 2.1. (a) Schematic of gas line mixing system and (b) photograph of the venturi mixing cylinder.....	34
Figure 2.2. (a) Schematic and (b) photograph of the NTP IR transmission cell.....	35
Figure 2.3. (a) - (d) photographs of the arrangement of the high voltage electrodes.....	36
Figure 2.4. (a) Photograph of the high voltage power supply and (b) photograph of the voltage controller.....	37

Figure 2.5	(a) Schematic of the NTP IR reflectance cell and (b) - (c) photograph of the NTP IR reflectance cell.....	39
Figure 2.6.	(a) photograph and (b) Schematic of the optical bench employed with the in-situ FTIR for reflectance cell.....	41
Figure 2.7.	(a) Photograph of the Agilent FTS7000 spectrometer and (b) photograph of the sample compartment of the spectrometer.....	42
Figure 2.8.	(a) Photograph of the FTIR Varian 670-IR spectrometer and (b) photograph of the Specac Environmental Chamber and diffuse reflectance unit.....	43
Figure 2.9.	Photograph of the environmental chamber employed for the in-situ FTIR experiments at varied temperature.....	44
Figure 2.10.	Schematic of light scattering from a powder sample.....	45
Figure 2.11.	Schematic of the diffuse reflectance optical system.....	45
Figure 2.12.	Photograph of the reflux apparatus.....	47
Figure 2.13.	Photograph of the hydrothermal synthesis apparatus: (a) the Teflon container, (b) the stainless steel autoclave and (c) the hydrothermal reactor.....	48
Figure 2.14.	Photograph of Macor disc in the sample cup.....	49
Figure 2.15.	Photograph of CeO ₂ in the sample cup.....	50
Figure 2.16.	Typical FTIR spectra processing: (a) (i) a reference spectrum, (S _R) collected from 200 cm ³ min ⁻¹ N ₂ and (ii) a sample spectrum, S _S collected after CH ₄ was admitted to the cell at a total flow rate of 200 cm ³ min ⁻¹ , and (b) the resultant absorbance spectrum = log ₁₀ (S _R / S _S).....	54
Figure 2.17.	Typical FTIR spectra processing: (a) (i) a reference spectrum, (S _R) collected from 200 cm ³ min ⁻¹ N ₂ and (ii) a sample spectrum, S _S collected after CO ₂ was admitted to the cell at a total flow rate of 200 cm ³ min ⁻¹ , and (b) the resultant absorbance spectrum = log ₁₀ (S _R / S _S).....	55
Figure 2.18.	Photograph of the PANalytical X'Pert Pro MPD x-Ray diffractometer.....	59
Figure 2.19.	(a) The XRD patters of the SnO ₂ 400 °C and 700 °C nanopowders prepared by hydrothermal synthesis and (b) The XRD patters of the CeO ₂ nanopowders purchased from Sigma Aldrich.	61

Chapter 3

Figure 3.1.	Typical reference spectrum (8 cm ⁻¹ resolution, 100 scans per scan set, and 60 seconds per spectrum) of the plasma transmission cell collected at a total flowrate of 200 cm ³ min ⁻¹	64
Figure 3.2.	(a) In situ FTIR spectra (8 cm ⁻¹ resolution, 100 co-added and averaged scans, 60 seconds per scanset) collected at the times shown on the figure at an input power of 28 W, (b) the CO ₂ fundamental region of figs. 3.2(a) and (c) the combination band region.	66
Figure 3.3.	(i) The spectrum collected after 20 minutes in figs. 3.2 and (ii) the spectrum collected immediately before the plasma was initiated: (a) CO ₂ asymmetric stretch region and (b) combination band region. (c) The result of simulating the spectrum of CO ₂ at 100 °C and subtracting it from the simulated spectrum of CO ₂ at room temperature.....	68
Figure 3.4.	The spectrum collected after 2 minutes in fig. 3.2 using the spectrum collected with no plasma and the 12.2% CO ₂ + 87.8% N ₂ feed gas as reference.....	69
Figure 3.5.	(i) The spectrum (8 cm ⁻¹ resolution, 100 scans per scan set, and 60 seconds per spectrum) of CO in a 1 cm pathlength transmission cell and the spectra collected after (ii) 2 minutes and (iii) 20 minutes during the experiment shown in figs. 3.2 and 3.4.....	70
Figure 3.6.	Plots of the integrated absorbance of the CO* band and the integrated absorbance of the CO ₂ * combination bands in fig. 3.2 as a function of time.....	74
Figure 3.7.	Plots of the integrated absorbances of the CO* and CO ₂ * combination bands in fig. 3.2 as a function of time. The plots were normalised to their maximum values.....	75
Figure 3.8.	(a) In situ FTIR spectra (8 cm ⁻¹ resolution, 100 co-added and averaged scans, 60 seconds per scanset) collected at the times shown on the figure at an input power of 24 W using the reflectance cell and nitrogen gas as the feed gas. The spectrum collected immediately before the plasma was initiated was employed as the reference. (b) The single beam spectra from the experiment in fig. 3.8(a)	78

Figure 3.9.	Plots of the integrated absorptions of the 1150 and 1210 cm^{-1} bands after 20 minutes operation as a function of input power from the experiment in fig. 3.8 and analogous experiments.....	79
Figure 3.10.	In situ FTIR spectra (8 cm^{-1} resolution, 100 co-added and averaged scans, 60 seconds per scanset) collected at the times shown on the figure at an input power of 24 W using the reflectance cell and 49% CO_2 + 51% N_2 as the feed gas.	80
Figure 3.11.	Plots of the normalized band absorptions of the 1150 cm^{-1} , 1210 cm^{-1} and CO_2 asymmetric stretch from the flushing experiment in fig. 3.10.....	81
Figure 3.12.	In situ FTIR spectra (8 cm^{-1} resolution, 100 co-added and averaged scans, 60 seconds per scanset) collected using the plasma reflectance cell at the times shown on the figure at an input power of 14 W.....	82
Figure 3.13.	In-situ FTIR spectra (8 cm^{-1} resolution, 100 co-added and averaged scans, 120 seconds per scanset) collected as a function of temperature from a 12.5 mm diameter, 2 mm thick Macor disc in the thermal system.....	84
Figure 3.14.	(a) In situ FTIR spectra (8 cm^{-1} resolution, 100 co-added and averaged scans, 60 seconds per scanset) collected from a 12.5 mm diameter Macor disc in a static atmosphere of 23% CO_2 + 77% N_2 at the temperatures shown on the figure. The temperature was ramped at 5 $^\circ\text{C min}^{-1}$. The spectra in (a) 25 $^\circ\text{C}$ to 600 $^\circ\text{C}$ (b) 25 $^\circ\text{C}$ to 250 $^\circ\text{C}$ and (c) 250 $^\circ\text{C}$ to 600 $^\circ\text{C}$	86
Figure 3.15.	(i) The FTIR spectrum (8 cm^{-1} resolution, 100 co-added and averaged scans, 120 seconds per scanset) collected at 600 $^\circ\text{C}$ in fig. 3.14, along with spectra collected at the same temperature in analogous experiments using (ii) 23% CO_2 + 77% N_2 , (iii) 36% CH_4 + 64% N_2 , and (iv) 21% CO_2 + 43% CH_4 + 36% N_2	87
Figure 3.16.	A plot of the absorbance at 2000 cm^{-1} of the spectra in fig. 3.14(a) as a function of temperature.....	87
Figure 3.17.	The spectrum collected at 100 $^\circ\text{C}$ in fig. 3.14(a).....	88

Figure 3.18.	A comparison of (i) the spectrum obtained in the thermal experiment in fig. 3.14(a) at 250 °C with (ii) that obtained after 20 minutes in the plasma experiment at 28 W in fig. 3.4.....	88
Chapter 4		
Figure 4.1.	A spectrum (8 cm ⁻¹ resolution, 100 spectra per scan set, and 1 minute per spectrum) of 8.5% + 13.1% + 78.4% at a total flow rate of 200 cm ³ min ⁻¹ through the plasma transmission cell at 25 °C prior to the experiment carried out at an input power of 24 W.....	92
Figure 4.2.	In situ FTIR spectra (8cm ⁻¹ resolution, 100 spectra per scan set, and 1 minute per spectrum) of the 8.5% CO ₂ + 13.1% CH ₄ + 78.4% N ₂ feed gas in the plasma transmission cell at a total flow rate of 200 cm ³ min ⁻¹ and a temperature of ca. 25 °C: (i) before initiating plasma and (ii) after 2 minutes operation at 24 W.....	93
Figure. 4.3.	(a) The spectrum in fig. 4.2 but using the single beam spectrum collected with no plasma and using 8.5% CO ₂ + 13.1% CH ₄ + 78.4% N ₂ as the feed gas as the reference spectrum. (b) & (c) Spectral simulations of the change in absorbance observed when the gas temperature is changed from 296 to 396 K.....	95
Figure. 4.4.	In-situ FTIR spectra (8 cm ⁻¹ resolution, 100 spectra per scan set, and 1 minute per spectrum) collected after 20 minutes operation with plasma as a function of input power.....	97
Figure 4.5.	The spectrum collected (i) after 20 minutes at 24 W in the experiment in fig. 4.4 along with (ii) that collected at the end of the same experiment after the cell had been sparged with N ₂ , the peaks in the latter thus being due to the liquid film on the CaF ₂ windows.....	98
Figure 4.6.	The spectrum collected after 2 minutes of plasma operation at 28 W in fig. 2, along with analogous experiments using gas feeds of various composition, as shown on the figure.....	100
Figure 4.7.	(i) The CO region of the spectrum in fig. 4.4 collected at 24 W; (ii) a spectrum collected after 2 minutes operation at 24 W using 13.4% CO ₂ + 86.6% N ₂ as the feed gas, reduced by a factor of 1.3 to render the 2116 cm ⁻¹ band the same intensity as that in (i); (iii) The difference between the two spectra in (i) and (ii).....	101

Figure 4.8.	Spectra collected after 2 minutes at the input powers and gas feed compositions shown on the figure. Plasma transmission cell, total flow rate $200 \text{ cm}^3 \text{ min}^{-1}$	102
Figure 4.9.	The spectrum collected after 2 minutes at 28 W using a feed gas of 8.3% CO_2 + 13.5% CH_4 + 78.2% Ar.....	109
Figure 4.10.	In-situ FTIR spectra (8 cm^{-1} resolution, 100 spectra per scan set, and 1 minute per spectrum) collected as a function of time at a fixed input power of 28 W. The gas composition was 12.3% CO_2 + 14.4% CH_4 + 73.3% N_2 at a total flow rate of $200 \text{ cm}^3 \text{ min}^{-1}$ and a temperature of ca. $25 \text{ }^\circ\text{C}$; the reference spectrum was collected under the same conditions but with no plasma.....	110
Figure 4.11.	(a) Plots of the intensities of the various features in fig. 4.10 as a function of time. (b) The plots in (a) normalised to their maximum values.....	111
Figure 4.12.	Analogous plots to those shown in figs. 4.11(a) and (b) for the various features observed at input powers of (a) & (b) 20 W and (c) & (d) 24 W.....	113
Figure 4.13.	Plots of the absorbance of the 3303 cm^{-1} band vs the broad absorbance at 1655 cm^{-1} for the experiment in fig. 4.10 and the analogous experiments carried out at input powers of (a) 20 W (b) 24 W and (c) 28 W.....	116
Figure 4.14.	(i) Spectrum of the liquid deposit formed on the CaF_2 windows of the transmission following a repeat of the experiment at 24 W in fig. 4.4. (ii) Spectrum of the liquid deposit on the CaF_2 window of the reflectance cell following an analogous experiment at 24 W to that depicted in fig. 4.4.....	117
Figure 4.15.	(a) In situ FTIR spectra (8 cm^{-1} resolution, 100 co-added and averaged scans, 60 seconds per scanset) collected at the times shown on the figure at an input power of 24 W using the reflectance cell and nitrogen gas as the feed gas. (b) Plots of the normalised absorbance of the 1150 and 1210 cm^{-1} with time before and after plasma exposure.....	119
Figure 4.16.	In-situ FTIR spectra (8 cm^{-1} resolution, 100 spectra per scan set, and 1 minute per spectrum) collected after 20 minutes operation at input	

	power of 28 W as a function of the gas compositions shown on the figure.....	120
Figure 4.17.	The spectrum (8 cm ⁻¹ resolution, 100 spectra per scan set, and 1 minute per spectrum) collected at 100 °C during an experiment in which a Macor disc was heated in a static atmosphere of 43% CH ₄ + 21% CO ₂ + 36% N ₂ and spectra collected from the disc as a function of temperature from 25 °C to 600 °C.....	122
Figure 4.18.	The spectrum (8 cm ⁻¹ resolution, 100 spectra per scan set, and 1 minute per spectrum) collected at the end of an experiment in which 11.0% CO ₂ + 15.0% CH ₄ + 74.0% N ₂ was bubbled through isoprene and fed to the transmission cell.....	125
Chapter 5		
Figure 5.1.	In situ FTIR spectra (8 cm ⁻¹ resolution, 100 co-added and averaged scans, 60 seconds per scanset) collected at the times shown on the figure at an input power of 24 W.....	132
Figure 5.2.	Plots of the absorbance of the CO ₂ at 3625 cm ⁻¹ and CH ₄ at 3085 cm ⁻¹ from the experiment in fig. 5.1 as a function of time.....	133
Figure 5.3.	Plots of the normalised absorbance in figs. 5.2 as a function of time....	134
Figure 5.4.	In-situ FTIR spectra (8 cm ⁻¹ resolution, 100 spectra per scan set, and 1 minute per spectrum) collected after 20 minutes operation with plasma as a function of dielectric/catalyst.....	135
Figure 5.5.	In-situ FTIR spectra (8 cm ⁻¹ resolution, 100 spectra per scan set, and 1 minute per spectrum) collected after 20 minutes operation with plasma as a function of SnO ₂ calcination temperature.....	136
Figure 5.6.	In-situ FTIR spectra (100 co-added scans and averaged scans at 8 cm ⁻¹ resolution ca. 100 seconds per scanset) collected using the environmental chamber during an experiment in which a spectrum was collected at 25 °C and the temperature ramped at 5 °C min ⁻¹ and further spectra taken at the temperatures shown.....	137
Figure 5.7.	The spectra in fig. 5.6 collected up to 300 °C.....	138
Figure 5.8.	Plot of the Kubelka-Munk as a function of temperature at 2000 cm ⁻¹ from fig 5.6.....	139
Figure 5.9.	In-situ FTIR spectra (100 co-added scans and averaged scans at 8 cm ⁻¹ resolution ca. 100 seconds per scanset) collected using the	

	environmental chamber during an experiment in which a spectrum was collected at 25 °C and the temperature ramped at 5 °C min ⁻¹ and further spectra taken at the temperatures shown.....	140
Figure 5.10.	In-situ FTIR spectra (100 co-added scans and averaged scans at 8 cm ⁻¹ resolution ca. 100 seconds per scanset) collected using the environmental chamber during an experiment in which a spectrum was collected at 25 °C and the temperature ramped at 5 °C min ⁻¹ and further spectra taken at the temperatures shown.....	143
Figure 5.11.	In situ FTIR spectra (8 cm ⁻¹ resolution, 100 co-added and averaged scans, 60 seconds per scanset) collected at the times shown on the figure at an input power of 20 W.....	144
Figure 5.12.	In-situ FTIR spectra (8 cm ⁻¹ resolution, 100 spectra per scan set, and 1 minute per spectrum) collected after 20 minutes operation with plasma as a function of dielectric/catalyst.....	145
Figure 5.13.	Spectra (4 cm ⁻¹ resolution, 100 co-added and averaged scans, 120 s per scanset) collected as a function of temperature during an experiment in which the temperature of 20 mg CeO ₂ + 80 mg KBr was ramped from 25 °C to 600 °C in a static N ₂ atmosphere. (a) the spectrum taken at 25 °C, (b) all spectra collected during the experiment and (c) the spectra taken at (i) 25 °C and (ii) 200 °C showing the CO ₂ asymmetric stretch region.....	147
Figure 5.14.	(a) The thermogravimetric response of 55.5 mg of CeO ₂ , heated in 40 cm ³ min ⁻¹ flowing air 5 °C min ⁻¹ from room temperature to 600 °C (Run 1). (b) & (c) The m/z = 18, 32 and 44 responses recorded during the first and second heating cycles (Runs 1 and 2, respectively) of the sample in (a): the m/z = 32 responses are enhanced by a factor of 3 and the m/z = 44 responses by a factor of 10. (d) The m/z = 18, 32 and 44 responses recorded during the third heating of the sample in (a), Run 3.....	152
Figure 5.15.	The spectra in fig. 5.13(a): (a) the spectrum taken at 25 °C subtracted from those collected at 50 and 100 °C; (b) the spectrum taken at 100 °C subtracted from those collected up to 250 °C; (c) the spectrum taken at 125 °C subtracted from those collected at 300, 350 and 400 °C, the spectra were moved up by 0.009, 0.025 and 0.050,	

respectively and (d) the spectrum taken at 400 °C subtracted from those collected up to 600 °C. The spectra collected at 450, 500, 550 and 600 °C were moved up by 0.030, 0.069, 0.110 and 0.155, respectively..... 154

Figure 5.16. The spectra in figs. 5.15(a) – (c) collected at 150 °C, 400 °C and 600 °C. (a) The spectra collected at 25 °C subtracted from those taken at 150 °C, (b) 400 °C – 150 °C and (c) 600 °C – 400 °C. The gas composition are: (i) 100% N₂, (ii), 25.5% CO₂ + 74.5% N₂, (iii) 10.6% CH₄ + 89.4% N₂ and (iv) 12% CO₂ + 38% CH₄ + 50% N₂..... 157

List of Tables

	Page
Chapter 1	
Table 1.1 Global abundances of CO ₂ , CH ₄ and N ₂ O in 2016.....	1
Table 1.2 UK greenhouse gas emission in 2016.....	2
Table 1.3 Dielectric constant of different dielectric materials.....	8
Table 1.4 A summary of the studies on the use of DBD reactors for the conversion of CO ₂ and CH ₄ to higher hydrocarbons.....	10
Table 1.5 A summary of the NTPs studies of the catalyst in contact with plasma....	19
Chapter 2	
Table 2.1 List of reagents employed in the work reported in this thesis.....	32
Table 2.2 The materials employed in the work reported in this thesis.....	33
Table 2.3 The composition of the solutions employed in the reflux step to produce nanoparticulate SnO ₂	47
Table 2.4 The feed gas compositions employed in the transmission cell experiments.....	51
Table 2.5 The feed gas compositions employed in the reflectance cell experiments	51
Table 2.6 The particle sizes of the CeO ₂ , SnO ₂ 400 °C and 700 °C nanopowders calculated from Scherrer's equation.....	60
Chapter 3	
Table 3.1 Summary of the data obtained in the experiments typified by IR plasma transmission cell.....	73
Chapter 4	
Table 4.1 The feed gas compositions employed in the work reported in this paper, and a summary of the data obtained from the spectra collected after 2 minutes during the various experiments.....	103
Table 4.2 Electron impact excitation and ionization threshold energies.....	105
Table 4.3 Mean electron energies for different percentage compositions calculated from BOLSIG+ at a reduced electric field of 200 Td and a temperature of 300 K.....	106
Table 4.4 A summary of the assignments of the various features in figs. 4.4 – 4.10.....	121

Chapter 5

Table 5.1	A summary of the assignments in the literature of various features in the IR spectra in fig. 5.6 and 5.7.....	139
Table 5.2	Summary of the assignments of various features observed in the IR studies of CO ₂ on CeO ₂	149

List of Abbreviations

Nomenclature

μm	Micrometre
mm	Millimetre
cm	Centimetre
dm	Decimetre
Hz	Hertz
V	Volt
W	Watt
s	Second
$^{\circ}\text{C}$	Celsius
g	Gram
M	Unit of concentration / mol dm^{-3}
min	Minute
J	Joule
A	Absorbance
c	Concentration / M
L	Optical path length / cm
K	Kelvin
A	Current / Ampere
\AA	Angstrom / 10^{-10} m
V_o	The discharge onset voltage / kV
C_g	The capacitance of the background gas within the discharge gap / F
d	Thickness / m
P	Power / W
m	Mass / kg
z	Charge number / C
ppm	parts per million
ppb	parts per billion

Greek symbols

ε	Molar decadic extinction coefficient / $\text{M}^{-1} \text{cm}^{-1}$
λ	wavelength / nm

ϵ_r	dielectric constant
ϵ_o	vacuum permittivity / $8.854 \times 10^{-12} \text{ F m}^{-1}$
η	Efficiency

Acronyms

FTIR	Fourier Transform Infrared
PTFE	Polytetrafluoroethylene
NTP	Non-thermal plasma
IR	Infrared
AC	Alternating current
DC	Direct current
HV	High voltage
KM	Kubelka-Munk function
R	Reflectance of a sample at infinite depth
S_R	Reference spectrum
S_s	Sample spectra
DI	De-ionised
SIE	Specific Input Energies
EE	Energy efficiency
XRD	X-ray diffraction
WMO	World Meteorological Organization
IPCC	Intergovernmental Panel on Climate Change
UNFCCC	United Nations Framework Convention on Climate Change
DBD	Dielectric Barrier Discharge
PBD	Packed Bed Discharge
VD	Volume Discharge
SD	Surface Discharge
FWHM	Full Width at Half Maximum
TGA	Thermogravimetric analysis
TG-DSC	Thermogravimetry-Differential Scanning Calorimetry
COM	Complex Organic Molecule
QMS	Quadrupole Mass Spectrometer
UV Vis	Ultraviolet-visible

Chapter 1. Introduction

The work reported in this thesis is focused on the potential application of non-thermal plasma to the conversion of carbon dioxide (CO₂) and methane (CH₄) to value-added chemicals. The key analytical technique employed was in-situ Fourier Transform Infra Red (FTIR) spectroscopy to study the plasma glow and the plasma/solid interface. The aim of this chapter is to provide a review of the appropriate literature.

1.1 Background

Carbon dioxide is the most dominant greenhouse gas from the Kyoto Protocol “basket” of greenhouse gasses and emitted primarily from the combustion of fossil fuels. The 13th Greenhouse Gas Report from World Meteorological Organization (WMO) based on global observation through 2016 states that the carbon dioxide concentrations reached 403.3 parts per million in 2016, increased from 400 ppm in 2015 with an average growth of 2.21 ppm/year [1, 2]. Significant increases have also occurred in the levels of CH₄ and nitrous oxide (N₂O), see table 1.1.

	CO ₂	CH ₄	N ₂ O
Global abundance in 2016	403.3 ± 0.1ppm	1853 ± 2 ppb	328.9 ± 0.1ppb
2016 abundance relative to year 1750	145%	257%	122%
2015-2016 absolute increase	3.3 ppm	9 ppb	0.8 ppb
2015-2016 relative increase	0.83%	0.49%	0.24%
Mean annual absolute increase during last 10 years	2.21 ppm/year	6.8 ppb/year	0.90 ppb/year

Table 1.1. Global abundances of CO₂, CH₄ and N₂O in 2016 [2].

In the United Kingdom (UK), net emissions of CO₂ in 2016 were provisionally estimated to be 378.9 million tonnes of carbon dioxide and accounting for 81 per cent of total UK greenhouse gas emission, see table 1.2, where the energy supply sector was the largest contributor to the carbon emission followed by the transport sector (32%), residential sector (18%), business sector (16%) and industrial process (3%) [3].

Gas	Metric tonnes
Net CO ₂ emissions (emissions minus removals)	378.9
Methane (CH ₄)	51.6
Nitrous oxide (N ₂ O)	21.4
Hydrofluorocarbons (HFC)	15.2
Perfluorocarbons (PFC)	0.4
Sulphur hexafluoride (SF ₆)	0.5
Nitrogen trifluoride (NF ₃)	0
Total greenhouse gas emissions	467.9

Table 1.2. UK greenhouse gas emission in 2016 [3].

Increasing demand for energy is by far the largest source of emissions of CO₂ in the UK and worldwide and is expected to grow with fossil fuels remaining the dominant source. Growing population, industrialization and associated energy use from fossil sources is further accelerating the emission of CO₂ and is consistent with the observed increase of global temperature as reported by Intergovernmental Panel on Climate Change (IPCC) [4], see fig. 1.1. The IPCC predicted that the global temperature will continue to warm during the 21st century if the fossil-fuel burning continues at a business rate as today and arguably contribute to severe climatic phenomenon such as droughts in tropical regions, hurricanes and economic disruptions.

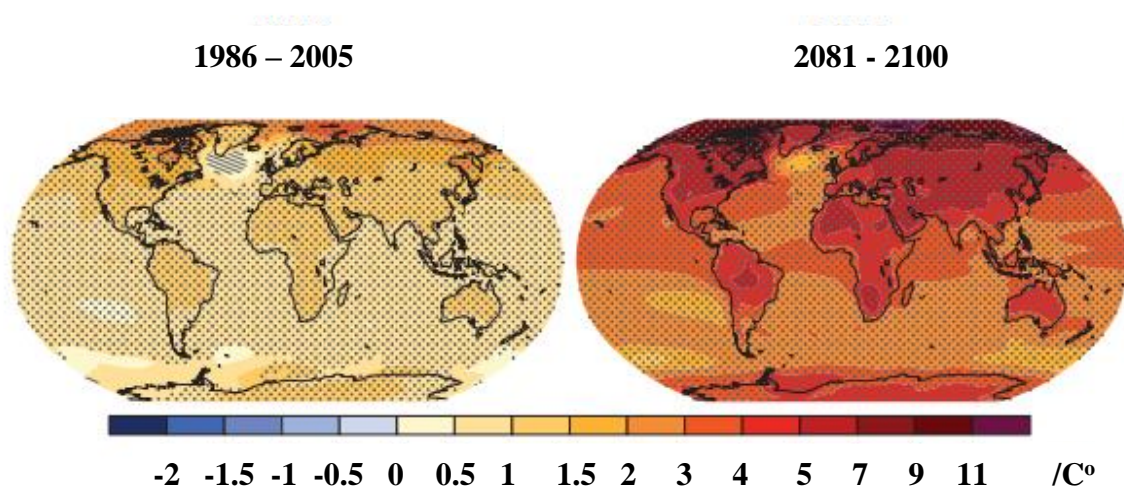


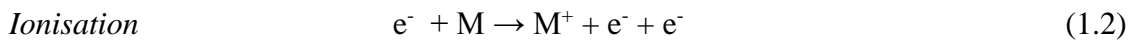
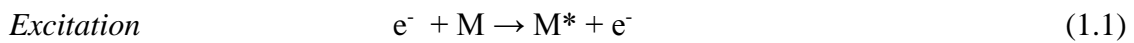
Figure 1.1. Change in average surface temperature reported in Climate Change 2014: Synthesis Report, by Intergovernmental Panel on Climate Change (IPCC)[4].

1.2 CO₂ and CH₄ mitigation and valorisation

Reducing greenhouse gas (mainly CO₂ and CH₄) emissions is an extensive and long-term task and considered as one of the major scientific and technological challenges of the 21st century [5, 6]. There has been increasing pressure for scientists to develop efficient CO₂/CH₄ capture, storage and utilization systems in parallel to the multilateral agreement adopted by the 175 United Nations Framework Convention on Climate Change (UNFCCC) members [7, 8] including the United Kingdom. Several novel technologies are being developed to convert these main greenhouse gasses into value added chemicals, not only to tackle climate change but also to provide alternative energy sources. Besides the traditional thermal gas conversion, several alternative technologies are being investigated such as electrochemical and solar thermochemical methods, as well as the new technology of plasma catalysis. [9].

1.3 Plasma

Plasma is widely regarded as the fourth state of matter and is characterized by the presence of atoms, molecules, ions, energetic electrons and radicals having internal energies (with the exception of the electrons) unevenly distributed over the three degrees of freedom [10]. Energetic electrons are generated by direct current (DC), alternating current (AC) or pulsed electric fields between two electrodes using voltages in the kV range. The electrodes are separated by a gap containing one or more dielectric materials. As well as ionising gas molecules, the electrons so generated collide with gas molecules and transfer their energy over about 10⁻¹⁵ to 10⁻⁸ s [11] via processes such as excitation, ionisation, dissociation and charge transfer to produced radicals, ions, neutral atoms or molecules, according to [10]:



where e^{-} is the electron, M is a gas atom and NM is a gas molecule.

The amounts and nature of these species (radicals, ions, neutral atom or molecules) are determined by several parameters such as feed gas composition, flow rate, gas temperature, and input power and thus make the design of plasma reactors critical.

In general, there are two types of artificial plasmas: thermal plasma and non-thermal plasma (NTP). Thermal plasma can be achieved in two ways, either using high temperatures, typically ca. 400 K to 20 000 K depending on the ease of ionization, or using high gas pressure [9]. Such plasmas find a wide range of applications including welding, coating and the treatment of hazardous waste materials [12]. However, thermal plasma is unsuitable for the efficient conversion of CO_2 as the ionization and subsequent chemical process in thermal plasmas are determined by the temperature, see fig. 1.2, which shows the reduction of CO_2 as an example [9].

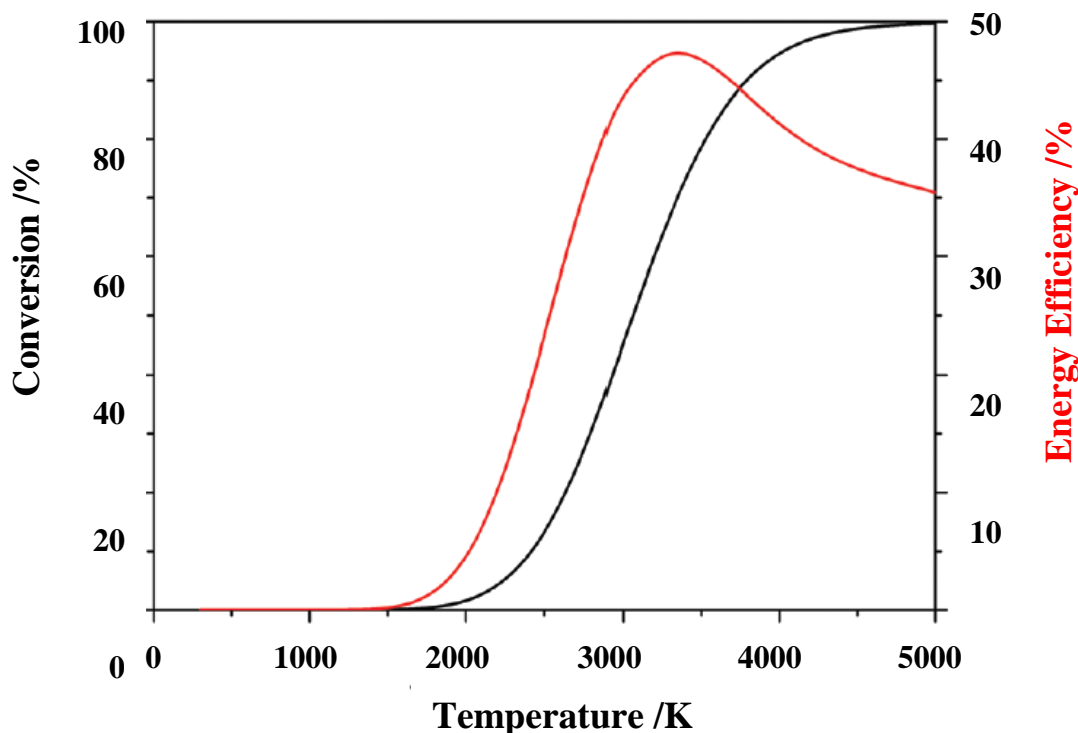


Figure 1.2. Calculated theoretical thermal conversion (left axis) and corresponding energy efficiency (right axis) as a function of temperature for the reduction of CO_2 to CO and O_2 . Adapted from Snoeckx [9].

As can be seen from fig. 1.2, the maximum energy efficiency in thermal plasmas is limited to the thermodynamic equilibrium efficiency and corresponding conversions of 47% and 80% at 3500 K as reported by Snoeckx and his co-workers [9]. This is in contrast to NTPs where efficiencies of up to 90% have been reported [9, 13].

1.4 Non thermal plasma

Non-thermal plasma at atmospheric pressure is produced by the partial ionization of a gas by electron impact using high AC or pulsed voltages in the kV range. The plasma is formed of many tiny current filaments or microdischarges with lifetimes of a few 10s of ns. These manifest themselves as current spikes in current/time profiles, typically monitored using high voltage probes and displayed on fast oscilloscopes. The temperature of the electrons in such plasmas is typically $10^4 - 10^5$ K [14], whilst the heavier species such as the ions and gas molecules remain at temperatures close to ambient. This generates radicals, ions and vibrationally and electronically excited species not normally present in thermal equilibrium at room temperature [15, 16]. Thus the key advantage of NTP chemistry is that it makes a range of chemistries available that by conventional means, would require extremes of temperature and/or pressure that would be technically challenging and economically unfeasible. Thus, for example, in principle, $\geq 95\%$ of the energy of the plasma discharge at room temperature can be transferred from the excited electrons to induce vibrational excitation of CO_2 to $\text{CO}_2^*(v)$ (eg. $v = 13$ and 24 [17]). Vibrational excitation leads to efficient dissociation to CO ($^1\Sigma$) and O (^3P), and vibrational excitation by NTP is a most effective means of stimulating the endothermic reactions relating to CO_2 dissociation.

The potential of the NTP technology is also exemplified by the work of Nozaki et al [13] on the conversion of $\text{CH}_4 + \text{water}$ in nitrogen to H_2 and C_2 hydrocarbons at 3 wt.%Ni/SiO₂ pellets in a plasma tube reactor. At temperatures > 200 °C, as well as improved conversion and efficiency, soot production was not observed, in contrast to the case in the absence of the catalyst. Overall, the performance of the reactor operating at 600 °C was 136 MJ/kg H_2 , 88% selectivity for H_2 and 64% conversion which compared well (for a non-optimised process) to standard steam reforming under the same conditions of 63 MJ/kg H_2 , 88% selectivity and 64% conversion.

1.5 Non thermal plasma reactor used for CO_2 and CH_4 conversion

1.5.1 Dielectric Barrier Discharge

Dielectric Barrier Discharge (DBD) is the most common NTP generator for CO_2 - CH_4 conversion [18-20] and such reactors have been extensively studied. DBD reactors are generally in the form of cylindrical packed bed discharge cells (PBDs, packed with dielectric

or catalyst pellets, not shown), planar volume discharge cells (VDs) or surface discharge reactors (SDs) as shown in figs. 1.3(a)-(c).

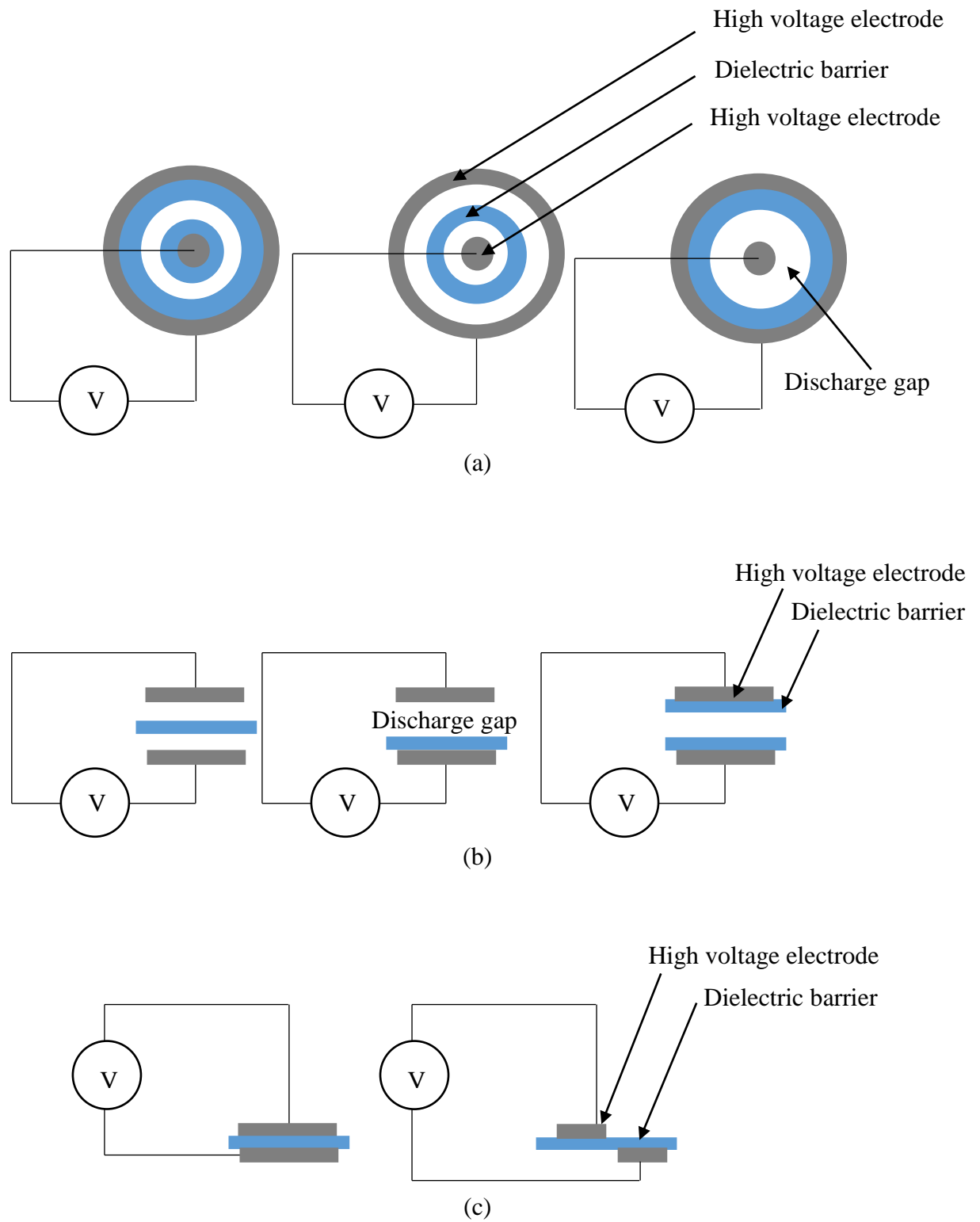


Figure 1.3. (a) PBD, (b) VD and (c) SD configurations [9, 21].

As can be seen from figs. 1.3(a)-(c), the arrangement of the electrodes and the dielectric materials are the main features that differentiate the various DBD reactors. In the volume discharge reactors, for example, streamers and plasma are generated between the two electrodes. However, unlike its volume-type counterpart, the plasma in the surface DBD discharge reactor is generated along the surface of one side of the dielectric layer [22].

In PBD reactors, additional dielectric pellets, eg. Al_2O_3 or SiO_2 , typically of mm diameter are added to fill the space between the rod electrode and the wall of the reactor. Interestingly in such reactors, surface discharge and volume discharge are generated simultaneously. Surface discharge forms at the surfaces of the dielectric beads and the dielectric layers, whilst volume discharge forms in the spaces between the beads. The influence of the dielectric beads is generally to increase the electric field around the bead contact points. This has the effect of increasing the electron energy resulting in more energetic collisions and hence would be expected to increase the conversion rates of chemical reactions in the plasma, see the Manley equation (1.5) and equation (1.6) [23]:

$$P = 4 f C_D V_{\min} \Delta V \quad (1.5)$$

where P = discharge power (W), f = voltage frequency (Hz), C_D = capacitance of the dielectric (F), V_{\min} = the minimum voltage to sustain a discharge and ΔV = the difference between V_{\min} and the operating voltage; equation (1.5) assumes that $C_D \gg$ capacitance of the gas. The capacitance of the dielectric, C_D , is given by:

$$C_D = \epsilon_r \epsilon_0 A/d \quad (1.6)$$

where ϵ_r is the relative dielectric constant, ϵ_0 is the vacuum permittivity ($8.854 \times 10^{-12} \text{ F m}^{-1}$), A is the dielectric surface area (m^2) and d is the thickness of the dielectric (m). Increasing the surface area of the dielectric, A , increases the capacitance, C_D . In turn, increasing the dielectric constant increases the capacitance and hence, from equation (1.5), increases the discharge power. Table 1.3 shows a selection of dielectric materials and their dielectric constants and table 1.4 summarises some of the findings in the conversion of CO_2 and CH_4 using PBD, VD and SD reactors.

Materials	Dielectric Constant	Reference
SiO ₂	3.8 - 3.9	[24]
Macor	6.03	[25]
Al ₂ O ₃	9.5 – 12	[26]
ZrSiO ₄	9.1	[27]
TiO ₂	31 - 114	[28]
SnO ₂	9 - 14	[29]
Teflon	1.89 – 1.93	[30]
CeO ₂	24.5	[31]
BaTiO ₃	130 - 1000	[32]
Zeolite	1.55 – 1.71	[33]
Quartz	4.2	[34]
Acrylic	2.6	[34]
Mica	6.0	[34]
Activated Charcoal	12	[35]
Si ₃ N ₄	7.5	[24]
Poly(octyl methacrylate)	3	[36]
Polypropylene)	2.2	[36]
Poly(isopropyl acrylate)	4.25	[36]
SiO ₂	3.9	[32]
Si ₃ N ₄	6	[32]
RbBr	4.7	[32]
LiF	9.2	[32]
PbTiO ₃	200 – 400	[32]
HfO ₂	40	[32]
TaO ₅	27	[32]
WO ₃	42	[32]

Table 1.3. Dielectric constant of different dielectric materials.

DBD type	Feed gas mixtures	Reaction products	Temperature /C°	Calcination temperature / C°	Dielectric materials	Ref.
PBD	CO ₂	carbon monoxide	ambient	550	Ni/SiO ₂	[37]
PBD	CH ₄	acetylene, ethylene, ethane, propene and propane	ambient	400 - 600	Pt/ γ -Al ₂ O ₃	[38]
PBD	CH ₄	ethane, ethylene, propane, propene and butane	ambient	400 - 600	Ru/TiO ₂	[39]
PBD	CH ₄ , N ₂ , O ₂	ethane, ethene, ethyne, carbon monoxide, carbon dioxide and nitrous oxide	ambient	n/a	BaTiO ₃	[40]
PBD	CH ₄ , CO ₂	acetylene, ethylene, ethane, propene, propane and carbon monoxide	ambient	n/a	Quartz	[41]
PBD	CH ₄ , CO ₂	carbon monoxide, H ₂	400 – 700	n/a	Ni/Al ₂ O ₃	[42]
PBD	CH ₄ , N ₂ , H ₂ O	carbon monoxide, H ₂ , ethane, propane and butane	200 – 700	n/a	Ni/SiO ₂	[43]
PBD	CH ₄ , CO ₂ , Ar	ethane, ethylene, propane, propylene, methanol, ethanol and carbon monoxide	120 – 290	n/a	Al ₂ O ₃	[44]
PBD	CH ₄ , CO ₂ , Ar	ethane, ethylene, propane, propylene, methanol, ethanol and carbon monoxide	120 – 290	n/a	Ag/Al ₂ O ₃	[44]
PBD	CH ₄ , CO ₂ , Ar	ethane, ethylene, propane, propylene, methanol, ethanol and carbon monoxide	120 – 290	n/a	Pd/Al ₂ O ₃	[44]
PBD	CH ₄ , CO ₂	ethylene, acetylene, and propylene, carbon monoxide, H ₂	ambient	n/a	Quartz	[45]
PBD	CO ₂ , N ₂	nitrous oxide, NO _x , carbon monoxide and O ₂	ambient	n/a	Quartz	[46]

PBD	CH ₄ , Ar	ethane, ethylene, acetylene, propane, propene, butane and H ₂	ambient	n/a	Al ₂ O ₃	[47]
PBD	CH ₄ , Ar	ethane, ethylene, acetylene, propane, propene, butane and H ₂	ambient	n/a	MgO/Al ₂ O ₃	[47]
PBD	CH ₄ , Ar	ethane, ethylene, acetylene, propane, propene, butane and H ₂	ambient	n/a	TiO ₂ /Al ₂ O ₃	[47]
PBD	CH ₄ , CO ₂	carbon monoxide, H ₂ , ethane, ethylene, acetylene, propane, propene, butane	20-150	n/a	Zeolite	[48]
PBD	CH ₄ , CO ₂ , N ₂	ethane, propane, carbon monoxide and H ₂	24 - 500	n/a	Quartz	[49]
PBD	CH ₄ , N ₂	acetylene, hydrogen cyanide, ethane and ammonia	ambient	n/a	Borosilicate glass	[50]
SD	CH ₄ , N ₂	ethane, ethylene, acetylene, propane, propene, butane, ammonia and H ₂	ambient	n/a	Al ₂ O ₃	[51]
SD	CH ₄ , CO ₂ , Ar	carbon monoxide, ethylene, ethane, tertibutylic, acetaldehyde, acetone and H ₂	ambient	n/a	Quartz	[52]
SD	CH ₄ , CO ₂ , N ₂	carbon monoxide, H ₂ and water	ambient	n/a	Pyrex glass	[53]
SD	CO ₂ , H ₂	carbon monoxide dimethyl ether, methane, H ₂ and water	ambient	n/a	Al ₂ O ₃	[54]
VD	CH ₄ , O ₂	methanol, carbon monoxide, carbon dioxide, water and ethane	ambient	n/a	Quartz	[55]
VD	CH ₄ , N ₂	hydrogen cyanide and N ₂	ambient	n/a	Pyrex glass	[56]

Table 1.4. A summary of the studies on the use of DBD reactors for the conversion of CO₂ and CH₄ to higher hydrocarbons.

As can be seen from table 1.4, to date and in general, studies of NTPs have been carried out at temperatures above ambient often to investigate the conversion of CO₂ and CH₄ as a function of the gas temperature [44, 57] or to study the effects of catalyst loading [58], particle size [47] or catalyst calcination temperature [38, 39]. Generally, CO₂ and CH₄ were fed from a pressurized gas cylinder and the gas mixture was heated to the desired temperature using a tubular heat exchanger [59] or by the outer electrical heater [43, 44, 49] and the gas temperature was then measured at the surface of the reactor wall [44] and/or in the gap between the dielectric and grounded electrode [40, 57]. Although, CO₂ and dry reforming methane are well known in NTP processing, the literature dealing with catalysis selection for the studies of such processes is quite limited [60]. Consequently, this leads to dielectric material/catalyst selection for NTP process being based on identifying those materials that are active for the same chemical processes when carried out in conventional, analogous thermal conversions operating under steady state conditions. However, plasmas are definitely not in a steady state as the plasma is itself driven by a succession of microdischarges (the amplitude and frequency of which depend strongly on the dielectric material between the electrode [61]) each with lifetime of a few tens of nanoseconds. The importance of this is that the lifetime of many species formed is only of this magnitude, with the result that decay of the molecular fragments takes place on timescales comparable to the discharges themselves. The assumption that catalysts active in thermal process will also be active in the analogous plasma-driven ones is something that should be scrutinized.

Interestingly, it was realized that certain dielectrics could also act as catalysts and steer the reaction to yield different products with different catalysts, but the trends observed when using a range of such catalysts are simply not understood [15, 43, 47, 62]. The NTP conversion of CO₂ to CO and O₂ for example is inefficient in the absence of catalyst due to the back reaction $\text{CO} + \text{O} \rightarrow \text{CO}_2$ and exhibits poor energy efficiencies. However, the conversion can be improved using an appropriate material such as Ca_{0.7} Sr_{0.3}TiO₃ where a stronger and denser micro discharge were generated compared to alumina or silica glass [61], see fig. 1.4.

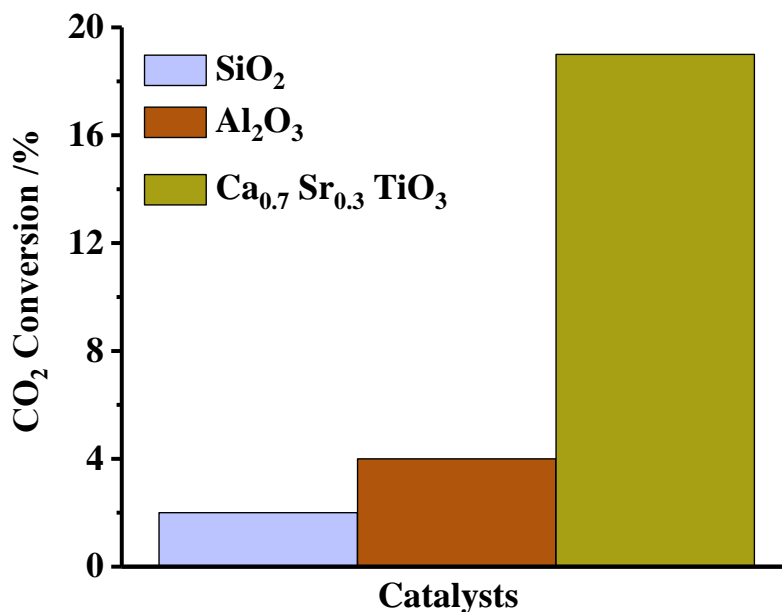


Figure 1.4. A comparison of CO₂ conversion using three different materials in the NTP conversion of CO₂ at a fixed frequency of 8 kHz. Adapted from Ruixing Li et al. [63].

As can be seen from the fig. 1.4, CO₂ conversion reached 18.8% when Ca_{0.7}Sr_{0.3}TiO₃ was used as a dielectric/catalyst compared to alumina (4.7%) or silica glass (3.8%). This is due to the fact that the value of C_D of Ca_{0.7}Sr_{0.3}TiO₃ (C_D = 431 pF) is higher than that of alumina (21 pF) and silica glass (9 pF) owing to the increasing of the permittivity and, in turn, increasing the plasma power (P) as discussed previously.

Zhang et al. [64] studied CO₂ and CH₄ conversion at SiO₂-based materials and also showed that the catalyst can have a significant effect upon the conversion of CO₂ and CH₄. The NTP conversion of CO₂ and CH₄ in the presence of Ni/SiO₂ resulted in lower conversion of CO₂ and CH₄, and this was attributed to the reverse reaction of CO and H₂ to CH₄ and CO₂. However, using NiFe/SiO₂ as the catalyst increased the conversion of CH₄ and CO₂, suggesting that the presence of Fe increased the selectivity to H₂ and enhanced the conversion of CH₄.

To date, it is generally perceived that plasma-driven catalytic (plasma catalytic) syntheses are too expensive in energy terms to compete with standard, thermal processes. However, one highly topical potential application where energy efficiency is not a primary driver is the use

of electricity from renewable sources to generate chemical products. Matching the production of electricity from renewable energy to demand is very difficult, and often the surplus is simply spilled: the storage of this surplus energy chemically by plasma catalysis is seen as a possible solution to this problem. The exciting prospect that plasma-catalysis may generate different, and potentially novel products, when compared to conventional thermal process also offers a firm foundation for the development of this pioneering technology, see fig. 1.5.

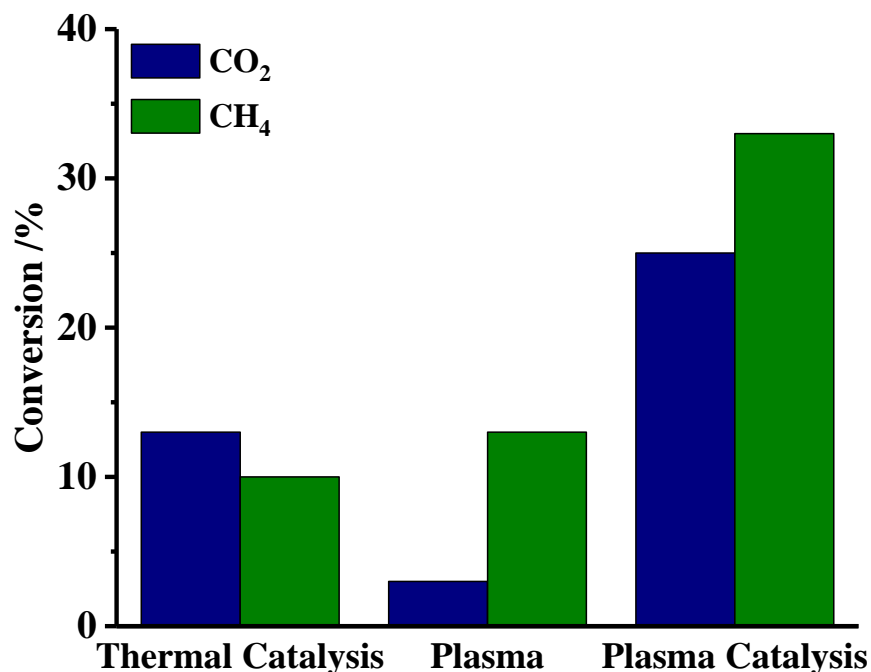


Figure 1.5. A comparison of CO₂ and CH₄ conversion by thermal catalysis, plasma-induced conversion and the combination of plasma and catalysis conversion using 1% Cu- 12% Ni/ γ -Al₂O₃ as the catalyst, 50% CH₄ + 50% CO₂ as the feed gas at a total flow rate of 60 cm³ min⁻¹ and a temperature of 450 °C. Adapted from Zhang et al. [58].

As can be seen from fig. 1.5, the effects of the plasma catalytic conversion of CH₄ and CO₂ was higher than the sum of thermal catalysis and plasma-induced conversion of CO₂ and CH₄. Under purely catalytic conditions, the catalyst was reported active at 300 °C and the conversions of CH₄ and CO₂ were about 10% and 13% respectively, at 450 °C. However, the conversions of CH₄ and CO₂ by plasma catalysis was greater than in the absence of catalyst and thermal catalysis, and the conversions of CH₄ and CO₂ were about 33% and 25%. Combining plasma with a catalyst clearly improves chemical conversion and/or offers

alternative mechanistic pathways with lower activation energies. The general working principle of a catalyst is shown in fig. 1.6.

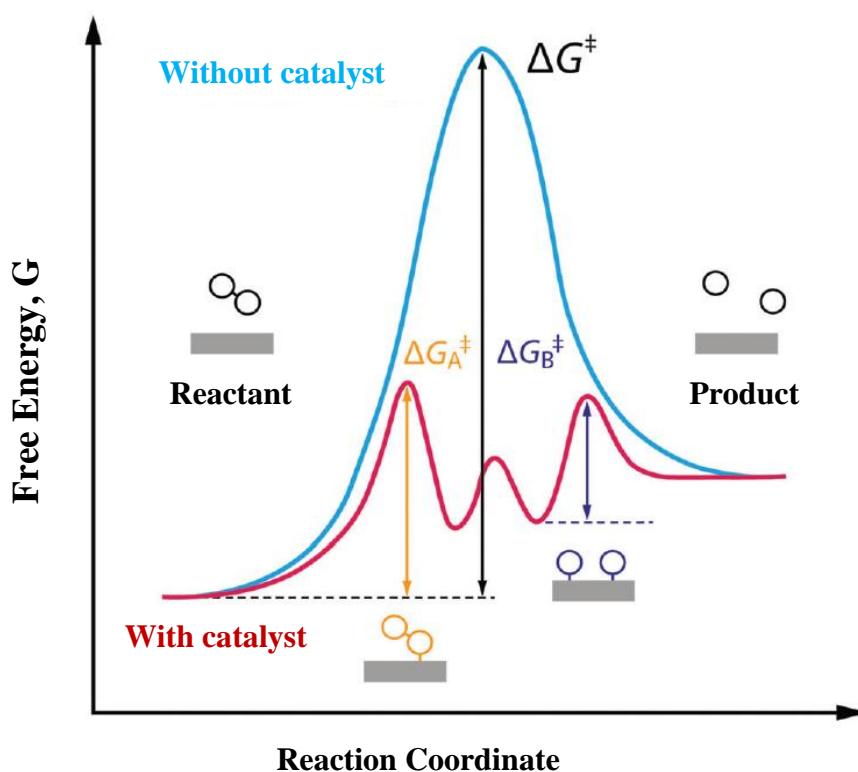


Figure 1.6. Energy diagram illustrating the working principle of a catalyst. Adapted from Snoeck [9].

As can be seen from fig. 1.6, the presence of the catalyst opens a different reaction pathway (shown in red) with a lower activation energy, ΔG_A^\ddagger : thus, reactive species are produced and interact with the catalyst at temperatures at which most purely thermally-driven processes would be slow. Further, vibrationally excited molecules can have markedly different sticking probabilities and different chemistries on the surface of catalysts in contact with plasma [65] and it should be possible to enhance targeted reactions and suppress others by controlling the number density of electrons and electron and gas temperatures.

Wang et al. [66] studied CO_2 and CH_4 conversion using three different catalyst materials in a DBD reactor, and also showed that plasma catalysis improved the chemical conversion of CO_2 and CH_4 and the selectivity of gaseous products compared to the analogous thermal process, see figs. 1.7.

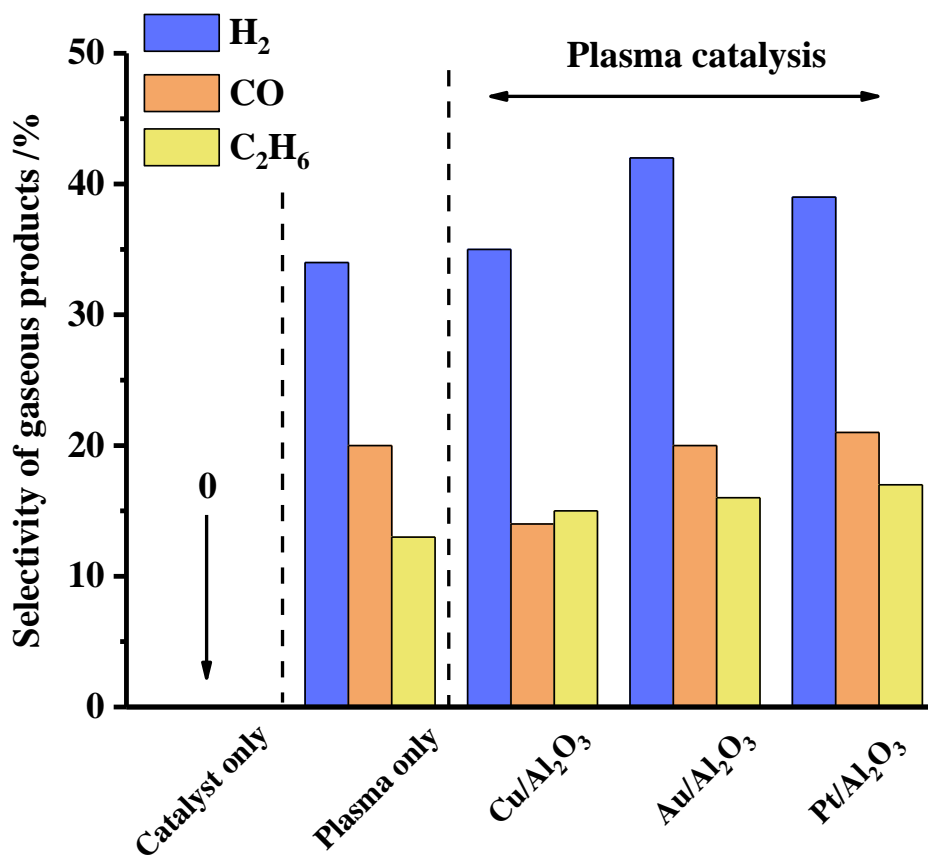


Figure 1.7. A comparison of CO₂ and CH₄ conversion and gaseous products selectivities for catalysis activation only, plasma-induced conversion and plasma catalysis for three different catalyst materials in a DBD reactor at 30 °C and atmospheric pressure. Adapted from Wang *et al.* [66] and Bogaerts and Neyts [67].

As can be seen from fig. 1.7, the selectivities of the gaseous products were found to be similar with H₂, CO and C₂H₆ being the major products in the plasma and plasma catalysis experiments. Using Cu/Al₂O₃ as a catalyst with thermal activation gave no conversion at ambient temperature. Interestingly, in contrast to the selectivities of the gaseous products, the selectivities of the liquid products were different when Pt/Al₂O₃ and Au/Al₂O₃ were used, see fig. 1.8.

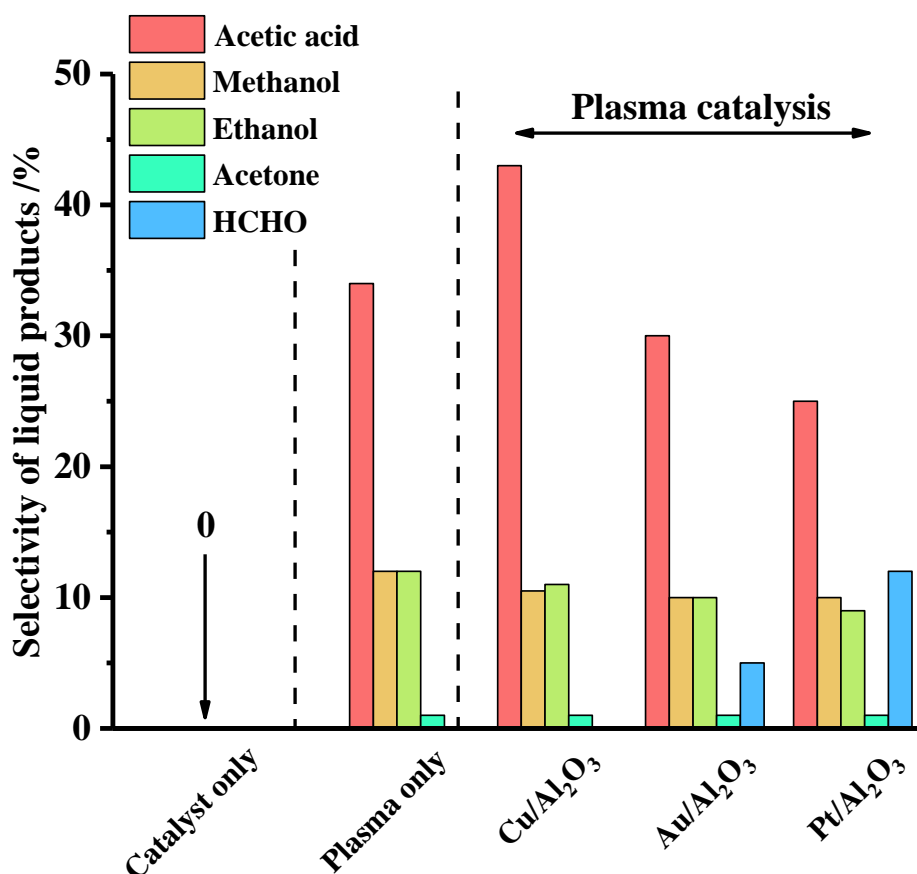


Figure 1.8. A comparison of CO_2 and CH_4 conversion and liquid products selectivities for catalysis activation only, plasma-induced conversion and plasma catalysis for three different catalyst materials in DBD at 30°C and atmospheric pressure. Adapted from Wang et al. [66] and Bogaerts and Neyts [67].

As can be seen from fig. 1.8, the main liquid products were acetic acid, methanol, ethanol and a small amount of acetone with a total selectivity of 59% in the plasma experiments. The combination of plasma and catalysis gave the same liquid products, but HCHO an additional product when $\text{Pt}/\text{Al}_2\text{O}_3$ and $\text{Au}/\text{Al}_2\text{O}_3$ were employed as the catalyst.

It is clear from the discussion above that the combination of plasma and catalysis has the potential to drive chemical process in new directions; however, the approach for chemical synthesis is relatively little-explored, probably because the fundamental understanding of such process is still lacking [67]. This, in turn, is due to the lack of analytical studies which are

able to provide molecular information. Hence the chemical mechanisms and kinetics involved are simply not understood [9, 15, 43, 47, 67].

1.6 The non-thermal plasma conversion of CO₂ and CH₄

Generally, NTP reactors for CO₂-CH₄ are most commonly of the packed-bed type, either as a variant of the tube reactors described in the previous section with the gap filled with the catalyst/dielectric pellets, or two plate electrodes separated by a gap filled with pellets [68]. It is not at all clear these configurations are optimum, as there is no theoretical basis for their design: such a basis requires the chemistry taking place in the reactor to be modelled. All designs so far have essentially been empirical; they have not as yet been formulated on the basis of known or estimated rate constants or reaction mechanisms. The interaction of highly excited and reactive species with solid surfaces is largely unknown, both in terms of the chemistry and the timescale over which such reactions take place [15]. For example, in the absence of information on the identities of the species present in non-thermal plasmas, and at the solid (dielectric and/or catalyst)/plasma interface, all possible species need to be included in the model (e.g. up to 150 molecules [69, 70]) which increases computing time and decreases the accuracy of the model. Previous Fourier Transform InfraRed (FTIR) spectroscopic studies in Newcastle strongly suggests that it should be possible to provide the hard experimental data required to aid effective modelling and hence reactor design [71]. Furthermore, whilst the potential synergy between NTP and catalysis is widely acknowledged in the NTP community, it has not been possible to include catalysis in models: indeed, even accounting for chemical reactions on the chemically simple surfaces of the HV electrodes has proven too challenging [72] due to the lack of chemical information on the species present.

1.7 Infrared Spectroscopy

Ultraviolet-visible (UV Vis) absorption and emission spectroscopies have been employed for a number of years in the study of plasma as may be expected given the inevitable emission of light from plasma. Such studies give useful information on excited species [73, 74]; however, it is generally recognised that such studies need to be complemented by those employing techniques able to provide molecular information, eg. FTIR spectroscopy, particularly if these

can be carried out at timescales sufficiently short to match the microdischarges and hence the lifetimes of likely intermediates [15].

The field of electrochemistry underwent a paradigm shift in the 1980s with the advent of in-situ analytical methods for the study of the electrocatalyst/electrolyte interface and, in particular, the application of in situ FTIR spectroscopy with its ability to determine the identity of adsorbed and solution intermediates and products [75, 76]. The field of NTP catalysis is at a similar stage of development as electrochemistry was in the mid-1980s: whilst the plasma/catalyst surface has not been investigated extensively with in-situ FTIR, such studies have started to appear. There are numbers of studies on the downstream analysis of the exhaust from NTPs, such as work of Zaenab Abd Allah [72] in Manchester who employed FTIR to identify species generated on decomposition of dichloromethane (DCM) as a function of oxygen concentration in nitrogen plasma, and the work of Abdullah Al-Abduly in Newcastle [71] who reported an in-situ and downstream spectroscopic study of NTP chemistry in an air-fed DBD plasma. However, studies of the catalyst in contact with plasma is only a recent phenomenon and are summarised in table 1.5.

Researchers	NTP Experiments	FTIR studies region	Reaction Products	Ref
Li et al.	Deposition of Si from hexamethyldisiloxane	Plasma region	CH ₃ , CH ₃ , Si-(CH ₃), SiO _x , Si-O-Si,	[77]
Rivallan et al.	Conversion of Isopropyl alcohol (IPA) at Al ₂ O ₃	Plasma/catalyst interface	acetaldehyde, acetone, crotonaldehyde, isobutene, isopropanol	[78]
Stere et al.	Hydrocarbon assisted-NO _x removal from simulated diesel fuel over silver-based catalyst	Plasma/catalyst interface	acetate, nitrate, carboxylate, isocyanate	[79]

Rodriguez et al.	Conversion of IPA at Al ₂ O ₃ , CeO ₂ , and TiO ₂	Plasma/catalyst interface	aldehyde, carbonate, carboxylic acid, CO, OH	[80]
Jia and Rousseau	Plasma-assisted reaction of acetone at CeO ₂	Plasma region	mesityl oxide, acetic acid, isobutene	[81]

Table 1.5. A summary of the FTIR studies of the catalyst in contact with plasma.

The quality of the information that can be obtained from in-situ FTIR is exemplified by the work of Li et al. [77], Rivallan et al. [78], Stere et al [79], Rodriguez [80] and Jia and Rousseau [81]. These studies employed the Difused Reflectance approach [79, 80], transmission through catalyst as a wafer [78, 81] or passed the IR beam through the plasma glow above the solid surface [71, 77]. Rivallan and co-workers [78] employed the step scan approach to study the gas phase reduction of CO₂ in a tube reactor (i.e they did not study the catalyst/plasma interface); however, they saw no reaction products or intermediates, although the authors did achieve a time resolution of ca. 400 μ s.

1.8 Plasma catalysis

Gas phase conversions in NTPs remain inefficient and costly in energy terms. To illustrate this, consider two of the most studied NTP reactions, the reduction of CO₂ to CO and O₂:

$\text{CO}_2 \rightarrow \text{CO}_2^*(\text{v}) \rightarrow \text{CO} + \text{O}$, $\text{O} + \text{O} \rightarrow \text{O}_2$, and methane conversion (reforming, partial oxidation etc). The reduction of CO₂ is inefficient due to the back reaction of O (³P) with CO, and a means must be found to stabilize the O atoms to prevent this. With respect to chemical conversions involving CH₄, it is generally accepted that the vibrational excitation of CH₄ to CH₄^{*}(v) is efficient, generating the vibrational excited state at up to 100x the number density of electrons [13]; however, this is wasted energy due to the short lifetime of CH₄^{*}(v) (ns) and low threshold energies (ie. < 2 eV compared to C-H bonding in most hydrocarbons of 3 – 6 eV [68]). The situation can be transformed if a suitable catalyst is employed, as can be seen from the work of Nozaki and co-workers detailed above (see section 1.4); in addition, it is clear that catalysis can have a significant effect upon the mechanism of a NTP-driven

chemical conversion: for example, the conversion of toluene in an NTP reactor in the presence of NiO/WO₃ results in total oxidation; however, using Mordenite as a catalyst favours phenol production while Faujasite favours partial oxidation and the formation of cresols [13, 73, 82].

As was stated in section 1.5, despite the clear potential benefits of catalysis, it appears that catalysts for plasma processing are primarily selected on the basis of the materials that have proven effective for the analogous thermal processes, rather than on the basis of a well-defined theoretical framework, which, if there is no interaction between plasma and catalyst is a fair assumption; however it is known, even on the physical level, that plasma induces changes in catalyst morphology, including particle size and roughness [83]. There are theories or part-theories to explain the effect of catalysis: eg. it is generally accepted that the sticking probabilities of vibrationally excited species, eg. CH₄^{*}(v), are 10 – 10⁴x greater than their ground states [68] and hence the addition of a suitable catalyst will significantly enhance the rate of a plasma reaction. But an effective, validated theoretical model is urgently required if catalysis selection is to be effective, progress is to be made, and the full potential of plasma processing realised. This has been, severely impeded by the absence of any information on the chemical identity and lifetimes of the reactive species in the plasma, and at the catalyst and/or dielectric/plasma interface (solid/plasma interface). A variety of active species have been postulated in plasmas depending (of course) on the gas feed, eg. in CO₂ plasmas containing also CH₄ (eg. re. reforming/partial oxidation to methanol) and/or H₂O these include: CO₂^{*}(v) (vibrationally excited CO₂), CH₄^{*}(v), CO₂⁺, CO₂⁻, O₂⁻, OH radicals, O₃, O (³P) and O (¹D). Of these, O₃ has been observed using UV Vis spectroscopy and O (³P) & CO₂⁺ by optical emission spectroscopy. Despite the fact that CO₂^{*} is postulated as a key intermediate in the chemistry of CO₂-containing plasmas [84], an excited form of CO₂ was directly observed for the first time by Al-Abduly in Newcastle [71], which was incorrectly identified at the time as vibrationally-excited CO₂. The work reported in this thesis showed this, in fact, to be rotationally-excited CO₂.

Plasma induced chemical conversions have been modelled using thermodynamic principles and literature rate constants; however, such models inevitably describe a fixed volume of gas [84] and hence do not take into account drift behaviour in the more relevant case of flowing gas. Further, whilst the very significant potential offered by catalysis is widely acknowledged

in the NTP community, it has not proven possible to include catalysis in models. A recurrent theme in the literature has been [85, 86] and remains [47, 62, 70] that trends observed when using a range of catalysts are not understood and the participation of the high voltage electrodes in chemical processes has been postulated [62] but remains unproven. Again, the absence of information on the actual species present enhances the challenges faced by those attempting to model the processes taking place in NTPs.

The lack of key information impacts on the design and optimisation of plasma reactors: thus NTP reactors are generally confined to gas phase reactions and are based on just three standard designs:

- (1) A (glass) tube reactor with a foil electrode on the outside and a rod electrode inside (in this case, the dielectric materials are the gas and glass reactor wall): the inner electrode could be coated with a catalyst such as Pt, Rh etc.
- (2) A previous but with the gap filled with dielectric beads or pellets.
- (3) A tube reactor with two disc electrodes separated by dielectric beads or pellets. In configurations (2) and (3) the dielectric material could be coated with a catalyst, eg Ni/SiO₂.

To date, there are no reliable quantifiable data on the identity of the species, active and otherwise, present in NTPs or on, or near, the solid/plasma surface. As a result, catalysis in plasmas is ill-understood and the range of catalysts employed in plasma-driven conversions remains limited. Further, the number of reactor designs is severely limited. Until such molecular information is available, catalyst selection will remain guesswork and the potential of plasma chemical conversions will remain unfulfilled. This conclusion is supported by the US Plasma 2010 Committee report [87] which concluded that the interactions of plasmas with solid surfaces is one of the six critical challenges that define the research frontier, a view that is still very much reflected in the literature [61, 85].

1.9 Dielectric/catalyst materials and plasma cells to be investigated

The dielectric/catalyst chosen for this work were Macor, CeO₂ and SnO₂ and were selected as dielectric materials in this work due to the following reasons:

- Firstly, Macor (quartz (35–50%), magnesium oxide (15–20%), aluminium oxide (15–20%) and fluoride (1–5%)) was chosen as the dielectric for its reasonable dielectric constant, ca 6, and its stability over the temperature range of interest, 25–600 °C [25] rather than for any possible catalytic activity, initially to provide benchmark data as it was assumed Macor would be catalytically inactive, and had good thermal stability for comparison between thermal and plasma experiments.
- Secondly, SnO₂ was chosen as it is a catalyst in various chemical processes including the electrochemical reduction of CO₂ to CO on SnO₂ [88, 89] and the total oxidation of CH₄ at SnO₂ [90]: more importantly, previous studies in Newcastle had provided a wealth of IR data on the effect of temperature on SnO₂ [91].
- Finally, CeO₂ has been studied with respect to the thermally and plasma – driven conversion of IPA [92] and chlorobenzene [93] by IR spectroscopy and hence data was available for comparison and interpretation.

1.10 Project aim and objectives

The overall project aim of the project is to study the processes taking place in non-thermal plasma using FTIR spectroscopy. The system chosen for study was CH₄ + CO₂ + N₂.

The objectives were to:

1. Commission IR plasma transmission and reflectance cells.
2. Employ these cells to study the chemistries taking place in the plasma glow and plasma/dielectric and plasma/catalyst interfaces as a function of experimental conditions and catalyst.

3. Compare and contrast plasma and thermally driven data obtained using the same reactants and catalyst and hence assess the validity of catalyst selection based on activity in thermal process.

1.11 References

1. *CO₂ Emissions From Fuel Combustion 2017: Overview*. 2017, International Energy Agency: International Energy Agency.
2. *WMO Greenhouse Gas Bulletin*. 2017, World Meteorological Organization
3. *UK Greenhouse Gas Emission, Final Figures. Statistical Release: National Statistics*. 2018, Department for Business, Energy & Industrial Strategy: United Kingdom.
4. Team, C.W., R.K. Pachaur, and L. Meyer, *Climate Change 2014: Synthesis Report. Contribution of Working Groups I, II and III to the Fifth Assessment Report of the Intergovernmental Panel on Climate Change*. 2014, IPCC: IPCC, Geneva, Switzerland.
5. Tomáš, K. and B. Annemie, *Splitting of CO₂ by vibrational excitation in non-equilibrium plasmas: a reaction kinetics model*. Plasma Sources Science and Technology, 2014. **23**(4): p. 045004.
6. Bogaerts, A., T. Kozak, K. van Laer, and R. Snoeckx, *Plasma-based conversion of CO₂: current status and future challenges*. Faraday Discussions, 2015. **183**(0): p. 217-232.
7. Saeidi, S., N.A.S. Amin, and M.R. Rahimpour, *Hydrogenation of CO₂ to value-added products—A review and potential future developments*. Journal of CO₂ Utilization, 2014. **5**: p. 66-81.
8. *Paris Agreement - Status of Ratification*. 2018 [cited 2018 March 22]; Available from: http://unfccc.int/paris_agreement/items/9444.php.
9. Snoeckx, R. and A. Bogaerts, *Plasma technology - a novel solution for CO₂ conversion?* Chemical Society Reviews, 2017. **46**(19): p. 5805-5863.
10. A Gicquel, S.C.a.J.A., *Heterogeneous catalysis in low-pressure plasmas*. Journal of Physics D: Applied Physics, 1983. **19**(11): p. 2013-2042.
11. Ibrahim, R.K.R., *Mid-infrared diagnostics of the gas phase in non-thermal plasma applications*, in *School of Chemical Engineering and Analytical Science 2011*, University of Manchester

12. Smith, R.W., D. Wei, and D. Apelian, *Thermal plasma materials processing—Applications and opportunities*. Plasma Chemistry and Plasma Processing, 1989. **9**(1): p. 135S-165S.
13. Tomohiro Nozaki, N.M., Shigeru Kadio, Ken Okazaki, *Dissociation of Vibrationally Excited Methane on Ni Catalyst: Part 2. Process Diagnostic by Emission Spectroscopy*. Catalysis Today, 2004. **89**(1-2): p. 67-74.
14. Christensen, P.A., A.H.B.M. Ali, Z.T.A.W. Mashhadani, and P.A. Martin, *A Direct Fourier Transform Infrared Spectroscopic Comparison of the Plasma- and Thermally-Driven Reaction of CO₂ at Macor*. Plasma Chemistry and Plasma Processing, 2018. **38**(2): p. 293-310.
15. Whitehead, J.C., *Plasma-catalysis: the known knowns, the known unknowns and the unknown unknowns*. Journal of Physics D: Applied Physics, 2016. **49**(24): p. 243001.
16. Aerts, R., T. Martens, and A. Bogaerts, *Influence of Vibrational States on CO₂ Splitting by Dielectric Barrier Discharges*. The Journal of Physical Chemistry C, 2012. **116**(44): p. 23257-23273.
17. Hsin Liang Chen, H.M.L., Shiaw Huei Chen, Yu Chao, Moo Been Chang, *Review of Plasma Catalysis on Hydrocarbon Reforming for Hydrogen Production - Interaction, Intergration, and Prospects*. Applied Catalysis B: Environmental, 2008. **85**: p. 1-9.
18. Kolb, T., J.H. Voigt, and K.-H. Gericke, *Conversion of Methane and Carbon Dioxide in a DBD Reactor: Influence of Oxygen*. Plasma Chemistry and Plasma Processing, 2013. **33**(4): p. 631-646.
19. Kolb, T., T. Kroker, J.H. Voigt, and K.-H. Gericke, *Wet Conversion of Methane and Carbon Dioxide in a DBD Reactor*. Plasma Chemistry and Plasma Processing, 2012. **32**(6): p. 1139-1155.
20. Motret, O., S. Pellerin, M. Nikravech, V. Massereau, and J.M. Pouvesle, *Spectroscopic Characterization of CH₄ + CO₂ Plasmas Excited by a Dielectric Barrier Discharge at Atmospheric Pressure*. Plasma Chemistry and Plasma Processing, 1997. **17**(4): p. 393-407.
21. Ayman, A.A., S. Takafumi, M. Abdel-Salam, and O. Yoshio, *Performance of a surface dielectric barrier discharge based reactor for destruction of naphthalene in an air stream*. Journal of Physics D: Applied Physics, 2012. **45**(11): p. 115201.

22. Šimek, M., S. Pekárek, and V. Prukner, *Influence of Power Modulation on Ozone Production Using an AC Surface Dielectric Barrier Discharge in Oxygen*. Plasma Chemistry and Plasma Processing, 2010. **30**(5): p. 607-617.
23. Eliasson, B. and U. Kogelschatz, *Discharge reactor and uses thereof*. 2000, Google Patents.
24. *Properties of SiO₂ and Si₃N₄ at 300K* 2018 [cited 2018 16 April]; Available from: <http://eesemi.com/sio2si3n4.htm>.
25. *MACOR - Machinable Glass Ceramic Data Sheet*. <http://psec.uchicago.edu/ceramics/MACOR%20Data%20Sheet.pdf> [cited 2016 19 January].
26. Khalid, Z.R., N. Mira, H.L. Edmund, C.N. Juan, A. Daniel, T. David, M. Raj, and L. Michael, *Broadband Dielectric Characterization of Aluminum Oxide (Al₂O₃)*. Journal of Microelectronics and Electronic Packaging, 2008. **5**(1): p. 2-7.
27. Varghese, J., D.R. Nair, P. Mohanan, and M.T. Sebastian, *Dielectric, thermal and mechanical properties of zirconium silicate reinforced high density polyethylene composites for antenna applications*. Physical Chemistry Chemical Physics, 2015. **17**(22): p. 14943-14950.
28. Berberich, L.J. and M.E. Bell, *The Dielectric Properties of the Rutile Form of TiO₂*. Journal of Applied Physics, 1940. **11**(10): p. 681-692.
29. Daal, H.J.v., *The Static Dielectric Constant of SnO₂*. Journal of Applied Physics, 1968. **39**(9): p. 4467-4469.
30. *PTFE - Properties Handbook*. [cited 2016 25 January]; Available from: http://www.rjchase.com/ptfe_handbook.pdf.
31. Ansari, S.A., M.M. Khan, M.O. Ansari, S. Kalathil, J. Lee, and M.H. Cho, *Band gap engineering of CeO₂ nanostructure using an electrochemically active biofilm for visible light applications*. RSC Advances, 2014. **4**(32): p. 16782-16791.
32. Gupta, T., *Copper Interconnect Technology*. 2014, Winchester, USA: Springer, New York.
33. Sun, M., W. Maichen, R. Pophale, Y. Liu, R. Cai, C.M. Lew, H. Hunt, M.W. Deem, M.E. Davis, and Y. Yan, *Dielectric constant measurement of zeolite powders by time-domain reflectometry*. Microporous and Mesoporous Materials, 2009. **123**(1): p. 10-14.

34. Taylan, O. and H. Berberoglu, *Discharge of Carbon Dioxide Using a Non-Thermal Plasma Reactor*. 2013(55485): p. V002T05A016.
35. *Dielectric Constants*. [cited 2018 16 April]; Available from: <https://krohne.com/en/services/dielectric-constants/>.
36. Riedel, C., *Dielectric and mechanical properties of polymers at macro and nanoscale*, in *Physics*. 2010, Université Montpellier 2.
37. Zhang, K., G. Zhang, X. Liu, A.N. Phan, and K. Luo, *A Study on CO₂ Decomposition to CO and O₂ by the Combination of Catalysis and Dielectric-Barrier Discharges at Low Temperatures and Ambient Pressure*. *Industrial & Engineering Chemistry Research*, 2017. **56**(12): p. 3204-3216.
38. Kim, S.-S., H. Lee, J.-W. Choi, B.-K. Na, and H.K. Song, *Methane conversion to higher hydrocarbons in a dielectric-barrier discharge reactor with Pt/ γ -Al₂O₃ catalyst*. *Catalysis Communications*, 2007. **8**(9): p. 1438-1442.
39. Kim, S.-S., B. Kwon, and J. Kim, *Plasma catalytic methane conversion over sol-gel derived Ru/TiO₂ catalyst in a dielectric-barrier discharge reactor*. *Catalysis Communications*, 2007. **8**(12): p. 2204-2207.
40. Ogata, A., K. Mizuno, S. Kushiyama, and T. Yamamoto, *Methane Decomposition in a Barium Titanate Packed-Bed Nonthermal Plasma Reactor*. *Plasma Chemistry and Plasma Processing*, 1998. **18**(3): p. 363-373.
41. Snoeckx, R., Y.X. Zeng, X. Tu, and A. Bogaerts, *Plasma-based dry reforming: improving the conversion and energy efficiency in a dielectric barrier discharge*. *RSC Advances*, 2015. **5**(38): p. 29799-29808.
42. Seigo, K., M. Ryo, Y. Takumi, A.P. Lukman, and N. Tomohiro, *Interfacial reactions between DBD and porous catalyst in dry methane reforming*. *Journal of Physics D: Applied Physics*, 2018. **51**(11): p. 114006.
43. Nozaki, T., N. Muto, S. Kado, and K. Okazaki, *Dissociation of vibrationally excited methane on Ni catalyst: Part I. Application to methane steam reforming*. *Catalysis Today*, 2004. **89**(1): p. 57-65.
44. Sentek, J., K. Krawczyk, M. Młotek, M. Kalczewska, T. Kroker, T. Kolb, A. Schenk, K.-H. Gericke, and K. Schmidt-Szałowski, *Plasma-catalytic methane conversion with carbon dioxide in dielectric barrier discharges*. *Applied Catalysis B: Environmental*, 2010. **94**(1): p. 19-26.

45. Liu, C.-J., B. Xue, B. Eliasson, F. He, Y. Li, and G.-H. Xu, *Methane Conversion to Higher Hydrocarbons in the Presence of Carbon Dioxide Using Dielectric-Barrier Discharge Plasmas*. Plasma Chemistry and Plasma Processing, 2001. **21**(3): p. 301-310.
46. Snoeckx, R., S. Heijkers, K. Van Wesenbeeck, S. Lenaerts, and A. Bogaerts, *CO₂ conversion in a dielectric barrier discharge plasma: N₂ in the mix as a helping hand or problematic impurity?* Energy & Environmental Science, 2016. **9**(3): p. 999-1011.
47. Kasinathan, P., S. Park, W.C. Choi, Y.K. Hwang, J.-S. Chang, and Y.-K. Park, *Plasma-Enhanced Methane Direct Conversion over Particle-Size Adjusted MO_x/Al₂O₃ (M = Ti and Mg) Catalysts*. Plasma Chemistry and Plasma Processing, 2014. **34**(6): p. 1317-1330.
48. Eliasson, B., C.-j. Liu, and U. Kogelschatz, *Direct Conversion of Methane and Carbon Dioxide to Higher Hydrocarbons Using Catalytic Dielectric-Barrier Discharges with Zeolites*. Industrial & Engineering Chemistry Research, 2000. **39**(5): p. 1221-1227.
49. Xuming, Z. and C. Min Suk, *Electron-induced dry reforming of methane in a temperature-controlled dielectric barrier discharge reactor*. Journal of Physics D: Applied Physics, 2013. **46**(41): p. 415205.
50. Horvath, G., N.J. Mason, L. Polachova, M. Zahoran, L. Moravsky, and S. Matejcik, *Packed Bed DBD Discharge Experiments in Admixtures of N₂ and CH₄*. Plasma Chemistry and Plasma Processing, 2010. **30**(5): p. 565-577.
51. Bai, M., Z. Zhang, M. Bai, X. Bai, and H. Gao, *Conversion of Methane to Liquid Products, Hydrogen, and Ammonia with Environmentally Friendly Condition-Based Microgap Discharge*. Journal of the Air & Waste Management Association, 2008. **58**(12): p. 1616-1621.
52. Rahmani, A. and M. Nikravech, *Impact of Argon in Reforming of (CH₄ + CO₂) in Surface Dielectric Barrier Discharge Reactor to Produce Syngas and Liquid Fuels*. Plasma Chemistry and Plasma Processing, 2018.
53. Gesser, H.D., N.R. Hunter, and D. Probawono, *The CO₂ Reforming of Natural Gas in a Silent Discharge Reactor*. Plasma Chemistry and Plasma Processing, 1998. **18**(2): p. 241-245.

54. Hayashi, N., T. Yamakawa, and S. Baba, *Effect of additive gases on synthesis of organic compounds from carbon dioxide using non-thermal plasma produced by atmospheric surface discharges*. Vacuum, 2006. **80**(11): p. 1299-1304.
55. Zhou, L.M., B. Xue, U. Kogelschatz, and B. Eliasson, *Partial Oxidation of Methane to Methanol with Oxygen or Air in a Nonequilibrium Discharge Plasma*. Plasma Chemistry and Plasma Processing, 1998. **18**(3): p. 375-393.
56. Pintassilgo, C.D., J. Loureiro, G. Cernogora, and M. Touzeau, *Methane decomposition and active nitrogen in a N₂-CH₄ glow discharge at low pressures*. Plasma Sources Science and Technology, 1999. **8**(3): p. 463.
57. Liu, C., B. Eliasson, B. Xue, Y. Li, and Y. Wang, *Zeolite-Enhanced Plasma Methane Conversion Directly to Higher Hydrocarbons Using Dielectric-Barrier Discharges*. Reaction Kinetics and Catalysis Letters, 2001. **74**(1): p. 71-77.
58. Zhang, A.-J., A.-M. Zhu, J. Guo, Y. Xu, and C. Shi, *Conversion of greenhouse gases into syngas via combined effects of discharge activation and catalysis*. Chemical Engineering Journal, 2010. **156**(3): p. 601-606.
59. Hammer, T., T. Kappes, and W. Schiene, *Plasma Catalytic Hybrid Reforming of Methane*, in *Utilization of Greenhouse Gases*. 2003, American Chemical Society. p. 292-301.
60. Loic, B., O. Alp, G. Eric, B. Thierry Visart de, and R. Francois, *Journal of Physics D: Applied Physics*, 2018.
61. Ruixing Li, Q.T., Shu Yin, Tsugio Sato, *Plasma Catalysis for CO₂ Decomposition by Using Different Dielectric Materials*. Fuel Processing Technology, 2006. **87**: p. 617-622.
62. Thejaswini, H.C., S. Peglow, V. Sushkov, and R. Hippler, *Infrared Spectroscopy of Infrared Spectroscopy of CH₄/N₂ and C₂H_m/N₂ (m=2,4,6) Gas Mixtures in a Dielectric Barrier Discharge*. Plasma Chemistry and Plasma Processing, 2014. **34**(5): p. 1157-1170.
63. Li, R., Q. Tang, S. Yin, and T. Sato, *Plasma catalysis for CO₂ decomposition by using different dielectric materials*. Fuel Processing Technology, 2006. **87**(7): p. 617-622.
64. Zhang, K., T. Mukhriza, X. Liu, P.P. Greco, and E. Chiremba, *A study on CO₂ and CH₄ conversion to synthesis gas and higher hydrocarbons by the combination of catalysts and dielectric-barrier discharges*. Applied Catalysis A: General, 2015. **502**: p. 138-149.

65. Hsin Liang Chen, H.M.L., Shiaw Huei Chen, Yu Chao, Moo Been Chang, *Review of Packed-Bed Plasma Reactor for Ozone Generation and Air Pollution Control*. Industrial & Engineering Chemistry Research, 2008. **47**: p. 2122-2130.
66. Li, W., Y. Yanhui, W. Chunfei, G. Hongchen, and T. Xin, *One-Step Reforming of CO₂ and CH₄ into High-Value Liquid Chemicals and Fuels at Room Temperature by Plasma-Driven Catalysis*. Angewandte Chemie International Edition, 2017. **56**(44): p. 13679-13683.
67. Bogaerts, A. and E.C. Neyts, *Plasma Technology: An Emerging Technology for Energy Storage*. ACS Energy Letters, 2018. **3**(4): p. 1013-1027.
68. Chen, H.L., H.M. Lee, S.H. Chen, and M.B. Chang, *Review of Packed-Bed Plasma Reactor for Ozone Generation and Air Pollution Control*. Industrial & Engineering Chemistry Research, 2008. **47**(7): p. 2122-2130.
69. Tomáš, K. and B. Annemie, *Evaluation of the energy efficiency of CO₂ conversion in microwave discharges using a reaction kinetics model*. Plasma Sources Science and Technology, 2015. **24**(1): p. 015024.
70. Yukinori, S., B.G. David, C. Hung-Wen, S. Tetsuji, and E.M. Gregor, *Plasma chemistry model of surface microdischarge in humid air and dynamics of reactive neutral species*. Journal of Physics D: Applied Physics, 2012. **45**(42): p. 425201.
71. Abdullah Al-Abduly, P.A.C., *An in situ and downstream study of non-thermal plasma chemistry in an air fed dielectric barrier discharge (DBD)*. Plasma Sources Science and Technology, 2015. **24**: p. 065006
72. Abd Allah, Z., J.C. Whitehead, and P. Martin, *Remediation of Dichloromethane (CH₂Cl₂) Using Non-thermal, Atmospheric Pressure Plasma Generated in a Packed-Bed Reactor*. Environmental Science & Technology, 2014. **48**(1): p. 558-565.
73. Jeong, J.Y., J. Park, I. Henins, S.E. Babayan, V.J. Tu, G.S. Selwyn, G. Ding, and R.F. Hicks, *Reaction Chemistry in the Afterglow of an Oxygen–Helium, Atmospheric-Pressure Plasma*. The Journal of Physical Chemistry A, 2000. **104**(34): p. 8027-8032.
74. Martin, P.A. and G. Guelachvili, *Velocity-modulation Fourier-transform spectroscopy of molecular ions*. Physical Review Letters, 1990. **65**(20): p. 2535-2538.
75. Christensen, P.A. and A. Hamnett, *Techniques and Mechanisms in Electrochemistry*. 1994, Glasgow: Blackie Academic & Professional
76. Christensen, P.A., *In-situ Fourier transform infra red spectroelectrochemistry as a probe of electrocatalysis in Spectroscopic Properties of Inorganic and*

- Organometallic Compounds: Techniques, Materials and Applications*, R.D. Jack Yarwood, Simon Duckett, Editor. 2010, Royal Society of Chemistry p. 125-165.
77. Li, K., O. Gabriel, and J. Meichsner, *Fourier transform infrared spectroscopy study of molecular structure formation in thin films during hexamethyldisiloxane decomposition in low pressure rf discharge*. *Journal of Physics D: Applied Physics*, 2004. **37**(4): p. 588.
78. Rivallan, M., E. Fourré, S. Aiello, J.-M. Tatibouët, and F. Thibault-Starzyk, *Insights into the Mechanisms of Isopropanol Conversion on γ -Al₂O₃ by Dielectric Barrier Discharge*. *Plasma Processes and Polymers*, 2012. **9**(9): p. 850-854.
79. Stere, C.E., W. Adress, R. Burch, S. Chansai, A. Goguet, W.G. Graham, and C. Hardacre, *Probing a Non-Thermal Plasma Activated Heterogeneously Catalyzed Reaction Using in Situ DRIFTS-MS*. *ACS Catalysis*, 2015. **5**(2): p. 956-964.
80. Rodrigues, A., J.-M. Tatibouët, and E. Fourré, *Operando DRIFT Spectroscopy Characterization of Intermediate Species on Catalysts Surface in VOC Removal from Air by Non-thermal Plasma Assisted Catalysis*. *Plasma Chemistry and Plasma Processing*, 2016. **36**(4): p. 901-915.
81. Jia, Z. and A. Rousseau, *Sorbent track: Quantitative monitoring of adsorbed VOCs under in-situ plasma exposure*. *Scientific Reports*, 2016. **6**: p. 31888.
82. Langleron, M., S. Cavadias, and J. Amouroux, *Study by mass spectrometry and gas chromatography of toluene oxidation in a low-pressure plasma reactor*. *Rapid Communications in Mass Spectrometry*, 1995. **9**(1): p. 18-22.
83. Xiaoteng, L., Z. Kui, L. Jianwei, L. Kun, G. Jinlong, K.P. Vinod, and S. Keith, *Determining the Effect of Plasma Pre-Treatment on Antimony Tin Oxide to Support Pt@Pd and the Oxygen Reduction Reaction Activity*. *ChemCatChem*, 2015. **7**(10): p. 1543-1546.
84. Robby Aerts, W.S., Annemie Bogaerts, *Carbon dioxide splitting in a dielectric barrier discharge plasma: a combined experimental and computational study*. *ChemSusChem*, 2015. **8**(4): p. 702-716.
85. Steven L. Suib, S.L.B., Manuel Marquez, Jian Luo, Hiroshige Matsumoto, Yuji Hayashi, *Efficient Catalytic Plasma Activation of CO₂, NO, and H₂O*. *J. Phys. Chem B*, 1998. **102**: p. 9661-9666.

86. J. Amouroux, P.S., *Carbon Dioxide A Raw Material and A Future Chemical Fuel for A Sustainable Energy Industry*. IOP Conf. Series: Materials Science and Engineering 2011. **19**.
87. *Plasma Science: Advancing Knowledge in the National Interest*. 2010 [cited 2015 24 July 2015]; Available from: http://nnsa.energy.gov/sites/default/files/nnsa/01-13-inlinefiles/nrc_plasma_science_report_2007.pdf.
88. Saravanan, K., Y. Basdogan, J. Dean, and J.A. Keith, *Computational investigation of CO₂ electroreduction on tin oxide and predictions of Ti, V, Nb and Zr dopants for improved catalysis*. Journal of Materials Chemistry A, 2017. **5**(23): p. 11756-11763.
89. Li, Q., J. Fu, W. Zhu, Z. Chen, B. Shen, L. Wu, Z. Xi, T. Wang, G. Lu, J.-j. Zhu, and S. Sun, *Tuning Sn-Catalysis for Electrochemical Reduction of CO₂ to CO via the Core/Shell Cu/SnO₂ Structure*. Journal of the American Chemical Society, 2017. **139**(12): p. 4290-4293.
90. Wang, X. and Y.-c. Xie, *Total Oxidation of ch₄ on Iron-Promoted tin Oxide: Novel and Thermally Stable Catalysts*. Reaction Kinetics and Catalysis Letters, 2001. **72**(2): p. 229-237.
91. Christensen, P.A., P.S. Attidekou, R.G. Egdell, S. Maneelok, and D.A.C. Manning, *An in situ FTIR spectroscopic and thermogravimetric analysis study of the dehydration and dihydroxylation of SnO₂: the contribution of the (100), (110) and (111) facets*. Physical Chemistry Chemical Physics, 2016. **18**(33): p. 22990-22998.
92. Jia, Z. and A. Rousseau, *Sorbent track: Quantitative monitoring of adsorbed VOCs under in-situ plasma exposure*. 2016. **6**: p. 31888.
93. Jiang, L., G. Nie, R. Zhu, J. Wang, J. Chen, Y. Mao, Z. Cheng, and W.A. Anderson, *Efficient degradation of chlorobenzene in a non-thermal plasma catalytic reactor supported on CeO₂/HZSM-5 catalysts*. Journal of Environmental Sciences, 2017. **55**: p. 266-273.

Chapter 2. Experimental

This chapter describes the fabrication of the plasma cells (transmission and reflectance), the experimental equipment employed, the methods used during the project, and the analytical techniques used to analyse the FTIR spectra.

2.1 Gases, Chemicals and Materials

2.1.1 Gases

N₂ (N5.5/100%), CO₂ (N5.0/100%), CH₄ (N4.5/100%), and Ar (N5.5/100%) were supplied by BOC Industrial gasses, UK. The gasses were mixed as appropriate and the compositions controlled using flow meters purchased from Roxspur Measurement & Control Ltd.

2.1.2 Chemicals

The reagents employed in the work presented in this thesis are shown in table 2.1.

Chemicals	Formula	Analysis	Supplier
Tin (IV) chloride pentahydrate	SnCl ₄ .5H ₂ O	≥ 98%	Sigma Aldrich
Cerium (IV) oxide	CeO ₂	99.995%	Sigma Aldrich
Potassium bromide	KBr	FTIR grade	Alfa Aesar
Silver Nitrate	AgNO ₃	≥ 98%	Riedel-de Haen

Table 2.1. List of reagents employed in the work reported in this thesis.

2.1.3 Materials

The materials employed throughout this work are shown in table 2.2.

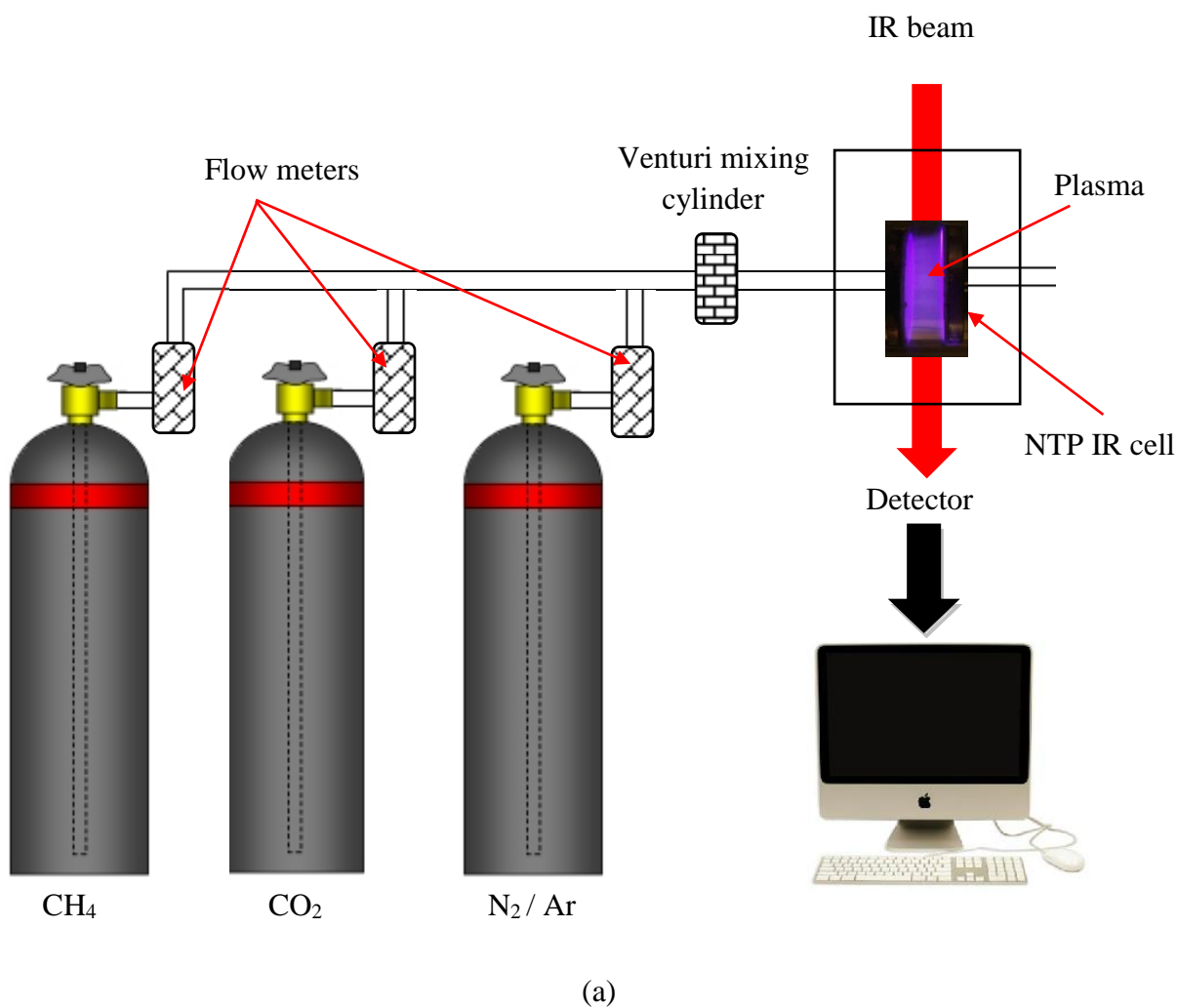
Materials	Description	Supplier
Macor	Quartz (35-50%), Magnesium oxide (15-20%), Aluminium oxide (15-20%) and Fluoride (1-5%) [1]	Goodfellow Cambridge
Stainless Steel Shim	Thickness, 0.007 cm	RS Components
Titanium Mesh, Ti	Thickness, 76.2 μm - 101.6 μm	Dexmet Corp, USA
Mirror	Aluminum with SiO ₂ protective coated mirror, 50mm x 30mm x 4mm	Simphoton, China

CaF ₂ windows	25 mm diameter, 3 mm thick	Crystran, UK
Polytetrafluoroethylene	PTFE	RS Components
Silicone glue	Loctite 595 transparent silicone glue	RS Components

Table 2.2. The materials employed in the work reported in this thesis.

2.2 The gas delivery system

The feed gasses were passed through a gas venturi mixing cylinder at a fixed flow rate and the composition was controlled using flow meters as shown in figs. 2.1(a) & (b). The venturi device was manufactured in-house and was made from a 18 cm long stainless steel tube.



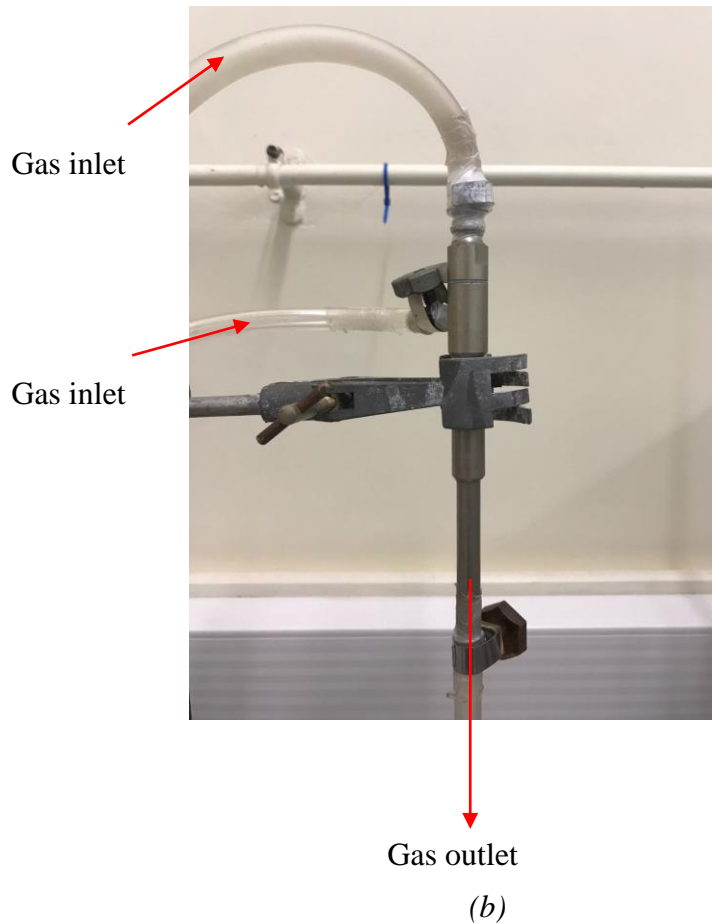
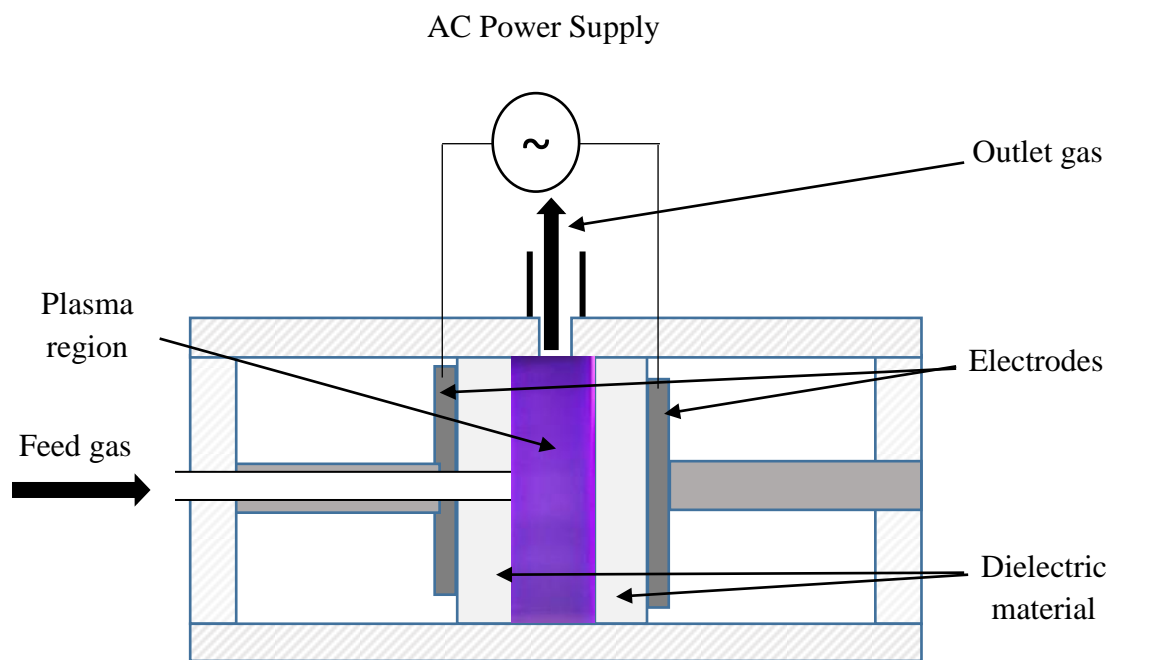


Figure 2.1. (a) Schematic of gas line mixing system and (b) photograph of the venturi mixing cylinder.

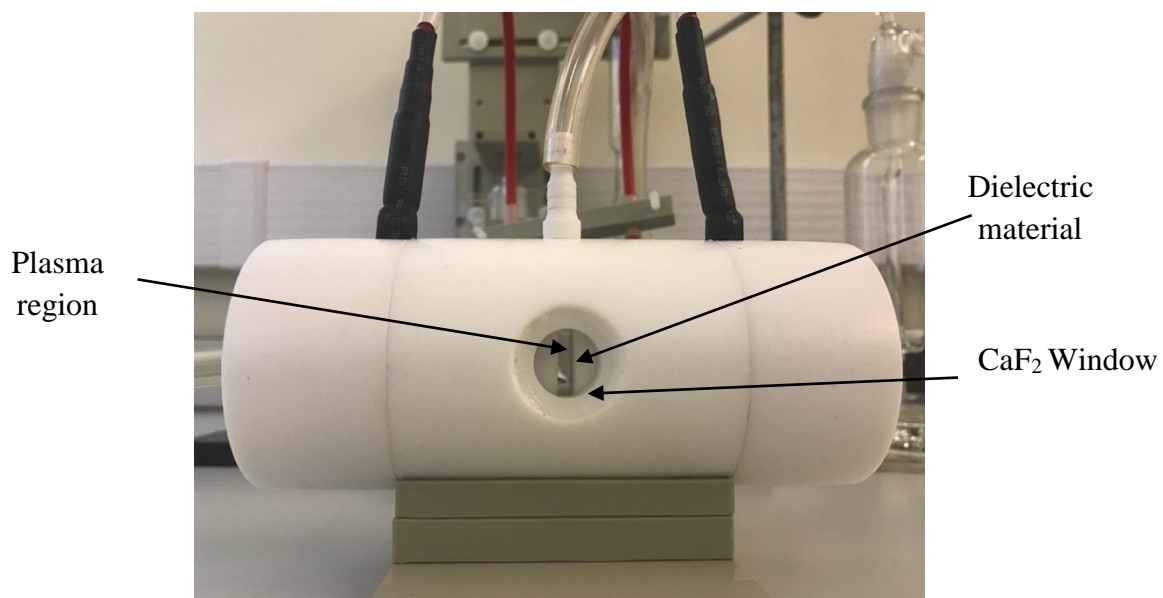
2.3 The non-thermal plasma infrared cells

2.3.1 The non-thermal plasma infrared transmission cell

The non-thermal plasma (NTP) infrared (IR) transmission cell, see figs. 2.2(a) & (b), was designed and fabricated in-house and was made from a 15 cm long cylindrical polytetrafluoroethylene (PTFE) tube with an outer diameter of 6.3 cm and inner diameter of 2.5 cm.



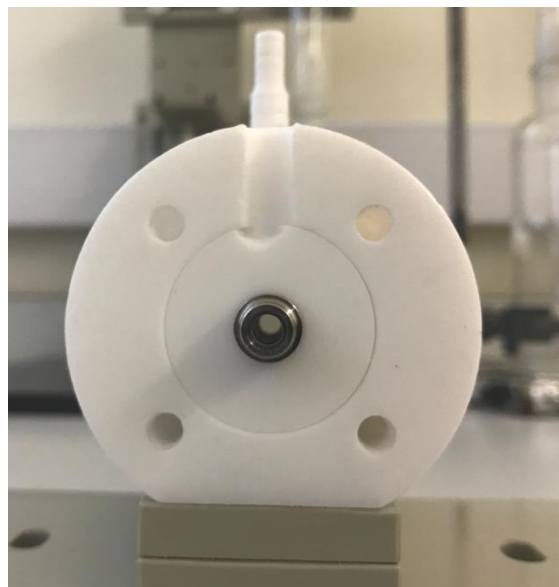
(a)



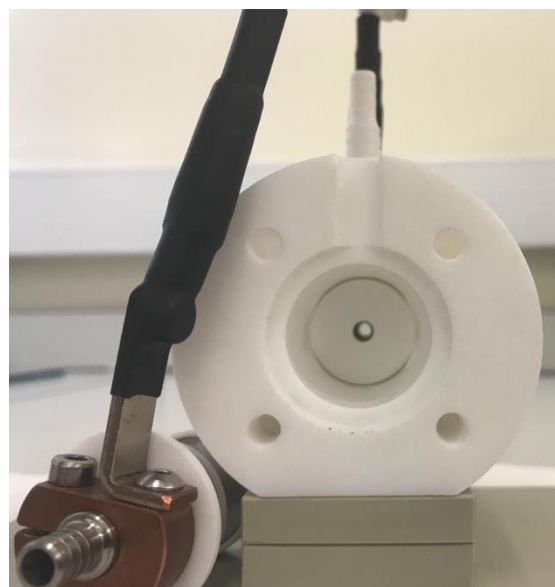
(b)

Figure 2.2. (a) Schematic and (b) photograph of the NTP IR transmission cell.

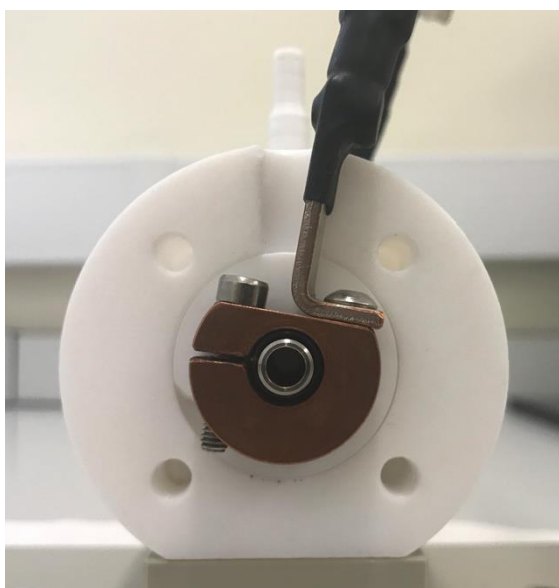
The high voltage electrodes were in the form of two plungers sealing against the inner walls of the PTFE via rubber 'O' rings. One of the plungers was hollow down its axis (a 4 mm diameter hole) and the feed gas was delivered via this channel and removed via an outlet in the top of the cell, see figs 2.3(a)-(d). The electrodes were covered with 8 mm thick Macor caps fitted snugly over each disc electrode, one of which had a hole aligned with the central gas delivery channel.



(a)



(b)



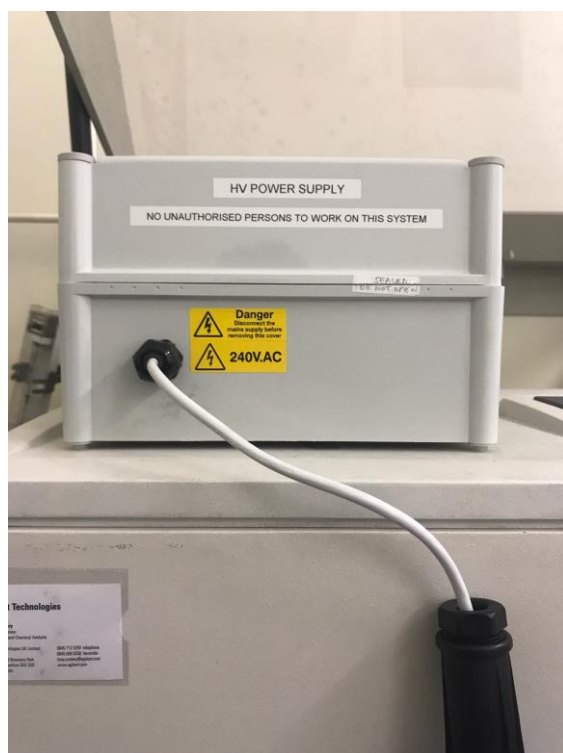
(c)



(d)

Figure 2.3. (a) - (d) photographs of the arrangement of the high voltage electrodes.

Two infrared transparent CaF_2 windows (25 mm diameter, 3 mm thick) were glued into PTFE cell using a silicone glue (Loctite 595, RS Components). The distance between the windows (pathlength) was 5.1 cm. The windows were positioned such that their centres aligned with the centre of the gap between the electrodes. The electrodes were connected to a NeonPro lamp transformer, NP100000-30 (Hyrite, China), see figs. 2.4(a) & (b), which provided an output up to 10 kV at a constant frequency of 24 kHz. A voltage controller (Carroll & Meynell) was used to control the input power to the high voltage (HV) transformers. The input power to the plasma was monitored using a digital power monitor, N67FU (Maplin, UK); the input powers quoted below were those obtained by subtracting the input power observed with plasma to the reading obtained with the system switched on but with no plasma initiated (4 W). The total plasma volume of the transmission cell was ca. 7.4 cm^3 and the residence time at a total flow rate of $200 \text{ cm}^3 \text{ min}^{-1}$ was 2.2 s.



(a)

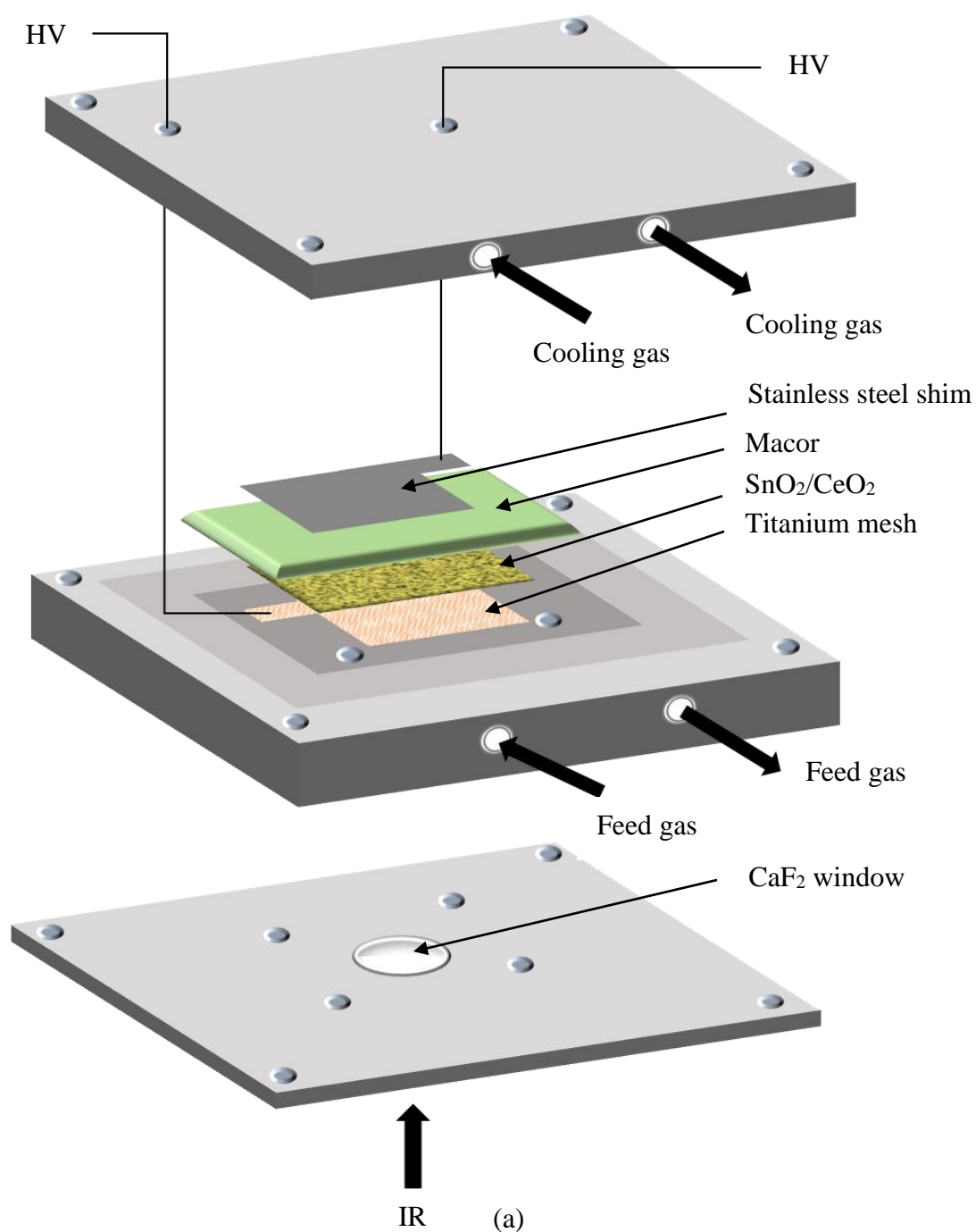


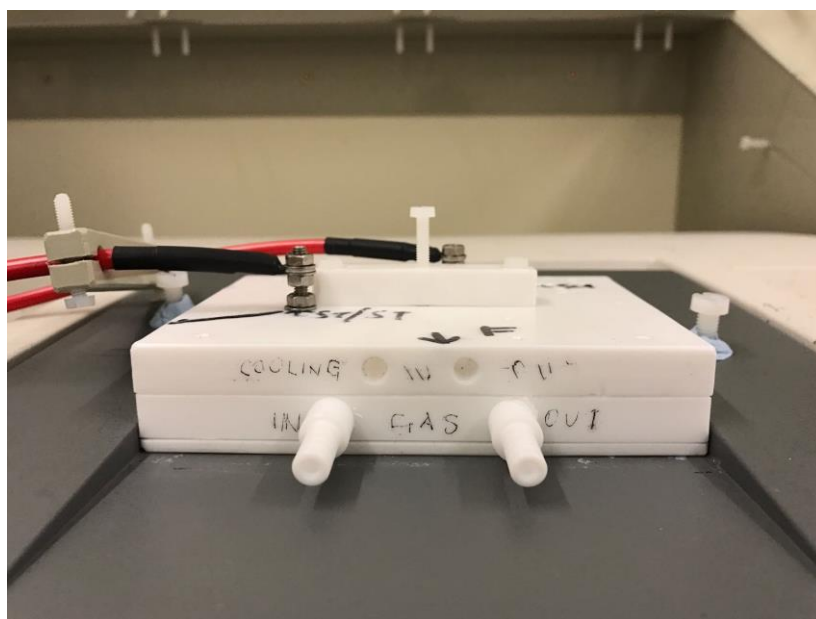
(b)

Figure 2.4. (a) Photograph of the high voltage power supply and (b) photograph of the voltage controller.

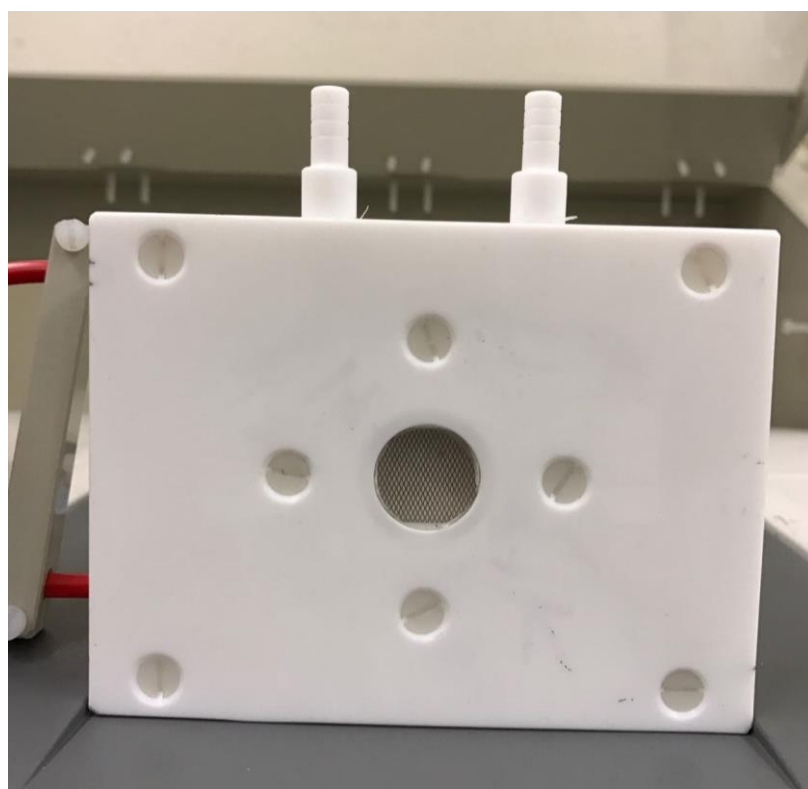
2.3.2 *The non thermal plasma infrared reflectance cell*

The IR NTP reflectance cell, see figs. 2.5(a) – (c), was designed and constructed in-house loosely based on the (non-spectroscopic) surface dielectric barrier discharge cell employed by Šimek and co-workers [2]. The cell was mounted horizontally on the lid of the sample compartment of the spectrometer and the cell was jacketed with air cooling unit to allow careful control of the temperature of the gas in the body of the cell.





(b)



(c)

Figure 2.5. (a) Schematic of the NTP IR reflectance cell and (b) & (c) photographs of the NTP IR reflectance cell.

As can be seen from figs. 2.5(a) – (d), the reflectance cell was rectangular, 12.7 cm x 9.5 cm x 3.5 cm, and fitted with cooling channels and channels for the input and exhaust of the feed gas. A stainless steel shim was employed as one electrode, hidden from the IR beam, on top of which was a 23 mm x 22 mm x 0.07 mm Al_2O_3 wafer and a 30 mm x 30 mm x 5 mm Macor plate. The Macor was covered by the second, Ti mesh electrode (50% open area) and both the Ti mesh and Macor were irradiated by the IR beam via a CaF_2 plate window (25 mm diameter, 2 mm thick). The gap between the Macor and the window was 5 mm.

The same power supply was employed for the reflectance cell as for the transmission cell. In contrast to the transmission cell, which generated a volume discharge between the two Macor caps, the reflectance cell generated a surface discharge across the Macor and Ti Mesh. The plasma volume was 2 cm^3 and the residence time at a flow rate of $30\text{ cm}^3\text{ min}^{-1}$ was 4 s.

Figures 26(a) & (b) show the in-house built optical bench which consisted of two mirrors at an angle of 57° to the vertical, 45 mm above the floor of the sample compartment and 100 mm apart. The mirrors were positioned such that the angle of incidence on the CaF_2 window was 24° and on 24° on the Macor.



(a)

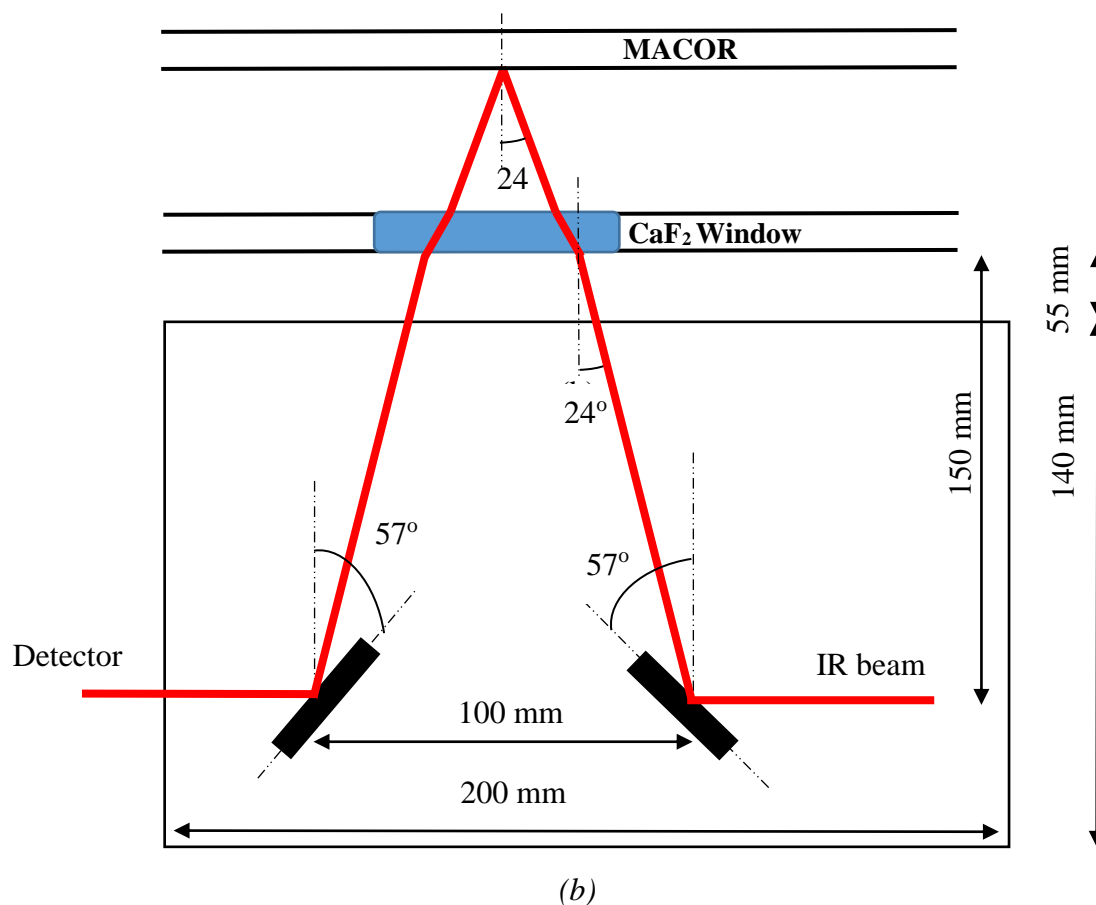
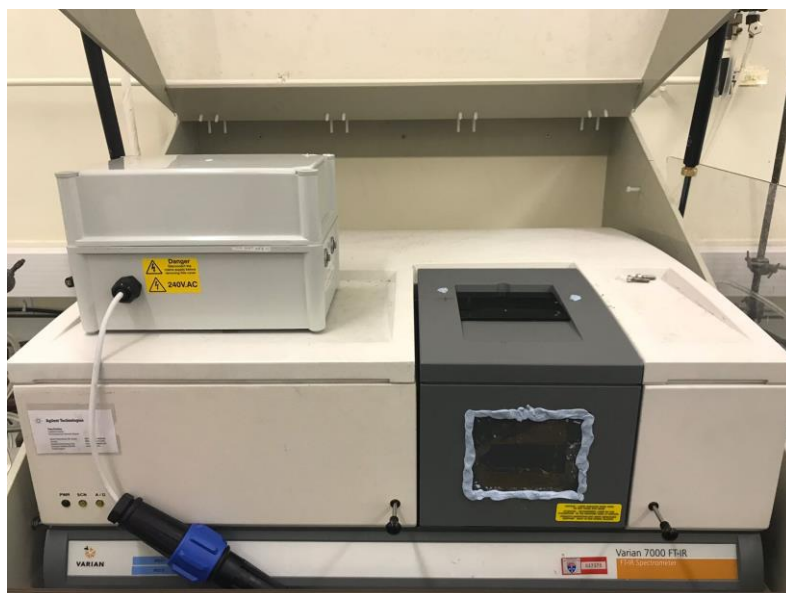


Figure 2.6. (a) photograph and (b) Schematic of the optical bench employed with the in-situ FTIR for reflectance cell.

2.4 The non-thermal plasma FTIR system

An Agilent FTS7000 FTIR spectrometer with a Deuterated TriGlycine Sulfate (DTGS) detector was employed, see fig. 2.7. The IR beam passed through the plasma via CaF_2 windows to the detector via an Amtir-1 filter, 25mm x 2mm (Spectra-Tech, USA) to remove any stray light from the plasma.



(a)



(b)

Figure 2.7. (a) Photograph of the Agilent FTS7000 spectrometer and (b) photograph of the sample compartment of the spectrometer.

2.5 The thermal FTIR system

In-situ FTIR experiments as a function of temperature were carried out using a Varian 670-IR spectrometer equipped with a ceramic air-cooled infrared source, a cooled DLaTGS detector and a Specac Environmental Chamber and diffuse reflectance unit [3], see fig. 2.8.



(a)



(b)

Figure 2.8. (a) Photograph of the FTIR Varian 670-IR spectrometer and (b) photograph of the Specac Environmental Chamber and diffuse reflectance unit.

The Specac reflectance accessory allows IR spectra to be collected under controlled atmosphere conditions from room temperature to 600 °C and pressures from vacuum to 34 atm at a ramp rate of 5° C/min. The IR beam was incident on the sample in the cell at angles from 20° to 76° with respect to the horizontal plane via a ZnSe window [4], see fig. 2.9.

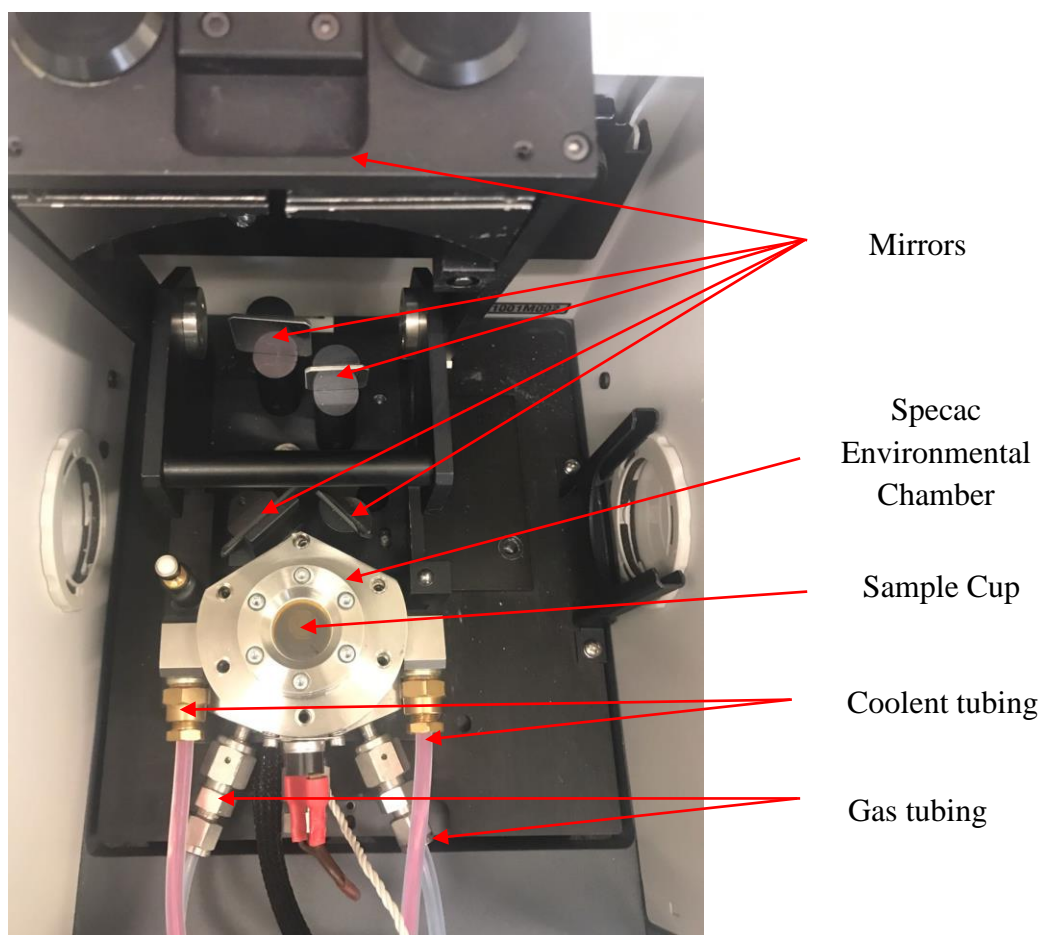


Figure 2.9. Photograph of the environmental chamber employed for the in-situ FTIR experiments at varied temperature.

As can be seen from fig. 2.9, the feed gas i.e. N₂ (N5.5/100%), Ar (N5.5/100%), CO₂ (N5.0/100%) and CH₄ (N4.5/100%) were mixed as appropriate and admitted into the Specac Environmental Chamber via polyethylene tubing. Prior to each experiment, the catalyst (Macor disc (12.5 mm diameter, 2 mm thick), SnO₂ or cerium (IV) oxide (CeO₂)) was ground and mixed with IR transparent KBr (except the Macor) in the ratio (by mass) of KBr to sample 4:1 and placed in the sample cup. The IR spectra were collected from the powder samples using the diffuse reflection, as shown in figs. 2.10 and 2.11.

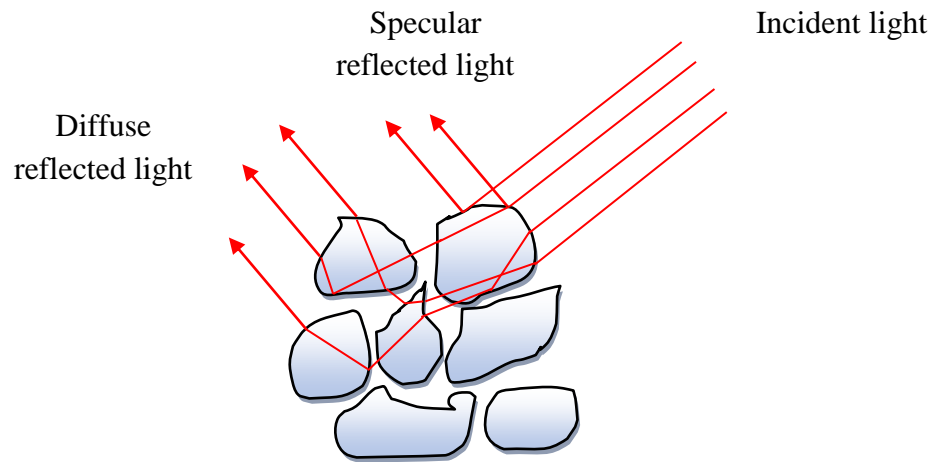


Figure 2.10. Schematic of light scattering from a powder sample [5].

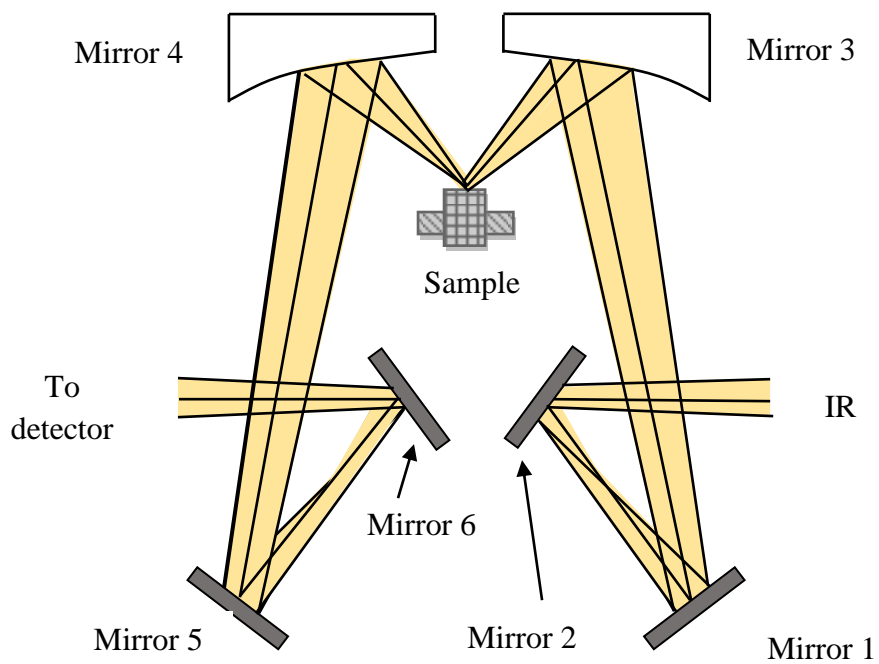


Figure 2.11. Schematic of the diffuse reflectance optical system. Redrawn from [5].

As may be seen from figs. 2.10 and 2.11, when IR light is incident on a powder sample it is reflected in all directions due to the variety of the powder shapes. Some of the IR beam is refracted as it enters the crystals and some is specularly reflected. Generally, when measuring an IR spectrum using the diffuse reflection method, the sample powder is normally diluted in an alkali halide powder such as KBr. Mixing the catalyst, i.e. SnO₂, with KBr allows for the IR beam to further penetrate the powder mixture and hence enhances the contribution of diffuse reflectance in order to maintain band shapes and intensities [6].

Spectra were recorded in reflectance mode and then converted to an effective absorption using the Kubelka-Munk equation [7]. Thus a reference spectrum (S_R , 100 co-added scans and averaged scans at 8 cm⁻¹ resolution, ca. 2 minutes per scanset) was collected from pure KBr at room temperature before the spectrum of the catalyst sample i.e. SnO₂/KBr was collected at 25 °C. The temperature of the sample was then increased at 5 °C min⁻¹ and a further spectrum collected at 50 °C, after which spectra S_S were collected every 50 °C up to 600 °C. The spectra were manipulated [7] according to:

$$KM = (1-R)^2/2R \quad (2.1)$$

where $R = S_R/S_S \quad (2.2)$

and KM is the Kubelka-Munk function, R is the reflectance of a sample at infinite depth, S_S is the single beam spectra of the powder, S_R is the single beam of the standard reference powder and the Kubelka-Munk function plotted vs wavenumber. This data manipulation results in difference spectra in which peaks with positive amplitude arise from the gain of absorbing species in S_S with respect to S_R , and peaks with negative amplitude to the loss of absorbing species. In order to remove unchanging absorptions, spectra were simply subtracted from each other (eg. KM600C – KM300C); i.e. no subtraction factor was employed.

2.6 Catalyst preparation

2.6.1 SnO_2 Synthesis Method

SnO_2 nanopowders were prepared by a hydrothermal synthesis using a method adapted from Fujihara and co-workers [8] and by Christensen and co-workers in Newcastle [3]. The first step on the preparation was to dissolve the appropriate salts (see table 2.3) in 200 cm^3 dionized water (Milipore Milli-Q, 18 $\text{M}\Omega$ cm) and reflux at 95 $^\circ\text{C}$ for 3 hours in order to promote hydrolysis and the formation of a white precipitate of SnO_2 , see fig. 2.12.

Sample	Concentration of SnCl_4 in final precursor solution/ M	% Mole ratio Sn: Sb: Ni	Mass of $\text{SnCl}_4 \cdot 5\text{H}_2\text{O}$ / g	Volume of H_2O / cm^3
SnO_2	0.1	100 : 0 : 0	7.01	200

Table 2.3. The composition of the solutions employed in the reflux step to produce nanoparticulate SnO_2 [3].

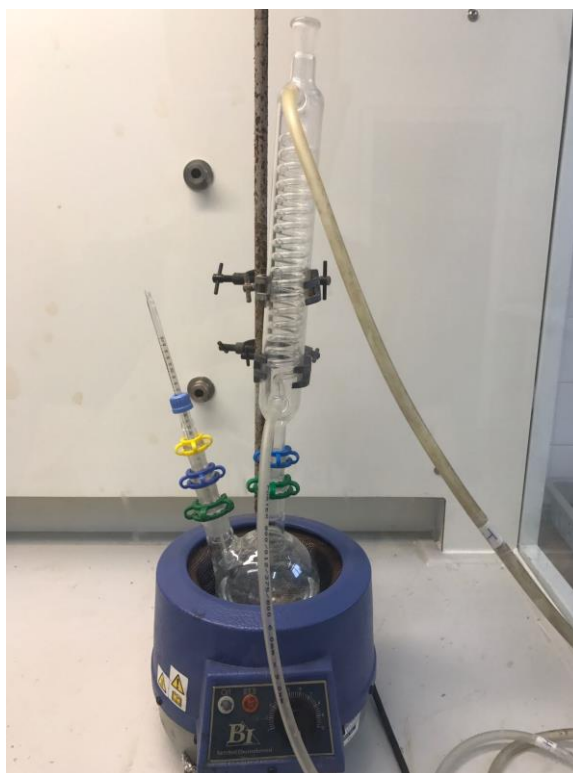


Figure 2.12. Photograph of the reflux apparatus.

Following refluxing, the nanoparticulate SnO₂ precipitate was centrifuged to separate the precipitate from the solvent and washed 15 times with de-ionised (DI) water until the chloride ions had been removed completely (as determined by the addition of aqueous 0.1M AgNO₃). The wet precipitate was then placed in a Teflon container (80 cm³, with lid), fitted into a stainless steel autoclave and heated at 180 °C (10 bar) for 24 hours, see figs 2.13(a) – (c).



(a)



(b)



(c)

Figure 2.13. Photograph of the hydrothermal synthesis apparatus: (a) the Teflon container, (b) the stainless steel autoclave and (c) the hydrothermal reactor.

After the hydrothermal treatment, the precipitate was then washed again with DI water until no further chloride appeared (as previous) and dried in an oven at 60 °C overnight. The powder was then calcined at 400 °C or 700 °C for 1 hour at a step rate of 6 °C min⁻¹ before cooling to room temperature and denoted as SnO₂ 400 °C and SnO₂ 700 °C, respectively.

2.6.2 *Macor*

A 12.5 mm diameter, 2 mm thick Macor disc was employed as the catalyst and placed in the sample cup as shown in fig. 2.14. A reference spectrum was first collected from the Macor before the spectrum of the Macor collected at 25 °C. The temperature of the sample was then increased at 5 °C min⁻¹ and a further spectrum collected at 50 °C, after which sample spectra were collected every 50 °C up to 600 °C. Spectra were recorded as absorbances.



Figure 2.14. Photograph of Macor disc in the sample cup.

2.6.3 *Cerium (IV) oxide*

Cerium (IV) oxide (CeO₂) was obtained from Sigma Aldrich and used without further treatment. The powder was placed on the sample cup as shown in fig. 2.15. A reference spectrum was first collected from pure KBr at room temperature and the spectrum of the KBr/CeO₂ was then collected at 25 °C. The temperature of the sample was then increased at 5 °C min⁻¹ and a further spectrum collected at 50 °C, after which sample spectra were collected every 50 °C up to 600 °C. Spectra were recorded in reflectance mode.

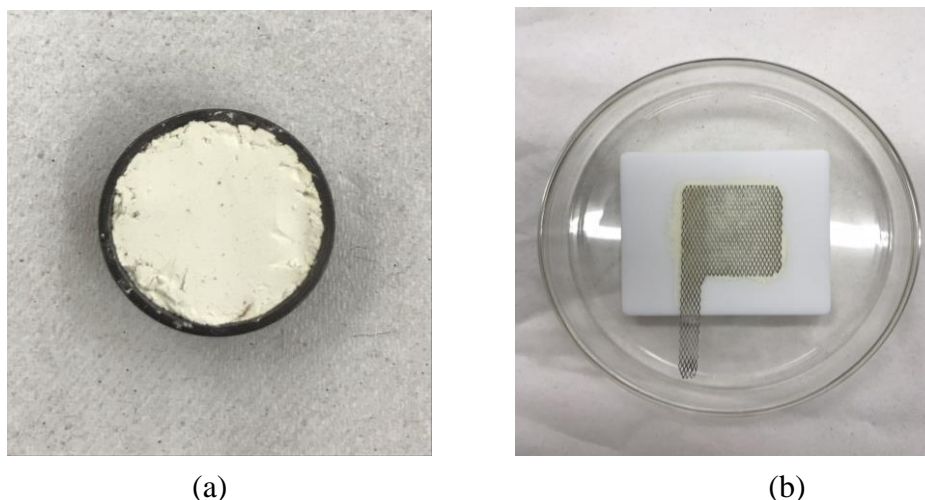


Figure 2.15. (a) Photograph of CeO₂ in the sample cup for thermally driven experiment and (b) Photograph of CeO₂ coated on Macor/Ti Mesh for plasmally driven experiment using IR reflectance cell.

2.7 Typical in-situ NTP FTIR experiments using the transmission cell

In a typical experiment using the IR transmission cell, the cell was first flushed with N₂ at a flowrate of 200 cm³ min⁻¹ for 30 minutes, after which the chosen feed composition was admitted to the cell at a total flow rate of 200 cm³ min⁻¹ and a reference spectrum (S_R , 100 co-added and averaged scans at 8 cm⁻¹ resolution, 60 seconds per scan set) was collected in the absence of plasma. Sample spectra, S_s , were then taken as a function of time after the high voltage power supply was switched on, and at regular intervals thereafter, up to 20 minutes. By using the first single beam (of the nitrogen gas with no plasma) as the reference spectrum (S_R) all of the infrared active species present in the plasma were observed; using the second single beam as the reference spectrum resulted in difference spectra, showing only the changes incurred on initiating the plasma. The methodology employed with the reflectance cell was the same except that a flow rate of 30 cm³ min⁻¹ was used to allow sufficient residence time. The compositions of the gas feeds employed in the experiments are summarized in tables 2.4 and 2.5.

	Composition CO₂/CH₄/N₂ or Ar	Power /W
1	10.6% CO ₂ / 13.4% CH ₄ / 76.0% N ₂	20
2	10.0% CO ₂ / 14.2% CH ₄ / 75.8% N ₂	24
3	12.3% CO ₂ / 14.4% CH ₄ / 73.3% N ₂	28
4	9.7 % CO ₂ / 90.3% Ar	14
5	14.0% CH ₄ / 76.0% N ₂	20
6	14.7% CH ₄ / 75.3% N ₂	24
7	13.9% CH ₄ / 76.1% N ₂	28
8	100% CO ₂	20
9	11.7% CO ₂ / 88.3% N ₂	22
10	13.3% CO ₂ / 86.7% N ₂	24
11	12.2% CO ₂ / 87.8% N ₂	26
12	12.2% CO ₂ / 87.8% N ₂	28
13	5.0% CO ₂ / 12.7% CH ₄ / 82.3% N ₂	28
14	9.0% CO ₂ / 16.0% CH ₄ / 75.0% Ar	20
15	8.3% CO ₂ / 13.5% CH ₄ / 78.2% Ar	28
16	54.0% CO ₂ / 20.0% CH ₄ / 16.0% N ₂	28

Table 2.4. The feed gas compositions employed in the transmission cell experiments.

	Composition CO₂/CH₄/N₂ or Ar	Power /W
1	24% CO ₂ / 76 % N ₂	18
2	28% CO ₂ / 72 % N ₂	24
3	32% CO ₂ / 68 % N ₂	24
4	49% CH ₄ / 51 % N ₂	18
5	46% CH ₄ / 54 % N ₂	24
6	100% N ₂	18
7	100% N ₂	24
8	12% CO ₂ / 39% CH ₄ / 49% N ₂	24
9	10% CO ₂ / 10% CH ₄ / 80 % Ar	14
11	31.1% CO ₂ / 68.9% Ar	24

Table 2.5. The feed gas compositions employed in the reflectance cell experiments.

The nominal composition intended for the gas feeds for the CO₂ + CH₄ + N₂ transmission cell experiments was 10% CO₂ + 10% CH₄ + 80% N₂, with three exceptions (5% CO₂, Ar instead of N₂, 54% CO₂). As examples, input powers i.e. of 20 W and 28 W correspond to Specific Input Energies (SIEs) of 6.0 kJ dm⁻³ and 8.4 kJ dm⁻³, respectively, defined as [9]:

$$\text{SIE (kJ dm}^{-3}\text{)} = \text{Discharge power (kW)} / \text{Total gas flow rate (dm}^3\text{)} \quad (2.4)$$

These correspond to average electron energies per feed gas molecule of 3.9 – 5.5 eV. The input power of 24W at a flow rate of 30 cm³ min⁻¹ for the plasma reflectance cell corresponds to an SIE of 48.0 kJ dm⁻³.

The temperature of the Macor caps of the transmission cell were monitored at an input power of 28 W using a RS-1327 IR Thermometer C infrared thermometer gun in experiments conducted without FTIR data collection (as the cover to the sample compartment had to be removed), the temperature of the Macor caps were found to increase to ca. 43 °C over 20 minutes. This measurement was not possible with the plasma reflectance cell for safety reasons as the cell could not be manipulated and the thermometer gun would not fit into the sample compartment. However, the reflectance cell did employ a cooling gas stream as described in section 2.3.2.

2.8 *Typical in-situ NTP FTIR analysis procedure*

The spectra obtained in the plasma-driven experiments are presented as:

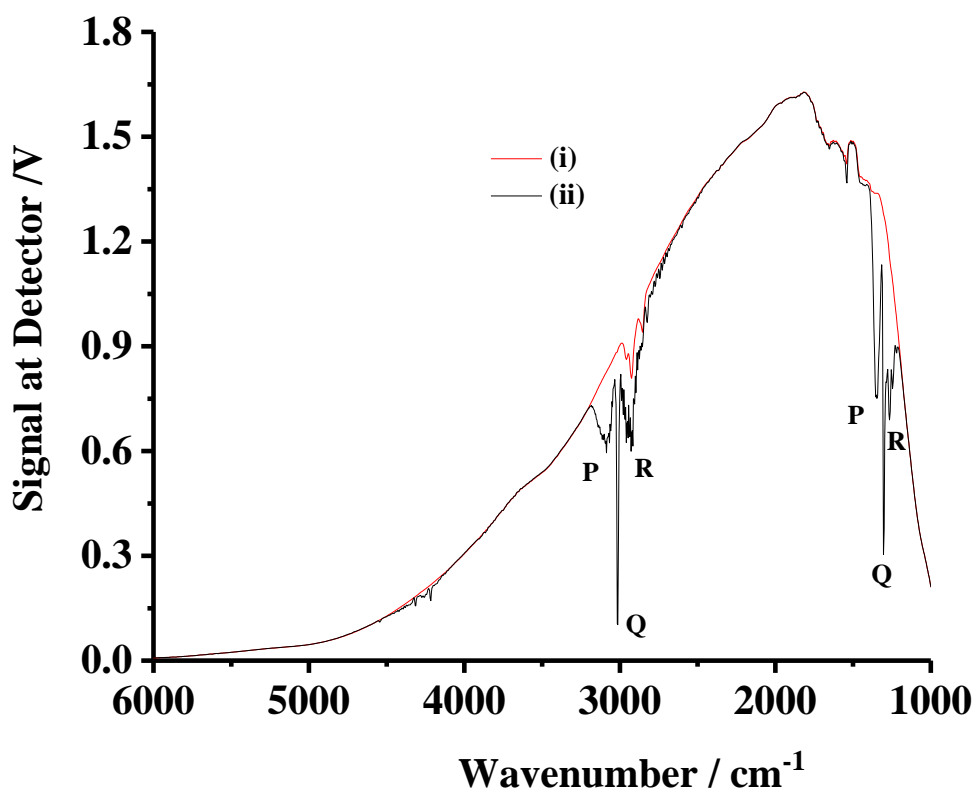
$$\text{Absorbance, } A = \log_{10} (S_R / S_S) \quad (2.5)$$

This results in difference spectra in which peaks pointing upwards (i.e. to + absorbance) represent a gain in absorbing species at S_S with respect to S_R, and peaks pointing down (to – absorbance) represent the loss of absorbing species. The concentrations of the various species observed in the plasma experiments were calculated using the Beer-Lambert law:

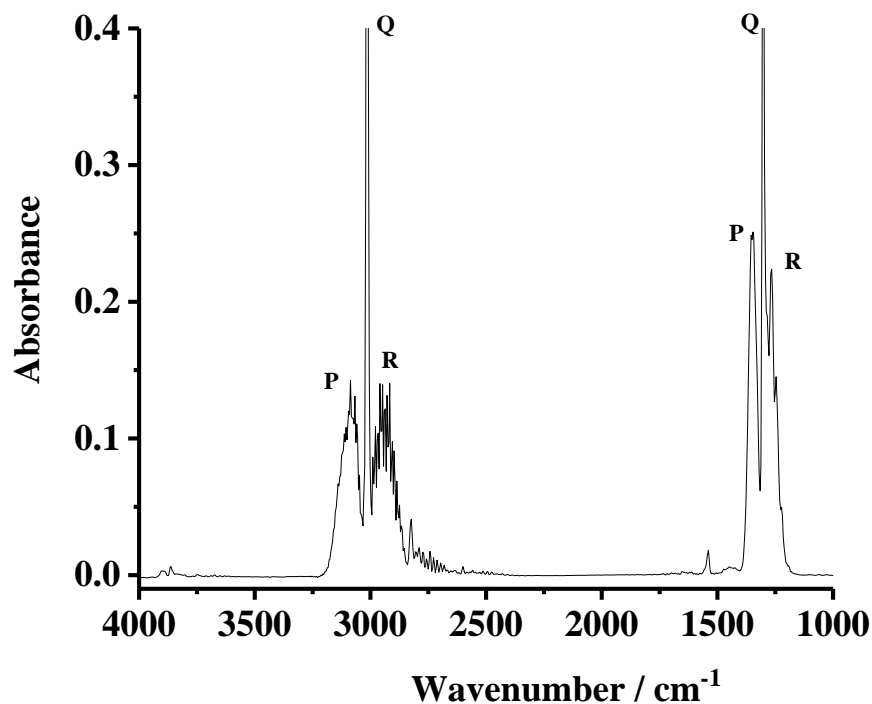
$$A = \epsilon cL \quad (2.6)$$

where: ϵ is the molar decadic extinction coefficient ($M^{-1} \text{ cm}^{-1}$), c = concentration (M) and L = optical path length (cm).

Figures 2.16 and 2.17 show examples of typical single beam spectra obtained from N_2 , $CH_4 + N_2$ and $CO_2 + N_2$ and the resulting absorbance spectra which were employed to determine the concentrations of CH_4 and CO_2 .

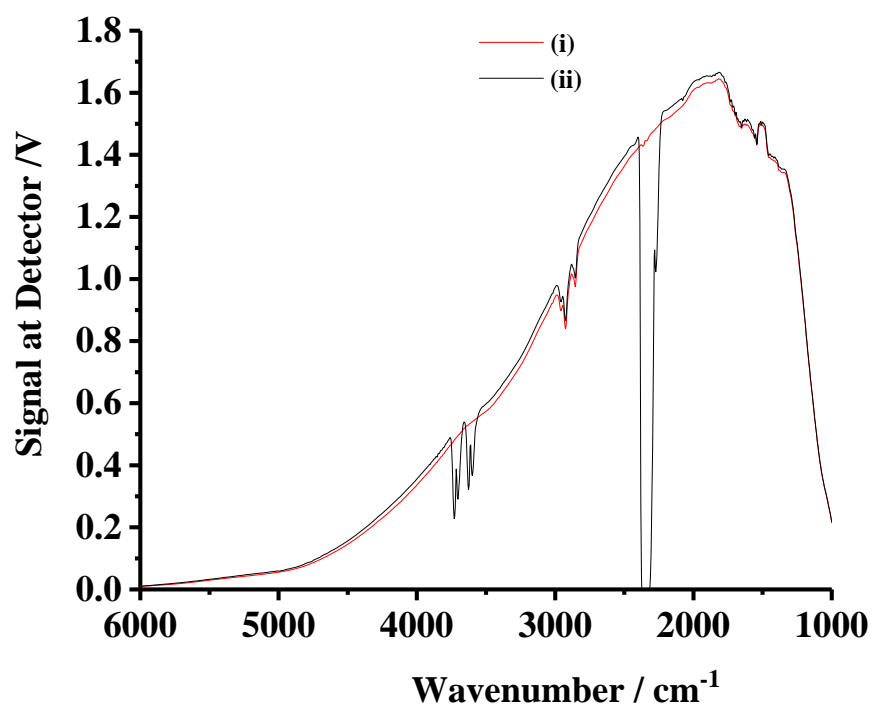


(a)

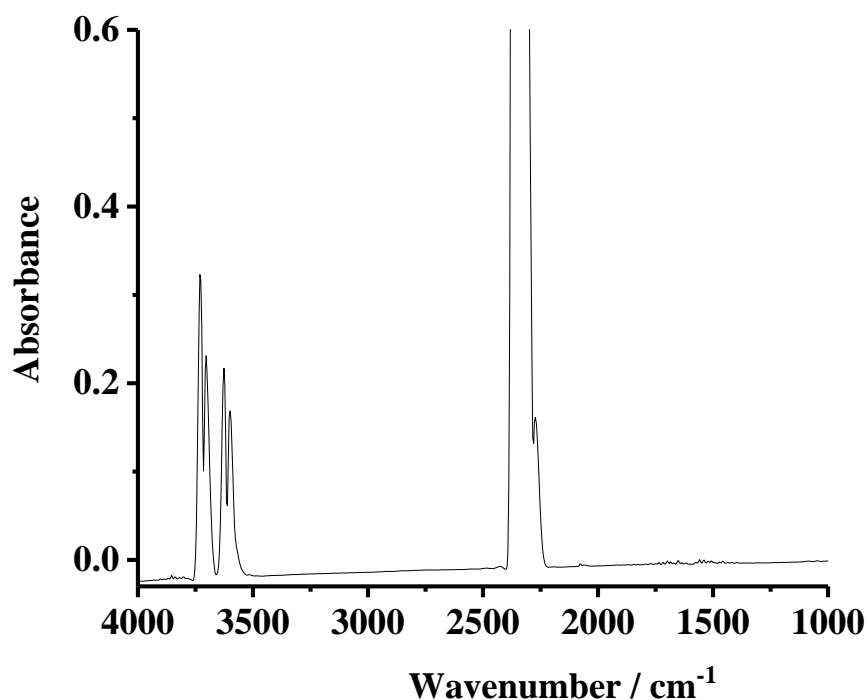


(b)

Figure 2.16. Typical FTIR spectra processing: (a) (i) a reference spectrum, (S_R) collected from $200 \text{ cm}^3 \text{ min}^{-1} \text{ N}_2$ and (ii) a sample spectrum, S_S collected after CH_4 was admitted to the cell at a total flow rate of $200 \text{ cm}^3 \text{ min}^{-1}$, and (b) the resultant absorbance spectrum $= \log_{10}(S_R/S_S)$. Note the intense Q branches of the two bands.



(a)



(b)

Figure 2.17. Typical FTIR spectra processing: (a) (i) a reference spectrum, (S_R) collected from $200 \text{ cm}^3 \text{ min}^{-1} \text{ N}_2$ and (ii) a sample spectrum, (S_S) collected after CO_2 was admitted to the cell at a total flow rate of $200 \text{ cm}^3 \text{ min}^{-1}$, and (b) the resultant absorbance spectrum = $\log_{10}(S_R/S_S)$. Note the fundamental bands are saturating.

As can be seen from fig. 2.16 (b), the bands with the intense features branches centred at 3017 and 1302 cm^{-1} may be attributed to the P, Q and R branches of the ν_3 and ν_4 fundamentals of CH_4 respectively [10]. Using the 1 cm gas cell and $100\% \text{ CH}_4$, the extinction coefficients at 3086 cm^{-1} and 1346 cm^{-1} were determined as $3.5 \pm 0.4 \text{ M}^{-1} \text{ cm}^{-1}$ and $6.4 \pm \text{M}^{-1} \text{ cm}^{-1}$, respectively. These values were checked using a 0.6 cm pathlength cell, repeated 5 times. However, the ν_3 band of the CH_4 was too distorted by the absorptions due to excited CH_4 , CH_4^* (see section 4.1) to allow any quantitative measurements, hence the absorbance at 1346 cm^{-1} of the ν_4 loss feature was employed to determine the degree of conversion of CH_4 . In terms of the production of CH_4^* , the only clear feature is the positive lobe of the ν_4 band at ca. 3008 cm^{-1} , but this is also distorted by the corresponding loss due to CH_4 , and hence this feature was only employed in a qualitative fashion.

The intense feature between 2300 and 2400 cm^{-1} in fig. 2.17 (b) is due to the P and R bands of the CO_2 fundamental absorption [10, 11] and the features between 3500 and 4000 cm^{-1} are CO_2 combination bands [12]. It is clear from the figure that the fundamental bands are saturating and hence cannot be employed for any quantitative measurements; hence it was decided to employ the CO_2 combination band to gain an idea of CO_2 conversion. The features are the least perturbed by the formation of excited CO_2 [13], see section 3.2.

The integrated extinction coefficient of $7.0 \times 10^5 \text{ cm mol}^{-1}$ reported by Bolis and co-workers [14] was employed for the CO absorption between 2002 and 2225 cm^{-1} . This value was checked by determining the extinction coefficient of CO using a 1 cm pathlength transmission cell with 100% CO at 24 °C, and the value so obtained compared to that of Bolis et al. and found to be within 10%, see appendix 1. The same cell was employed to determine the integrated extinction coefficient of the combination bands of CO_2 between 3491 and 3769 cm^{-1} , and this was found to be $6.5 \times 10^5 \text{ cm mol}^{-1}$, see appendix 2. Using the thermal FTIR system and a static atmosphere of 3.7% CO_2 + 96.3% N_2 , the integrated extinction coefficient of the CO_2 combination bands was found to remain constant over the temperature range from 25 °C to 150 °C of interest in this work.

2.9 Data manipulation

The conversion of CO_2 and CH_4 (%) is defined as:

$$\% \text{CO}_2 = 100 \times ([\text{CO}_2]_{\text{feed}} - [\text{CO}_2]_{\text{glow}}) / [\text{CO}_2]_{\text{feed}} \quad (2.7)$$

where $[\text{CO}_2]_{\text{glow}}$ is the concentration of CO_2 in the plasma glow and $[\text{CO}_2]_{\text{feed}}$ is that in the feed to the plasma cell, both measured using the integrated areas of the CO_2 combination band.

Similarly, the conversion of CH_4 :

$$\% \text{CH}_4 = 100 \times ([\text{CH}_4]_{\text{feed}} - [\text{CH}_4]_{\text{glow}}) / [\text{CH}_4]_{\text{feed}} \quad (2.8)$$

determined using the 1346 cm^{-1} feature.

The percentage of the CO₂ in the feed gas, %CO_{2 feed} is defined as:

$$\%CO_{2 \text{ feed}} = ([CO_2]_{\text{feed}} / 0.0408 \text{ M}) \times 100\% \quad (2.9)$$

where 0.0408 M is the concentration of 1 mole of ideal gas at 298 K and 1 atm.

Similarly, percentage of the CH₄ in the feed gas, %CH_{4 feed}:

$$\%CH_{4 \text{ feed}} = ([CH_4]_{\text{feed}} / 0.0408 \text{ M}) \times 100\% \quad (2.10)$$

In the plasma experiments, the conversion of CO₂ to rotationally-excited CO is:

$$\%CO^* = 100 \times [CO^*]_{\text{glow}}/[CO_2]_{\text{feed}} \quad (2.11)$$

where [CO₂]_{feed} is the concentration of CO₂ in the feed to the plasma cell and [CO*]_{glow} is the concentration of CO in the plasma glow. The corresponding CO selectivity, %S_{CO*} is:

$$\%S_{CO^*} = 100 \times [CO^*]_{\text{glow}}/([CO_2]_{\text{feed}} - [CO_2^*]_{\text{glow}}) \quad (2.12)$$

The carbon balance, %C, is:

$$\%C = 100 \times ([CO^*]_{\text{glow}} + [CO_2^*]_{\text{glow}})/[CO_2]_{\text{feed}} \quad (2.13)$$

The energy efficiency for the production of CO is:

$$\eta_{CO} / \% = 100\Delta H/E_{p,l} \quad (2.14)$$

where ΔH is the enthalpy (279.8 kJ mol⁻¹) of the process [15]:



at 300K. $E_{p,CO}$ is the energy expended in producing 1 mole of CO and assuming that the IR spectra record an average picture over the 1 minute data collection time.

All the calculations presented in this chapter are based on the integrated areas of the CO₂ and CO₂* combination bands and the P and R branches of the CO* absorption. These are all subject to inevitable experimental error, particularly with respect to determining baselines: this is particularly relevant to the determination of the integrated absorptions of the CO* features as these are adjacent to the very strong CO₂* fundamental.

For the experiments employing the transmission cell, the estimated error in the baseline calculations of the CO* bands, i. e. between employing a linear vs curved baseline between the extremes of the spectral ranges employed, was ca. 10%. The experimental error associated with the plasma reflectance cell was somewhat higher as the optical pathlength could not be measured directly (as was the case with the transmission cell) but was determined from calculations based on the optical configuration and the integrated intensity of the CO₂ combination bands of 100% CO₂. On this basis, the pathlength of the reflectance cell was ca. five times lower than that of the transmission cell (5.1 cm cff. ca. 1 cm) making baseline correction even less accurate due to the weaker CO absorptions.

2.10 Material characterisation techniques

2.10.1 X-ray diffraction (XRD)

XRD analyse of the SnO₂ and CeO₂ were performed using PANalytical X'Pert Pro MPD, powered by a Philips PW3040/60 X-ray generator fitted with an X'Celerator detector, see fig. 2.18. The diffraction data were acquired by exposing powder samples to Cu-K_α X-ray radiation, which has a characteristic wavelength (λ) of 1.5418 Å and X-rays were generated from a Cu anode supplied with 40 kV and a current of 40 mA.

The goal of the XRD analysis was to identify particle size, the interplanar spacing (d-spacing), crystalline phases and the lattice parameters. The data were collected over a range of 2-100°2 θ with a step size of 0.0334°2 θ and nominal time per step of 400 s, using the scanning X'Celerator detector and a nickel filter on the incident beam. Fixed anti-scatter and divergence slits of 1/4° were used together with a beam mask of 10 mm and all scans were carried out in 'continuous' mode. Average particle size was determined by using the Full Width at Half Maximum (FWHM) intensity of selected peaks via Scherrer's equation:

$$t = 0.9 \lambda / B \cdot \cos \theta \quad (2.26)$$

where t is the particle size (\AA), λ is the wavelength of the Cu- K_{α} radiation (1.5406 \AA), B is the FWHM in radians and θ is the Bragg angle.



Figure 2.18. Photograph of the PANalytical X'Pert Pro MPD x-Ray diffractometer.

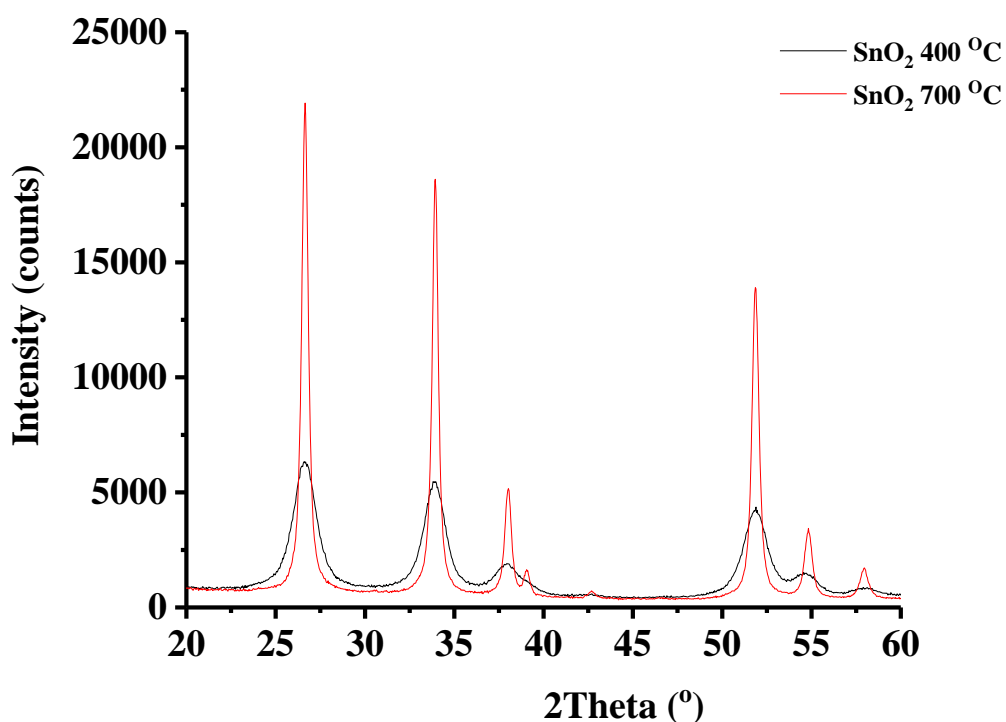
Phase identification was carried out by means of the X'Pert accompanying software program PANalytical High Score Plus in conjunction with the ICDD Powder Diffraction File 2 Database (1999), ICDD Powder Diffraction File 4 - Minerals (2012), the American Mineralogist Crystal Structure Database (March 2010) and the Crystallography Open Database.

All XRD measurement were carried out by Ms. Maggie White from School of Engineering, Newcastle University and table 2.6 summarises the particle size calculated from Scherrer's equation of the CeO_2 , SnO_2 400 °C and 700 °C nanopowders.

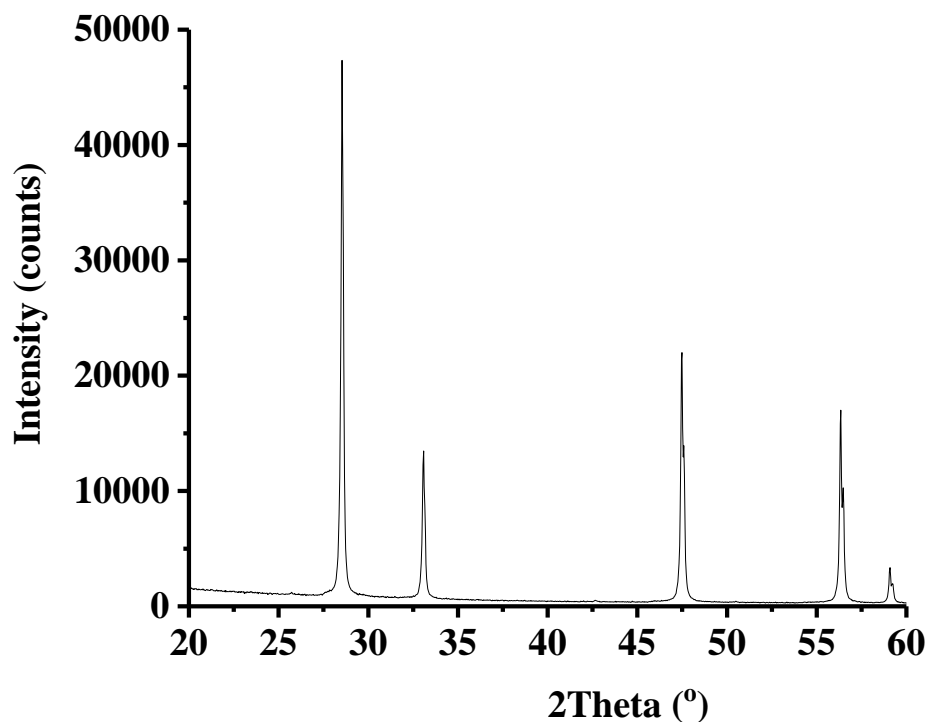
Sample	Calcination Temperature / °C	Particle size /nm
SnO ₂	400	6.09
SnO ₂	700	17.06
CeO ₂	As prepared	47.00

Table 2.6. The particle sizes of the CeO₂, SnO₂ 400 °C and 700 °C nanopowders calculated from Scherrer's equation.

As may be seen from the table 2.6, the particle size of the SnO₂ increased from 6.09 nm to 17.06 nm after calcining at 700 °C indicates crystal growth due to sintering [16]. Similar trends were observed in the work of Maneelok in Newcastle [17, 18] who reported the evolution of the particle size as a function of temperature. Furthermore, as can be seen in figs. 2.19(a), the FWHM of the SnO₂ nanopowder peaks decreased with increasing temperature and the peaks became sharper suggesting that the crystallinity improved [8] with increasing temperature, in agreement with the literature [17-20].



(a)



(b)

Figure 2.19. (a) The XRD patterns of the SnO_2 400 °C and 700 °C nanopowders prepared by hydrothermal synthesis and (b) The XRD patterns of the CeO_2 nanopowders purchased from Sigma Aldrich.

2.10.2 The thermogravimetric analysis system

The thermogravimetric analysis (TGA) measures the amount and rate of change in the mass of a sample, i.e. CeO_2 , as a function of temperature or time in a controlled atmosphere. In this work, TGA were carried out in an atmosphere of flowing ($40 \text{ cm}^3 \text{ min}^{-1}$) O_2 -free nitrogen, in a Netzsch STA 449C TG-DSC (Thermogravimetry-Differential Scanning Calorimetry, or TG-DSC) system, connected to a Netzsch Aeolos 403C Quadrupole Mass Spectrometer (QMS; m/z range 10-300). 95.5 mg of the CeO_2 was placed in an alumina crucible and the temperature was then ramped from room temperature to 600 °C at a ramp rate of 5 °C min^{-1} . At 600 °C, temperature was held for 10 minutes then cooled at 5 °C min^{-1} to room temperature. All TGA measurement were carried out by Mr. Bernard Bowler from School of Natural and Environmental Sciences, Newcastle University and results of the TGA analyses are further discussed in Chapter 5.

2.11 References

1. *Macor Machinable Glass Ceramic - Rod*. 2017 [cited 2017 29 Aug]; Available from:
http://www.goodfellow.com/catalogue/GFCat4J.php?ewd_token=3ogp4un2GrWg8NaKcFB076aAzMsZu9&n=H0knwRBzWxB7BMVGZzlGumlDPWHwN.
2. M, S., S. Pekarek, V. Prukner, *Influence of Power Modulation on Ozone Production Using an AC Surface Dielectric Barrier Discharge in Oxygen*. *Plasma Chemistry and Plasma Processing*, 2010. **30**: p. 607-617.
3. P. A. Christensen, P.S.A., R. G. Egdell, S. Maneelok and D. A. C. Manning, *An in situ FTIR spectroscopic and thermogravimetric analysis study of the dehydration and dihydroxylation of SnO₂: the contribution of the (100), (110) and (111) facets*. *Physical Chemistry Chemical Physics*, 2016. **18**(33): p. 22990-22998.
4. P. A. Christensen, S.W.M.J., *An in situ FTIR study of undoped PolyBenzoImadazole as a function of relative humidity*. *Polymer Degradation and Stability* 2014. **105**: p. 211-217.
5. *Shimadzu Fourier Transform Infrared Spectrophotometers*. FTIR Series Accessories [cited 2017 24 August]; Available from:
<http://www.ssi.shimadzu.com/products/literature/spectroscopy/c103-e005h.pdf>.
6. Jentoft, F., *Lecture series in Heterogeneous Catalysis. Diffuse Reflectance IR and UV-Vis Spectroscopy, Modern Methods in Heterogeneous Catalysis*. 2008.
7. Kubelka, P., *New Contributions to the Optics of Intensely Light-Scattering Materials. Part I*. *Journal of the Optical Society of America*, 1948. **38**(5): p. 448-457.
8. Fujihara, S., T. Maeda, H. Ohgi, E. Hosono, H. Imai, and S.-H. Kim, *Hydrothermal Routes To Prepare Nanocrystalline Mesoporous SnO₂ Having High Thermal Stability*. *Langmuir*, 2004. **20**(15): p. 6476-6481.
9. Hyun-Ha Kim. Atsushi Ogata, S.F., *Application of Plasma-Catalyst hybrid Processes For The Control of NO_x And Volatile Organic Compounds in Trends in Catalysis Research* L.P. Bevy, Editor. 2006, Nova Science Publisher, Inc. : New York. p. 15.
10. Stein, S.E. "Infrared Spectra" in *NST Chemistry Webbook, NIST Standard Reference Database Number 69*. [cited 2017 September 5]; Available from:
<http://webbook.nist.gov/cgi/cbook.cgi?Contrib=MSDC-IR>.
11. Herzberg, G., *Molecular spectra and molecular structure* Vol. Vol.2: Infrared and Raman spectra of polyatomic molecules. 1945, New York Van Nostrand Reinhold.

12. Bennett, C.J., C.S. Jamieson, and R.I. Kaiser, *Mechanistical studies on the formation and destruction of carbon monoxide (CO), carbon dioxide (CO₂), and carbon trioxide (CO₃) in interstellar ice analog samples*. Physical Chemistry Chemical Physics, 2010. **12**(16): p. 4032-4050.
13. Abdullah Al-Abduly, P.A.C., *An in situ and downstream study of non-thermal plasma chemistry in an air fed dielectric barrier discharge (DBD)*. Plasma Sources Science and Technology, 2015. **24**: p. 065006
14. Bolis, V., B. Fubini, E. Garrone, and C. Morterra, *Thermodynamic and vibrational characterization of CO adsorption on variously pretreated anatase*. Journal of the Chemical Society, Faraday Transactions 1: Physical Chemistry in Condensed Phases, 1989. **85**(6): p. 1383-1395.
15. Robby Aerts, W.S., Annemie Bogaerts, *Carbon dioxide splitting in a dielectric barrier discharge plasma: a combined experimental and computational study*. ChemSusChem, 2015. **8**(4): p. 702-716.
16. Jeon, H.-J., M.-K. Jeon, M. Kang, S.-G. Lee, Y.-L. Lee, Y.-K. Hong, and B.-H. Choi, *Synthesis and characterization of antimony-doped tin oxide (ATO) with nanometer-sized particles and their conductivities*. Materials Letters, 2005. **59**(14): p. 1801-1810.
17. Christensen, P.A., P.S. Attidekou, R.G. Egdell, S. Maneelok, and D.A.C. Manning, *An in situ FTIR spectroscopic and thermogravimetric analysis study of the dehydration and dihydroxylation of SnO₂: the contribution of the (100), (110) and (111) facets*. Physical Chemistry Chemical Physics, 2016. **18**(33): p. 22990-22998.
18. Maneelok, S., *The relationship between the composition and structure of Ni/Sb-SnO₂ and electrochemical ozone activity*, in *School of Chemical Engineering and Advanced Materials*. 2017, Newcastle University Newcastle University
19. Wang, Y.-X., J. Sun, X. Fan, and X. Yu, *A CTAB-assisted hydrothermal and solvothermal synthesis of ZnO nanopowders*. Ceramics International, 2011. **37**(8): p. 3431-3436.
20. Aziz, M., S. Saber Abbas, and W.R. Wan Baharom, *Size-controlled synthesis of SnO₂ nanoparticles by sol-gel method*. Materials Letters, 2013. **91**: p. 31-34.

Chapter 3. An in-situ study of non-thermal plasma fed with CO₂, and N₂ in plasma- and thermally driven experiments at Macor

3.1 Introduction

The aim of the work reported in this chapter was to study the non-thermal plasma – driven reduction of CO₂ to CO and O in-situ infrared spectroscopy via a plasma transmission cell and a plasma reflectance cell. It was hoped that the comparison of the data obtained from the two cells would allow discrimination between processes taking place purely in the plasma glow from those at the plasma/dielectric surface. This chapter also reports, for the first time, a direct comparison of the IR spectroscopy of plasma- and thermally- driven reactions of CO₂.

3.2 The plasma-driven reaction of CO₂ at Macor

3.2.1 Plasma transmission cell

Figure 3.1 shows a single beam spectrum of the plasma transmission cell at 25 °C with flowing 12.2% CO₂ + 87.8% N₂ and no plasma.

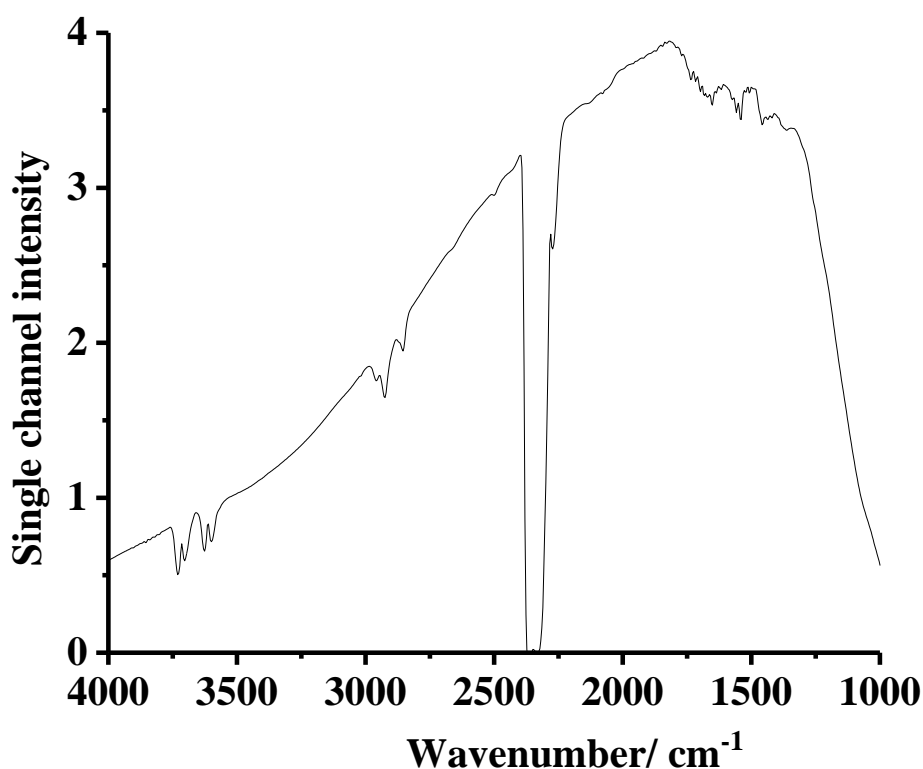
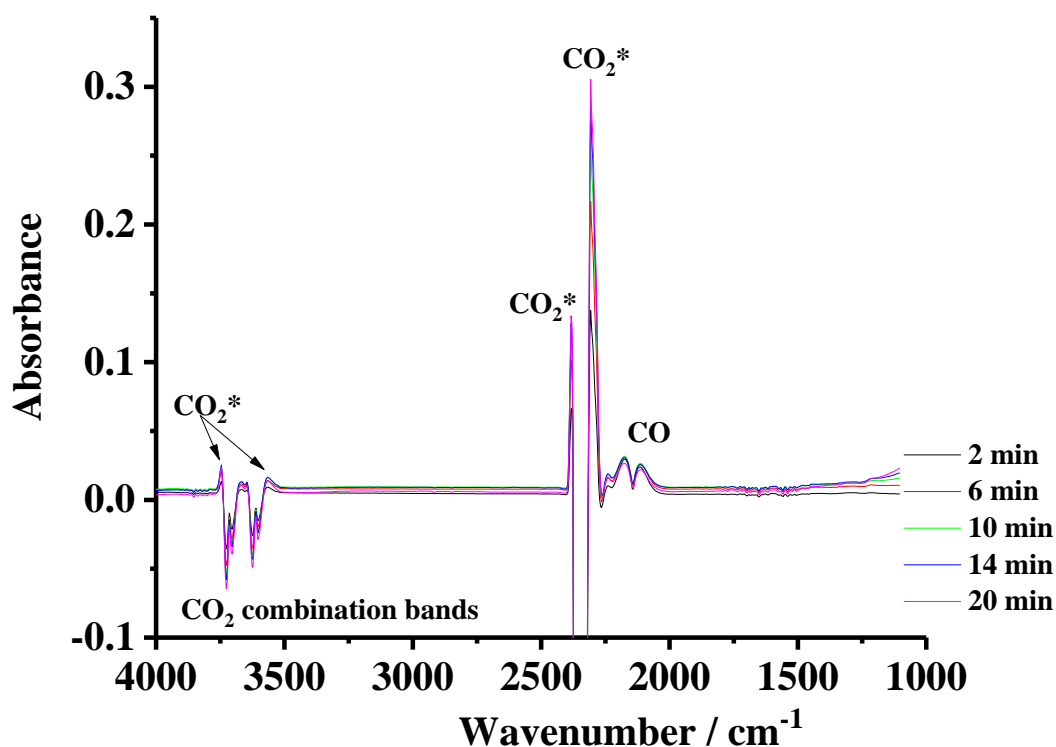


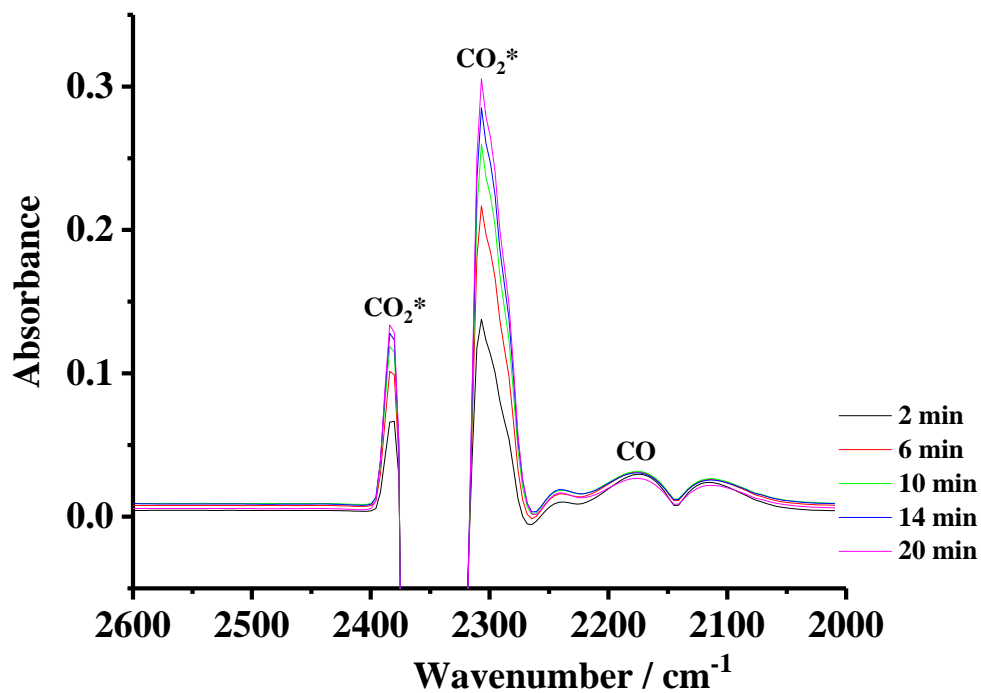
Figure 3.1. Typical reference spectrum (8 cm⁻¹ resolution, 100 scans per scan set, and 60 seconds per spectrum) of the plasma transmission cell collected at a total flowrate of 200 cm³ min⁻¹. The gas composition was 12.2% CO₂, 87.8% N₂ with no plasma.

The P and R asymmetric stretch (ν_3) bands of CO_2 at 2340 and 2360 cm^{-1} [1-3] are clearly saturated, hence it was decided to employ the integrated intensities of the CO_2 combination bands at 3728 cm^{-1} to gain some qualitative and quantitative indication of the conversion of CO_2 during the plasma experiments as discussed in section 2.8. The small feature around 2260 cm^{-1} may be attributed to the $^{13}\text{C}^{16}\text{O}_2$ fundamental [4].

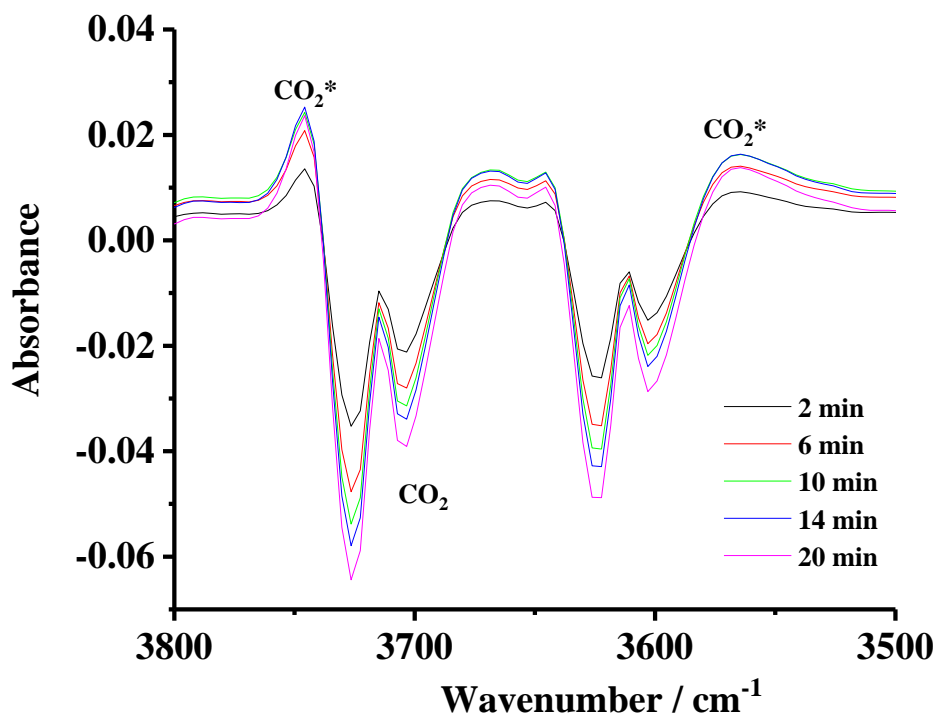
Figure 3.2(a) shows selected spectra collected as a function of time at 28W input power employing the spectrum collected in fig. 3.1 as the reference. The experiment in figs. 3.2(a) to (c) was repeated at input powers of 20, 22, 24 and 26 W, with no additional bands being observed. As can be seen, the loss features at 3728, 3625, 2360 and 2340 cm^{-1} are due to CO_2 and the gain features at 2163 and 2116 cm^{-1} maybe attributed unambiguously to carbon monoxide [1, 5]. The structure between 2250 and 2500 cm^{-1} is due to the superposition of CO_2 loss features at 2360 and 2340 cm^{-1} on the gain features at 2306 and 2383 cm^{-1} due to rotationally-excited (CO_2^*). The CO_2^* bands are highly distorted due to the fact they are superimposed on the CO_2 loss features, see the work of Al-Abduly et al. [6] and fig. 3.2 (b).



(a)



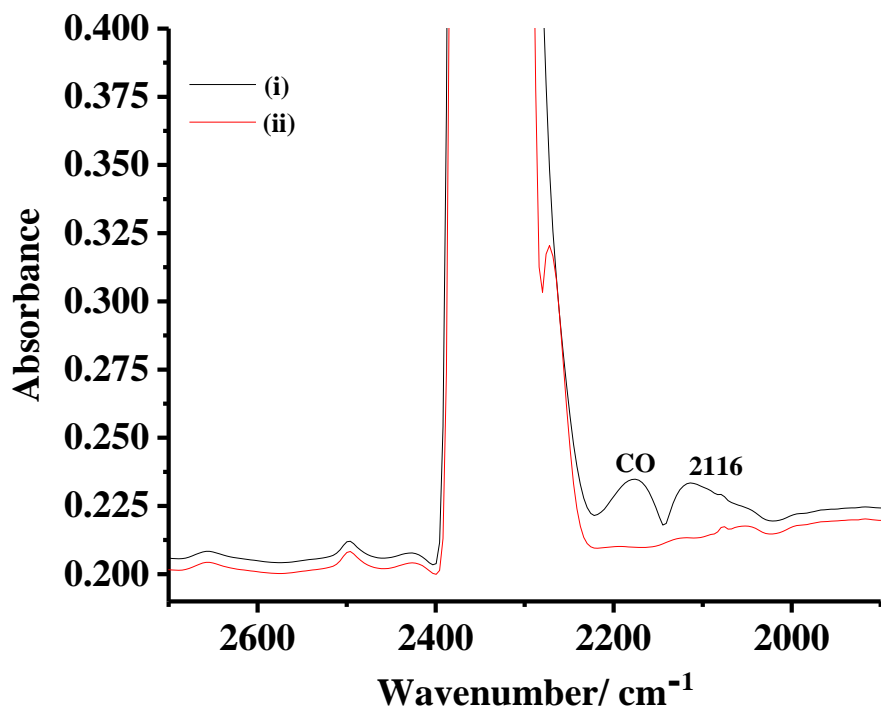
(b)



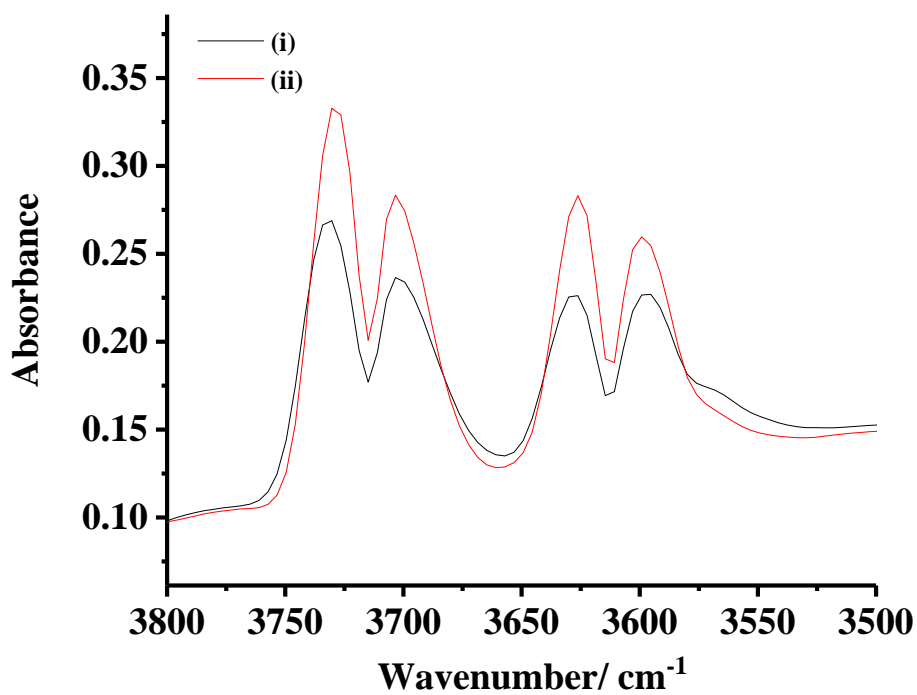
(c)

Figure 3.2. (a) In situ FTIR spectra (8cm^{-1} resolution, 100 co-added and averaged scans, 60 seconds per scanset) collected at the times shown on the figure at an input power of 28 W, (b) the CO_2 fundamental region of figs. 3.2(a) and (c) the combination band region. The gas composition was 12.2% CO_2 + 87.8% N_2 and the reference spectrum was that taken with no plasma.

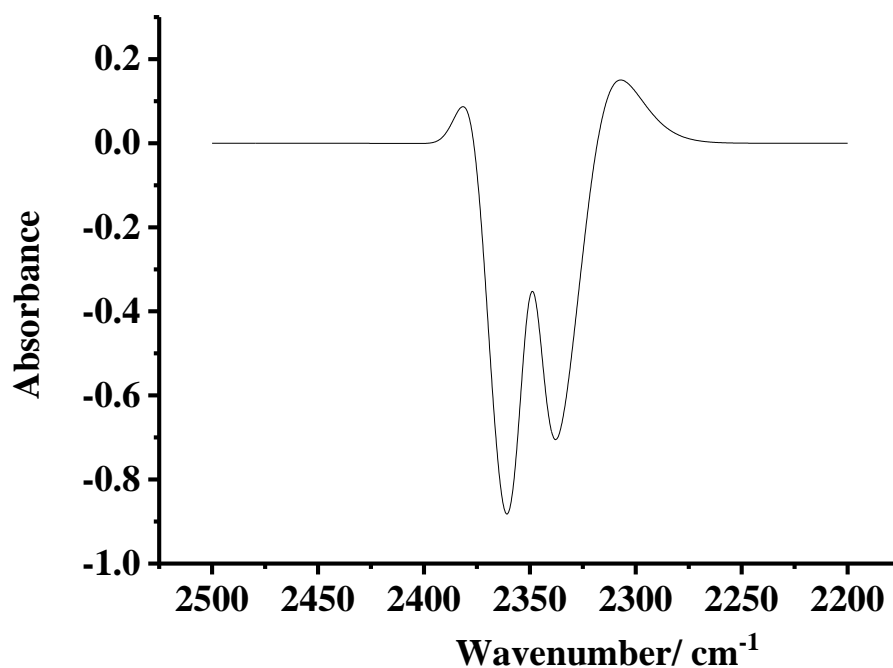
Figures 3.3(a) and (b) show the spectrum collected after 20 minutes in fig. 3.2 and the spectrum collected immediately prior to the plasma being initiated: in both cases, the reference spectrum employed was that taken with a nitrogen feed and no plasma. In other words, the spectra are “absolute” rather than “difference” spectra.



(a)



(b)



(c)

Figure 3.3. (i) The spectrum collected after 20 minutes in fig. 3.2 and (ii) the spectrum collected immediately before the plasma was initiated: (a) CO_2 asymmetric stretch region and (b) combination band region. (c) The result of simulating the spectrum of CO_2 at 100°C and subtracting it from the simulated spectrum of CO_2 at room temperature. See text for details.

Although the intensities of the combination bands decreased on application of the plasma, it is clear that the bands were broadened. Given that the molecules present in the non-thermal plasma are at thermal equilibrium, then the spectra in figs. 3.2, 3.3(a) and 3.3(b) suggest that any CO_2 present in the plasma is rotationally excited [6], and that this species is responsible for the combination and asymmetric stretch features in fig. 3.2.

Figure 3.4 shows the spectrum collected after 2 minutes in fig. 3.2 using as the reference the single beam spectrum collected of the CO_2/N_2 feed with no plasma. As can be seen from the figure, the CO_2^* bands are very clear, as are the structures between 2200 and 2400 cm^{-1} and 3500 and 3800 cm^{-1} due to the loss of ground state CO_2 bands superimposed upon the CO_2^* gain features.

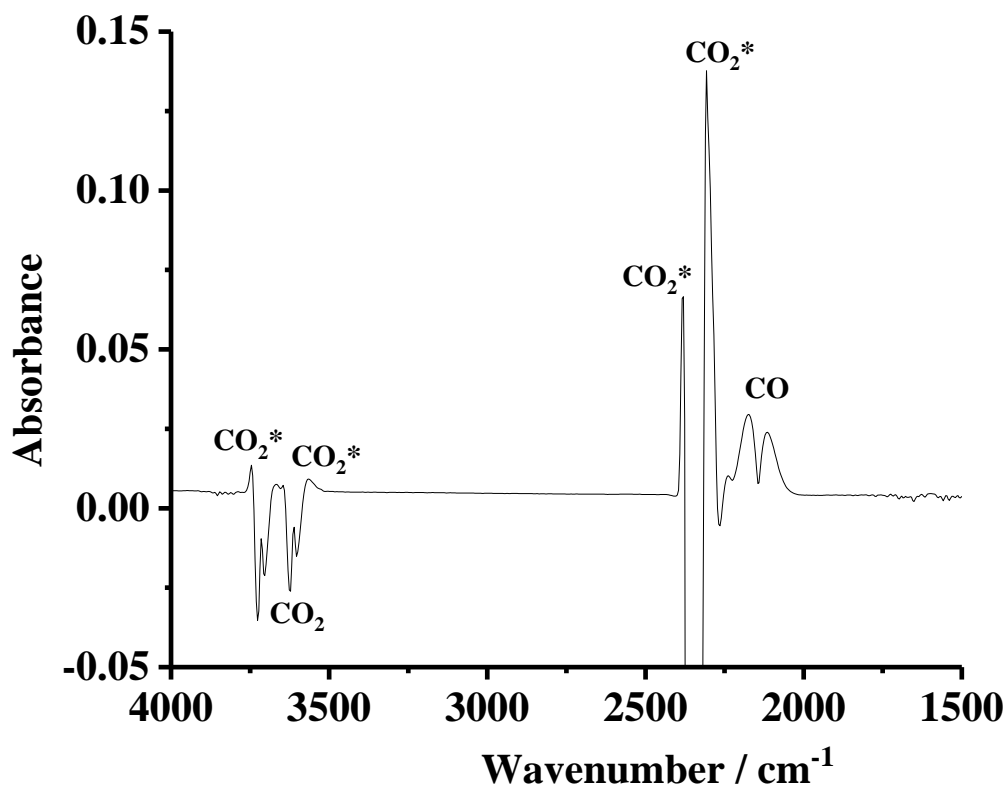


Figure 3.4. The spectrum collected after 2 minutes in fig. 3.2 using the spectrum collected with no plasma and the 12.2% CO₂ + 87.8% N₂ feed gas as reference.

The features between 2200 and 2400 cm⁻¹ in figs. 3.3 and 3.4 were modelled by Prof. Phillip Martin, School of Chemical Engineering and Analytical Science, The University of Manchester, using Spectralcalc and Origin and the difference spectrum obtained by subtracting the spectrum of CO₂ at room temperature from that of the excited CO₂ at 396 K are shown in fig 3.3(c). The figure supports the assignment of the gain features in fig. 3.2 to higher temperature, rotationally excited CO₂ (CO₂*). This assignment was further supported by the behaviour of the CO absorption in the plasma experiments and the thermal experiment, see section 3.2.3.

From figs. 3.2 and 3.3(a) it is apparent that there are clear gain features due to the P and R bands of CO near 2116 and 2176 cm⁻¹ [1, 5] and these are due to the higher temperature, rotationally excited gas, as may be expected from the discussion above. Thus, fig. 3.5 shows the spectra collected after 2 minutes and 20 minutes in the experiment in fig. 3.2, using the spectrum collected with the same gas feed but without plasma as the reference, with a

spectrum of CO gas in a 1 cm pathlength transmission cell at room temperature. The pure CO and 2 minute spectra were scaled down to allow comparison.

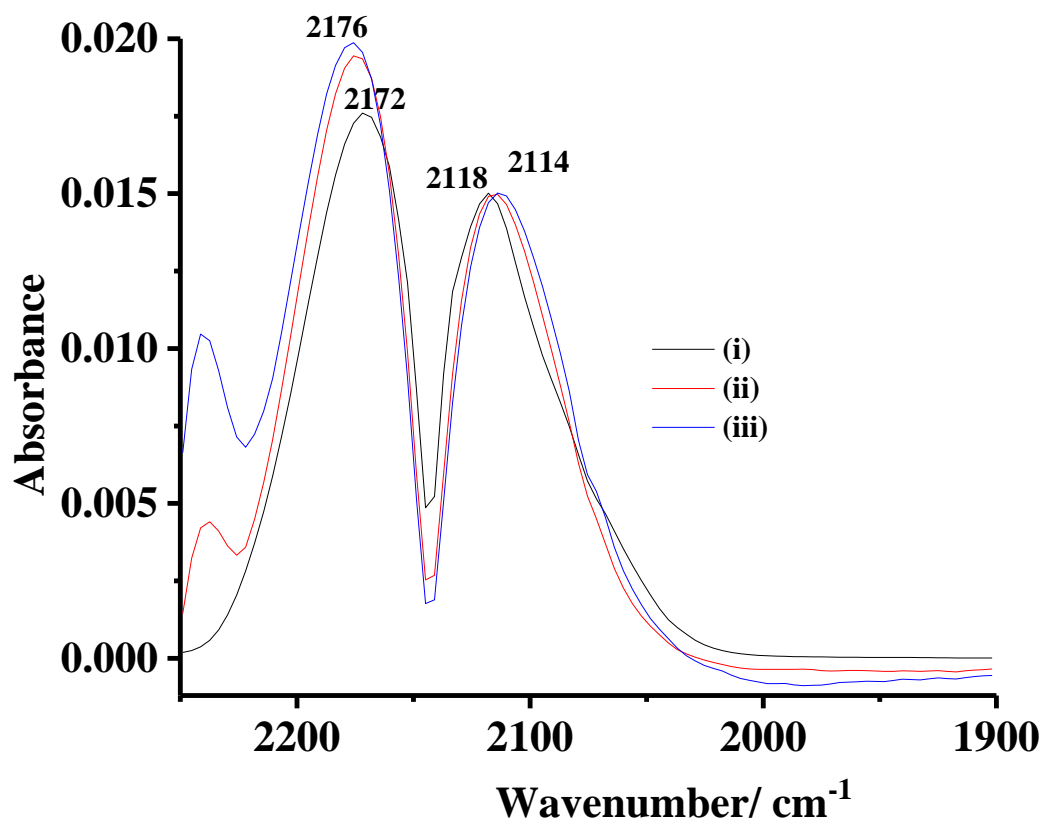


Figure 3.5. (i) The spectrum (8 cm^{-1} resolution, 100 scans per scan set, and 60 seconds per spectrum) of CO in a 1 cm pathlength transmission cell and the spectra collected after (ii) 2 minutes and (iii) 20 minutes during the experiment shown in figs. 3.2 and 3.4. The CO spectrum was reduced by a factor of 16.8 and that taken after 2 minutes in the plasma experiment by a factor of 1.3 in order to aid comparison. The plasma spectra employed the spectrum collected with same feed gas composition without plasma as the reference, and the CO spectrum employed the spectrum collected with the cell filled with nitrogen gas as the reference.

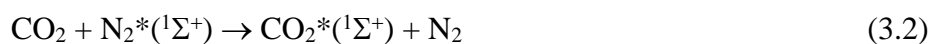
As may be seen from the fig. 3.5, the CO bands in the spectra collected during the plasma experiment are somewhat broader than those of the room temperature CO, and the P and R maxima move apart as would be expected for CO if the molecule was rotationally excited (CO^*). Bauerecker et al. [7] observed the rotation-vibration bandwidth of $^{13}\text{C}^{16}\text{O}$ to be

reduced by about 40% on cooling the gas from 300 K to 45 K, without any change in band centre. The resolution of the spectra obtained in the experiments reported in this work (8 cm^{-1}) was chosen as the highest possible allowing for a reasonable data collection time. However, temperature calculations based on the maxima of the P and R branches of CO [5] gave wide ranges when the resolution was taken into account: e.g. allowing $\pm 4 \text{ cm}^{-1}$ for P and R branches nominally at 2172 and 2118 cm^{-1} resulted in temperatures between 210 and 382 K. Hence, in order to allow comparison within the data sets, ambient temperature was employed.

The vibrationally excited form of the ground electronic state of CO_2 , $\text{CO}_2^*(^1\Sigma^+)$, is generally accepted as being the intermediate in the plasma-induced reduction of CO_2 to CO and O_2 for plasmas with lower mean electron energies than those in dielectric barrier discharges [8]. This is clearly not the same species as the rotationally-excited CO_2^* observed in figs 3.2 and 3.5. $\text{CO}_2^*(^1\Sigma^+)$ may be formed directly through collisions with electrons in the plasma [9, 10]:



or via collisional energy transfer from vibrationally excited species such as $\text{N}_2^*(^1\Sigma^+)$ [10]:



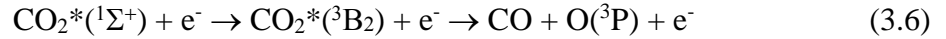
whilst $\text{CO}_2^*(^1\Sigma^+)$ decay can take place through relaxation to CO_2 and photon emission or dissociation into CO and atomic oxygen [3, 4]:



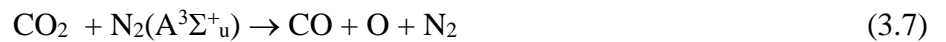
The dissociation of CO_2 via reaction (3.3) can take place by two possible routes [8, 11]. (i) Excitation to vibrational levels of the ground excited state of CO_2 which exceed the energy of the dissociation threshold, this results in ground state CO and singlet oxygen:



(ii) Excitation to the first excited triplet state of CO_2 via intersystem crossing resulting in ground state CO and ground state atomic oxygen:



The latter is favoured due to the non-adiabatic intersystem crossing and the reduction in the energy required for dissociation [12, 13]. In CO_2 feeds diluted with nitrogen, Snoeckx and co-workers [14] postulate that the dissociation of CO_2 depends upon the partial pressure of N_2 : thus, at low nitrogen pressure, the main reaction is the direct electron excitation of CO_2 and subsequent reduction to CO and O_2 , as discussed above, equations 3.1 to 3.6. In contrast, at high nitrogen partial pressure it is:



In other words, as the partial pressure of nitrogen increases, the electron energy is primarily employed to excite the nitrogen molecules to the metastable $\text{A}^3\Sigma_u^+$ state rather than for direct electron excitation of CO_2 , which may be the reason vibrationally excited CO_2 was not detected in these experiments.

The integrated absorption intensities of the CO_2 combination bands and the CO fundamental were employed to gain some quantitative insight into the chemistry of the plasma glow, and the results are summarized in table 3.1.

Input power /W	Time /Min	[CO ₂] _{feed} /10 ⁻³ M	[CO ₂ *] _{glow} /10 ⁻³ M	[CO*] _{glow} /10 ⁻⁴ M	%CO*	η _{co} /%	%C
20	2	5.2	4.7	5.1	9.9	2.4	101
	6		4.6	4.9	9.4	2.3	97.7
	10		4.5	4.6	8.8	2.1	95.6
	20		4.4	4.1	7.9	1.9	93.4
22	2	4.8	4.3	4.3	10.2	2.1	99.6
	6		4.1	4.1	9.3	1.9	96.0
	10		4.1	4.1	8.7	1.8	94.1
	20		4.0	4.0	7.8	1.6	92.3
24	2	5.4	4.9	5.1	9.4	2.0	98.9
	6		4.7	4.5	8.3	1.8	94.5
	10		4.6	4.2	7.6	1.6	92.7
	20		4.6	3.7	6.7	1.4	90.7
26	2	5.0	4.4	5.3	10.7	1.9	99.2
	6		4.2	4.5	9.1	1.6	94.5
	10		4.2	4.1	8.2	1.5	91.8
	20		4.1	3.5	7.0	1.2	89.4
28	2	5.0	4.3	5.3	10.7	1.8	96.6
	6		4.1	4.5	9.1	1.5	91.1
	10		4.0	4.0	8.1	1.3	88.9
	20		4.0	3.4	6.8	1.1	86.7
20 (100% CO ₂) [‡]	2	40.8	-	14.1	3.5	6.6	-
	6		-	13.0	3.2	6.0	-
	10		-	11.8	2.9	5.5	-
	20		-	9.8	2.4	4.6	-
24 (100% CO ₂) [‡]	2	40.8	-				-
	6		-				-
	10		-				-
	20		-				-
14 (Ar)	2	4.4	3.9	4.6	10.3	3.1	98.9
	6		3.8	4.2	9.5	2.8	95.6
	10		3.8	4.0	8.9	2.6	93.4
	20		3.7	3.4	7.7	2.3	90.2

[‡] CO₂ and CO₂* absorptions were saturated, rendering calculation of their concentrations etc. not feasible.

Table 3.1. Summary of the data obtained in the experiments typified by IR plasma transmission Cell.

In general, the concentrations of both CO* and CO₂* declined with time at all input powers, leading to a loss in carbon inventory, as is shown in table 3.1. Figure 3.6 shows a plot of the integrated absorbance of the CO band and the CO* combination bands in fig. 3.2 as a function of time, and fig. 3.7 the analogous plots normalized to their maximum values.

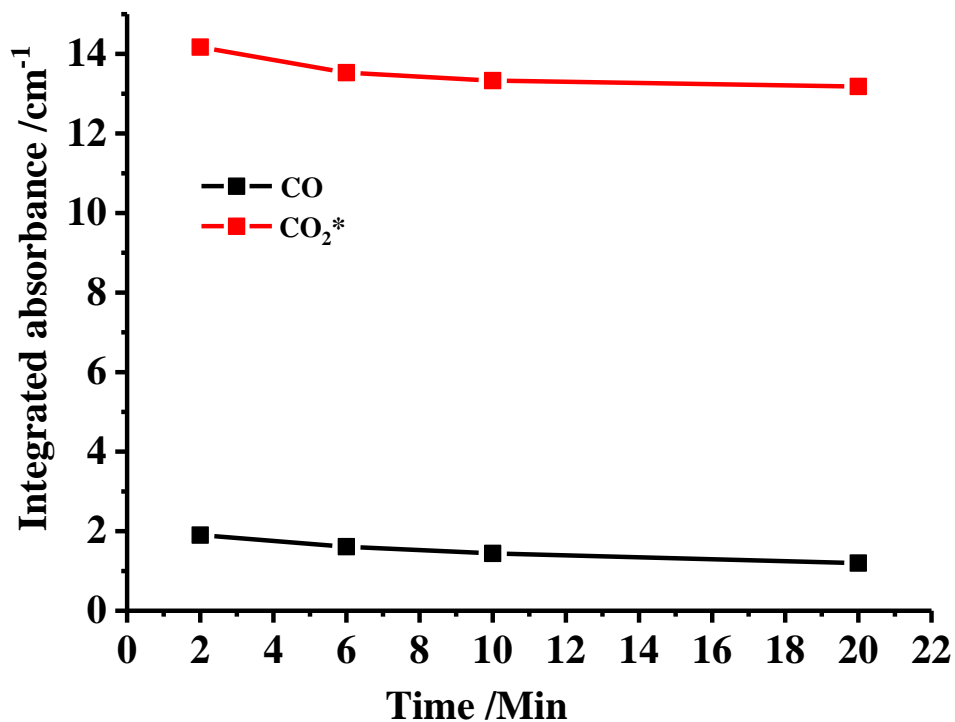


Figure 3.6. Plots of the integrated absorbance of the CO* band and the integrated absorbance of the CO₂* combination bands in fig. 3.2 as a function of time.

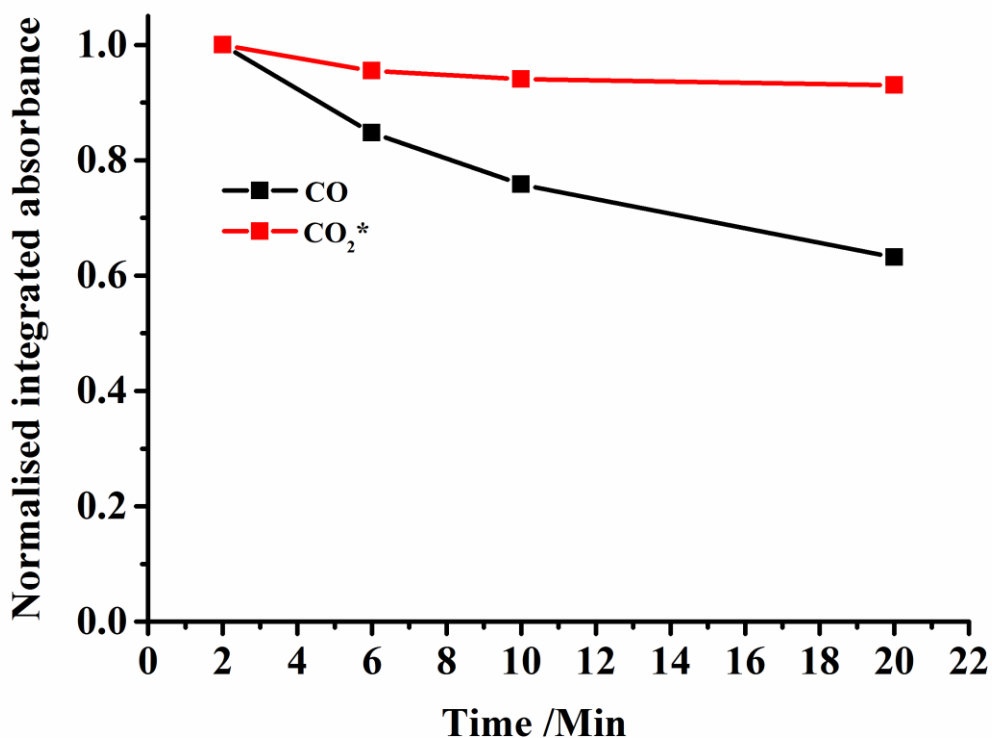
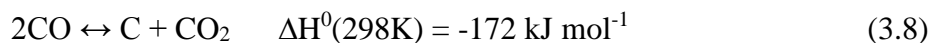


Figure 3.7. Plots of the integrated absorbances of the CO* and CO₂* combination bands in fig. 3.2 as a function of time. The plots were normalised to their maximum values.

The broadening of the CO₂ and CO features suggests the decline in the concentration of CO* is accompanied by a concomitant increase in the temperature of the gases in the plasma, and the two appear to be linked. The chemical simplicity of the plasma system and lack of any additional product absorptions suggests that there is a process, or processes, taking place leading to carbon-containing products that are infrared inactive or present at steady-state concentrations below the detection limit of the FTIR system. One example of the former is the Boudard reaction [15], which is commonly observed in plasma systems involving CO/CO₂:



No carbon deposits were observed on the walls or windows of the cell, but these could have been swept away by the feed gas. As was stated above, the plasma temperature increased with operational time and input power: due to the exothermicity of reaction (3.8) and its

negative reaction entropy, the equilibrium constant for the process decreases with temperature, and hence less loss of CO due to the Boudouard reaction would be expected with time, in contrast to the observed results.

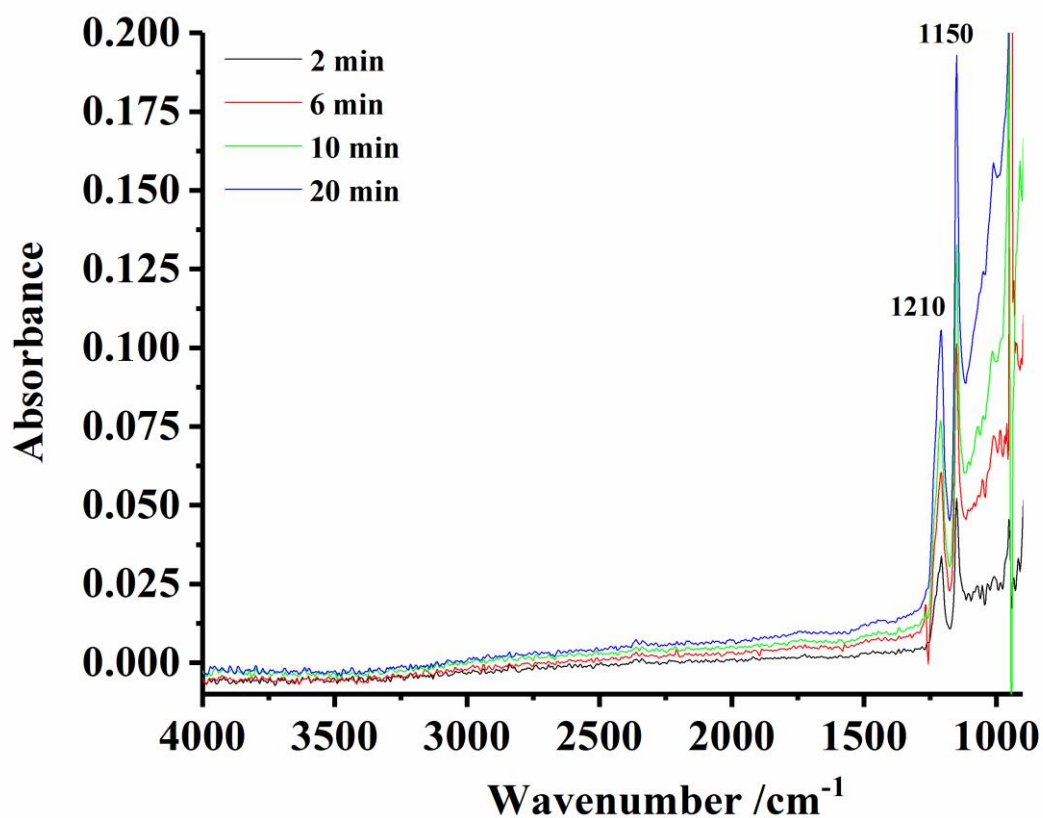
As can be seen from table 3.1, the conversion of CO₂ to CO after 2 minutes was ca. 10 – 11% irrespective of the input power, declining with time, as expected on the basis of figs. 3.6 and 3.7. The former observation was unexpected as an increase in conversion with increasing plasma power would be qualitatively expected on the basis of an increasing frequency of electron/gas collisions due to an increase in the discharge current ($I = P/V_0$), as shown by Manley's equation [16], see section 1.5.

The IR plasma cell was in no way optimised for energy efficient operation, but a comparison of the energy efficiency for, for example, CO production with the literature values would at the least give confidence that the plasma system under study was not atypical, and this was confirmed. Thus table 3.1 shows the values of η_{CO} observed during the various experiments. As may be seen from the table, the energy efficiency of CO production decreased with increasing operational time and increasing input power: e.g. at 20 W, η_{CO} declined from 2.4% after 2 minutes to 1.9% after 20 minutes, with analogous values of 1.8% to 1.1% at 28 W. Overall, the efficiency for CO production were broadly comparable to those reported in the literature, ie. ca. 1 - 2% [14, 17-19].

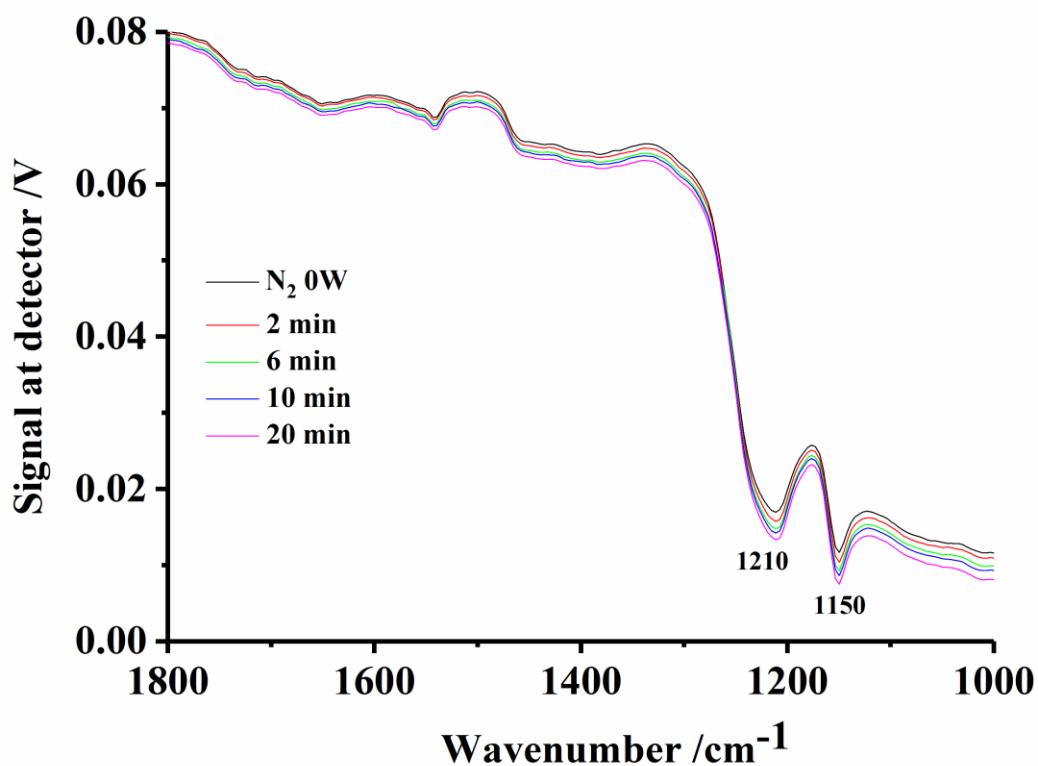
Table 3.1 also summarizes the data obtained using 100% CO₂ and CO₂ + Ar. With respect to the former, it can be seen that, whilst the increase in CO₂ results in an increase in the absolute amount of CO produced and the energy efficiency as would be expected, the fraction of CO₂ converted to CO decreases, from ca. 10% after 2 minutes to ca. 6 – 7%. These data support the positive role of N₂ in terms of its direct involvement in the reduction of CO₂, see row (8) – (14) as well as the data obtained using Ar, see Table 3.1, where comparable conversion and energy efficiencies to those obtained using CO₂ + N₂ were obtained but at significantly lower input energy and ca. 20% lower CO₂ in the feed gas. Further, adding N₂ or Ar is generally reported as rendering plasmas easier to ignite and having significant effect upon electron energy distribution functions [20].

3.2.2 Plasma reflectance cell

Figure. 3.8(a) shows selected sample spectra collected at an input power of 24 W and a nitrogen flow rate of $30 \text{ cm}^3 \text{ min}^{-1}$ using the plasma reflectance cell. The spectrum collected immediately before the plasma was initiated was employed as the reference and sample spectra were collected every 2 minutes up to 20 minutes after the plasma was turned on.



(a)



(b)

Figure 3.8. (a) *In situ* FTIR spectra (8 cm^{-1} resolution, 100 co-added and averaged scans, 60 seconds per scanset) collected at the times shown on the figure at an input power of 24 W using the reflectance cell and nitrogen gas as the feed gas. The spectrum collected immediately before the plasma was initiated was employed as the reference. (b) The single beam spectra from the experiment in fig. 3.8(a).

As may be seen from the figs. 3.8, the spectra are featureless apart from two strong bands at 1210 cm^{-1} (broad) and 1150 cm^{-1} , that increase in intensity steadily with time. Figure 3.9 shows plots of the integrated absorptions of the two bands obtained from analogous experiments to that in fig. 3.8(a) as a function of input power from the spectra taken after 20 minutes operation. As can be seen from the figure, clearly, the features also increase in intensity with input power.

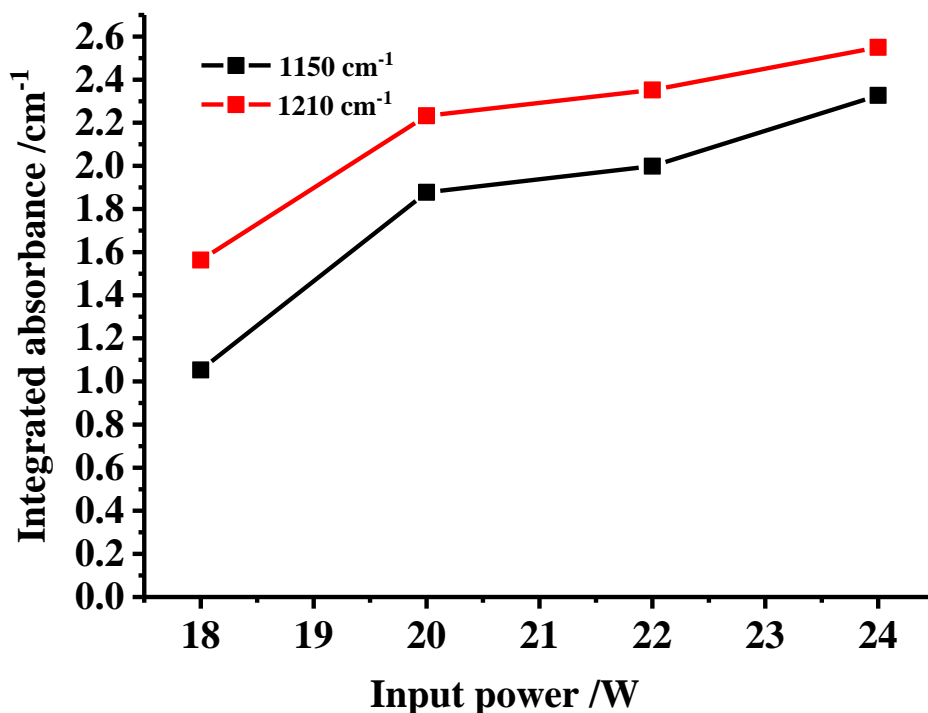


Figure 3.9. Plots of the integrated absorptions of the 1150 and 1210 cm^{-1} bands after 20 minutes operation as a function of input power from the experiment in fig. 3.8 and analogous experiments.

Figure 3.8(b) shows the single beam spectra corresponding to the absorbance spectra in fig. 3.8(a) along with the reference spectrum collected immediately before the plasma was initiated. As can be seen from the figure, the 1150 and 1210 cm^{-1} features were present before the plasma was initiated and simply increase in intensity as the plasma is turned on and with time thereafter. This suggests that the features have their origin in the oxides on the surface of the Macor and/or the Ti mesh.

Figure. 3.10 shows a repeat of the experiment in figs. 3.8, using a feed gas composition of 49% CO_2 + 51% N_2 . In addition to the features due to CO^* and CO_2^* , the bands at 1150 and 1210 cm^{-1} are also present, and again grow with operational time.

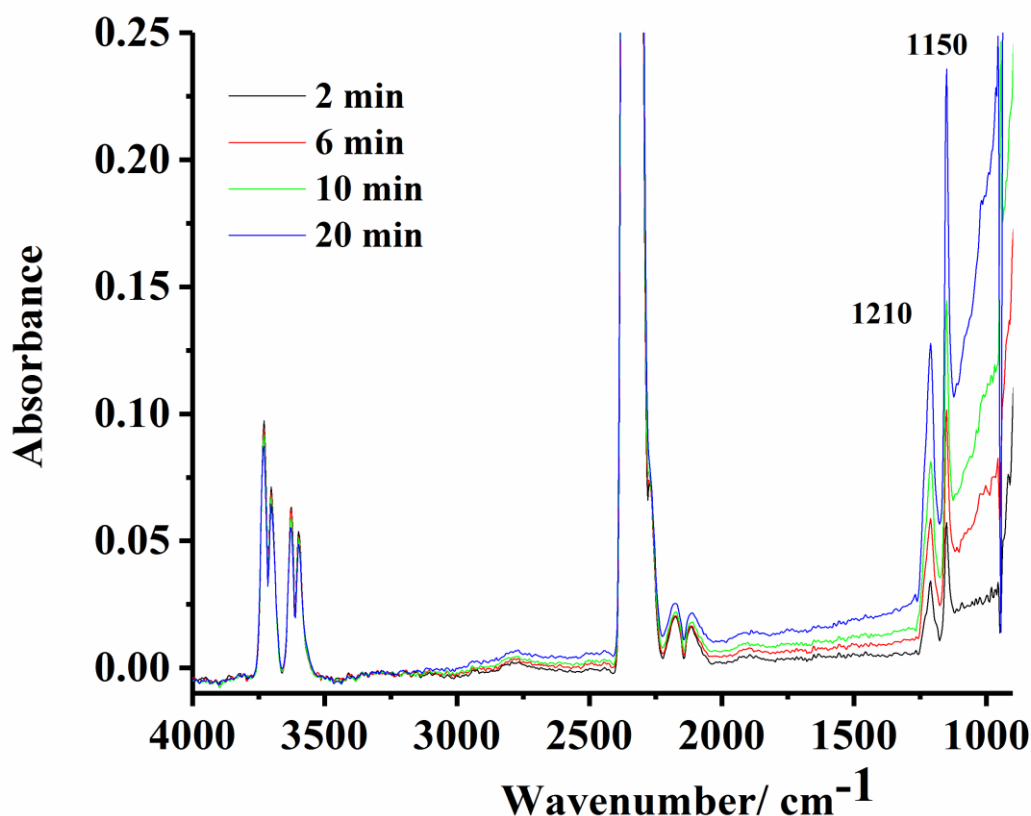


Figure 3.10. *In situ* FTIR spectra (8 cm^{-1} resolution, 100 co-added and averaged scans, 60 seconds per scanset) collected at the times shown on the figure at an input power of 24 W using the reflectance cell and 49% CO_2 + 51% N_2 as the feed gas. The spectrum collected immediately before the plasma was initiated was employed as the reference.

Figure 3.11 shows the corresponding plots of the normalised integrated absorptions of the 1150 and 1210 cm^{-1} features, and that of the ν_3 CO_2 asymmetric stretch in fig. 3.10, as a function of time after the plasma was switched off and the cell flushed with nitrogen. The absorptions were normalised to their values after 2 minutes flushing, to aid comparison. The absorptions of the two features do not track the CO_2 absorption, and the latter declines more rapidly. This suggests that the 1150 and 1210 cm^{-1} bands are not due to a gas-phase species (as, perhaps, may be expected from the fact that they were not observed in the transmission cell experiments discussed above, although the presence of the Ti mesh is an additional factor in the reflectance experiments). The relatively slow ‘relaxation’ of these bands argues against their being due to some form of electric field enhancement of the Ti-O bonds on the mesh or

the metal-oxygen bonds of the Macor, as such would be expected to relax as soon as the field was removed.

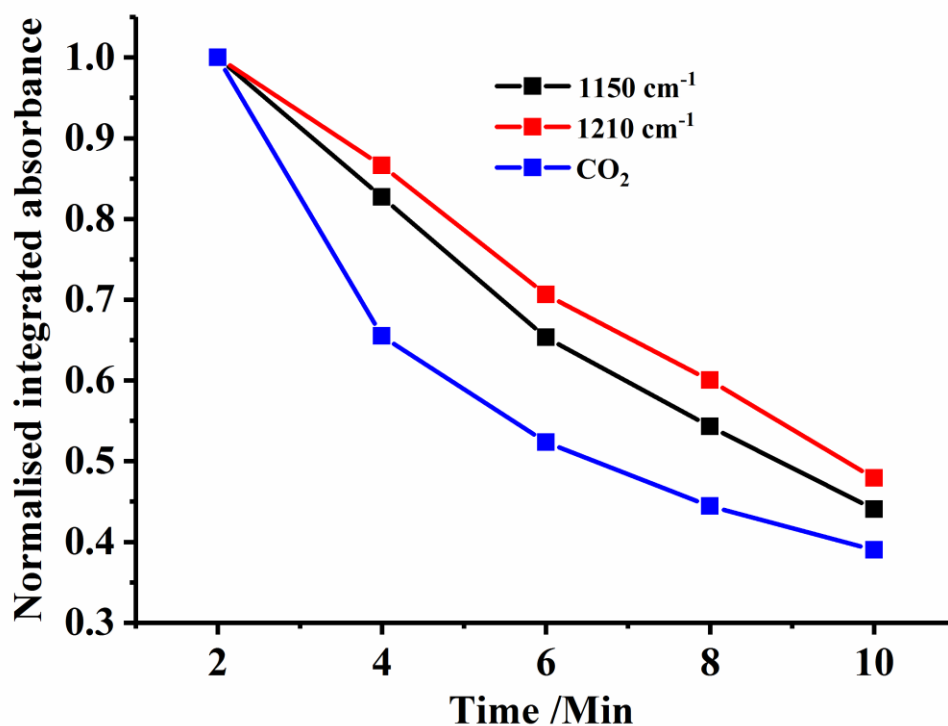


Figure 3.11. Plots of the normalized band absorptions of the 1150 cm⁻¹, 1210 cm⁻¹ and CO₂ asymmetric stretch from the flushing experiment in fig. 3.10.

In addition, the features also appeared in experiments where N₂ was replaced by argon. Figure 3.12 which shows an analogous experiment to that shown in fig. 3.10, except using a feed gas composition of 31.0% CO₂ + 69.0% Ar and an input power of 14 W (when Argon was employed in the feed, it was found that plasma was initiated and sustained at lower input power than when using N₂, and the maximum power that could be employed was also lower); the 1150 and 1210 cm⁻¹ features are clearly visible, growing with time, showing they are not due to nitrogen-containing species.

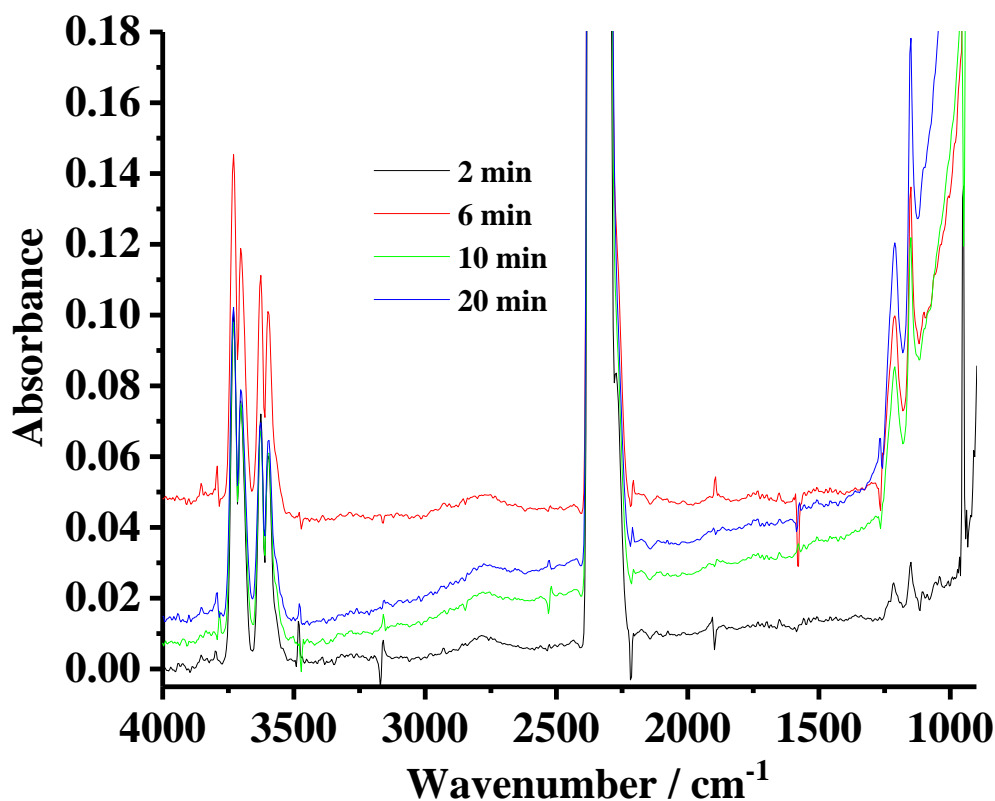


Figure 3.12. *In situ* FTIR spectra (8cm^{-1} resolution, 100 co-added and averaged scans, 60 seconds per scanset) collected using the plasma reflectance cell at the times shown on the figure at an input power of 14 W. The gas composition was 31.0% CO_2 + 69.0% Ar and the reference spectrum was that taken with no plasma and a N_2 gas feed. Spectra were taken every 2 minutes after the plasma was initiated up to 20 minutes, but spectra are omitted for clarity.

These features may be due to the transverse optical (TO) mode at 1210 cm^{-1} and the longitudinal optical (LO) mode at 1150 cm^{-1} of amorphous SiO_2 present in the macor. These have previously been observed in the growth of thin films of SiO_2 [21] and were observed on the high wavenumber side of the large SiO_2 transverse optical peak due to the asymmetric stretch at 1070 cm^{-1} . They are thought to be due to disorder-induced mode coupling in amorphous SiO_2 with the exact positions varying dependent on conditions. In Lange's work [21] they were shown to be stronger with ion bombardment. Whilst very interesting, it is not clear that the species responsible for the 1150 and 1210 cm^{-1} features participate in the

reduction of CO₂ and hence are not relevant to the aim of this work. Further work is recommended to elucidate this chemistry.

Given the experimental uncertainties associated with the reflectance cell, and the fact that it is still under development, it is not possible to draw any meaningful, quantitative data from the spectra in fig. 3.9: suffice to state that the production of CO₂* fell from 92% of the CO₂ in the feed gas after 2 minutes operation to 89% after 20 minutes. However, the data in fig. 3.7 strongly suggests that this decrease in the formation of CO₂* was not reflected in an increase in the conversion to CO*.

The absence of any features due to the oxides of nitrogen in the various spectra discussed above is worthy of note, as such species have been observed in CO₂ and N₂ plasmas [14, 22] and the specific energy densities employed by these authors were comparable to those employed in the current work. The absence of such species may be due to catalytic activity of the Macor and/or differences in construction of the reactors leading to different electric fields and electron energies.

3.2.3 The thermally driven reaction of CO₂ at Macor

The uncatalysed thermolysis of CO₂ into CO and O₂ takes place at negligible rates at temperatures < 1500 °C but the process is catalysed by metal oxides such as ZrO₂, CeO₂ and mixed Ce/Zr oxides such that thermolysis occurs at temperatures > 1200 °C [23]. Figure 3.13 shows spectra collected from the Macor disc under nitrogen up to 600 °C, showing only the spectra taken every 100 °C, for clarity.

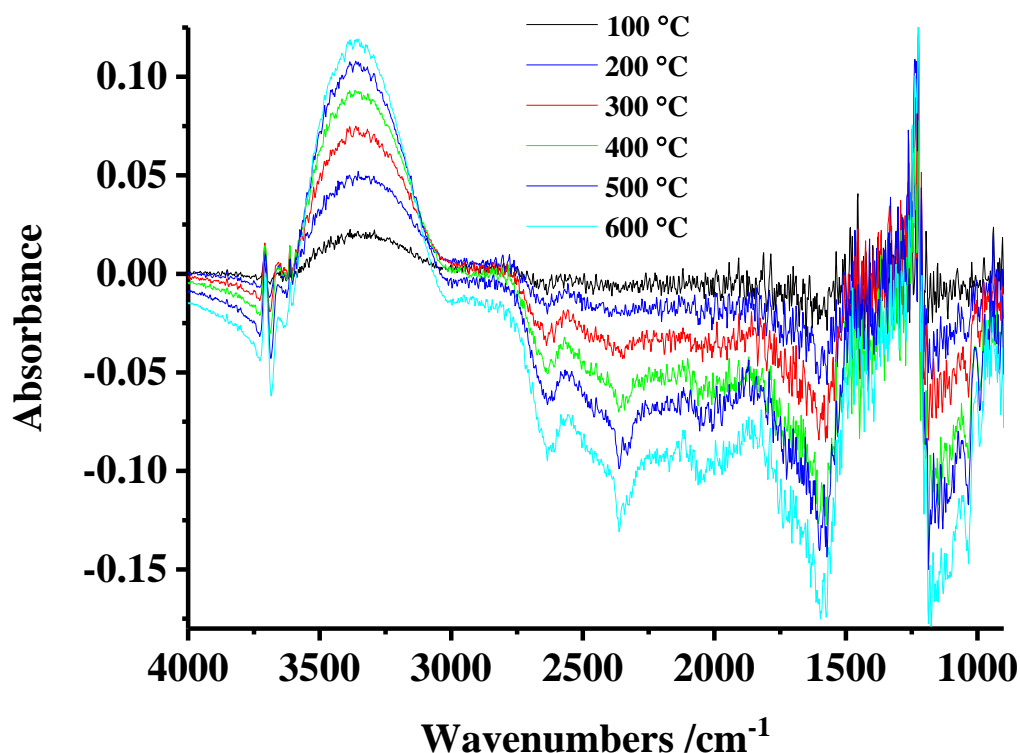
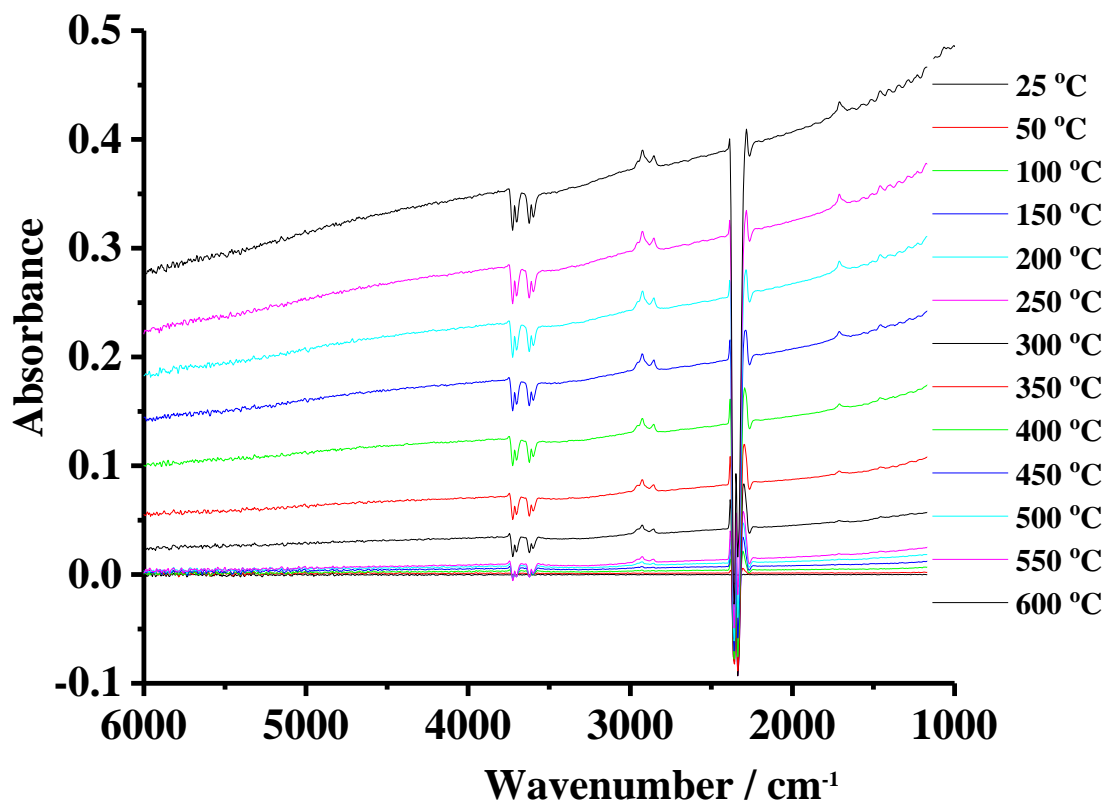


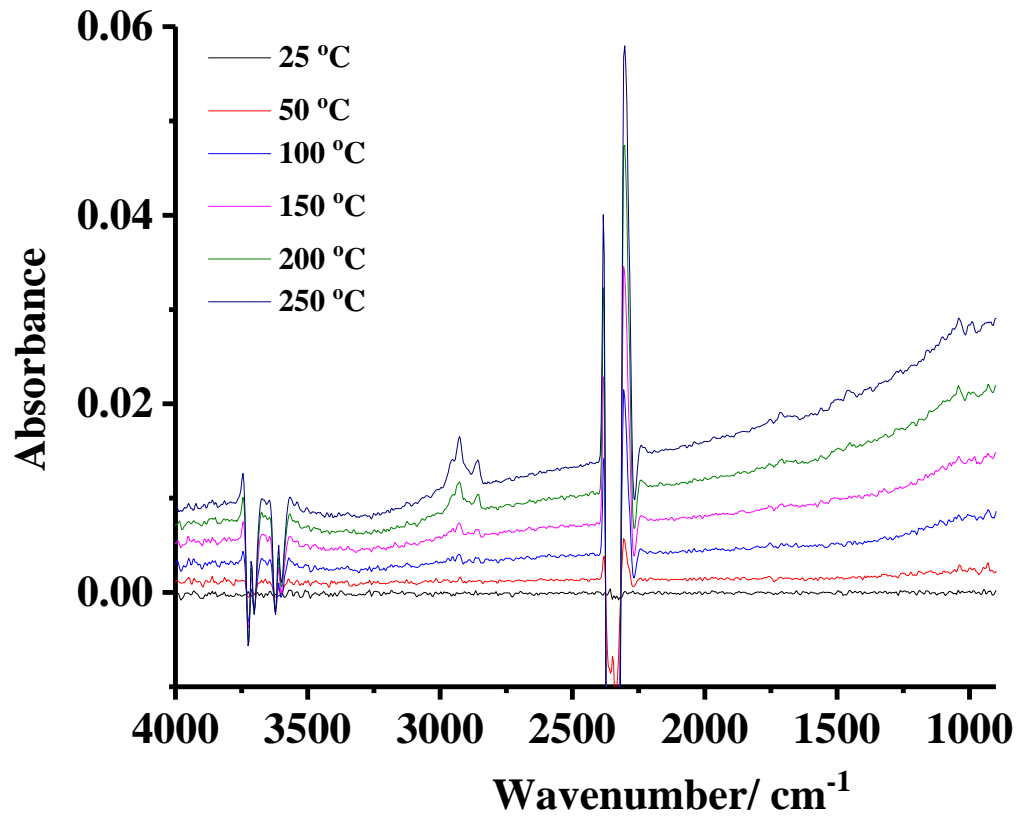
Figure 3.13. In-situ FTIR spectra (8 cm^{-1} resolution, 100 co-added and averaged scans, 120 seconds per scanset) collected as a function of temperature from a 12.5 mm diameter, 2 mm thick Macor disc in the thermal system. The atmosphere above the disc was N_2 . Spectra were collected at 25 and 50 °C, then every 50 °C but not all spectra are shown, for clarity.

As can be seen from the figure, the spectra are dominated by a structured, broad loss between 3000 and 1000 cm^{-1} , the broad gain of an O-H stretch with a maximum around 3360 cm^{-1} , and sharp loss and gain features near 3700 cm^{-1} which may be attributed to isolated O-H stretches [24].

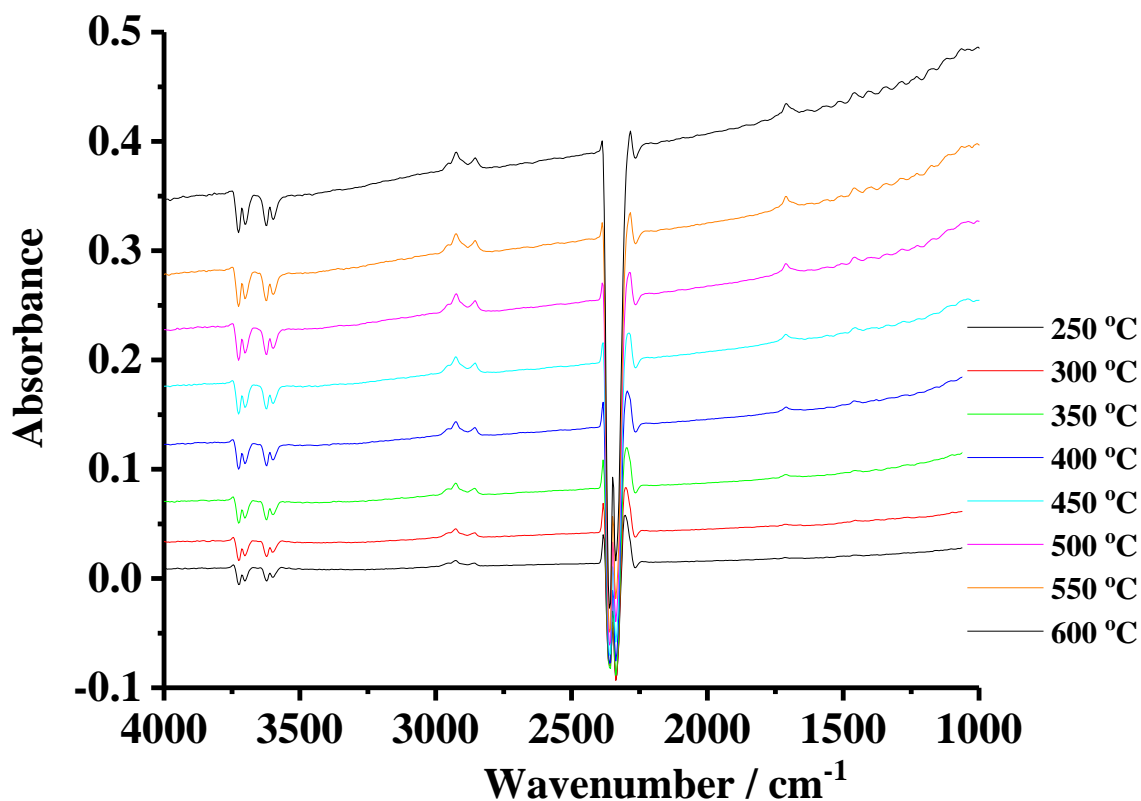
Figures 3.14(a) – (c) show the reflectance spectra collected in 23% CO_2 + 77% N_2 as a function of temperature up to 600 °C where fig. 3.14(a) shows all the spectra, fig. 3.14(b) the spectra up to 250 °C and fig. 3.14(c) the spectra from 250 to 600 °C.



(a)



(b)



(c)

Figure 3.14. (a) In situ FTIR spectra (8 cm^{-1} resolution, 100 co-added and averaged scans, 60 seconds per scanset) collected from a 12.5 mm diameter Macor disc in a static atmosphere of 23% CO_2 + 77% N_2 at the temperatures shown on the figure. The temperature was ramped at $5\text{ }^\circ\text{C min}^{-1}$. The spectra in (a) up to 600 °C (b) 25 °C to 250 °C and (c) 250 °C to 600 °C.

For comparison, fig. 3.15 shows the spectrum collected at 600 °C in fig. 3.14 along with spectra collected at the same temperature in analogous experiments using 36% CH_4 + 64% N_2 and 21% CO_2 + 43% CH_4 + 36% N_2 , and fig. 3.16 shows a plot of the absorbance at 2000 cm^{-1} in fig. 3.14(a) vs temperature.

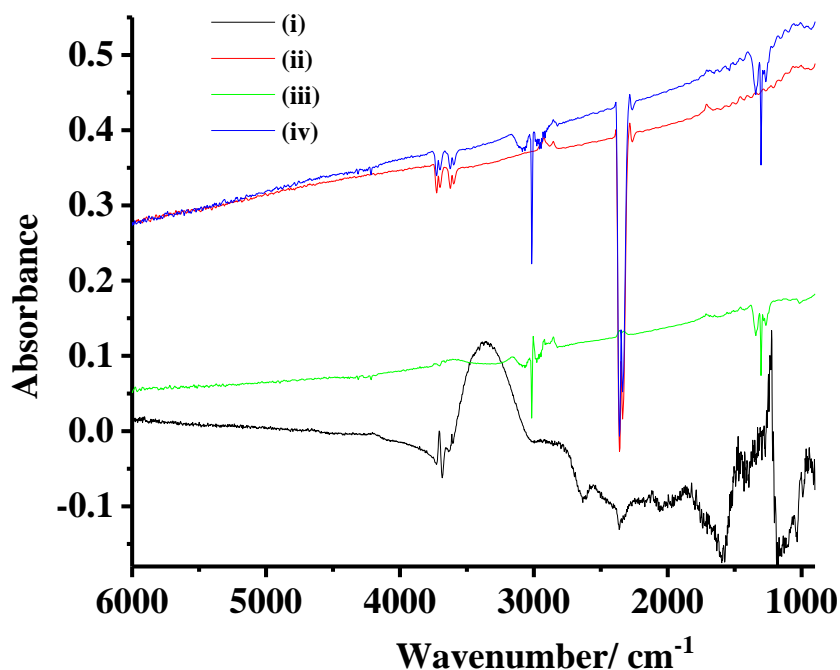


Figure 3.15. (i) The FTIR spectrum (8 cm^{-1} resolution, 100 co-added and averaged scans, 120 seconds per scanset) collected at $600\text{ }^{\circ}\text{C}$ in fig. 3.13, along with spectra collected at the same temperature in analogous experiments using (ii) 23% CO_2 + 77% N_2 , (iii) 36% CH_4 + 64% N_2 , and (iv) 21% CO_2 + 43% CH_4 + 36% N_2 .

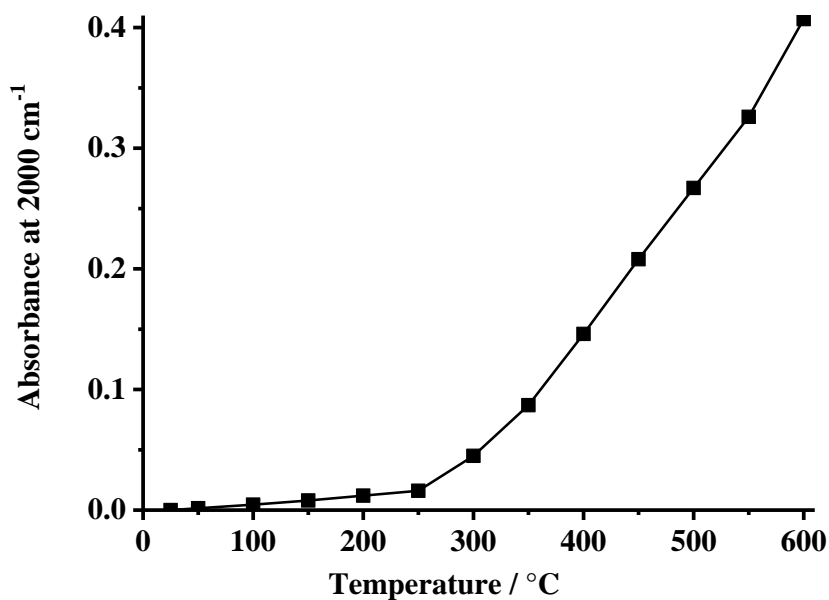


Figure 3.16. A plot of the absorbance at 2000 cm^{-1} of the spectra in fig. 3.14(a) as a function of temperature.

Figures. 3.14(a) – (c) are dominated by the very intense CO_2 loss features at 2360 and 2340 cm^{-1} , and the $\text{CO}_2/\text{CO}_2^*$ combination bands between 3500 and 4000 cm^{-1} are also clearly

seen, as are the structures due to the overlay of the asymmetric stretches due to the loss of CO_2 and gain of CO_2^* . Figure 3.17 shows the spectrum collected at 100°C in fig. 3.14(a), and fig. 3.18 which compares the bands obtained in the thermal and plasma experiments directly.

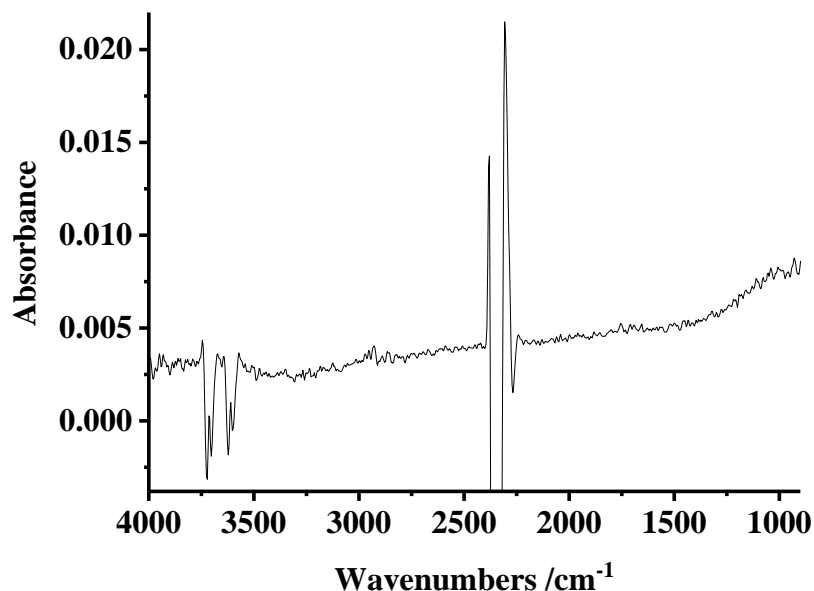


Figure 3.17. The spectrum collected at 100°C in fig. 3.14(a).

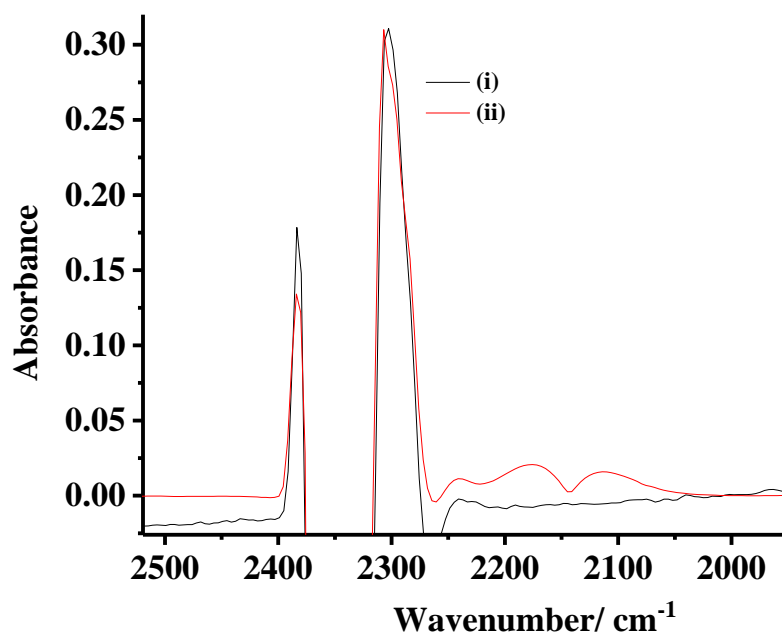


Figure 3.18. A comparison of (i) the spectrum obtained in the thermal experiment in fig. 3.14(a) at 250°C with (ii) that obtained after 20 minutes in the plasma experiment at 28 W in fig. 3.4. Both spectra were offset to zero and the spectrum in (i) enhanced by a factor of 7.4 to aid comparison.

As expected, the P and R bands due to CO are absent from the thermal spectra and, given the noise on the spectra in figs. 3.14(a) – (c) is ca. 4×10^{-4} , this suggests the CO absorption at 2116 cm^{-1} must be $\leq 4 \times 10^{-4}$, hence $[\text{CO}] \leq 1.2 \times 10^{-5} \text{ M}$ and the conversion of CO_2 to CO is $\leq 0.1\%$, i.e. very low, as would be expected on the basis of the literature [23] and in complete contrast to the plasma experiments. The bands around 2900 cm^{-1} are due to the protective polymer film on the beamsplitter of the spectrometer.

3.3 Conclusions

The combination of the FTIR reflectance and transmission plasma cells allowed reasonable estimations of the conversion of CO_2 to CO, and provided a direct method of assessing the temperature of the gases in the plasma glow using the broadening of the CO absorption. The conversion and energy efficiencies observed were comparable to those routinely reported in the literature, giving confidence in the approach. Further, and for the first time, the same chemical system was studied driven both by plasma and thermally, and the data compared and contrasted: whilst up to 9% conversion of the CO_2 to CO was observed in the plasma experiments, no conversion was observed in the thermal experiment up to $600 \text{ }^\circ\text{C}$.

Finally, strong plasma-induced absorptions were observed on the Ti/Macor which remained for some time after the plasma was stopped which remain unassigned, but have been tentatively attributed to transverse and longitudinal optical modes of SiO_2 and further work is needed to obtain definitive identification of these and the implications of their formation.

3.4 References

1. Herzberg, G., *Molecular spectra and molecular structure* Vol. Vol.2: Infrared and Raman spectra of polyatomic molecules. 1945, New York Van Nostrand Reinhold.
2. Stein, S.E. "Infrared Spectra" in *NIST Chemistry Webbook, NIST Standard Reference Database Number 69*. [cited 2017 September 5]; Available from: <http://webbook.nist.gov/cgi/cbook.cgi?Contrib=MSDC-IR>.
3. Earle K. Plyler, Lamdin R. Blaine, and E.D. Tidwell, *Infrared absorption and emission spectra of carbon monoxide in the region from 4 to 6 microns*. *Journal of Research of the National Bureau of Standards* 1955. **55**: p. 183-189.

4. Bennett, C.J., C.S. Jamieson, and R.I. Kaiser, *Mechanistical studies on the formation and destruction of carbon monoxide (CO), carbon dioxide (CO₂), and carbon trioxide (CO₃) in interstellar ice analog samples*. *Physical Chemistry Chemical Physics*, 2010. **12**(16): p. 4032-4050.
5. Herzberg, G., *Molecular spectra and molecular structure. Vol 1: Infrared and Raman spectra of diatomic molecules*. Vol. 2nd Edition. 2008, New York: Van Nostrand Reinhold.
6. Abdullah Al-Abduly, P.A.Christensen., *An in situ and downstream study of non-thermal plasma chemistry in an air fed dielectric barrier discharge (DBD)*. *Plasma Sources Science and Technology*, 2015. **24**: p. 065006
7. Sigurd, B., T. Michael, W. Claus, and K.C. Heiko, *Liquid-helium temperature long-path infrared spectroscopy of molecular clusters and supercooled molecules*. *Review of Scientific Instruments*, 2001. **72**(10): p. 3946-3955.
8. Fridman, A., *Plasma Chemistry*. 2008, Cambridge: Cambridge University Press.
9. Gordillo-Vázquez, F.J., *Air plasma kinetics under the influence of sprites*. *Journal of Physics D: Applied Physics*, 2008. **41**(23): p. 234016.
10. Rond, C., A. Bultel, P. Boubert, and B.G. Chéron, *Spectroscopic measurements of nonequilibrium CO₂ plasma in RF torch*. *Chemical Physics*, 2008. **354**(1): p. 16-26.
11. Jaffe, R., *Vibrational and Rotational Excitation and Dissociation of CO₂ Reexamined*, in *49th AIAA Aerospace Sciences Meeting including the New Horizons Forum and Aerospace Exposition*. 2011: Orlando, Florida.
12. Moore, C.E., *Atomic energy levels: Volume 1*. 1949, Washington, DC: Circular of the National Bureau of Standards 467.
13. Malcom W. Chase, J., *NIST-JANAF Thermochemical Tables (Journal of Physical and Chemical Reference Data, Monograph No 9)*. 1998, American Institute of Physics: New York.
14. Snoeckx, R., S. Heijkers, K. Van Wesenbeeck, S. Lenaerts, and A. Bogaerts, *CO₂ conversion in a dielectric barrier discharge plasma: N₂ in the mix as a helping hand or problematic impurity?* *Energy & Environmental Science*, 2016. **9**(3): p. 999-1011.
15. Hunt, J., A. Ferrari, A. Lita, M. Crosswhite, B. Ashley, and A.E. Stiegman, *Microwave-Specific Enhancement of the Carbon–Carbon Dioxide (Boudouard) Reaction*. *The Journal of Physical Chemistry C*, 2013. **117**(51): p. 26871-26880.

16. Manley, T.C., *The Electric Characteristics of the Ozonator Discharge*. Transactions of The Electrochemical Society, 1943. **84**(1): p. 83-96.
17. Robby Aerts, W.S., Annemie Bogaerts, *Carbon dioxide splitting in a dielectric barrier discharge plasma: a combined experimental and computational study*. ChemSusChem, 2015. **8**(4): p. 702-716.
18. Wang, J.-Y., G.-G. Xia, A. Huang, S.L. Suib, Y. Hayashi, and H. Matsumoto, *CO₂ Decomposition Using Glow Discharge Plasmas*. Journal of Catalysis, 1999. **185**(1): p. 152-159.
19. Zheng, G., J. Jiang, Y. Wu, R. Zhang, and H. Hou, *The Mutual Conversion of CO₂ and CO in Dielectric Barrier Discharge (DBD)*. Plasma Chemistry and Plasma Processing, 2003. **23**(1): p. 59-68.
20. Snoeckx, R. and A. Bogaerts, *Plasma technology - a novel solution for CO₂ conversion?* Chemical Society Reviews, 2017. **46**(19): p. 5805-5863.
21. Lange, P., *Evidence for disorder-induced vibrational mode coupling in thin amorphous SiO₂ films*. Journal of Applied Physics, 1989. **66**(1): p. 201-204.
22. Xu, S., J.C. Whitehead, and P.A. Martin, *CO₂ conversion in a non-thermal, barium titanate packed bed plasma reactor: The effect of dilution by Ar and N₂*. Chemical Engineering Journal, 2017. **327**(Supplement C): p. 764-773.
23. Jiang, Q., Z. Chen, J. Tong, M. Yang, Z. Jiang, and C. Li, *Direct thermolysis of CO₂ into CO and O₂*. Chemical Communications, 2017. **53**(6): p. 1188-1191.
24. P. A. Christensen, P.S.A., R. G. Egdell, S. Maneelok and D. A. C. Manning, *An in situ FTIR spectroscopic and thermogravimetric analysis study of the dehydration and dihydroxylation of SnO₂: the contribution of the (100), (110) and (111) facets*. Physical Chemistry Chemical Physics, 2016. **18**(33): p. 22990-22998.

Chapter 4. An in-situ study of non-thermal plasma fed with CO₂, CH₄ and N₂ in plasma- and thermally driven experiments at Macor.

4.1 Introduction

The aim of work reported in this chapter was to extend the initial studies described in Chapter 3 to the in-situ FTIR investigation of the dry reforming of CO₂ and CH₄ at Macor. The work in this chapter is structured as follows: firstly, the initial characterisation of the system after a short run time is described, followed by a detailed study of the changes observed after longer run times; and finally the unexpected results so obtained are discussed and possible mechanisms are proposed which could pave the way for exploiting the major, untapped potential of plasma catalysis.

4.2 Plasma transmission cell

Figure 4.1 shows a spectrum taken before the 24 W run using 8.5% CO₂ + 13.1% CH₄ + 78.4% N₂ feed gas without plasma at a total flow rate of 200 cm³ min⁻¹, referenced to N₂ gas at the same flow rate, at 25 °C.

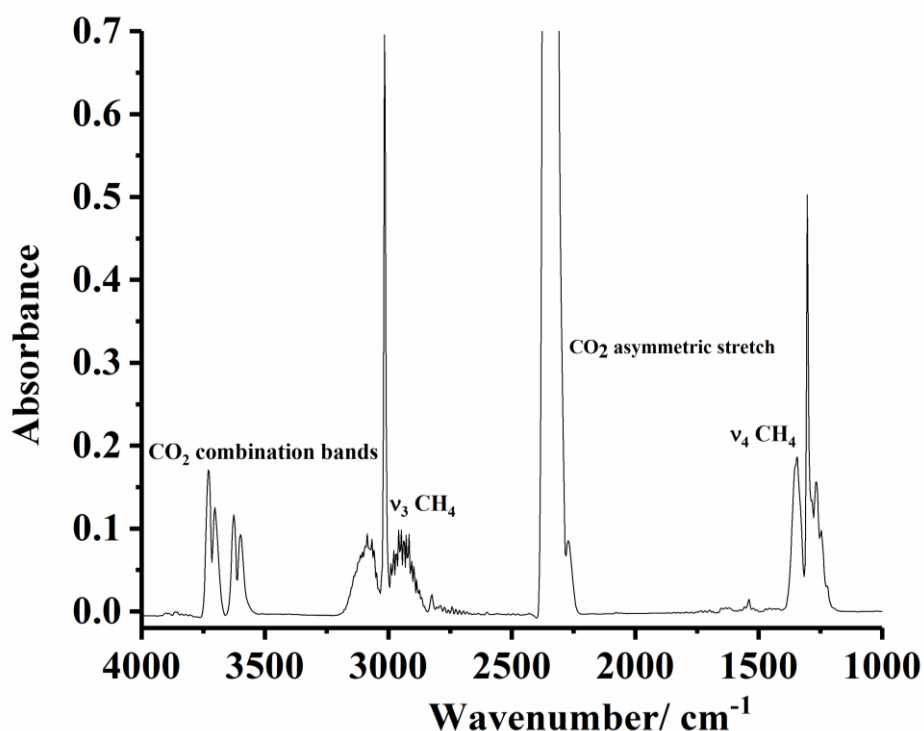


Figure 4.1. A spectrum (8 cm⁻¹ resolution, 100 spectra per scan set, and 1 minute per spectrum) of 8.5% CO₂ + 13.1% CH₄ + 78.4% N₂ at a total flow rate of 200 cm³ min⁻¹ through the plasma transmission cell at 25 °C prior to experiment carried out at an input power of 24 W. The reference spectrum was N₂ gas at the same flow rate and temperature.

As was discussed in section 2.8, the intense feature between 2300 and 2400 cm^{-1} is due to the P and R bands of the CO_2 asymmetric stretch (ν_3) fundamental absorption [1, 2] and the features between 3500 and 4000 cm^{-1} are CO_2 combination bands ($\nu_1 + \nu_3$ and $2\nu_2 + \nu_3$) [3]. It is clear from the figure that the fundamental bands are saturating and hence cannot be employed for any quantitative measurements; hence it was decided to employ the integrated areas of the CO_2 combination bands between 3491 and 3769 cm^{-1} to estimate the CO_2 conversion, the absorption coefficient employed was $6.5 \times 10^5 \text{ cm mol}^{-1}$ [4] as was described in Chapter 2. Figure 4.2 shows the spectrum collected after 2 minutes at 24 W and the spectrum collected of the same $\text{CO}_2/\text{CH}_4/\text{N}_2$ feed gas with no plasma, both using the nitrogen single beam spectrum as reference.

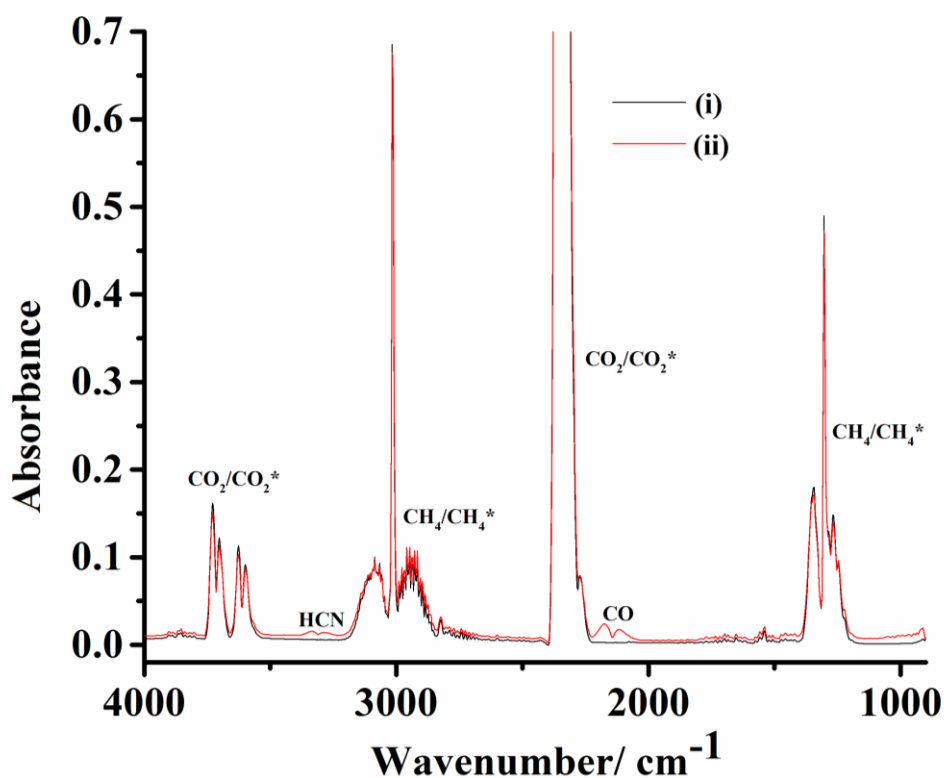
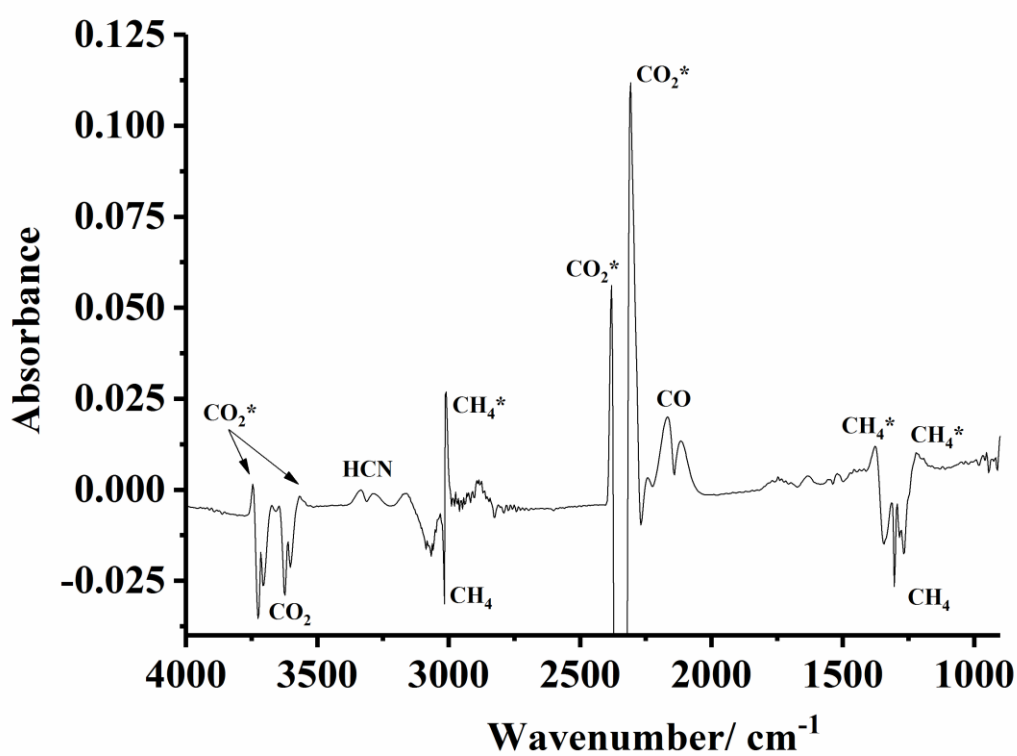
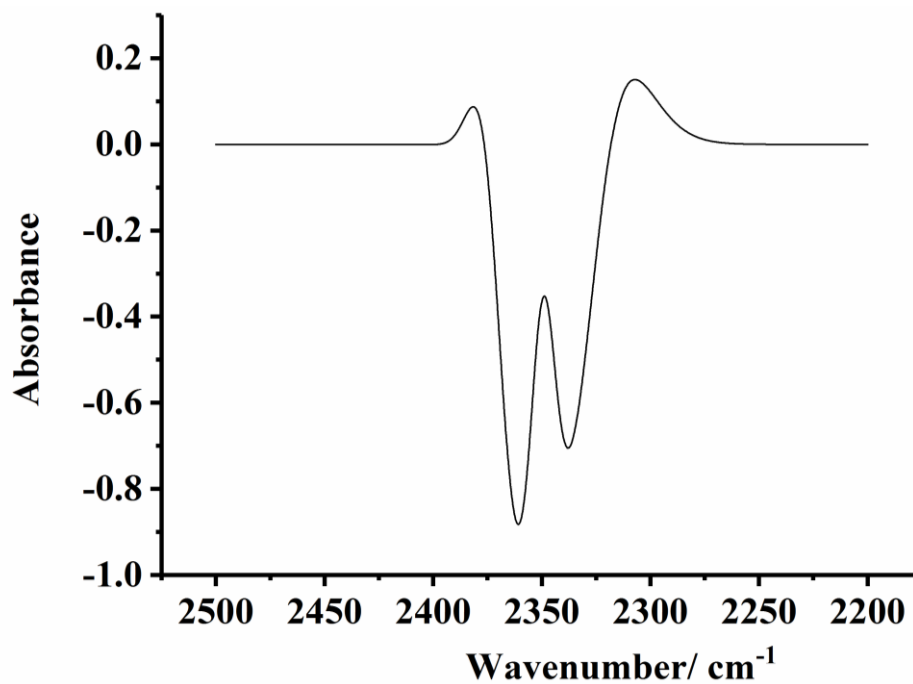


Figure 4.2. *In situ* FTIR spectra (8 cm^{-1} resolution, 100 spectra per scan set, and 1 minute per spectrum) of the 8.5% CO_2 + 13.1% CH_4 + 78.4% N_2 feed gas in the plasma transmission cell at a total flow rate of $200 \text{ cm}^3 \text{ min}^{-1}$ and a temperature of ca. $25 \text{ }^\circ\text{C}$: (i) before initiating plasma and (ii) after 2 minutes operation at 24 W. In both cases, the reference spectrum was collected using nitrogen gas as the feed and without plasma.

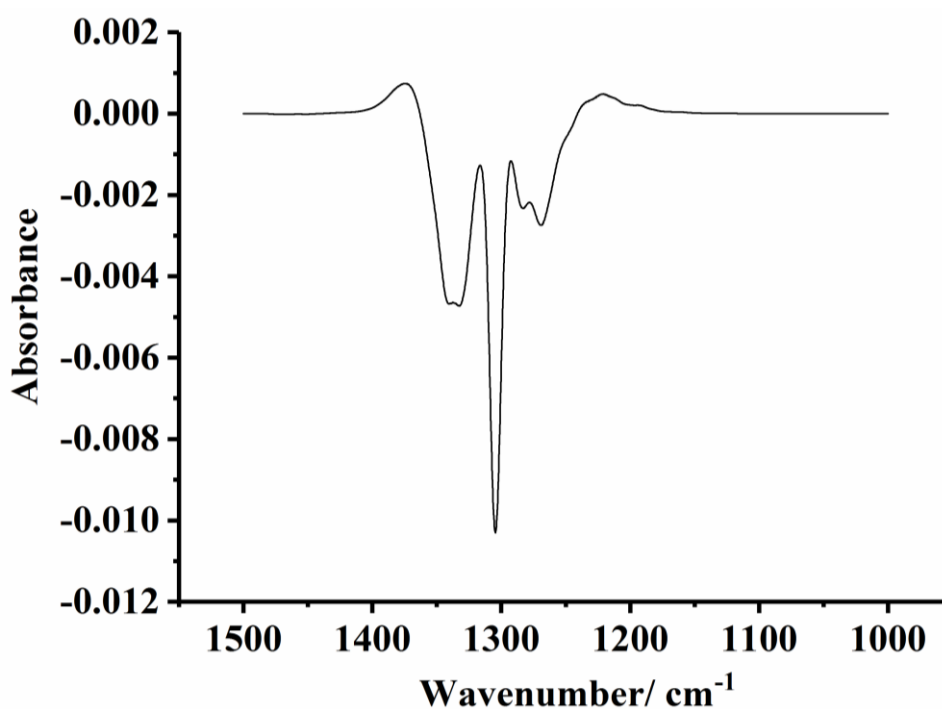
Bands due to HCN and CO were observed and are discussed below. After 2 minutes plasma operation, although the features other than HCN and CO appear to be due to room temperature CO₂ and CH₄ bands they are all marginally broader and the Q branches of the ν_4 and ν_3 bands of CH₄ are also shifted slightly. This can be seen more clearly in fig. 4.3(a) which shows the spectrum in fig. 4.2 using the single beam spectrum collected with no plasma but with the same feed gas (8.5% CO₂, 13.1% CH₄ 78.4% N₂) , i.e. fig. 4.3(a) is a difference spectrum.



(a)



(b)



(c)

Figure 4.3. (a) The spectrum in fig. 4.2 but using the single beam spectrum collected with no plasma and using 8.5% CO_2 + 13.1% CH_4 + 78.4% N_2 as the feed gas as the reference spectrum. (b) & (c) Spectral simulations of the change in absorbance observed when the gas temperature is changed from 296 to 396 K. The simulated spectrum at 296 K was subtracted from that at 396 K so that a positive change (gain) in absorbance indicates an increase in

absorbance when the plasma is on. (b) CO₂ in the asymmetric stretch region for a CO₂ mixing ratio of 0.01 in air and an absorption path length of 1 cm with a spectral resolution of 8 cm⁻¹; (c) CH₄ under the same simulation conditions. The features assigned as CO₂ and CH₄* are indicated by the positive change in absorbance features. Calculated using Spectralcalc (www.spectralcalc.com) and Origin.*

The broadening of the various features in fig. 4.2 compared to the room temperature absorptions of the feed gases can be seen in fig. 4.3(a) as the gain of “wings” either side of the CO₂ and CH₄ loss features, the much reduced fine structure on the ν_4 band and, in the case of the Q branches of the CH₄ bands, as significantly reduced absorptions and the bipolar nature of the ν_3 Q branch. The ν_3 band of CH₄ and the asymmetric CO₂ stretch were simulated by Prof. Phillip Martin, School of Chemical Engineering and Analytical Science, The University of Manchester, using Spectralcalc and the difference spectra obtained by subtracting the room temperature spectra from those at 396 K are shown in figs. 4.3(b) and (c): thus the gain features in fig. 4.2 were assigned to rotationally excited CO₂, CO₂* [5, 6] and CH₄, CH₄*, due to higher temperatures in the plasma leading to increased rotational excitation. There is no evidence of non-thermal vibrational excitation enhancement. This is supported by the experiment carried out using the thermal FTIR system, see section 4.4.

Figure 4.4 shows spectra collected after 20 minutes operation with plasma at 20, 24 and 28 W, all using the spectra collected with the same gas feed but without plasma as the reference spectra. As can be seen, in addition to CO₂* and CH₄*, other species were clearly produced in both liquid and gas phases: with respect to the former, a pale brown liquid was found to coat the internal walls and windows of the cell and subsequent experiments (see below) showed this to be composed of a number of species.

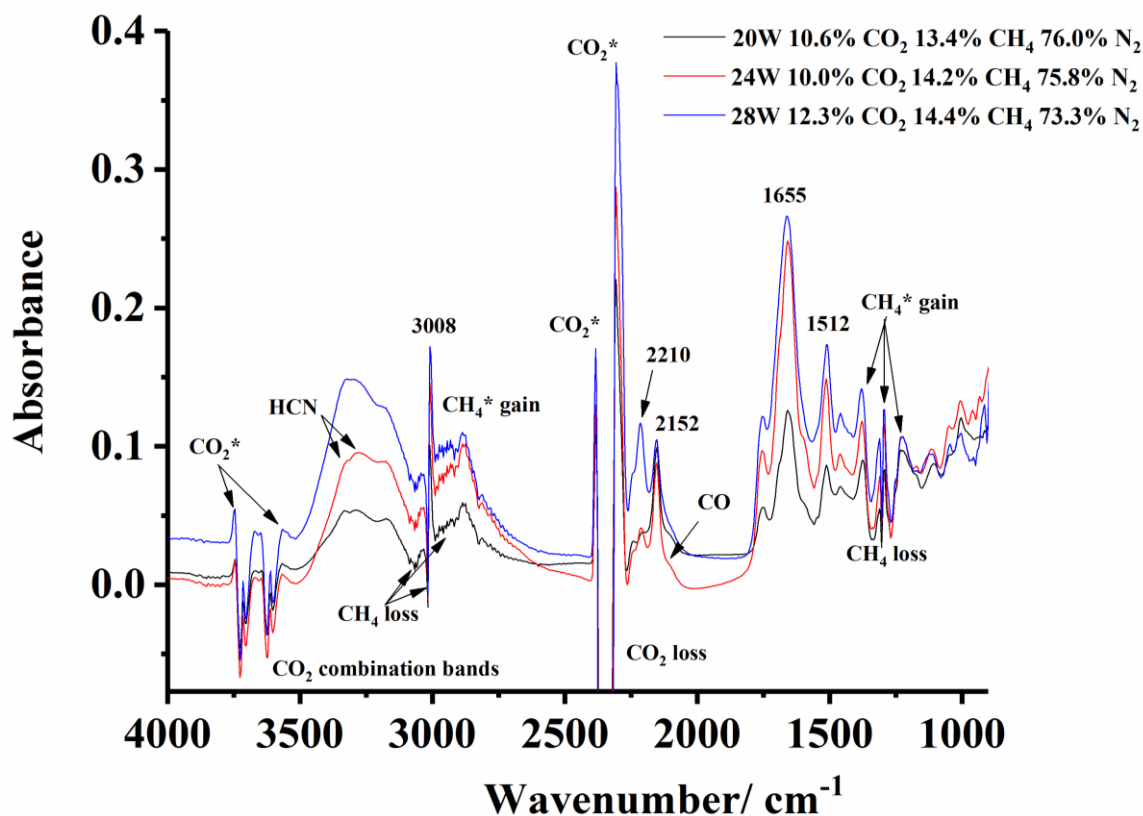


Figure 4.4. In-situ FTIR spectra (8cm^{-1} resolution, 100 spectra per scan set, and 1 minute per spectrum) collected after 20 minutes operation with plasma as a function of input power. The gas compositions are as shown on the figure at a total flow rate of $200\text{ cm}^3\text{ min}^{-1}$ and a temperature of ca. $25\text{ }^\circ\text{C}$; the reference spectrum was collected under the same conditions but with no plasma. Sample spectra were collected every 2 minutes up to 20 min.

It was decided to obtain a spectrum of the liquid: thus fig. 4.5 shows the spectrum collected after 20 minutes at 24 W in fig. 4.4 along with the spectrum collected at the end of the same experiment after the cell had been purged with N_2 to remove all gas phase species: the latter spectrum was thus of the liquid film on the CaF_2 windows. The spectrum taken after 20 minutes operation had that taken after 2 minutes subtracted: the reason for this can be seen in fig. 4.4, where the peaks between 2000 and 2250 cm^{-1} in fig. 4.4 are overlying the P and R bands of gas phase CO (see below) which remain essentially unchanged with time, indicating that the CO rapidly attains a steady state concentration: this is also the case for HCN and these observations are discussed further below.

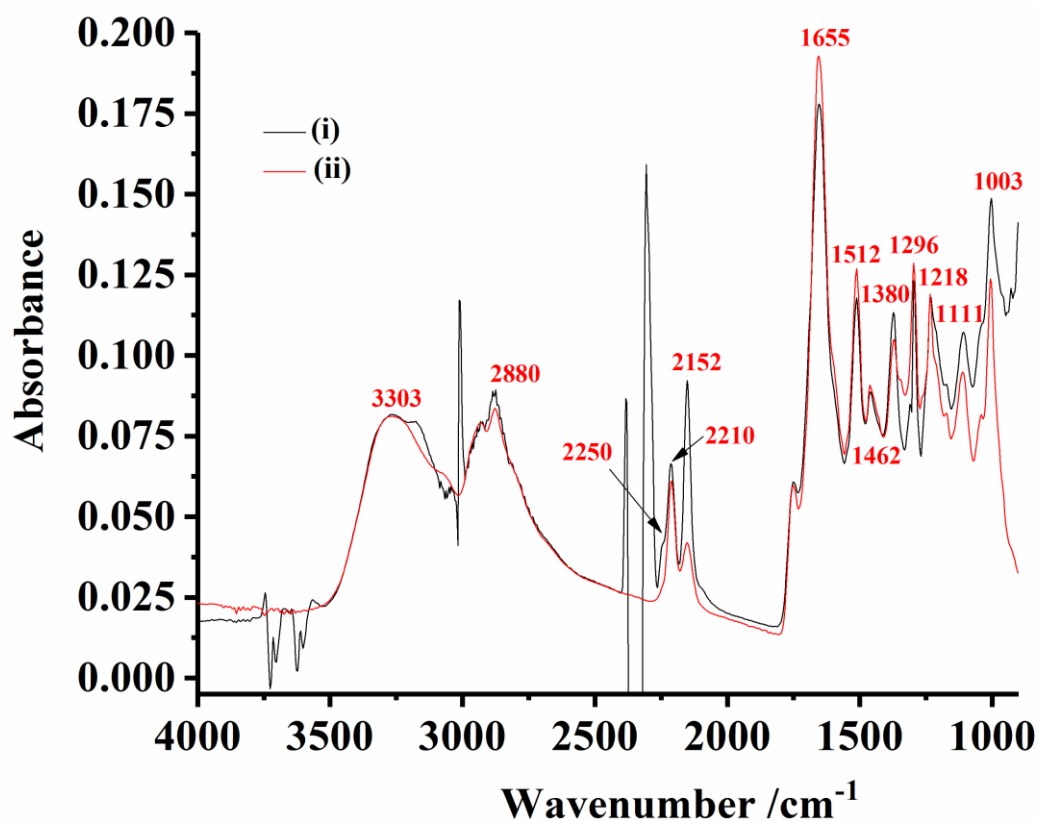


Figure 4.5. The spectrum collected (i) after 20 minutes at 24 W in the experiment in fig. 4.4 along with (ii) that collected at the end of the same experiment after the cell had been sparged with N_2 , the peaks in the latter thus being due to the liquid film on the CaF_2 windows. The spectrum collected after 2 minutes was subtracted from the spectrum taken after 20 minutes to remove the unchanging CO and HCN absorptions, see text for details.

By subtracting the spectrum taken after 2 minutes, the features between 2000 and 2250 cm^{-1} were clearer, and this approach was adopted below. The IR spectra obtained at an input power of 24 W were typical of those obtained at 20, 22, 26 and 28 W, differing only in the relative intensities of the various features.

The 1655 cm^{-1} band is directly associated with one or more of the components of the liquid film: as can be seen in fig. 4.4, the exact position of the band maximum and the peak shape varied from experiment to experiment suggesting contributions from more than one species however, for clarity, it is referred to as the 1655 cm^{-1} band in the discussion below. As may be seen from fig. 4.5, as well as the liquid film (represented by the 1655 cm^{-1} band), gaseous products were observed, one of which showed a strong absorption at 2152 cm^{-1} which consistently decreased in intensity when the cell was sparged with N_2 . This feature may be

attributed to ketene [7, 8], a carbon chain oxide; and the band at 2210 cm^{-1} in figs. 4.4 and 4.5 may be attributed to another carbon chain oxide, C_5O_2 [9-11] which is a liquid at room temperature, hence its presence in the deposit [12].

This is an important observation: the production of neither ketene nor C_5O_2 has been observed previously in NTP experiments irrespective of the nature or composition of the catalyst or dielectric, and this was achieved by using a catalyst comprised of earth-abundant elements. Further, ketenes and their dimers are important reactants that find use in the production of a wide range of chemicals [13-15] in a diverse range of industries including pigments, pharmaceuticals and agrochemicals and as intermediates for the paper industry. The 2152 cm^{-1} and 2210 cm^{-1} bands are in a distinctive spectral region that is populated by relatively few functional groups: in addition, their intensities do not, in general, track those of the other bands in figs. 4.4 and 4.5, lending support to their identification as chain oxides. Further, ketene has been observed in a matrix FTIR study of products of benzene transformations in a pulsed glow discharge at low pressure in highly diluted mixtures of benzene with argon in the presence of small amounts of oxygen [16]. As an interesting aside, the observation of the production of ketene and C_5O_2 in a non-thermal plasma catalysed by common elements has direct relevance to the origin of life: e.g. C_5O_2 is a powerful tracer of the temperature history of formerly carbon monoxide-rich ices in molecular clouds and star-forming regions [17] and ketene is one of the Complex Organic Molecules (COMs) formed in prestellar cores [18].

It is interesting to note from fig. 4.4 that the relative yield of ketene and C_5O_2 depends strongly on the input power, whilst the production of the liquid film does not appear to be so dependent; this suggests one method of potentially controlling the product distribution from the plasma process.

4.3 The spectra collected after 2 minutes

Figure 4.6 shows the spectra collected after 2 minutes of plasma operation at 28 W in the experiments shown in fig. 4.4 and analogous experiments carried out at the same input powers with varying gas feed compositions.

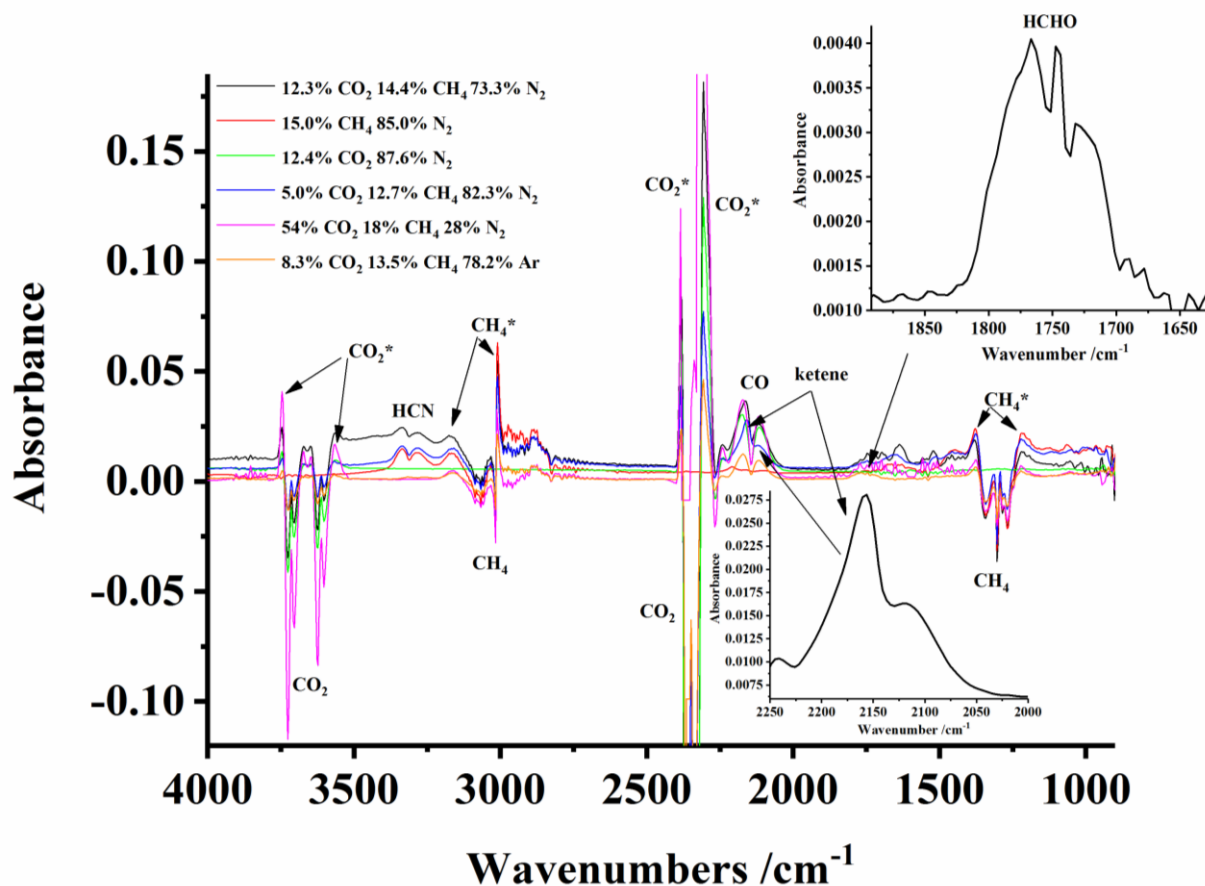


Figure 4.6. The spectrum collected after 2 minutes of plasma operation at 28 W in fig. 4.4, along with analogous experiments using gas feeds of various composition, as shown on the figure. The insets show the spectral regions where formate and ketene absorb in the experiment carried out using 5.0% CO₂ + 12.7% CH₄ + 82.3% N₂.

The bands at 3334 cm⁻¹ and 3286 cm⁻¹ in fig. 4.6 were attributed to the P and R branches of HCN based on the work of Choi and Barker [19]; the paper also allows an estimate of the extinction coefficient of the 3334 cm⁻¹ band of 2.8 M⁻¹ cm⁻¹. The features at 2167 and 2116 cm⁻¹ in fig. 4.6 may be attributed to CO [2, 4, 20]: the frequency of the former, in some cases, shifted by the presence of an underlying absorption, as shown by the inset of the spectrum from the experiment using 5.0% CO₂ + 12.7% CH₄ + 82.3% N₂ in the figure.

Figure 4.7 shows the CO region of the spectrum collected at 2 minutes and 24 W in the experiment in fig. 4.4, as well as that of a spectrum collected after 2 minutes operation at 24 W in 13.4% CO₂ 86.6% N₂, the latter was reduced by a factor of 1.3 to render the 2116 cm⁻¹ bands the same intensity. The figure also shows the spectrum resulting from the

subtraction of the $\text{CO}_2 + \text{N}_2$ spectrum from that of $\text{CO}_2 + \text{CH}_4 + \text{N}_2$: clearly, the CO bands are of the same intensities and frequencies, with the difference due to the presence of the 2152 cm^{-1} ketene feature. As stated in section 2.8, the integrated absorption coefficient of the CO band between 2002 and 2225 cm^{-1} was found to be $7.0 \times 10^5 \text{ cm mol}^{-1}$ in agreement with the work of Bolis and et. al. [21].

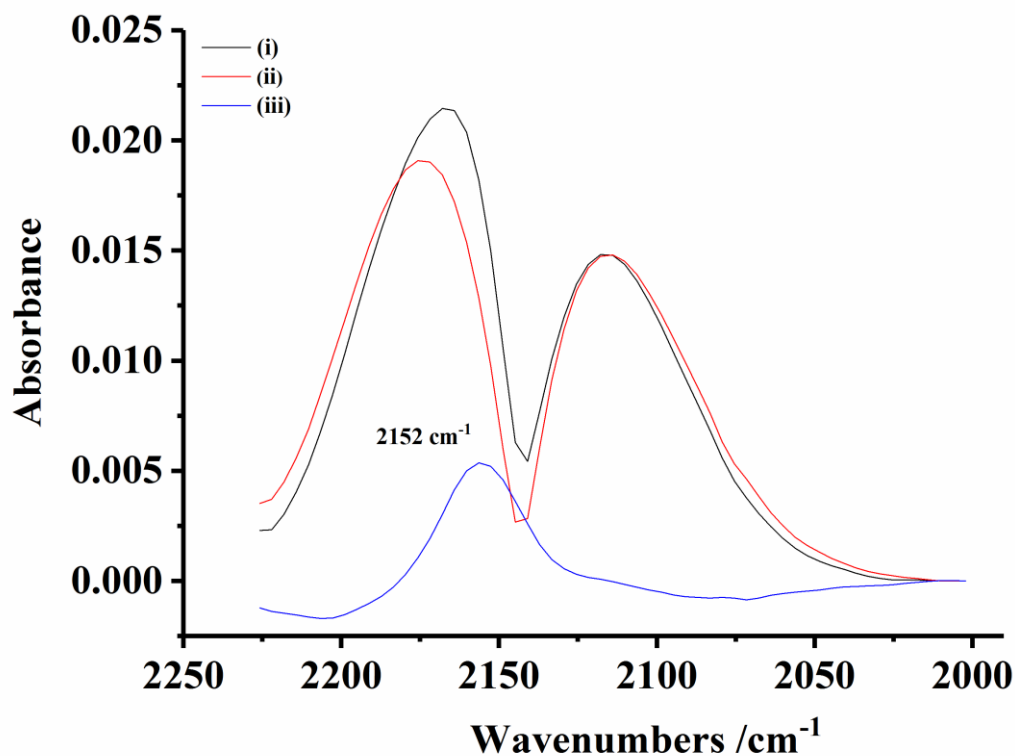


Figure 4.7. (i) The CO region of the spectrum in fig. 4.4 collected at 24 W; (ii) a spectrum collected after 2 minutes operation at 24 W using 13.4% $\text{CO}_2 + 86.6\% \text{ N}_2$ as the feed gas, reduced by a factor of 1.3 to render the 2116 cm^{-1} band the same intensity as that in (i); (iii) The difference between the two spectra in (i) and (ii).

Figure 4.8 which shows the spectra collected after 2 minutes in experiments utilising the feed gas compositions and input powers shown in rows 1(a) & (b), 3(a) & (b) and 5(a) & (b) of table 4.1 (ie nominally 10% $\text{CO}_2 + 10\% \text{ CH}_4 + 80\% \text{ N}_2$ at 20W, 24W and 28W) and that taken after 2 minutes during the experiment using 5.0% $\text{CO}_2 + 12.7\% \text{ CH}_4 + 82.3\% \text{ N}_2$ as feed gas (row 16), with the analogous spectra obtained using $\text{CO}_2 + \text{N}_2$, scaled and subtracted to annul the CO absorptions in each spectrum; the intensities of the ketene band so obtained are presented in the last column of table 4.1 which summarizes the data obtained from the experiments in fig. 4.6 along with data obtained in analogous experiments carried out as

blanks (omitting CO₂ or CH₄), replacing N₂ with Ar and to probe the effect of input power, etc. The spectra from the blank experiments are not included in this work for brevity: as the experiments using CO₂ alone as the feed gas have been fully described in the previous chapter.

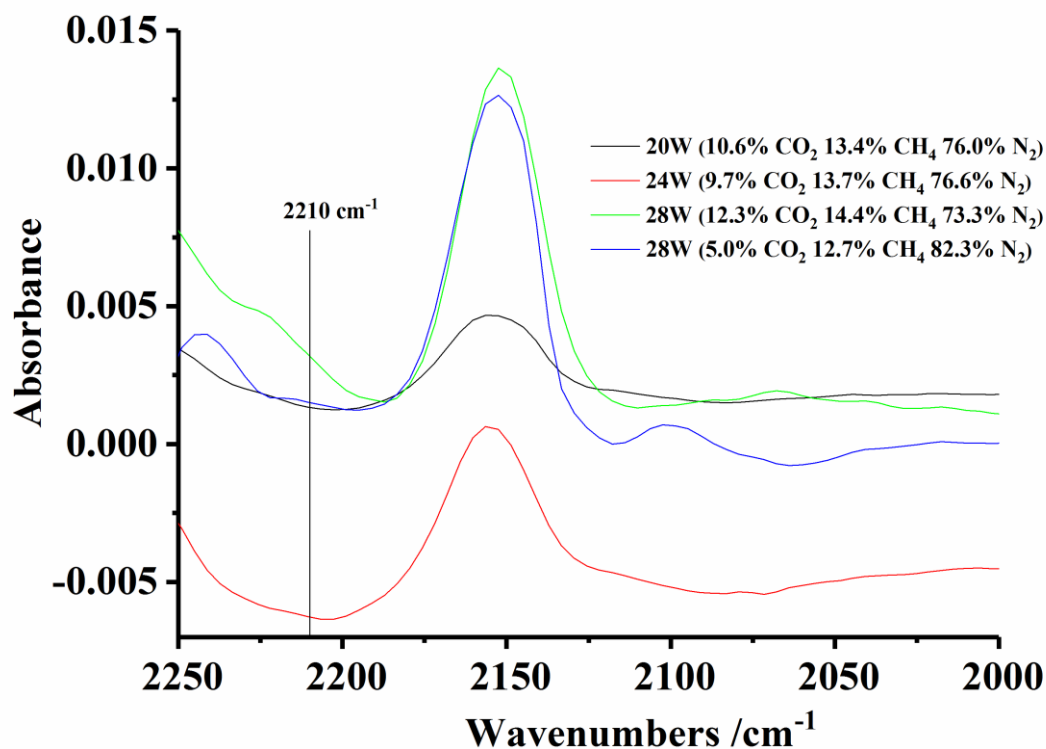
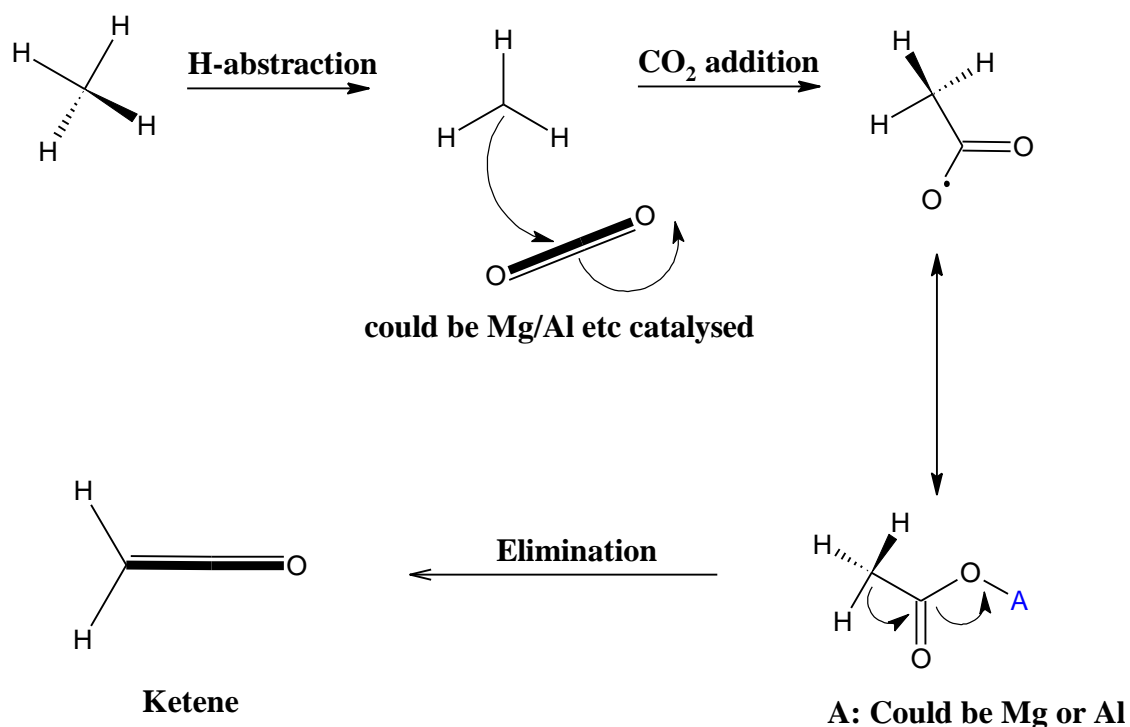


Figure 4.8. Spectra collected after 2 minutes at the input powers and gas feed compositions shown on the figure. Plasma transmission cell, total flow rate 200 cm³ min⁻¹. All the spectra had the analogous spectra obtained using CO₂+N₂ at the same power scaled and subtracted to annul the CO absorptions in each spectrum.

	Composition CO ₂ /CH ₄ /N ₂ or Ar	Power /W	[CO ₂] _{feed} /10 ⁻³ M	[CH ₄] _{feed} /10 ⁻³ M	Gain CO /10 ⁻⁴ M	%CO	Gain HCN /10 ⁻⁴ M	Gain HCHO /10 ⁻⁴ M	Abs 2152 cm ⁻¹ /10 ⁻³
1a	10.6%/13.4%/76.0%	20	4.3	5.5	3.7	8.6	2.5	0.04	3.2
1b	12.7%/15.9%/71.4%	20	5.2	6.5	6.7	12.9	3.9	?	6.3
2	8.7%/12.8%/78.5%	22	3.5	5.2	3.5	10.0	2.8	?	0
3a	9.7%/13.7%/76.6%	24	4.0	5.6	4.7	11.8	3.0	0.05	6.5
3b	8.5%/13.1%/78.4%	24	3.5	5.3	3.7	10.6	3.2	?	0
4	7.4%/11.0%/81.6%	26	3.0	4.5	4.0	13.0	3.9	?	7.1
5a	12.3%/14.4%/73.3%	28	5.0	5.9	6.2	12.4	3.6	?	12.2
5b	9.8%/15.7%/74.5%	28	4.0	6.4	5.3	13.3	5.0	?	24.0
6	15.0% CH ₄ 85.0% N ₂	20	0	6.1	0	0	5.7	0	0
7	12.3% CH ₄ 87.7% N ₂	22	0	5.0	0	0	4.2	0	0
8	16.2% CH ₄ 83.8% N ₂	24	0	6.6	0	0	4.6	0	0
9	13.0% CH ₄ 87% N ₂	26	0	5.3	0	0	6.4	0	0
10	15.0% CH ₄ 85.0% N ₂	28	0	6.1	0	0	6.0	0	0
11	12.9% CO ₂ /87.1% N ₂	20	5.3	0	5.8	10.9	0	0	0
12	9.7% CO ₂ /90.3% N ₂	22	4.0	0	5.5	13.8	0	0	0
13	13.4% CO ₂ /86.6% N ₂	24	5.5	0	6.0	10.9	0	0	0
14	12.3% CO ₂ /87.7% N ₂	26	5.0	0	6.0	12.0	0	0	0
15	12.4% CO ₂ /87.6% N ₂	28	5.3	0	6.1	11.5	0	0	0
16	5.0%/12.7%/ 82.3% N ₂	28	2.0	5.2	3.1	15.5	4.7	0	11.8
17	9.6%/16.0%/74.4% Ar	20	3.9	6.5	2.8	7.2	0	0.07	0
18	8.3%/13.5%/78.2% Ar	28	3.4	5.5	2.7	7.9	0	0.05	0
19	54.0%/18.0%/28.0%	28	22.0	7.3	8.8	4.0	0	0	0

Table 4.1. The feed gas compositions employed in the work reported in this paper, and a summary of the data obtained from the spectra collected after 2 minutes during the various experiments. Abs 2152 cm⁻¹ is the absorbance of the ketene band after subtracting the absorbance of CO, and %CO is the percentage of the CO₂ feed converted to CO, see text for details. Rows 1(a) & (b), 3(a) and (b) and 5(a) and (b) show duplicate experiments carried out several months apart. ? entries indicate experiments in which the formaldehyde absorption could not be discerned clearly, e.g. due to overlying water bands due to adventitious water vapour.

It is very clear from the table that the production of ketene (and indeed the liquid products seen at longer times, see below) requires all three gases. Further, at fixed composition, the gain of ketene increases with input power. This may be due to the formation of the methyl radical from CH_4 as the first intermediate in the production of ketene (see scheme 4.1): CH_3 is known to be an important intermediate for example in the formation of acetic acid from CO_2 and CH_4 [22].



Scheme 4.1

The second inset on fig. 4.6 shows the spectral range between 1640 and 1900 cm^{-1} of the experiment using $8.3\% \text{ CO}_2 + 13.5\% \text{ CH}_4 + 78.2\% \text{ Ar}$: the feature may be attributed to the P, Q and R branches of the ν_2 fundamental absorption of formaldehyde [2, 23]. The integrated extinction coefficient of formaldehyde over the range $1660 - 1820\text{ cm}^{-1}$ is ca. $1.25 \times 10^{-17}\text{ cm mol}^{-1}$ [24] and this was employed to calculate the concentration of formaldehyde in the plasma glow region.

It is clear from fig. 4.6 and table 4.1 that there is some conversion of CO₂ and CH₄ to CO, HCN and formaldehyde after 2 minutes, but that the major fraction of the reactant gases remain unreacted and present at an increased gas kinetic temperature with broadening due to higher rotational excitation as a result of the higher gas temperature: this is a reasonable assumption for atmospheric pressure. In the absence and presence of CH₄, the conversion of CO₂ to CO (rows 1 – 5 and 11 – 15 in table 4.1) appears to be largely independent of input power, which is unexpected as the mean electron energy increases with power, and hence more conversion would be expected. The conversions in CO₂/N₂ are comparable to those in CO₂/CH₄/N₂ suggesting that CH₄ played no part in the reduction of CO₂ to CO. This is because the main process is the single step electron dissociation of CO₂.

Increasing the dilution of the CO₂ by N₂ and N₂+CH₄ (rows 16, 5(a) & (b), 15 and 19) reduced the conversion of CO₂ to CO by a factor of 4: ie. from 15.5% at 5.0% CO₂ to 4% at 54.0% CO₂. Xu and co-workers [25] interpret such behaviour in terms of an increase in the number density of higher energy electrons in CO₂ non-thermal plasma on dilution with N₂ or Ar. The mean electron energy per molecule ranges from 3.9 to 5.5 eV at the lowest and highest input energies employed by us: given that the threshold energies for the excitation and ionization of CO₂, N₂, CH₄ and Ar are all significantly above these values [26-29], see table 4.2, this suggests that electrons in the high energy tail of the distribution must play a significant role.

Species	Excitation threshold /eV	Ionization threshold /eV
CO ₂	6.2	13.8
CH ₄	10	12.65
Ar	11.5	15.8
N ₂	7.7	14.5

Table 4.2. Electron impact excitation and ionization threshold energies [25-27, 29].

When N₂ was replaced by Ar, the input power had little or no effect (rows 17 and 18), neither did changing the feedgas at 20 W. However, at 28 W, the conversion to CO was reduced by ca. 36% compared to using N₂. The latter effect is unsurprising as the ionization energy of Ar

is high, 15.76 eV [30] and it is generally accepted that, at the high concentrations of N₂ employed (70 – 90%), metastable N₂ states will be primarily responsible for the conversion of both CO₂ and CH₄ [26, 30]:



and the Penning dissociation of CH₄:



Table 4.3 shows the calculated mean electron energies for different compositions of CO₂/CH₄/N₂/Ar assuming a reduced electric field, Td, of 200 and a temperature of 300 K using BOLSIG+ [31]. The first excitation threshold of N₂ is 7.7 eV (see table 4.2) and the electron energy distribution in this work possesses a significant population with energy greater than this and so this mechanism is feasible in the plasma cell.

CO ₂	CH ₄	N ₂	Ar	Mean electron energy /eV
100	0	0	0	5.896
0	100	0	0	5.523
0	0	100	0	5.056
0	0	0	100	7.905
50	50	0	0	5.612
25	25	0	50	6.521
25	25	50	0	5.409

Table 4.3. Mean electron energies for different percentage compositions calculated from BOLSIG+ [31] at a reduced electric field of 200 Td and a temperature of 300 K.

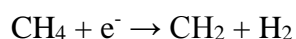
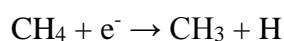
In the absence of CO₂, 9 – 12% of the CH₄ (rows 6 – 10) was converted to HCN. Although HCN is not a desired product, the presence of HCN shows that nitrogen fixation has occurred and it is produced in comparable quantities to CO, so its origin is of interest: as would be expected, CH₄ is clearly essential for its formation, but a comparison of rows 1 – 5, 6 – 10, 16

and 19 strongly suggests that CO₂ suppresses this process, due to the production of reactive O atoms favouring the oxidation pathways.

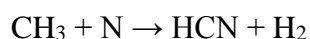
The production of HCN increased with input power (see rows 1 – 5) in the presence of CO₂ and CH₄, but showed no dependence upon power in the experiments using just CH₄ and N₂ (rows 6 – 10). The study of the plasma driven conversion of CH₄/N₂ mixtures is topical due to their relevance to the atmospheres of Titan and Triton (and the postulate that these are models for the early development of Earth) [32-34] and also with respect to natural gas conversion [35]. Horvath et al [34] have observed HCN at similar concentrations using the same SIE as here: thus the authors employed a cylindrical, co-axial quartz reactor packed with borosilicate beads and supplied with 10% CH₄/N₂ at SIEs of 1 to 30 kJ dm⁻³. At an SIE of ca. 8.4 kJ dm⁻³ the authors observed 10,500 ppm HCN in the exhaust from the reactor, ca. 5×10^{-4} M and comparable to the 6.0×10^{-4} M observed in this work in the plasmaglow at the same SIE.

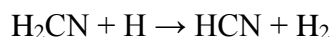
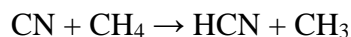
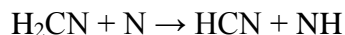
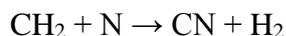
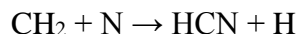
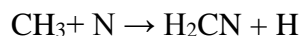
Horvath and co-workers postulated that the formation of HCN occurs via the reaction of CH_x radicals with N atoms: however, the dissociation energy of N₂ is 9.756 eV [36] and the authors observed HCN at SIE as low as 1 kJ dm⁻³, equivalent to an average electron energy per molecule of 0.25 eV for a uniform electric field. However, in the packed bed plasma configuration enhanced electric fields are likely to arise between the beads leading to higher electron energies [22]. The high energy part of the electron energy distribution function is thus likely to be able to directly dissociate N₂.

The gas phase production of HCN in the plasma region is most likely produced by the following mechanism [34]. The initial step is electron impact reaction with CH₄ which requires electron energies greater than 10 eV. The CH_x radicals can then react further with N to produce HCN:

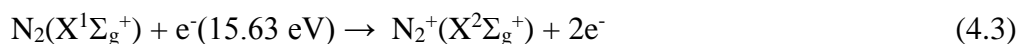


Followed by:





In contrast, Snoeckx and co-workers [35] in their cylindrical reactor without packing observed HCN at concentrations an order of magnitude lower than the findings in this work and Horvath: eg. at 6 kJ dm^{-3} using N_2 concentrations from 1 to 87% Snoeckx et al. observed HCN at concentrations from $4.0 \times 10^{-7} \text{ M}$ to $1.7 \times 10^{-5} \text{ M}$, respectively. The authors attributed the very low HCN production to the fact that the SIE was lower than required to generate N_2^+ which the authors and others have postulated ([35] and refs therein) are the intermediates in the formation of HCN [34], eg.:



However, it is not clear from the cited papers how N_2 is an intermediate in the formation of HCN.

As stated above, in this work, there was no clear relationship between the concentration of HCN in the plasma glow and the SIE: this and the lower dissociation energy of N_2 favours the mechanism proposed by Horvath et al. Interestingly, when N_2 was replaced by Ar (table 4.1, rows 17 and 18), a new absorption appeared with branches at 3315 and 3263 cm^{-1} which we attribute to acetylene [2], see fig. 4.9.

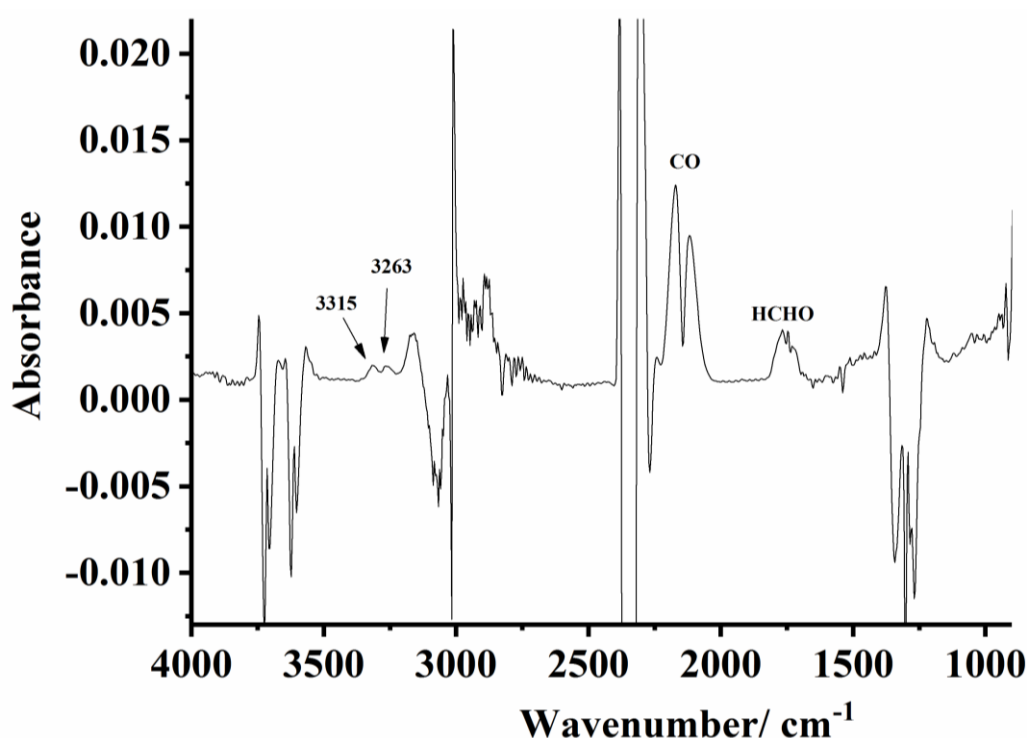


Figure 4.9. The spectrum collected after 2 minutes at 28 W using a feed gas of 8.3% CO_2 + 13.5% CH_4 + 78.2% Ar.

In general, η_{CO} was ca. 1 – 3%, which is in broad agreement with the literature where efficiencies are generally quoted as $\leq 10\%$ [27]: in addition, the cell was designed to allow spectroscopic monitoring of the plasma, rather than to maximize conversion efficiencies. It is estimated that bands due to O_3 , NO_2 and N_2O at 1051, 1628 and 2237 cm^{-1} [6] (having absorbances of 0.02) would be easily discerned in the spectra in fig. 4.4: using the reported extinction coefficients for these species [6], and therefore that if they are present it is at concentrations $< ca. 10^{-5} M$.

4.4 The spectra collected at later times

In order to maximize the peak intensities observed, the spectra collected during the experiment carried out at 28 W were selected for further study. In addition, as stated above, given that the HCN and CO bands in general did not change with time in any of the experiments, the spectrum collected after 2 minutes at 28 W was subtracted from the spectra collected at later times, and the results are shown in fig. 4.10.

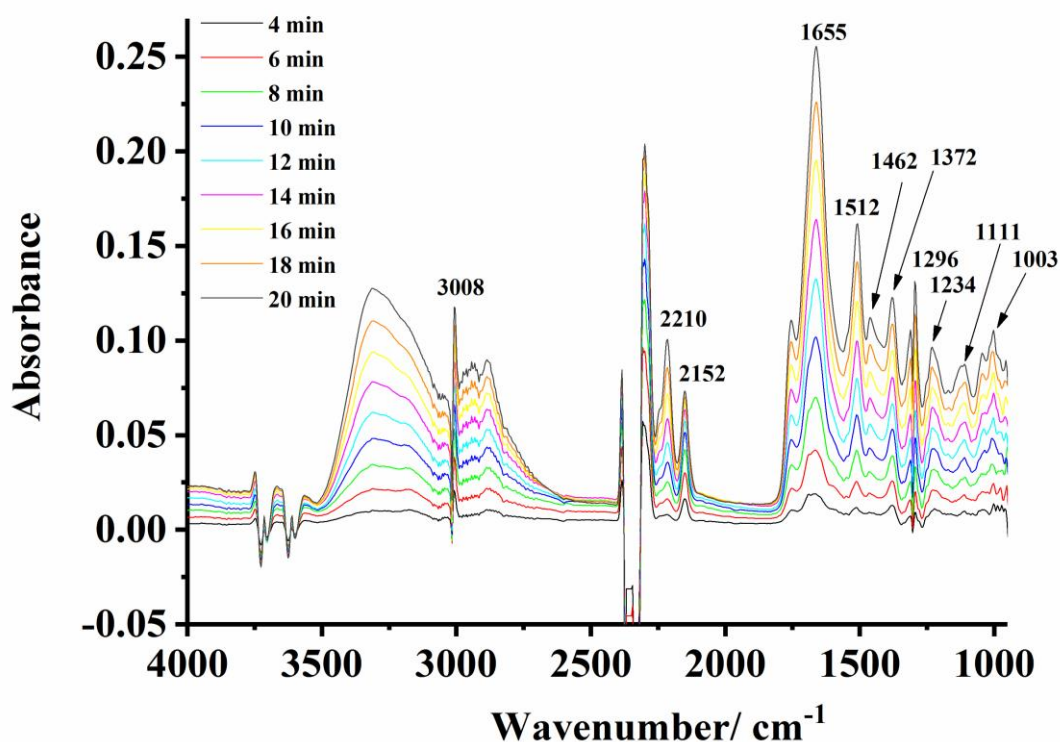


Figure 4.10. In-situ FTIR spectra (8cm^{-1} resolution, 100 spectra per scan set, and 1 minute per spectrum) collected as a function of time at a fixed input power of 28 W. The gas composition was 12.3% CO_2 + 14.4% CH_4 + 73.3% N_2 at a total flow rate of $200\text{ cm}^3\text{ min}^{-1}$ and a temperature of ca. $25\text{ }^\circ\text{C}$; the reference spectrum was collected under the same conditions but with no plasma. Spectra were collected every 2 minutes up to 20 min. The spectrum collected at 2 minutes was subtracted from those taken at longer times, see text for details.

The loss and gain features in the CH_4 and CO_2 regions of the figure reflect the increased gas kinetic temperature of these species with time: in other words, the loss features are due to the less rotationally excited species. The HCN and CO bands are clearly absent, showing that these species had reached steady state concentrations in the plasma by 2 minutes. Plots of the various features in fig. 4.10 are shown in figs. 4.11(a) and (b), and the analogous plots for the experiments carried out at the other input powers, are shown in figs. 4.12(a) - (d). The absorbance at 2295 cm^{-1} on the wing of the CO_2^* feature and absorbance at 3008 cm^{-1} on any wing of CH_4^* band were taken as indications of the increasing rotational excitation of these species with temperature.

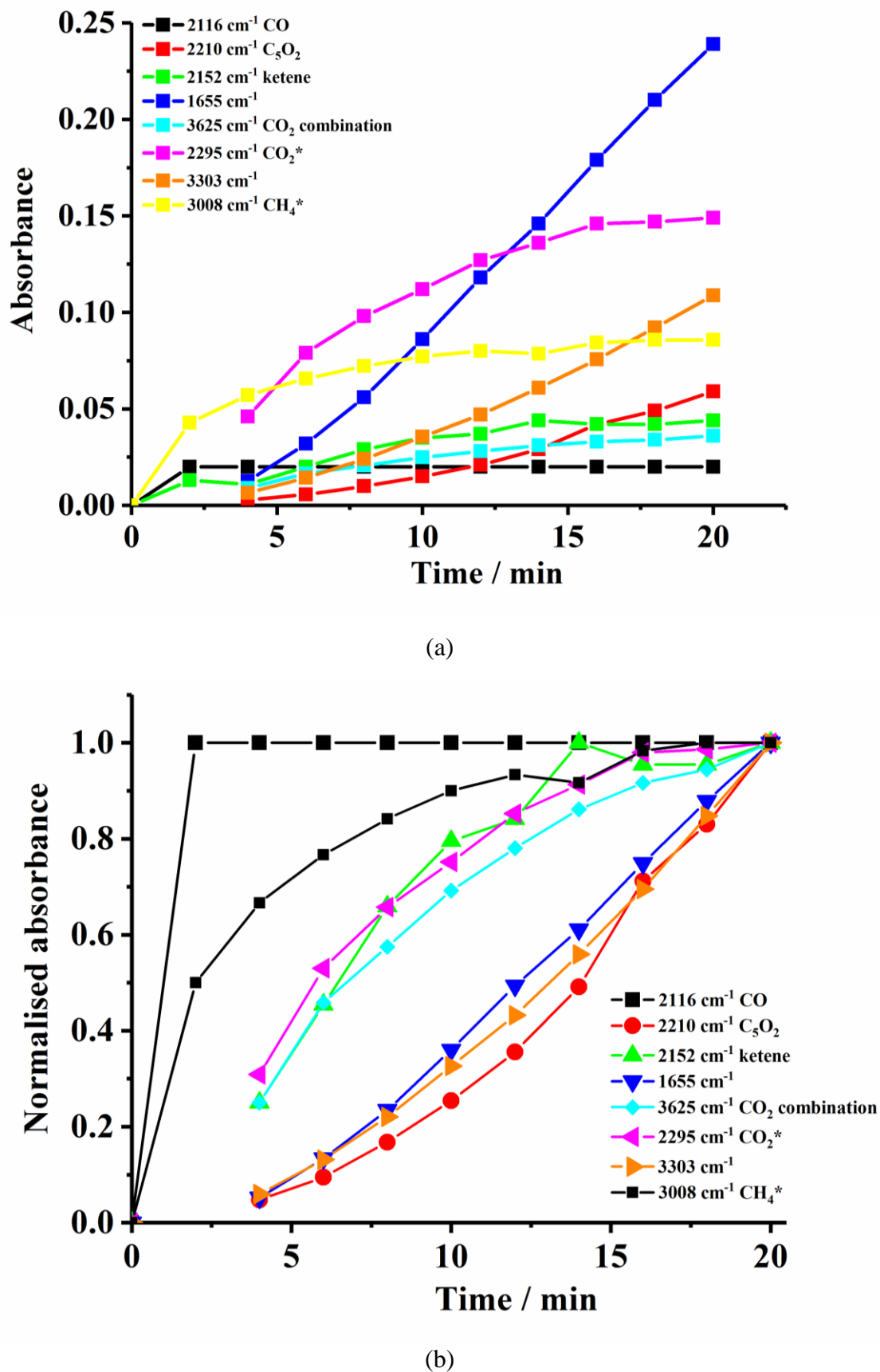
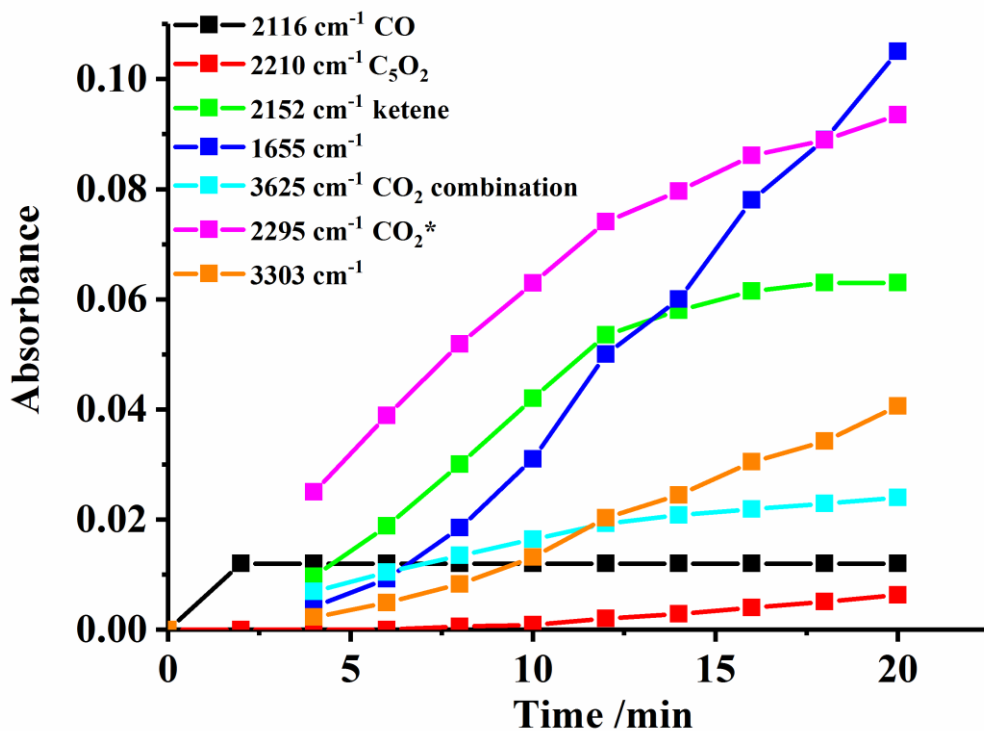
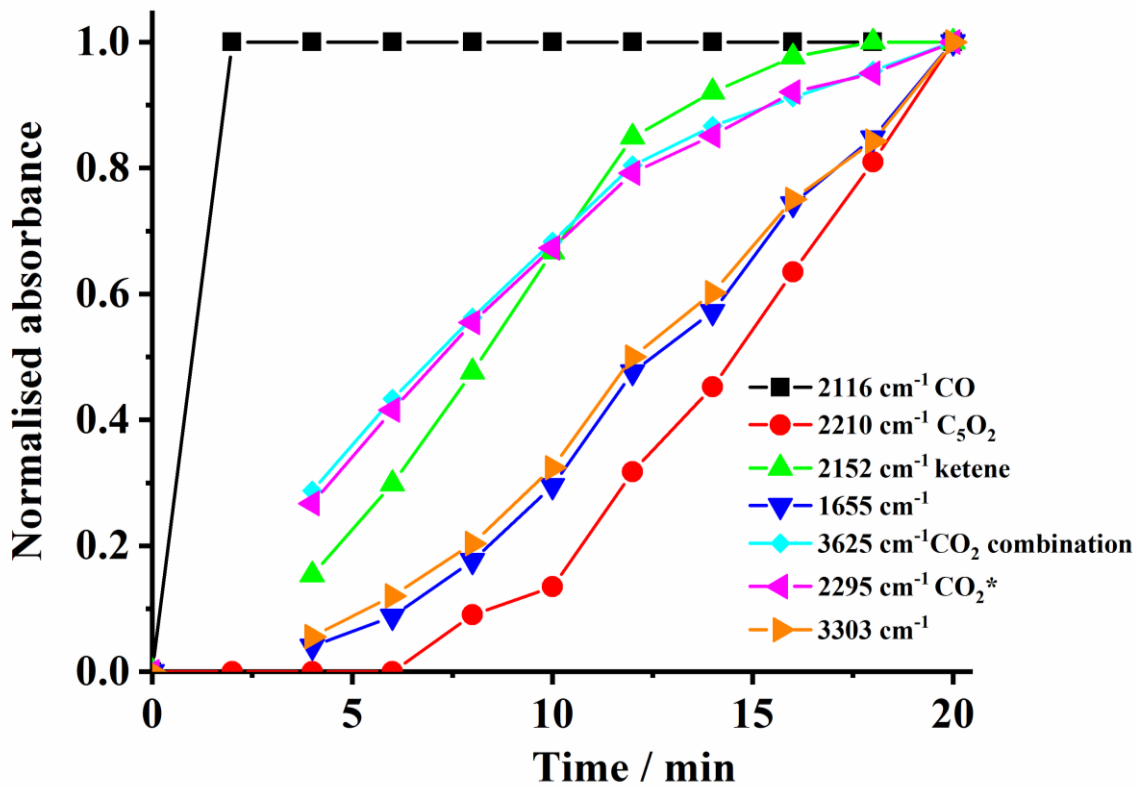


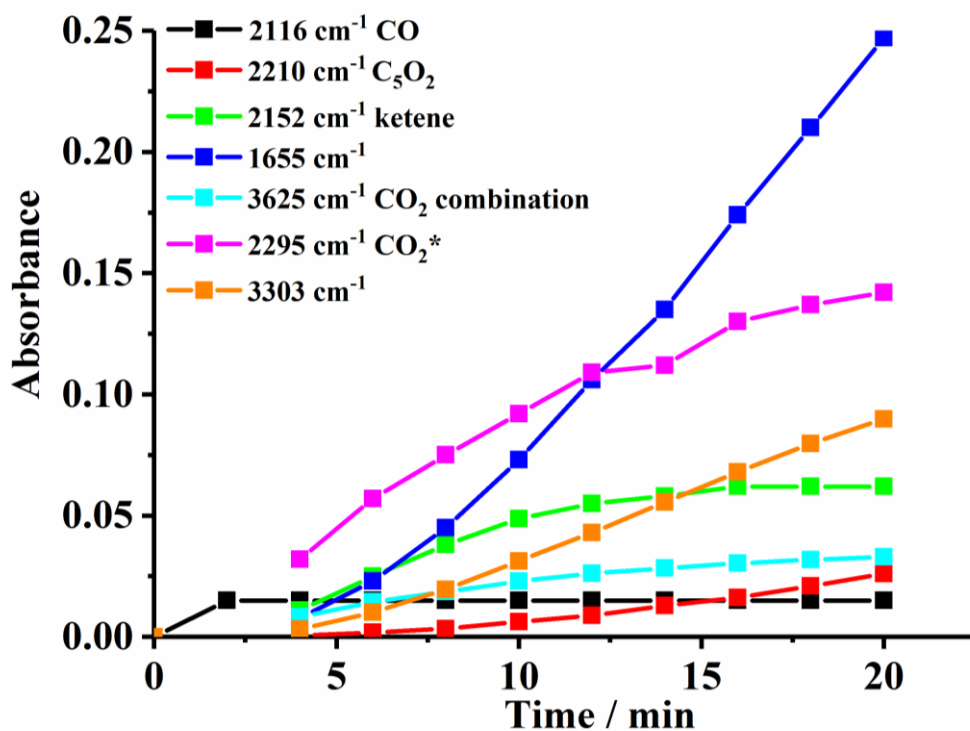
Figure 4.11. (a) Plots of the intensities of the various features in fig. 4.10 as a function of time. (b) The plots in (a) normalised to their maximum values.



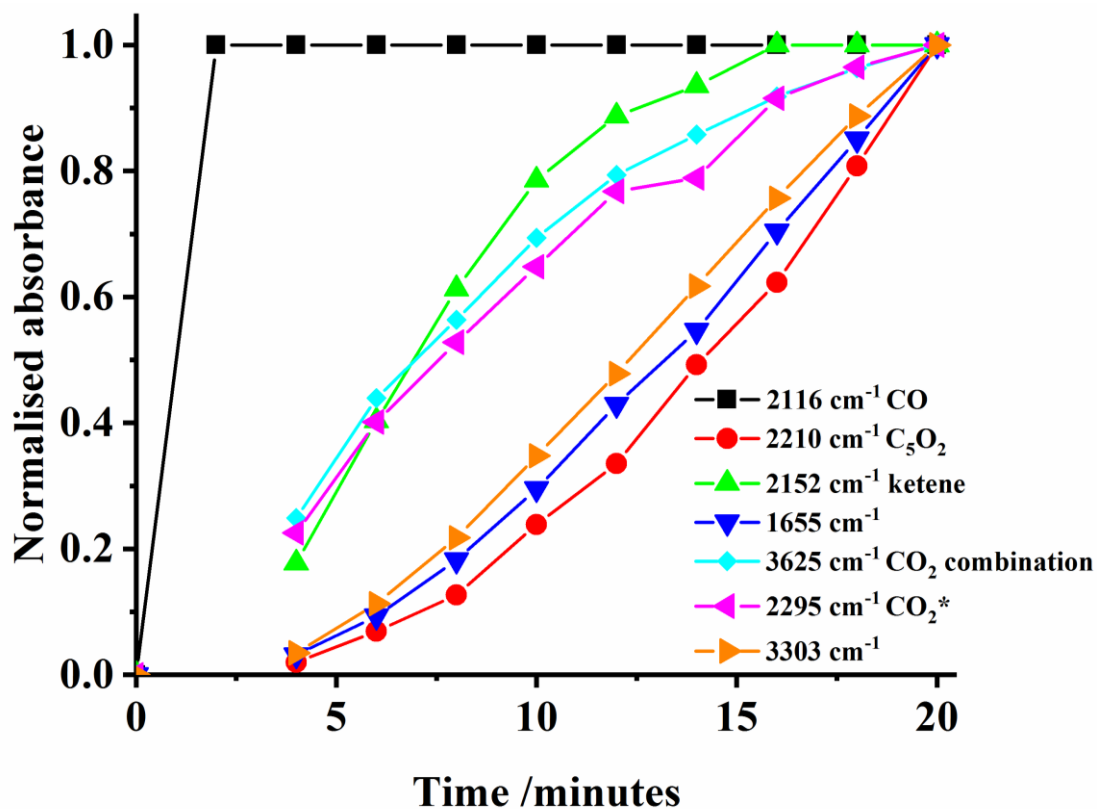
(a)



(b)



(c)



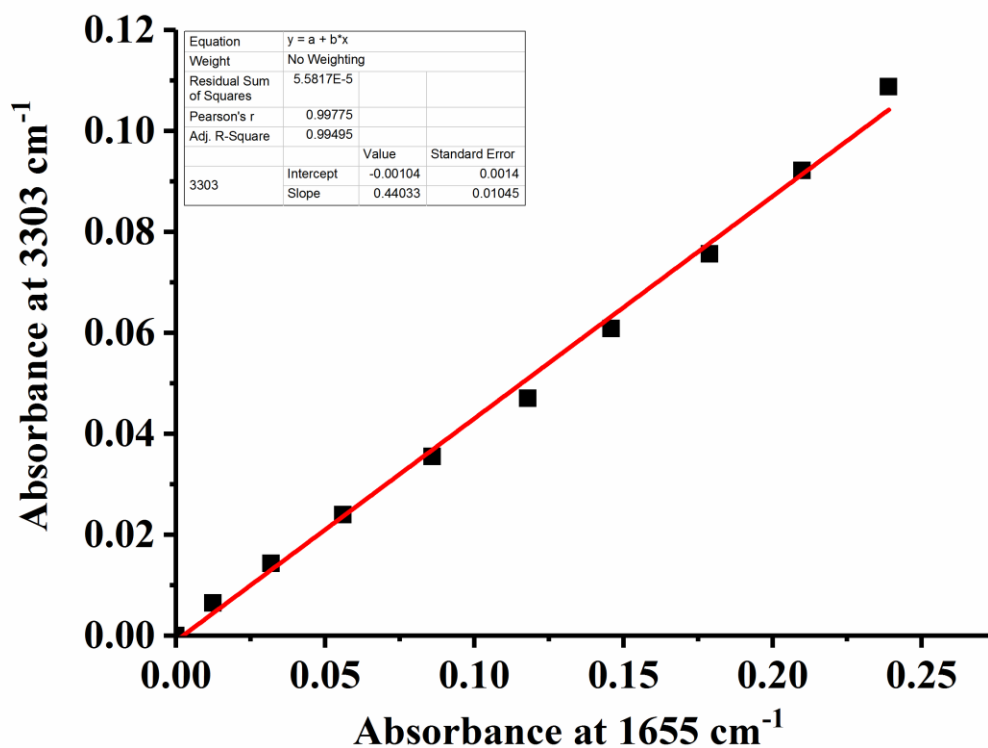
(d)

Figure 4.12. Analogous plots to those shown in figs. 4.11(a) and (b) for the various features observed at input powers of (a) & (b) 20 W and (c) & (d) 24 W.

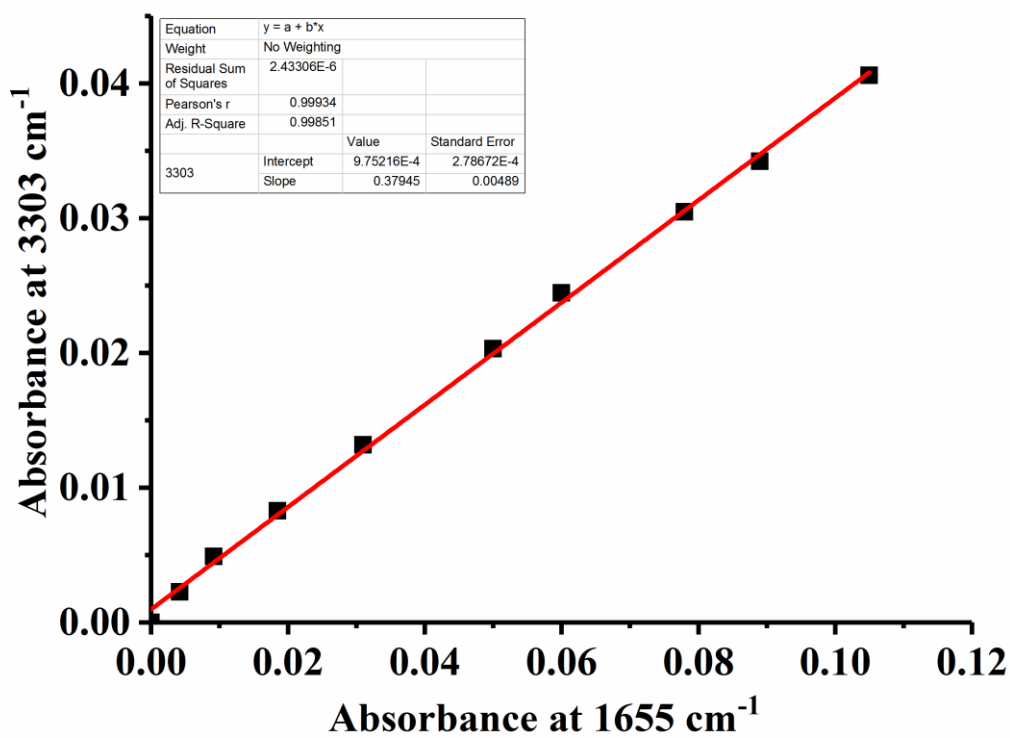
Figure 4.11(a) shows plots of the band intensities as a function of operation time and fig. 4.11(b) the corresponding plots of the intensities normalised to their maximum values. The plots of CO intensity at 2116 cm^{-1} were calculated with respect to the reference spectrum taken with no input power, all other features were calculated from the difference spectra, with the spectrum collected at 2 minutes subtracted: the plots of the normalised intensities of the CO band can also be taken as representative of HCN.

It is clear from figs. 4.10, 4.11(a), 4.11(b) and 4.12(a) – (d) that the intensities of the various features observed show that the species responsible show three types of behaviour: HCN and CO rapidly attain a steady state irrespective of the formation of the liquid film, suggesting these take place entirely in the plasma region. The CO_2 , CO_2^* and 2152 cm^{-1} ketene bands show a rapid initial increase which tails away at longer times, but their concentrations in the plasma continue to grow: in contrast, the 2210 cm^{-1} C_5O_2 , 1655 cm^{-1} and 3303 cm^{-1} bands take longer to develop and then increase fairly steadily. This suggests that the three types of behaviour are due to species produced or consumed by three distinct processes although links between them may also be present.

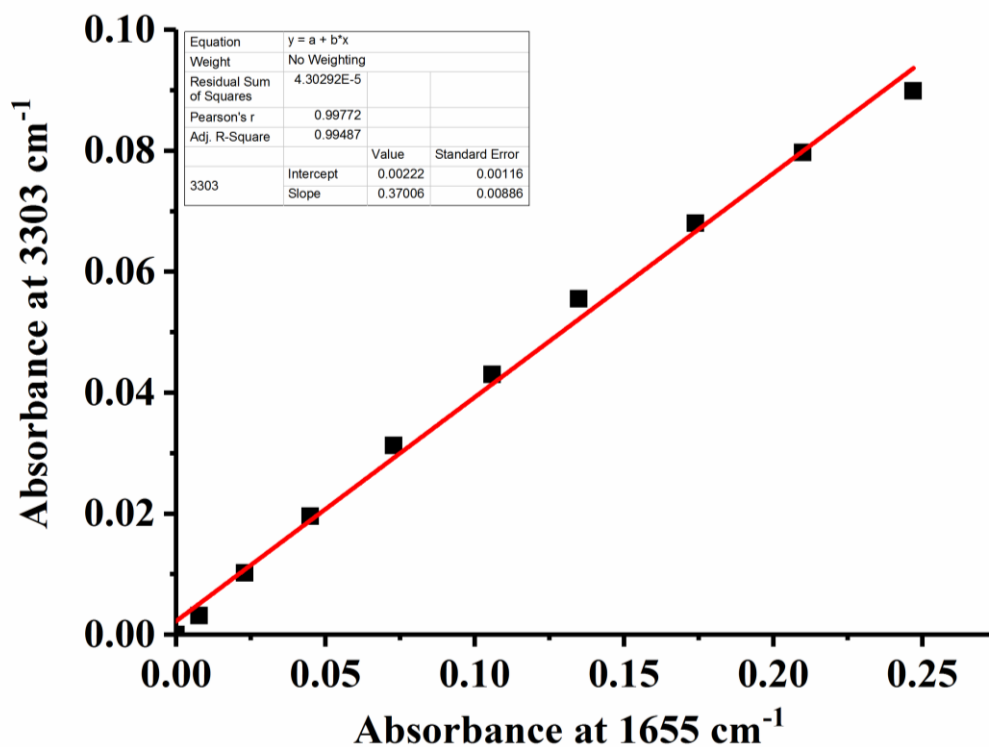
From fig. 4.10, it appears that the broad gain feature between 2500 and 3500 cm^{-1} , which is distorted somewhat by $\nu_3\text{ CH}_4^*$ absorptions, is due to the same species as the 1655 cm^{-1} feature and this was confirmed by plotting the intensities of the two features against each other, see figs. 4.13(a) – (c) for the experiments conducted at input powers of 20 to 28W (only the data for 20, 24 and 28W are shown for clarity). The same procedure confirmed that the 1512 cm^{-1} band was also due to this species, see Appendix 3. A clue to the identity of this species was provided by the lack of any intense bands due to C-H stretches in figs. 4.2, 4.6, 4.10 etc, along with the broad absorption between $2500 - 3500\text{ cm}^{-1}$ which appeared to comprise two bands. On the basis of the literature [2, 37, 38], the broad feature between 2500 and 3500 cm^{-1} may be attributed to the N-H stretch of acetamide, the weak 2880 cm^{-1} band to the asymmetric C-H stretch and the 1655 and 1512 cm^{-1} bands to the amide I (C=O stretch) and amide II (N-H in plane deformation), respectively. As well as the carbon chain oxides, acetamide is also important to the study of prebiotic life as it is the largest interstellar molecule bearing the critical amide functionality [39].



(a)



(b)



(c)

Figure 4.13. Plots of the absorbance of the 3303 cm^{-1} band vs the broad absorbance at 1655 cm^{-1} for the experiment in fig. 4.10 and the analogous experiments carried out at input powers of (a) 20 W (b) 24 W and (c) 28 W. (Corresponding to rows 1(a), 3(a) and 5(a) in table 4.1).

The 1655 cm^{-1} feature also has contributions from the in-plane N-H bend, C-N stretch and C-C-N deformation. This is clearly not the only species present in the liquid film which shows a plethora of clearly defined (but as yet unidentified) bands below 2000 cm^{-1} as well as a significant broad underlying absorption suggesting a number of overlapping bands. Further, the liquid film is a yellowish colour suggesting, for example, conjugated C=C and C=N bonds. The postulate that the 1655 cm^{-1} band is a composite of a number of absorptions is supported by close inspection of the spectra collected after 4 minutes and 20 minutes in fig. 4.10, where it can be seen that the absorption around 1655 cm^{-1} in the 4 minute spectrum comprises a number of peaks.

Figure 4.14 shows preliminary data obtained using the plasma reflectance cell during a repeat of the experiment in fig. 4.4 experiment in which spectra were collected every 2 minutes after initiating the plasma at an input power of 24 W.

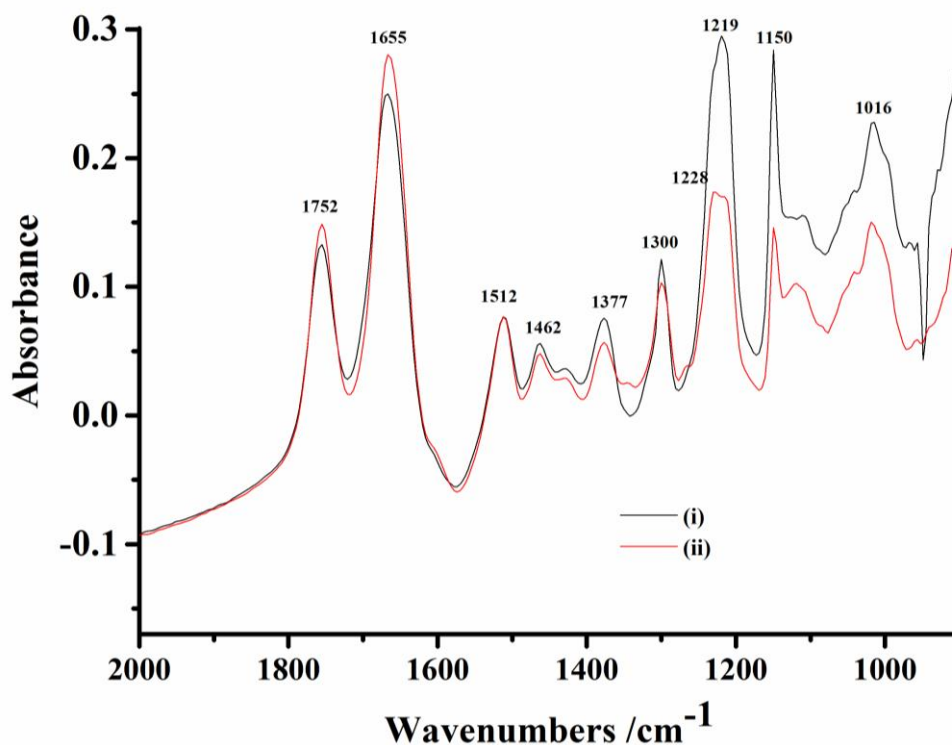
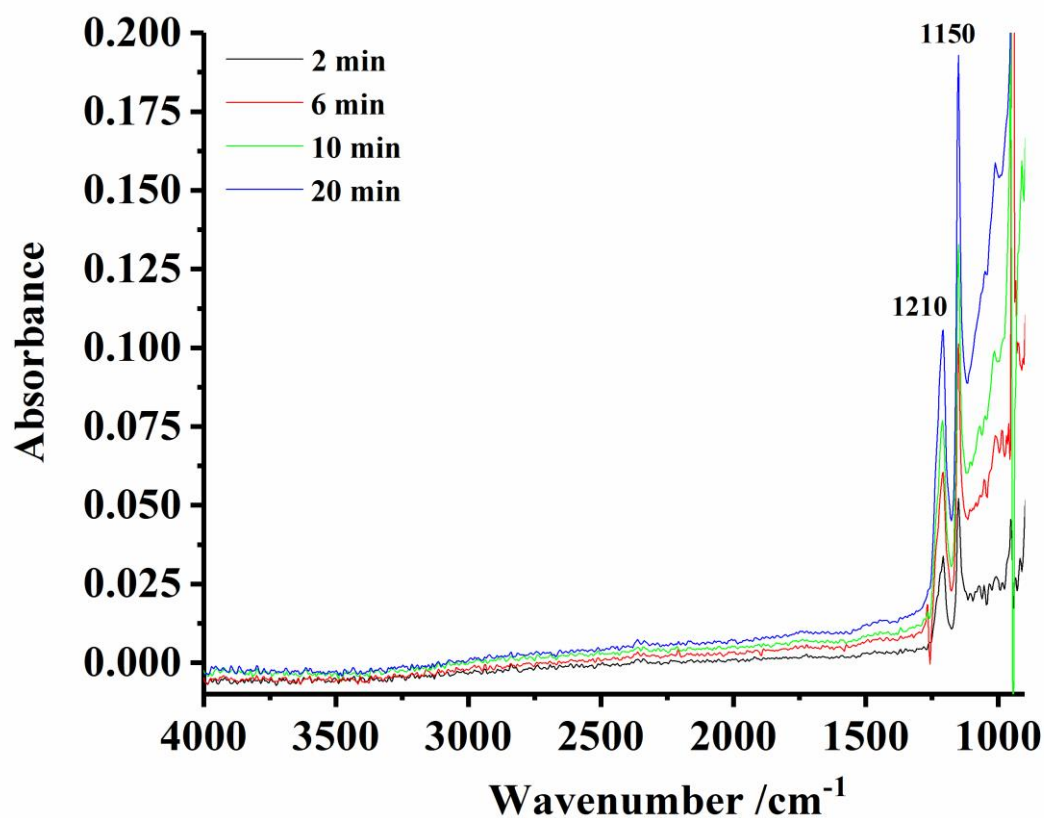


Figure 4.14. (i) Spectrum of the liquid deposit formed on the CaF_2 windows of the transmission cell following a repeat of the experiment at 24 W in fig. 4.4. At the end of the experiment, the cell was flushed thoroughly with N_2 and a spectrum collected using the spectrum taken of the cell containing nitrogen prior to the experiment as the reference. (ii) Spectrum of the liquid deposit on the CaF_2 window of the reflectance cell following an analogous experiment at 24 W to that depicted in fig. 4.4. See text for details.

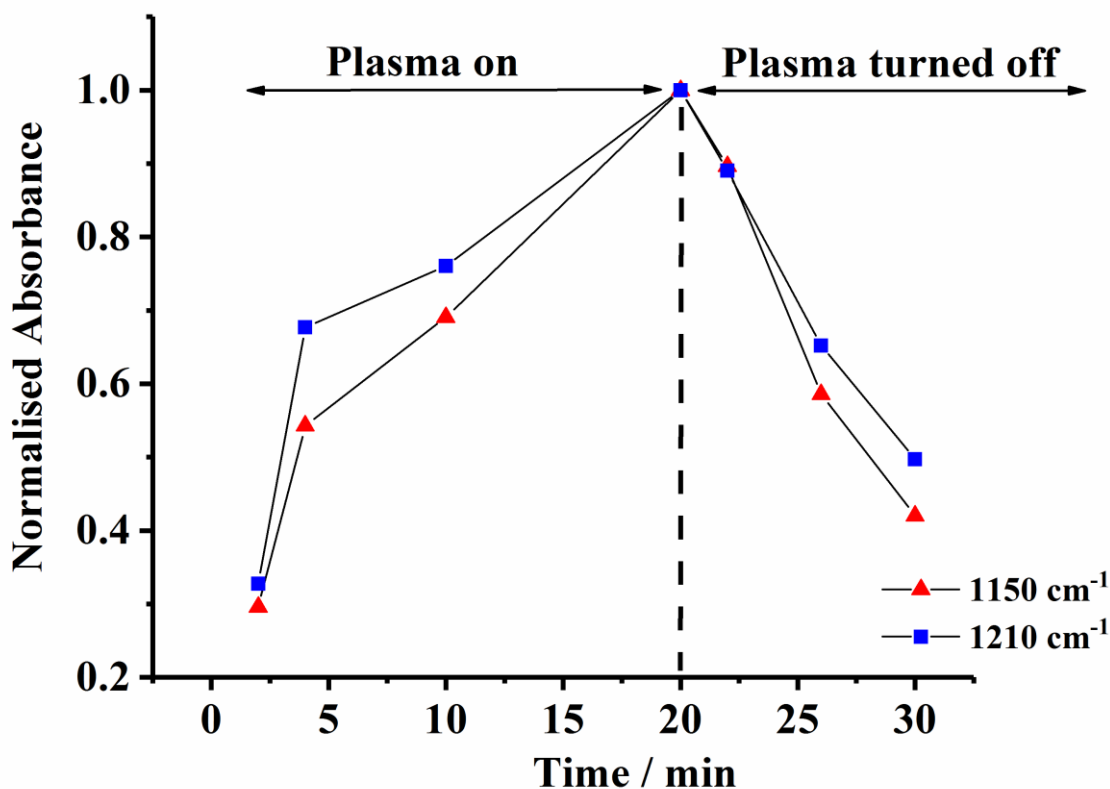
Figure 4.14 shows the spectrum collected after 20 minutes plasma operation and the spectrum of the deposit which remained after 10 minutes flushing with N_2 . As a result of the shorter pathlength of the reflectance cell (1 cm), the CH_4 ν_4 bands are much weaker, revealing underlying absorptions due to the components of the liquid film: thus there are additional features at 1300 cm^{-1} (the 1296 cm^{-1} band in fig. 4.10 perturbed by the loss features due to CH_4^*) and 1016 cm^{-1} . In contrast to all the spectra observed using nominally the same feed gas composition in the transmission cell, where the 1752 cm^{-1} feature is relatively weak, this band is comparable in intensity to the feature at 1655 cm^{-1} in fig. 4.14.

The spectrum collected using the reflectance cell includes information from both the window and the Macor, in contrast to the transmission cell spectrum which only shows the deposit on

the windows of the cell. Further, the reflectance cell has one exposed Ti mesh electrode. This suggests that the 1752 cm^{-1} feature may be attributed to a species present in a higher amount at the Macor/Ti mesh than on the CaF_2 window, and that this may be produced as a result of contact of the plasma with the mesh. That the Macor and/or Ti are contributing to the spectrum in fig. 4.14(i) is shown by the bands at 1150 and 1219 cm^{-1} . As may be seen, both features decreased in intensity as the cell was flushed with N_2 ; however, the latter band ceased to decrease, and changed structure. This was due to the presence of two bands, one at ca. 1228 cm^{-1} (correlating with the 1234 cm^{-1} feature in fig. 4.10) due to the liquid film and a second, at 1210 cm^{-1} that increased in intensity in concert with the 1150 cm^{-1} band. The 1150 and 1210 cm^{-1} bands are associated with the Ti/Macor surface, as they appear in experiments using pure N_2 as the feed gas, see figs. 4.15(a) and (b).



(a)



(b)

Figure 4.15. (a) *In situ* FTIR spectra (8cm^{-1} resolution, 100 co-added and averaged scans, 60 seconds per scanset) collected at the times shown on the figure at an input power of 24 W using the reflectance cell and nitrogen gas as the feed gas. The spectrum collected immediately before the plasma was initiated was employed as the reference (b) Plots of the normalised absorbance of the 1150 cm^{-1} and 1210 cm^{-1} with time before and after plasma exposure.

As can be seen in figs. 4.15(a) and (b), the 1210 cm^{-1} and 1150 cm^{-1} bands were induced by the plasma and relaxed slowly, i.e. over many minutes, when the plasma is turned off. Unfortunately, it has been unable to identify the species responsible for these absorptions to date and, whilst interesting, it is not clear that these species participate in the processes observed and hence are not relevant to the aim of this chapter. Further work is recommended to investigate this chemistry.

Figure 4.16 compares the spectra obtained after 20 minutes at an input power of 28 W with the corresponding spectra collected after 2 minutes subtracted using feed gas compositions selected to investigate the effect of CO₂ and N₂.

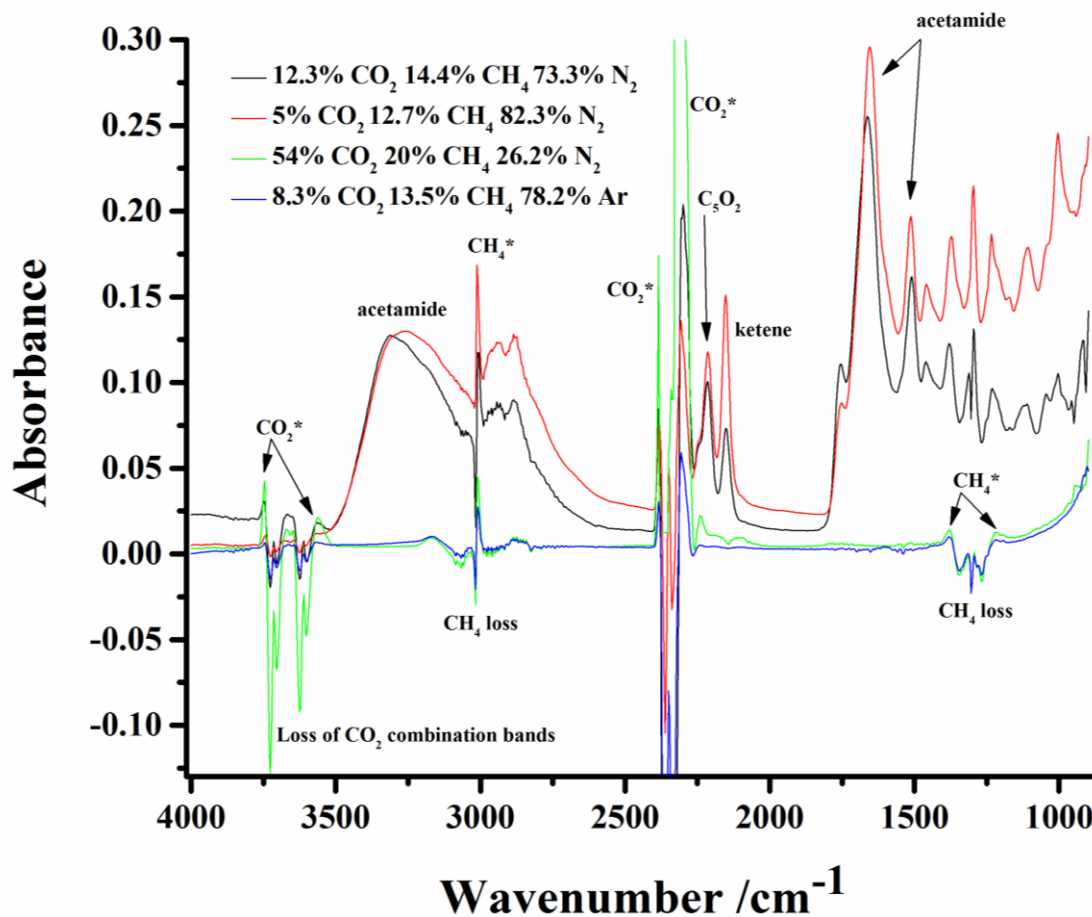


Figure 4.16. In-situ FTIR spectra (8 cm^{-1} resolution, 100 spectra per scan set, and 1 minute per spectrum) collected after 20 minutes operation at input power of 28 W as a function of the gas compositions shown on the figure. In each case, the corresponding spectrum collected after 2 minutes operation was subtracted. Total flow rate was $200\text{ cm}^3\text{ min}^{-1}$ the temperature ca. $25\text{ }^\circ\text{C}$ using the transmission cell.

As can be seen, it is clear that excess CO₂ or replacing N₂ with Ar both prevent the production of the chain oxides and the liquid film, despite the presence of methane in both cases. Thus the feed gas composition has a major effect upon the products observed. The relative absorbances of the various hot CO₂ and hot CH₄ features essentially reflect the initial concentrations of the ground state species in the feed gas.

A summary of all the assignments is presented in table 4.4.

Peak/ cm ⁻¹	Assignment
3017	Q branch of ν_3 band of CH ₄
1302	Q branch of ν_4 band of CH ₄
3726	Combination bands of CO ₂
3704	
3625	
3600	
2167	P branch CO
2116	R branch CO
3334	P branch HCN
3286	R branch HCN
2210	C ₅ O ₂
2152	H ₂ C=C=O, ketene
ca. 1767	P branch HCHO
1745	Q branch HCHO
ca. 1724	R branch HCHO
ca. 3303	N-H stretch of acetamide and underlying liquid film absorption
2880	Asymmetric C-H stretch of acetamide
1655	Acetamide I and underlying liquid film absorption
1512	Acetamide II and underlying liquid film absorption

Table 4.4. A summary of the assignments of the various features in figs. 4.4 – 4.10. See text for details.

4.5 Thermal experiments

Figure 4.17 shows the spectrum collected at 100 °C during an experiment in which the reference spectrum was collected at 25 °C and the temperature increased in steps up to 600 °C, with further spectra collected at each step. The spectra were collected from the Macor disc in 43% CH₄ + 21% CO₂ + 36% N₂ in the sealed system (ie. batch mode).

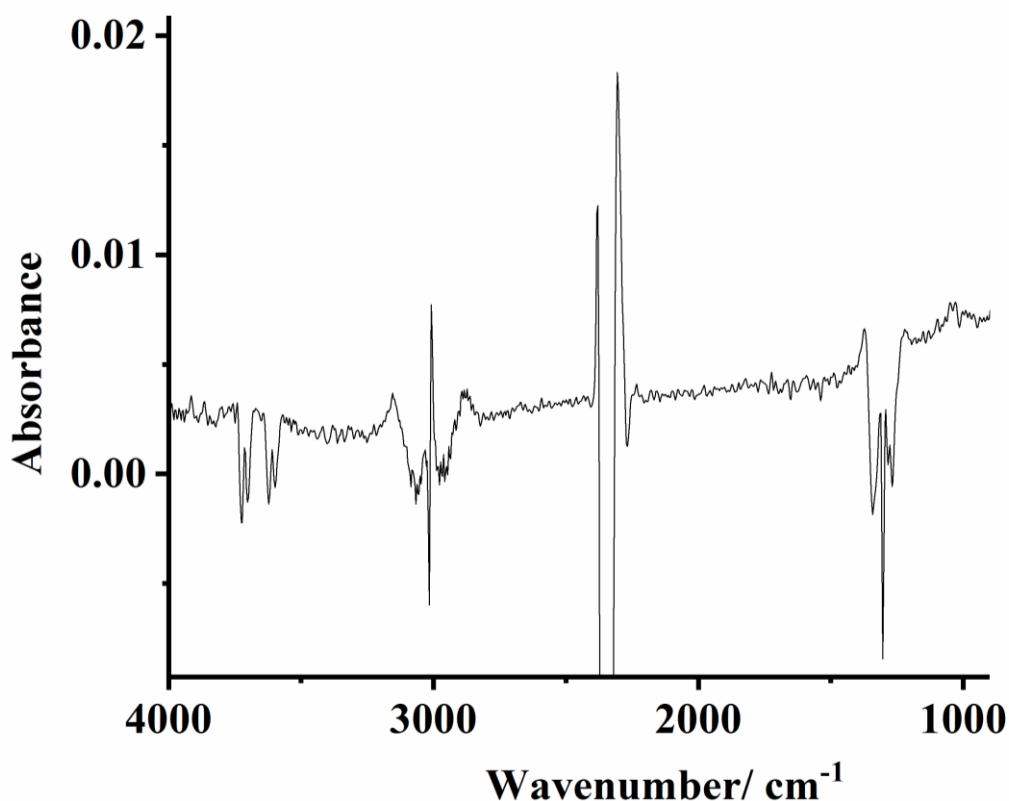


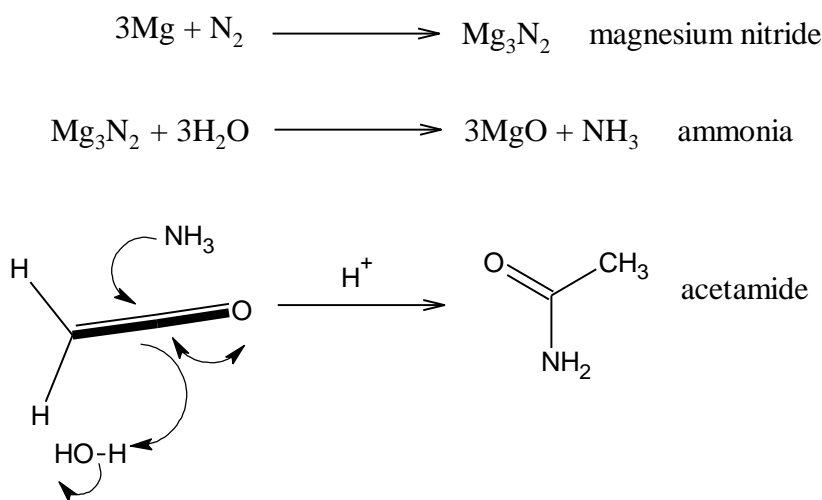
Figure 4.17. The spectrum (8 cm^{-1} resolution, 100 spectra per scan set, and 1 minute per spectrum) collected at $100\text{ }^{\circ}\text{C}$ during an experiment in which a Macor disc was heated in a static atmosphere of $43\% \text{CH}_4 + 21\% \text{CO}_2 + 36\% \text{N}_2$ and spectra collected from the disc as a function of temperature from $25\text{ }^{\circ}\text{C}$ to $600\text{ }^{\circ}\text{C}$. The reference spectrum was collected at $25\text{ }^{\circ}\text{C}$. See text for details.

It is clear from the figure the same features are observed in the ν_3 and ν_4 regions of the CH_4 absorption and either side of the fundamental absorption of CO_2 as in the plasma experiments, supporting the assignments to CH_4^* and CO_2^* . No other products were observed up to $600\text{ }^{\circ}\text{C}$, clearly showing that catalyst selection for plasma driven systems cannot be based solely on materials that work in thermally-activated processes.

4.6 The reaction zones above Macor

The plasma transmission and reflectance cells are both flow systems i.e. reactants were constantly supplied and products removed: however, the plots in figs. 4.10, 4.11(a) & (b) and figs. 4.12(a) - (d) show that the concentrations of CO_2^* and CH_4^* change relatively little with time, whilst the concentration of ketene in the plasma, and C_5O_2 in the liquid film increase.

Given that the input power and flow rate did not vary during the experiments, this suggests that the rate of formation of these products increased with time, whilst the rates of formation of HCN and CO (and possibly formaldehyde) remained constant. As stated above, this suggests parallel and separate reaction pathways: in addition, the data indicate that some aspect of the system is changing and steadily increasing the rate of formation of ketene etc. A logical postulate would be the increasing build-up of reactive intermediates on the Macor surface: eg magnesium carboxylate and magnesium nitride, see schemes 4.1 and 4.2.



Scheme 4.2

The higher chain oxide C_5O_2 could then be produced via the reaction of methane and ketene (see scheme 4.1) according to:



However, in all the 20 minute experiments discussed above, the reactions near to the Macor proceeded and indeed accelerated, as the liquid film formed. In contrast, by the end of a two-hour experiment, using essentially the same feed gas composition as that in fig. 4.10 and 28 W input power, the production of all the species observed in fig. 4.10 had ceased, presumably as the Macor was completely covered, or covered beyond a maximum thickness of the liquid film: the latter possibility arises due to the fact that in all the experiments employing the nominal gas feed composition to the naked eye both the Macor caps were covered with the liquid film after only 20 minutes plasma operation. Thus, it does not seem unreasonable to

postulate that, at thicknesses lower than some critical maximum, the film facilitates the production of the ketene and C_5O_2 : for example, it has been reported that the penetration depth of electrons into an aqueous solution is ca. 12 nm [40]: in our case, the third reaction zone could be a layer within the liquid droplets defined by the penetration depth of the electrons, analogous in some ways to the catalysis taking place at the boundary between metal particles and oxide substrates [41]. Above the critical maximum thickness, defined presumably by the dielectric constant of the liquid film, the electric field decreases below that necessary to sustain the plasma.

The data gained in this work thus suggest the presence of at least two reaction zones: one at the Macor/plasma interface and one that is the plasma bulk. A third zone involves the liquid, perhaps at its boundaries. This model is a development of the two-zone model proposed by Kim et al. [42] in which the active species in the plasma such as OH radicals and ground state O atoms occupy a thin layer perhaps 50 μm thick above the catalyst and are available for reaction at the catalyst: above this layer, species produced in the plasma react in the same way as in the absence of catalyst.

Our model is supported by an experiment in which isoprene was added to 11.0% CO_2 + 15.0% CH_4 + 74.0% N_2 in an attempt to trap ketene via a cycloaddition reaction [43]: instead, whilst CO_2^* , CO and HCN were still observed, wholly different liquid products were produced, the spectrum of which was identical to that reported by Scarduelli et al. [44], see fig. 4.18, and the isoprene simply polymerized on the Macor caps.

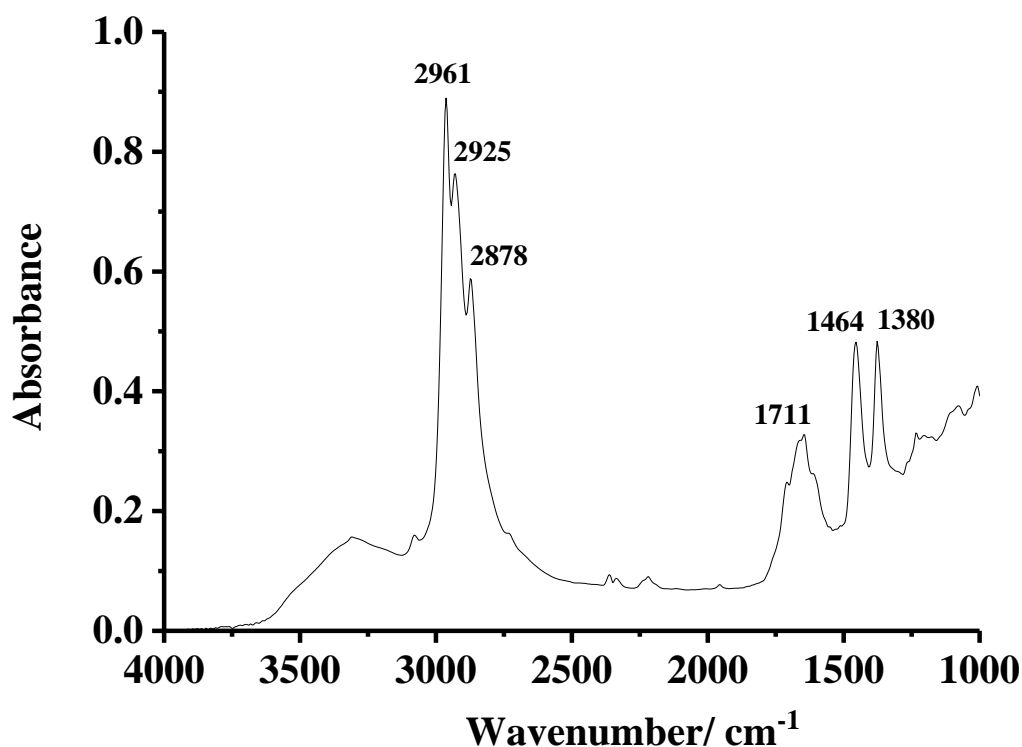


Figure 4.18. The spectrum (8 cm^{-1} resolution, 100 spectra per scan set, and 1 minute per spectrum) collected at the end of an experiment in which 11.0% CO_2 + 15.0% CH_4 + 74.0% N_2 was bubbled through isoprene and fed to the transmission cell. Plasma was then initiated at 28 W for 20 minutes, after which the plasma was turned off and the cell flushed with N_2 . The spectrum was then collected using a spectrum collected of the N_2 -filled cell prior to the experiment as the reference.

Scarduelli and co-workers employed a conventional NTP tube reactor fed with a 60:40 mixture of CH_4 and CO_2 (no nitrogen); both electrodes of the reactor were isolated from the plasma by silica glass such that the plasma contacted only silica. Our data and the results of Scarduelli et al. strongly suggest that the polymerization of the isoprene on the Macor essentially masked its catalytic properties and the reaction zone was thus confined to the plasma itself. In other words, the presence of the Macor is essential for the specific liquid film composition obtained in our experiments discussed above, nitrogen is required to activate the Macor and the liquid film then has a direct influence on the production of ketene and C_5O_2 , for example either by providing a liquid reaction zone where reactants/reactive intermediates can be concentrated, or by acting as a catalyst.

The chemical species observed here, namely: CO, HCN, HCHO, CH₂CO, C₂O₅, and acetamide are very much a subset of the product species expected in the dry reforming reaction. H₂ is one of the main products but could not be observed by our FTIR detection methods. However it would have been expected to observe hydrocarbons: C₂H₆, C₂H₄ and C₂H₂ which were either obscured in the spectra and/or below our detection limits. The one-dimensional fluid model for a typical DBD plasma reactor for CO₂/CH₄ by de Bie et al [45] predicts these species as products but in this work with added N₂ the routes to C₂ species may be diverted by reaction with N atoms to preferentially form HCN. It is interesting that de Bie et al also predict ketene (CH₂CO) but did not include C₅O₂ in the calculation. Interestingly, this is the first time that such carbon chain oxide have been observed in dry reforming reactions.

4.7 Conclusions

Macor contains the oxides of the earth-abundant elements Mg, Al and Si: despite its relatively simple composition it catalyses the production of a rich variety of products from the non-thermal plasma conversion of CH₄ and CO₂ in nitrogen. The processes observed include the fixing of nitrogen to both HCN and acetamide, and the production of the chain oxides C₅O₂ and ketene. CO and formaldehyde are produced, in addition to unreacted but rotationally-excited CO₂ and CH₄, and a multicomponent liquid film. The Macor is essential to the formation of the liquid film, as is nitrogen gas, and the liquid film, in turn, plays an important role in the production of C₅O₂ and ketene. The formation of liquid products has been observed by others (see, for example, [45, 46]) but the possible wider significance of this has not hitherto been recognised: for example, by careful modification of the liquid film with added solvent and/or by careful choice of model liquids, it could be possible to ensure that the plasma-induced chemistry takes place at and close to the plasma/liquid interface as modelling of the potential distribution using slabs of dielectrics shows that the discontinuity in the electric field will be highest at this interface. Hence it is believe this approach may offer a new dimension to plasma catalytic chemistry, one that helps to transform the technology into a viable option for large scale chemical syntheses through a paradigm shift in plasma catalysis and reactor design.

Finally, it is clear that using Macor as a catalyst in the plasma-driven conversion of $\text{CO}_2 + \text{CH}_4 + \text{N}_2$ results in radically-different chemical processes to those observed in the analogous thermal experiments, supporting the contention that the two processes demand different, tailor-made catalysts identified using in-depth investigations of mechanism and kinetics.

4.8 References

1. Herzberg, G., *Molecular spectra and molecular structure* Vol. Vol.2: Infrared and Raman spectra of polyatomic molecules. 1945, New York Van Nostrand Reinhold.
2. Stein, S.E. "Infrared Spectra" in *NIST Chemistry Webbook, NIST Standard Reference Database Number 69*. [cited 2017 September 5]; Available from: <http://webbook.nist.gov/cgi/cbook.cgi?Contrib=MSDC-IR>.
3. Bennett, C.J., C.S. Jamieson, and R.I. Kaiser, *Mechanistical studies on the formation and destruction of carbon monoxide (CO), carbon dioxide (CO₂), and carbon trioxide (CO₃) in interstellar ice analog samples*. *Physical Chemistry Chemical Physics*, 2010. **12**(16): p. 4032-4050.
4. Christensen, P.A., A.H.B.M. Ali, Z.T.A.W. Mashhadani, and P.A. Martin, *A Direct Fourier Transform Infrared Spectroscopic Comparison of the Plasma- and Thermally-Driven Reaction of CO₂ at Macor*. *Plasma Chemistry and Plasma Processing*, 2018. **38**(2): p. 293-310.
5. Abdullah Al-Abduly, P.A.C., *An in situ and downstream study of non-thermal plasma chemistry in an air fed dielectric barrier discharge (DBD)*. *Plasma Sources Science and Technology*, 2015. **24**: p. 065006
6. Al-abduly, A.J., *Fundamental and applied studies of non-thermal plasma*, in *School of Chemical Engineering and Advanced Materials* 2016, Newcastle University
7. Frederick, H. and W. Van Zandt, *The Infra-Red Spectrum of Ketene*. *The Journal of Chemical Physics*, 1947. **15**(8): p. 552-559.
8. Ni, C.-K., E.A. Wade, M.V. Ashikhmin, and C.B. Moore, *Infrared Spectroscopy of Ketene by Two-Step Photodissociation*. *Journal of Molecular Spectroscopy*, 1996. **177**(2): p. 285-293.
9. Corey, S.J., M.M. Alexander, and I.K. Ralf, *Understanding the Kinetics and Dynamics of Radiation-induced Reaction Pathways in Carbon Monoxide Ice at 10 K*. *The Astrophysical Journal Supplement Series*, 2006. **163**(1): p. 184.

10. Alexandre, T. and L.B. Robert, *Carbon-Chain Oxides in Proton-Irradiated CO Ice Films*. The Astrophysical Journal, 2004. **612**(2): p. 1214.
11. Sicilia, D., S. Ioppolo, T. Vindigni, G.A. Baratta, and M.E. Palumbo, *Nitrogen oxides and carbon chain oxides formed after ion irradiation of CO:N₂ ice mixtures*. A&A, 2012. **543**: p. A155.
12. *British Chemical Abstracts*. Section A: General Physical and Inorganic Chemistry Nov. 1937: p. 575.
13. Taeschler, C., *Ketenes, Ketene Dimers, and Related Substances*, in *Kirk-Othmer Encyclopedia of Chemical Technology*. 2000, John Wiley & Sons, Inc.
14. *Ketene Market - Global Industry Analysis, Size, Share, Growth, Trends and Forecast 2014 - 2020*. 2017, Transparency Market Research Albany NY, United States.
15. Allen, A.D. and T.T. Tidwell, *Ketenes and Other Cumulenes as Reactive Intermediates*. Chemical Reviews, 2013. **113**(9): p. 7287-7342.
16. Boganov, S.E., S.V. Kudryashov, A.Y. Ryabov, A.I. Suslov, S.S. Rynin, M.P. Egorov, and O.M. Nefedov, *Matrix IR Study of Benzene Transformations in a Pulsed Glow Discharge in the Absence and the Presence of Oxygen*. Plasma Chemistry and Plasma Processing, 2014. **34**(6): p. 1345-1370.
17. Marko, F., M. Pavlo, M.M. Alexander, and I.K. Ralf, *Pentacarbon Dioxide (C₅O₂) Formation and Its Role as a Tracer of Solar System Evolution*. The Astrophysical Journal Letters, 2016. **818**(2): p. L30.
18. Vastel, C., C. Ceccarelli, B. Lefloch, and R. Bachiller, *The Origin of Complex Organic Molecules in Prestellar Cores*. The Astrophysical Journal Letters, 2014. **795**(1): p. L2.
19. Choi, K.N. and E.F. Barker, *Infrared Absorption Spectrum of Hydrogen Cyanide*. Physical Review, 1932. **42**(6): p. 777-785.
20. Herzberg, G., *Molecular spectra and molecular structure. Vol 1: Infrared and Raman spectra of diatomic molecules*. Vol. 2nd Edition. 2008, New York: Van Nostrand Reinhold.
21. Bolis, V., B. Fubini, E. Garrone, and C. Morterra, *Thermodynamic and vibrational characterization of CO adsorption on variously pretreated anatase*. Journal of the Chemical Society, Faraday Transactions 1: Physical Chemistry in Condensed Phases, 1989. **85**(6): p. 1383-1395.

22. Martini, L.M., G. Dilecce, G. Guella, A. Maranzana, G. Tonachini, and P. Tosi, *Oxidation of CH₄ by CO₂ in a dielectric barrier discharge*. Chemical Physics Letters, 2014. **593**(Supplement C): p. 55-60.
23. Henry Hess, B.J., *The Infrared Absorption Spectrum of Formaldehyde Vapor*. 1955, Ohio State University. p. 28-31.
24. Gratien, A., B. Picquet-Varrault, J. Orphal, E. Perraudin, J.F. Doussin, and J.M. Flaud, *Laboratory intercomparison of the formaldehyde absorption cross sections in the infrared (1660–1820 cm⁻¹) and ultraviolet (300–360 nm) spectral regions*. Journal of Geophysical Research: Atmospheres, 2007. **112**(D5).
25. Xu, S., J.C. Whitehead, and P.A. Martin, *CO₂ conversion in a non-thermal, barium titanate packed bed plasma reactor: The effect of dilution by Ar and N₂*. Chemical Engineering Journal, 2017. **327**(Supplement C): p. 764-773.
26. Ramakers, M., I. Michielsen, R. Aerts, V. Meynen, and A. Bogaerts, *Effect of Argon or Helium on the CO₂ Conversion in a Dielectric Barrier Discharge*. Plasma Processes and Polymers, 2015. **12**(8): p. 755-763.
27. Snoeckx, R., S. Heijkers, K. Van Wesenbeeck, S. Lenaerts, and A. Bogaerts, *CO₂ conversion in a dielectric barrier discharge plasma: N₂ in the mix as a helping hand or problematic impurity?* Energy & Environmental Science, 2016. **9**(3): p. 999-1011.
28. Danko, M., J. Orszagh, M. Ďurian, J. Kočišek, M. Daxner, S. Zöttl, J.B. Maljković, J. Fedor, P. Scheier, S. Denifl, and M. Š, *Electron impact excitation of methane: determination of appearance energies for dissociation products*. Journal of Physics B: Atomic, Molecular and Optical Physics, 2013. **46**(4): p. 045203.
29. Stano, M., S. Matejčík, J.D. Skalný, and T.D. Märk, *Electron impact ionization of CH₄ : ionization energies and temperature effects*. Journal of Physics B: Atomic, Molecular and Optical Physics, 2003. **36**(2): p. 261.
30. Velchev, I., W. Hogervorst, and W. Ubachs, *Precision VUV spectroscopy of Ar I at 105 nm*. Journal of Physics B: Atomic, Molecular and Optical Physics, 1999. **32**(17): p. L511.
31. Hagelaar, G.J.M. and L.C. Pitchford, *Solving the Boltzmann equation to obtain electron transport coefficients and rate coefficients for fluid models*. Plasma Sources Science and Technology, 2005. **14**(4): p. 722.
32. Quirico, E., G. Montagnac, V. Lees, P.F. McMillan, C. Szopa, G. Cernogora, J.-N. Rouzaud, P. Simon, J.-M. Bernard, P. Coll, N. Fray, R.D. Minard, F. Raulin, B.

- Reynard, and B. Schmitt, *New experimental constraints on the composition and structure of tholins*. *Icarus*, 2008. **198**(1): p. 218-231.
33. Imanaka, H., B.N. Khare, J.E. Elsila, E.L.O. Bakes, C.P. McKay, D.P. Cruikshank, S. Sugita, T. Matsui, and R.N. Zare, *Laboratory experiments of Titan tholin formed in cold plasma at various pressures: implications for nitrogen-containing polycyclic aromatic compounds in Titan haze*. *Icarus*, 2004. **168**(2): p. 344-366.
34. Horvath, G., N. Mason, L. Polachova, M. Zahoran, L. Moravský, and S. Matejcek, *Packed Bed DBD Discharge Experiments in Admixtures of N₂ and CH₄*. Vol. 30. 2010. 565-577.
35. Snoeckx, R., M. Setareh, R. Aerts, P. Simon, A. Maghari, and A. Bogaerts, *Influence of N₂ concentration in a CH₄/N₂ dielectric barrier discharge used for CH₄ conversion into H₂*. *International Journal of Hydrogen Energy*, 2013. **38**(36): p. 16098-16120.
36. Frost, D.C. and C.A. McDowell, *The Dissociation Energy of the Nitrogen Molecule*. *Proceedings of the Royal Society of London. Series A, Mathematical and Physical Sciences*, 1956. **236**(1205): p. 278-284.
37. Roeges, N.P.G., *A Guide to the Complete Interpretation of Infrared Spectral of Organic Structures*. 1994: Wiley.
38. Socrates, G., *Infrared and Raman Characteristic Group Frequencies: Tables and Charts*. 1980, Chichester: John Wiley and Sons.
39. Hollis, J.M., F.J. Lovas, J.R. Anthony, P.R. Jewell, V.V. Ilyushin, and I. Kleiner, *Detection of Acetamide (CH₃CONH₂): The Largest Interstellar Molecule with a Peptide Bond*. *The Astrophysical Journal Letters*, 2006. **643**(1): p. L25.
40. Rumbach, P., D.M. Bartels, R.M. Sankaran, and D.B. Go, *The solvation of electrons by an atmospheric-pressure plasma*. *Nature Communications*, 2015. **6**: p. 7248.
41. Maeda, Y., Y. Iizuka, and M. Kohyama, *Generation of Oxygen Vacancies at a Au/TiO₂ Perimeter Interface during CO Oxidation Detected by in Situ Electrical Conductance Measurement*. *Journal of the American Chemical Society*, 2013. **135**(2): p. 906-909.
42. Kim, H.-H., Y. Teramoto, N. Negishi, and A. Ogata, *A multidisciplinary approach to understand the interactions of nonthermal plasma and catalyst: A review*. *Catalysis Today*, 2015. **256**(Part 1): p. 13-22.
43. Hyatt, J.A. and P.W. Reynolds, *Ketene Cycloadditions*, in *Organic Reactions*. 2004, John Wiley & Sons, Inc.

44. Scarduelli, G., G. Guella, D. Ascenzi, and P. Tosi, *Synthesis of Liquid Organic Compounds from CH₄ and CO₂ in a Dielectric Barrier Discharge Operating at Atmospheric Pressure*. *Plasma Processes and Polymers*, 2011. **8**(1): p. 25-31.
45. De Bie, C., J. van Dijk, and A. Bogaerts, *The Dominant Pathways for the Conversion of Methane into Oxygenates and Syngas in an Atmospheric Pressure Dielectric Barrier Discharge*. *The Journal of Physical Chemistry C*, 2015. **119**(39): p. 22331-22350.
46. Havran, V., M.P. Duduković, and C.S. Lo, *Conversion of Methane and Carbon Dioxide to Higher Value Products*. *Industrial & Engineering Chemistry Research*, 2011. **50**(12): p. 7089-7100.

Chapter 5. In-situ FTIR studies of non-thermal plasma fed with CO₂, CH₄ and N₂ over SnO₂ and CeO₂ and a comparison to the analogous thermally-driven process.

5.1 Introduction

This chapter reports the application of in-situ reflectance FTIR spectroscopy to the study of the thermal and plasma driven reaction of CO₂, CH₄ and N₂ at two other potential catalysts: SnO₂ – coated Macor and CeO₂ – coated Macor. The data so obtained were compared to those obtained using uncoated Macor.

5.2 The plasma- driven reaction of CO₂, CH₄ and N₂ at Macor/Ti mesh with SnO₂

Figure 5.1 shows spectra collected using the plasma reflectance cell with a gas feed of CO₂, CH₄ and N₂ with SnO₂ 700 °C coated Macor/Ti mesh at a total flow rate of 30 cm³ min⁻¹ and 24 W input power. The spectrum collected immediately before the plasma was initiated was employed as the reference and sample spectra were collected every 2 minutes up to 20 minutes.

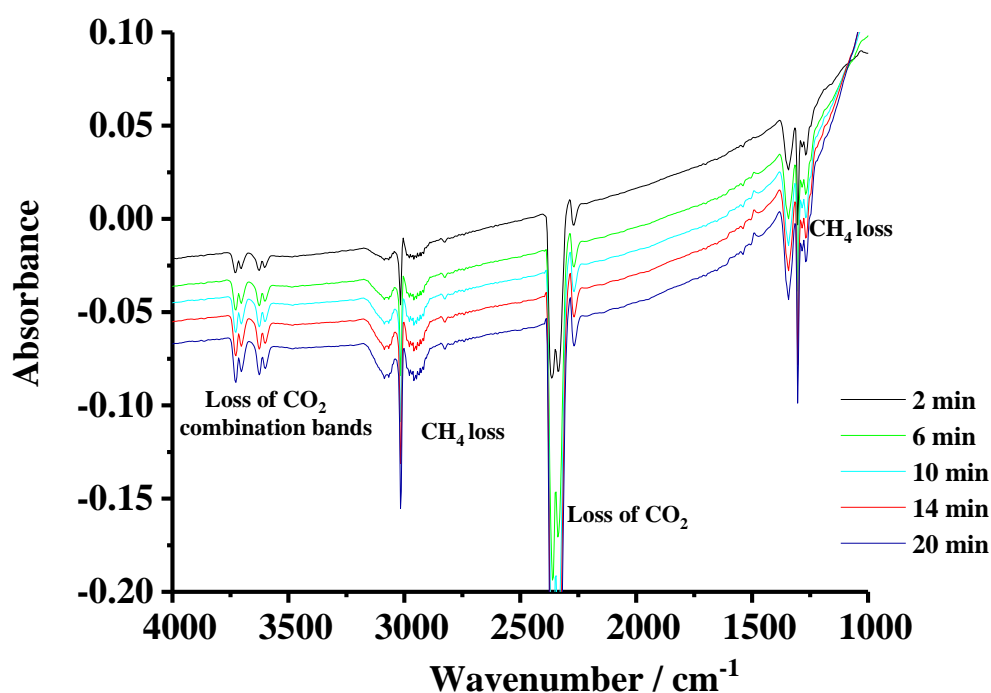


Figure 5.1. In situ FTIR spectra (8 cm⁻¹ resolution, 100 co-added and averaged scans, 60 seconds per scanset) collected at the times shown on the figure at an input power of 24 W. The gas composition was 10% CO₂ + 24% CH₄ + 66% N₂ and the reference spectrum was that taken with no plasma.

As can be seen in fig. 5.1, no other species being observed other than the loss of CO_2 and CH_4 . Bands due to CH_4^* are not apparent in fig. 5.1: however, a comparison of the figure with fig. 4.3(a) clearly shows the CH_4 Q bands in fig. 5.1 are much smaller than those in fig. 4.3(a), strongly suggesting that rotationally excited CH_4^* is indeed produced. The experiment in fig 5.1 was repeated at an input power of 20 W, with no additional bands being observed.

Figure 5.2 shows a plot of the absorbances of the CO_2 combination band at 3625 cm^{-1} and CH_4 band at 3085 cm^{-1} as a function of time, and fig. 5.3 shows the analogous plots normalized to their maximum values.

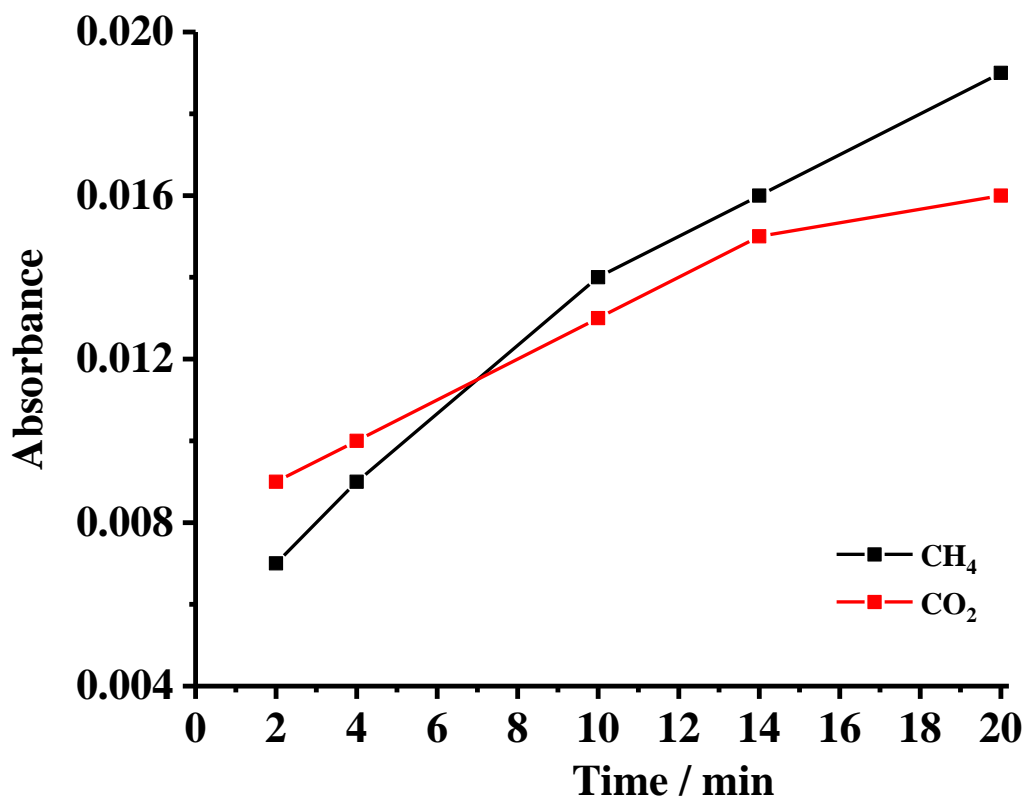


Figure 5.2. Plots of the absorbance of the CO_2 at 3625 cm^{-1} and CH_4 at 3085 cm^{-1} from the experiment in fig. 5.1 as a function of time.

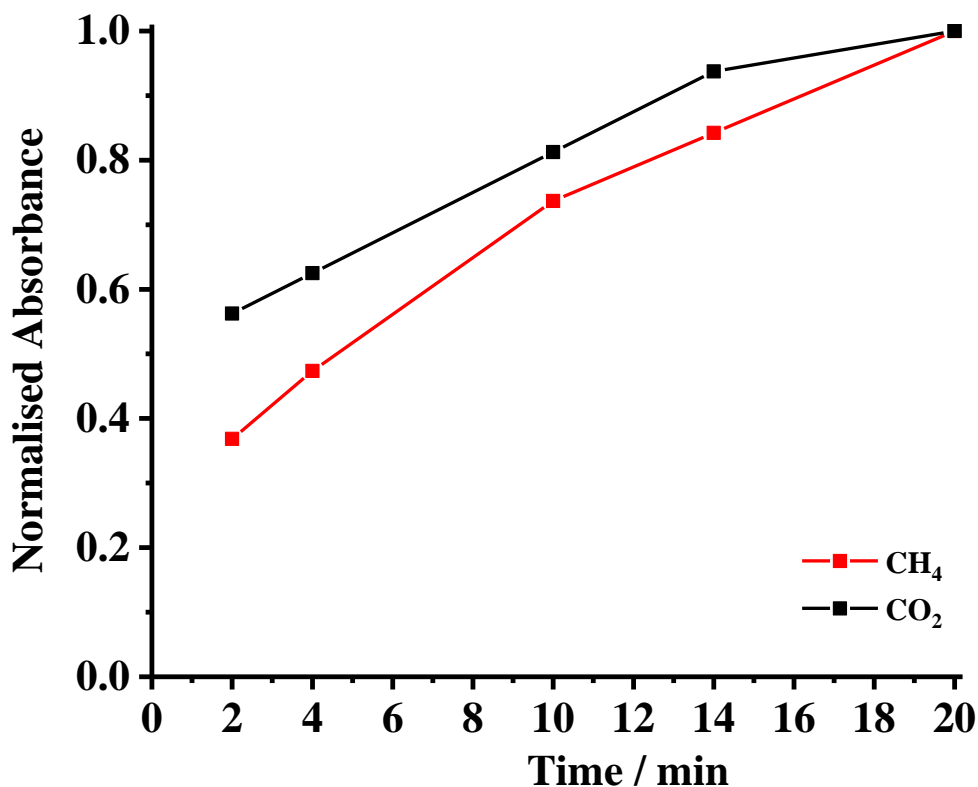


Figure 5.3. Plots of the normalised absorbance in figs. 5.2 as a function of time.

As can be seen in figs 5.2 and 5.3, the CH₄ and CO₂ loss features increase in intensity with time. The increasing loss of CO₂ and CH₄, and the reduced intensities of the CH₄ Q branches suggest that CH₄ (and CO₂) are simply being rotationally excited in the plasma. In the transmission cell, the CO absorbance at 2176 cm⁻¹ was typically 0.018 corresponding to 0.018/5.1 ~ 0.003 in the reflectance cell which would not be discernible in fig. 5.1 and hence CO may have been produced but the reduced pathlength of the cell resulted in an absorbance below the detection limit.

Figure 5.4 compares the spectrum collected after 20 minutes in fig. 5.1 to that collected in an analogous experiment using SnO₂ 400 °C coated Macor under the same experimental conditions.

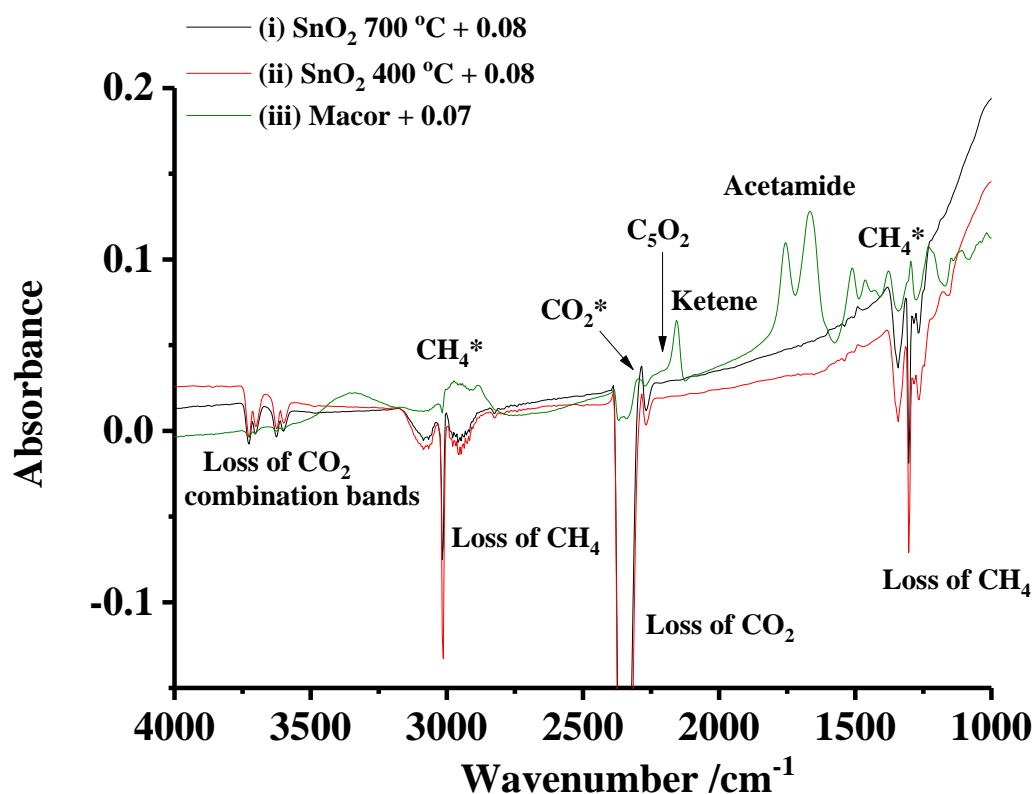
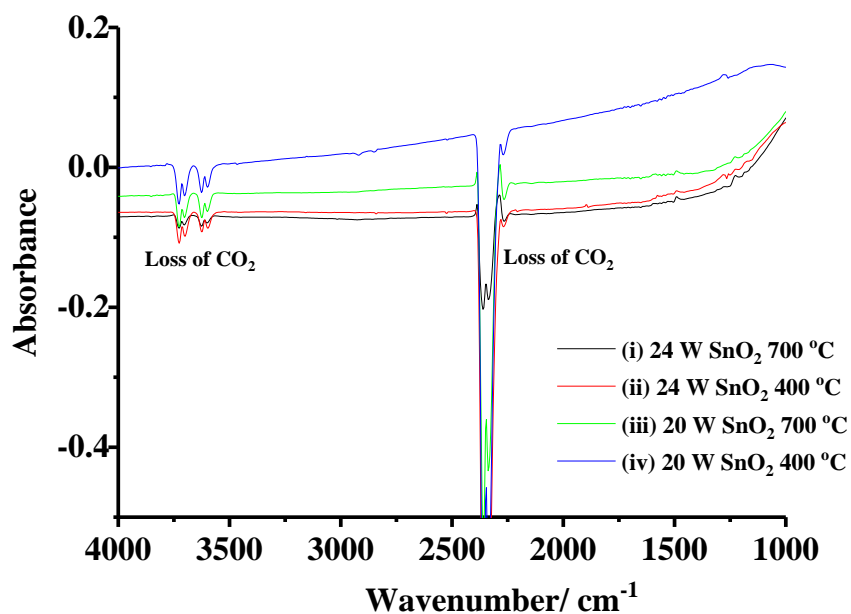
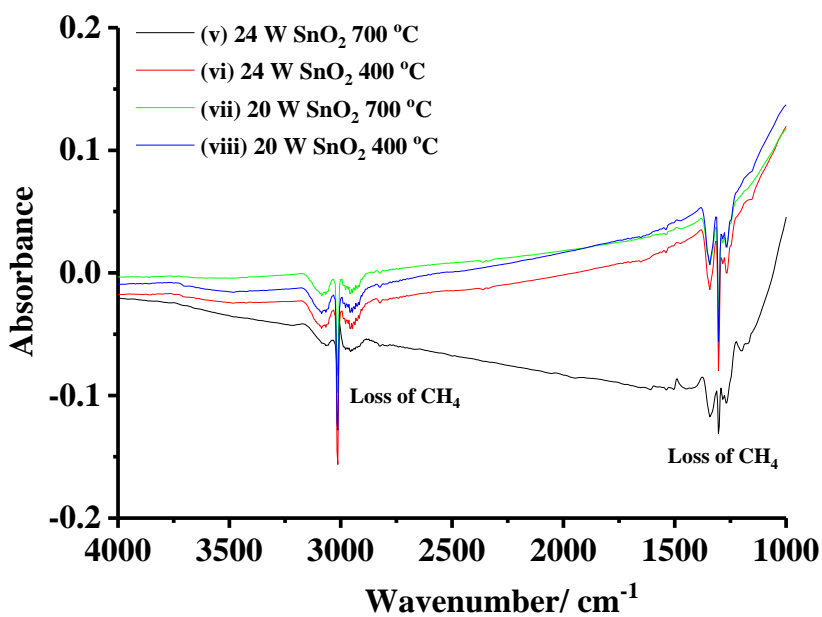


Figure 5.4. In-situ FTIR spectra (8 cm^{-1} resolution, 100 spectra per scan set, and 1 minute per spectrum) collected after 20 minutes operation with plasma as a function of dielectric/catalyst. The gas compositions were: (i) 9% CO_2 + 22% CH_4 + 69% N_2 , (ii) 9% CO_2 + 26% CH_4 + 65% N_2 and (iii) 3% CO_2 + 9% CH_4 + 88% N_2 at a total flow rate of $30\text{ cm}^3\text{ min}^{-1}$; the reference spectrum was collected under the same conditions but with no plasma. The spectra were moved up by the absorbances shown in order to facilitate comparison.

As can be seen, coating the Macor/Ti mesh with SnO_2 in the plasma reflectance cell resulted in no observed products, even at higher input power. Thus it is clear that Macor has a direct catalytic influence on the production of ketene, acetamide and C_5O_2 , as reported in Chapter 4. The experiment in fig 5.4 was repeated at input powers of 20 and 24 W for all blank experiments i.e $\text{N}_2 + \text{CO}_2$ and $\text{N}_2 + \text{CH}_4$, with no observed products as expected, see figs 5.5(a) and (b).



(a)



(b)

Figure 5.5. In-situ FTIR spectra (8 cm^{-1} resolution, 100 spectra per scan set, and 1 minute per spectrum) collected after 20 minutes operation with plasma as a function of SnO_2 calcination temperature. The gas compositions were: (i) 15.4% CO_2 + 84.6% N_2 , (ii) 26% CO_2 + 74% N_2 , (iii) 19.2% CO_2 + 80.8% N_2 , (iv) 23.8% CO_2 + 76.2% N_2 , (v) 26.5% CH_4 + 73.5% N_2 , (vi) 21.5% CH_4 + 78.5% N_2 , (vii) 23.6% CH_4 + 76.4% N_2 and (viii) 31.8% CH_4 + 68.2% N_2 at a total flow rate of $30\text{ cm}^3\text{ min}^{-1}$; the reference spectrum was collected under the same conditions but with no plasma.

5.3 The thermally driven reaction of CO₂, CH₄ and N₂ with SnO₂

Figure 5.6 shows spectra collected during an experiment in which 20 mg SnO₂ 400 °C powder + 80 mg spectroscopic KBr were heated from 25 to 600 °C in the 100% N₂ atmosphere. As can be seen from the figure, there is a clear decrease intensity of the bands at 1260, 1625, 3479, 3555 cm⁻¹ and the broad absorptions band between 2500 and 3500 cm⁻¹ corresponding to the loss of some form of water in agreement with the literature [1-3].

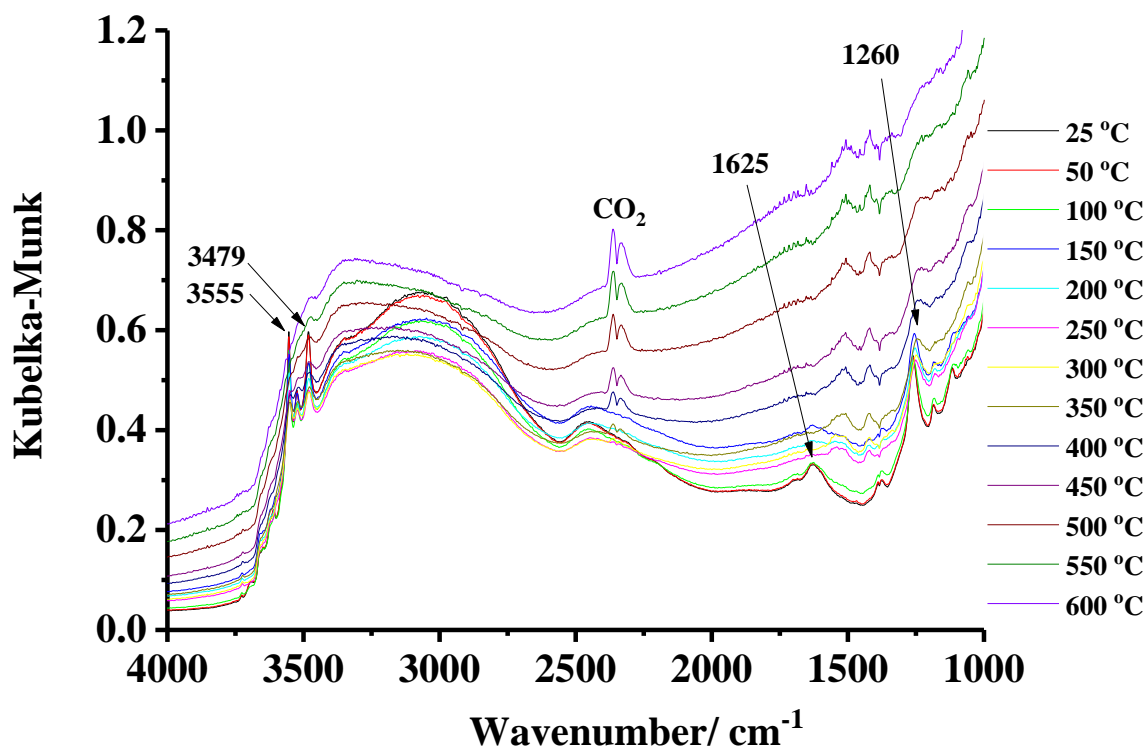


Figure 5.6. In-situ FTIR spectra (100 co-added scans and averaged scans at 8 cm⁻¹ resolution ca. 100 seconds per scanset) collected using the environmental chamber during an experiment in which a spectrum was collected at 25 °C and the temperature ramped at 5 °C min⁻¹ and further spectra taken at the temperatures shown. The sample was SnO₂ powder + KBr in the ratio 1:5 calcined at 400 °C in a static environment of 100% N₂. The reference spectrum was collected in 100% N₂ using pure KBr.

As can be seen from fig. 5.6, there is a gain feature at 2340 and 2360 cm⁻¹ attributed to CO₂ which may be due to impurities present in the sample compartment which react and release CO₂ at temperatures ≥ 300 °C. In order to highlight the changes in the spectra in fig. 5.6 up to

300 °C more clearly, the spectrum collected at 25 °C was subtracted from those taken at higher temperatures, and the results are presented in fig. 5.7.

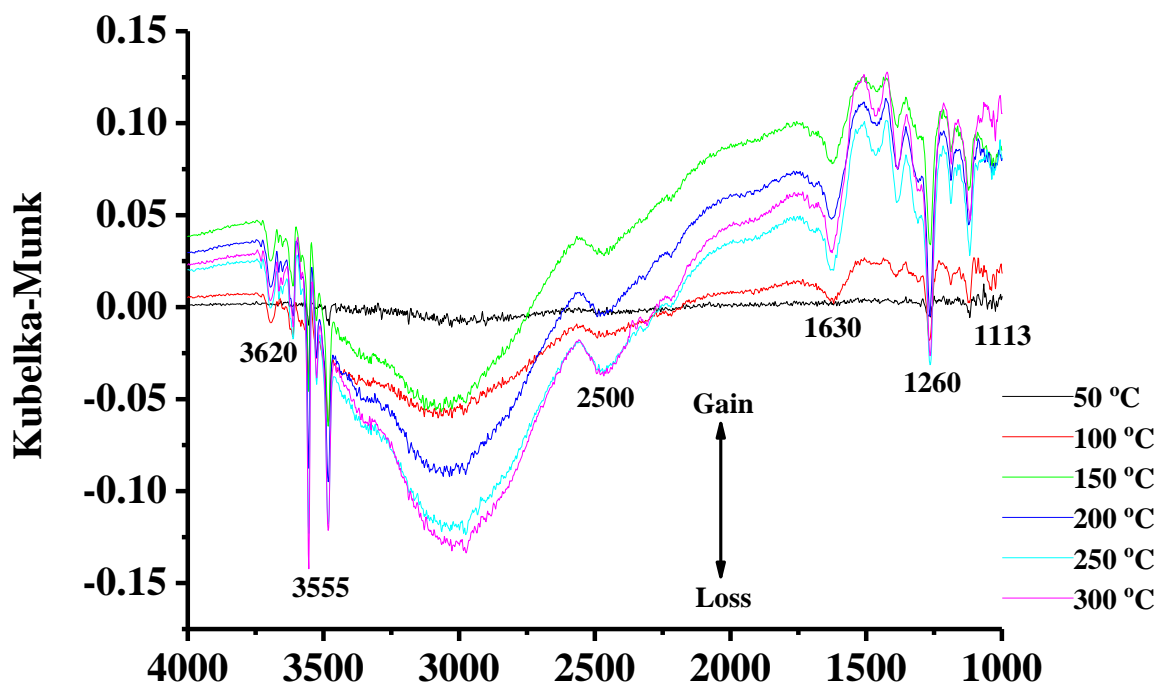


Figure 5.7. The spectra in fig. 5.6 collected up to 300 °C with the spectrum taken at 25 °C subtracted.

Al-abadleh and Grassian [4], Devlin and co-workers [5] and Maneelok in Newcastle [6] observed similar features to those in fig. 5.7. Sharp loss features at 3620 cm^{-1} and 3552 cm^{-1} may be attributed to the O-H stretches of isolated Sn-O-H groups; such features have been observed at 3610 cm^{-1} – 3640 cm^{-1} [7], 3467 cm^{-1} [8], 3620 cm^{-1} , 3595 cm^{-1} and 3560 cm^{-1} [6,9]. The broad loss feature with a maximum near 3000 cm^{-1} has been observed by other groups and has been attributed to the loss of the O-H stretches of hydrogen bonded Sn-OH groups [6,7]. A summary of the literature assignments of the various water features in fig. 5.7 is presented in table 5.1.

Band /cm ⁻¹	Assignment	Ref
1245	O-H	[1]
1630	H-O-H deformation	[5]
2500	O-H	[1]
3000	O-H	[7]
3555	O-H stretches Sn-O-H	[7]
3620	O-H	[9]

Table 5.1. A summary of the assignments in the literature of various features in the IR spectra in fig. 5.6 and 5.7.

Figure 5.8 shows a plots of the Kubelka-Munk function at 2000 cm⁻¹ from the spectra in fig. 5.6. As can be seen, the number of free electrons is varying as the temperatures is increased, but not in a homologous fashion and there are three clear regions: (I) 25 – 150 °C, (II) 150 – 250 °C and (III) 250 – 600 °C.

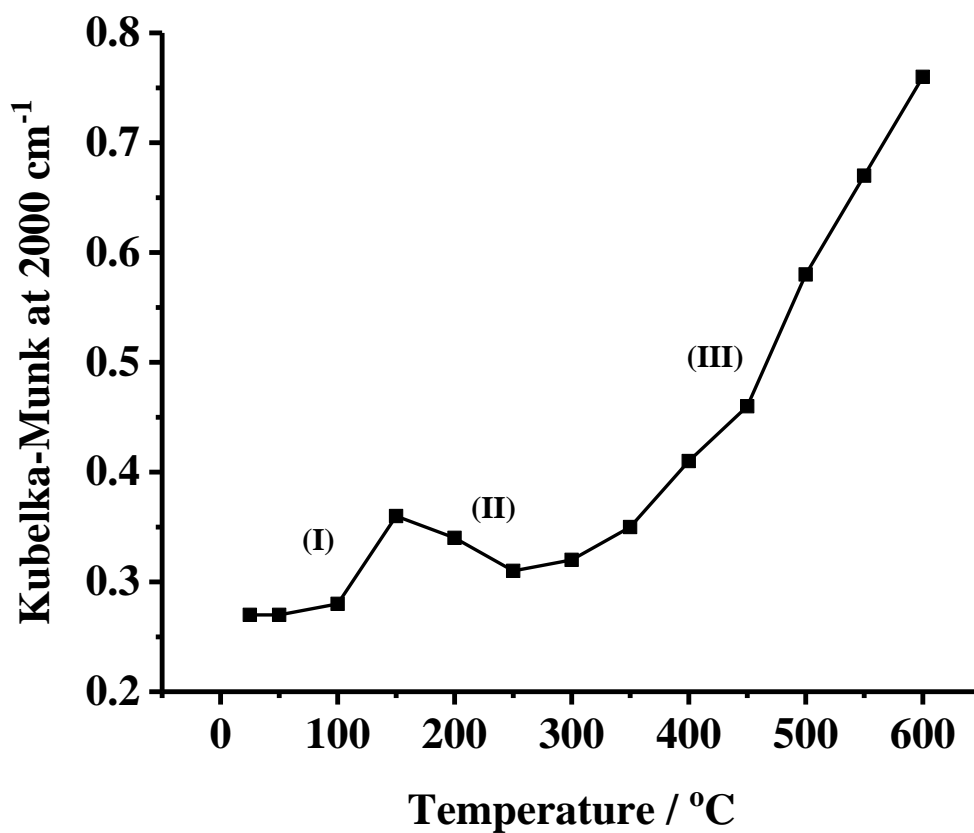


Figure 5.8. Plot of the Kubelka-Munk function with temperature at 2000 cm⁻¹ from the spectra in fig 5.6.

In region (I), there is very little change in the electronic absorption followed by a fall in region (II) and a steep increase in region (III). At temperatures $> 250\text{ }^{\circ}\text{C}$, the water and other surface features on the SnO_2 are lost as the free electron absorption increases suggesting that the increasing electronic conductivity of the SnO_2 may be causing an increasing fraction of the refracted IR light to be fully absorbed with the consequent loss of information on surface species, in agreement with the work of Maneelok in Newcastle [6].

Figure 5.9 shows spectra collected during an experiment in which a SnO_2 $700\text{ }^{\circ}\text{C}$ powder sample was heated from 25 to $600\text{ }^{\circ}\text{C}$ in $20\% \text{CO}_2 + 8\% \text{CH}_4 + 72\% \text{N}_2$ atmosphere using KBr as the reference spectrum.

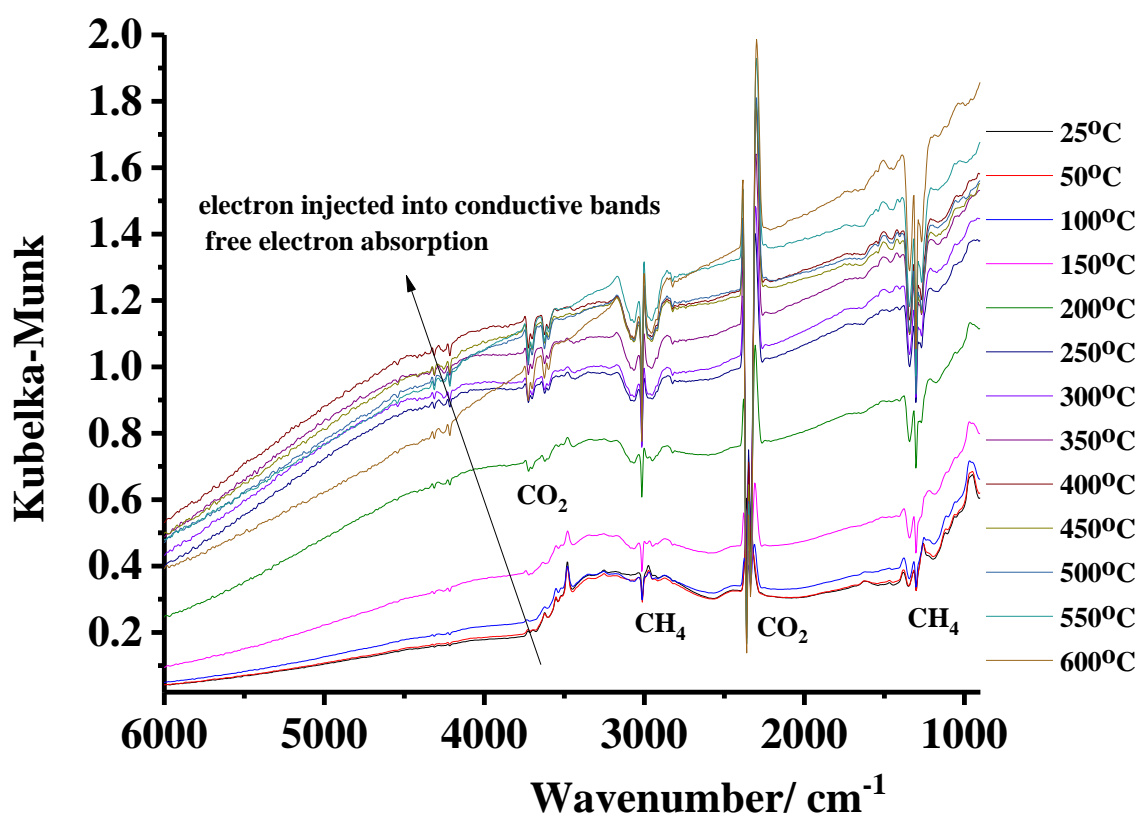
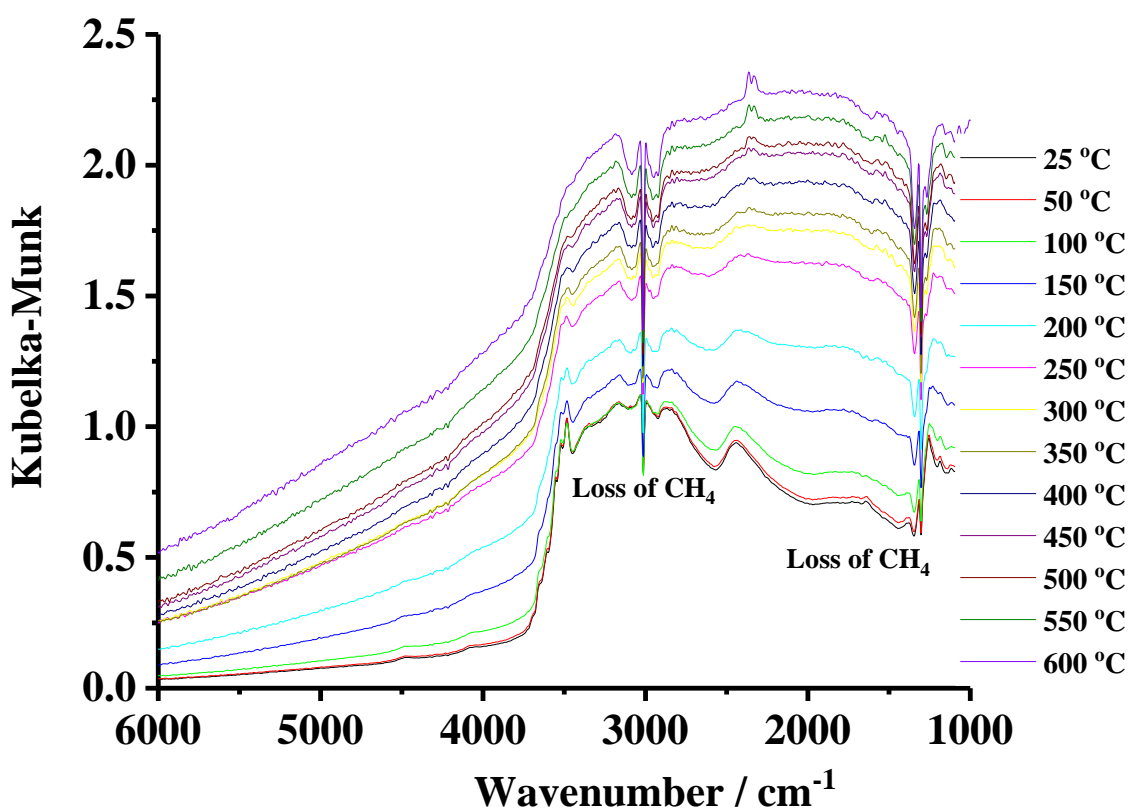
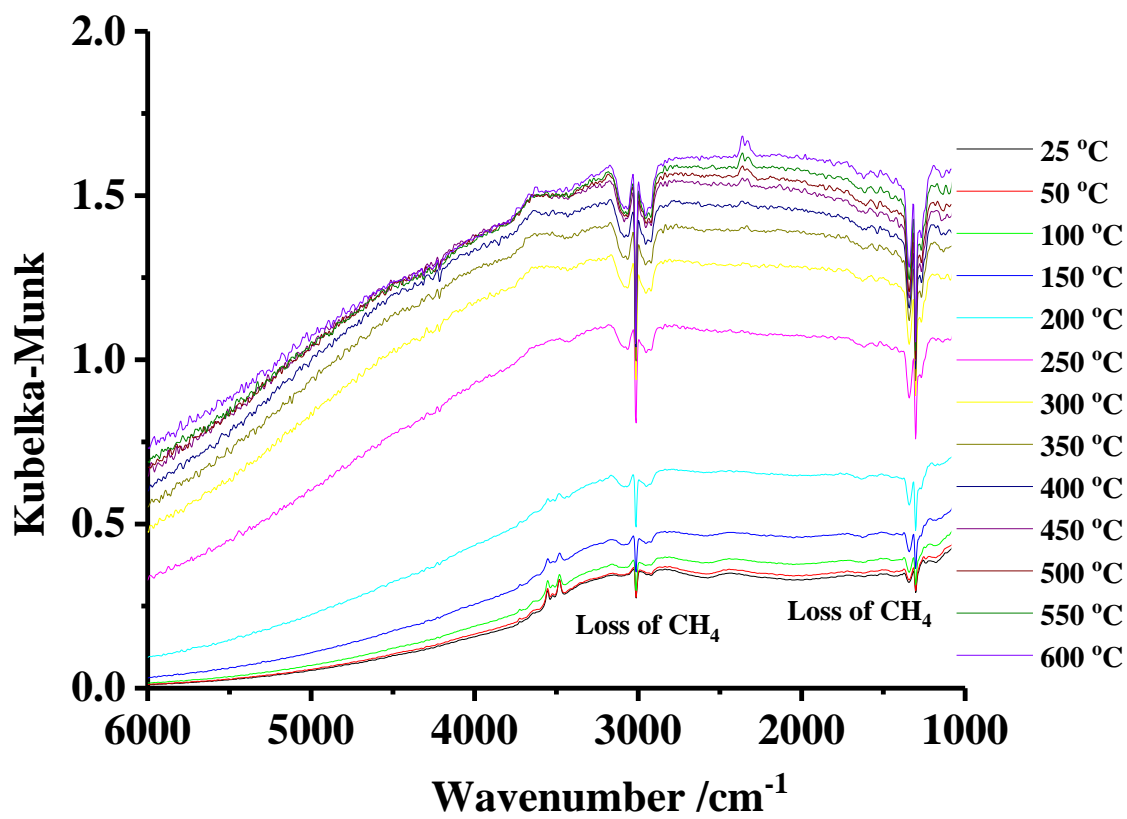


Figure 5.9. In-situ FTIR spectra (100 co-added scans and averaged scans at 8 cm^{-1} resolution ca. 100 seconds per scanset) collected using the environmental chamber during an experiment in which a spectrum was collected at $25\text{ }^{\circ}\text{C}$ and the temperature ramped at $5\text{ }^{\circ}\text{C min}^{-1}$ and further spectra taken at the temperatures shown. The sample was SnO_2 powder + KBr in the ratio 1:5 calcined at $400\text{ }^{\circ}\text{C}$ in a static environment of $\text{CH}_4 + \text{CO}_2 + \text{N}_2$. The reference spectrum was collected in $20\% \text{CO}_2 + 8\% \text{CH}_4 + 72\% \text{N}_2$ using pure KBr.

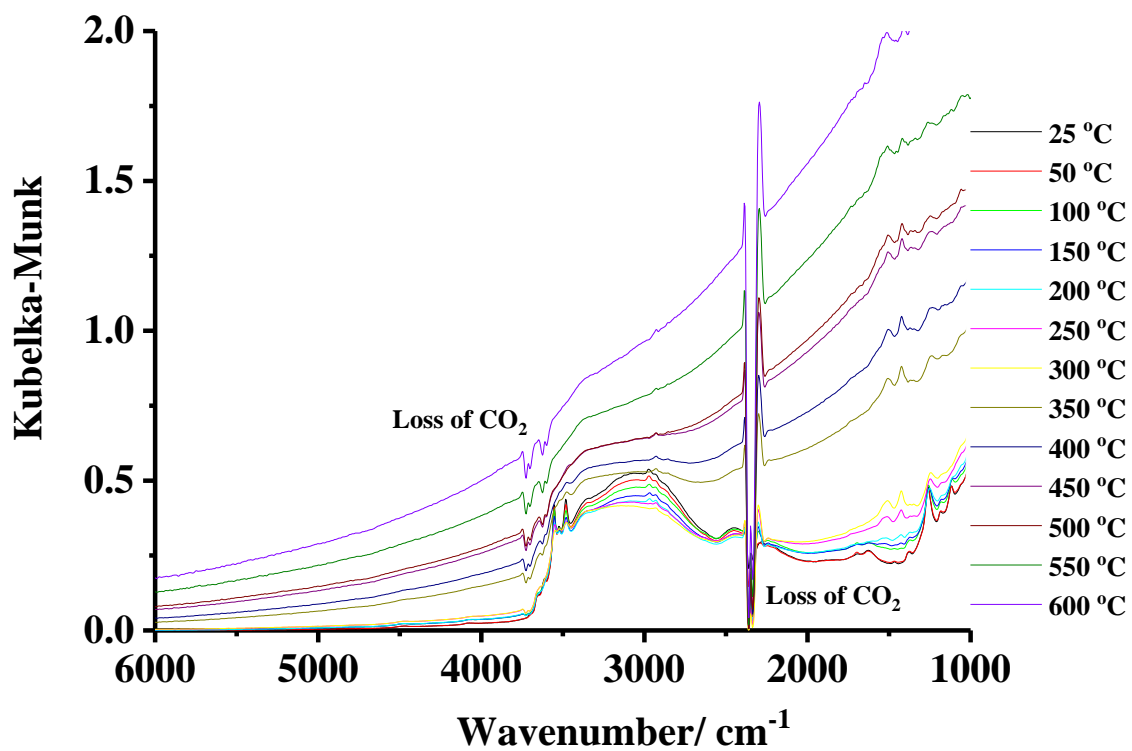
As can be seen from the figure, there are a number of bands superimposed upon a curving baseline and there is a clear decrease intensity in Kubelka-Munk function in the band at 2500 cm^{-1} and 3500 cm^{-1} corresponding to the loss of some form of water [1-3] as discussed previously. There is also clear loss of both CO_2 and CH_4 with no additional product bands being observed. At temperatures $> 250\text{ }^\circ\text{C}$, the CO_2 loss at $3500\text{--}3700\text{ cm}^{-1}$ became clearer as the overlying broad O-H absorption of water started to disappear. The experiment in fig 5.9 was repeated with all blank experiments (i.e $\text{N}_2 + \text{CO}_2$ and $\text{N}_2 + \text{CH}_4$) for SnO_2 $400\text{ }^\circ\text{C}$ and $700\text{ }^\circ\text{C}$ respectively, with no features attributable to products being observed, see figs 5.10 (a)-(d).



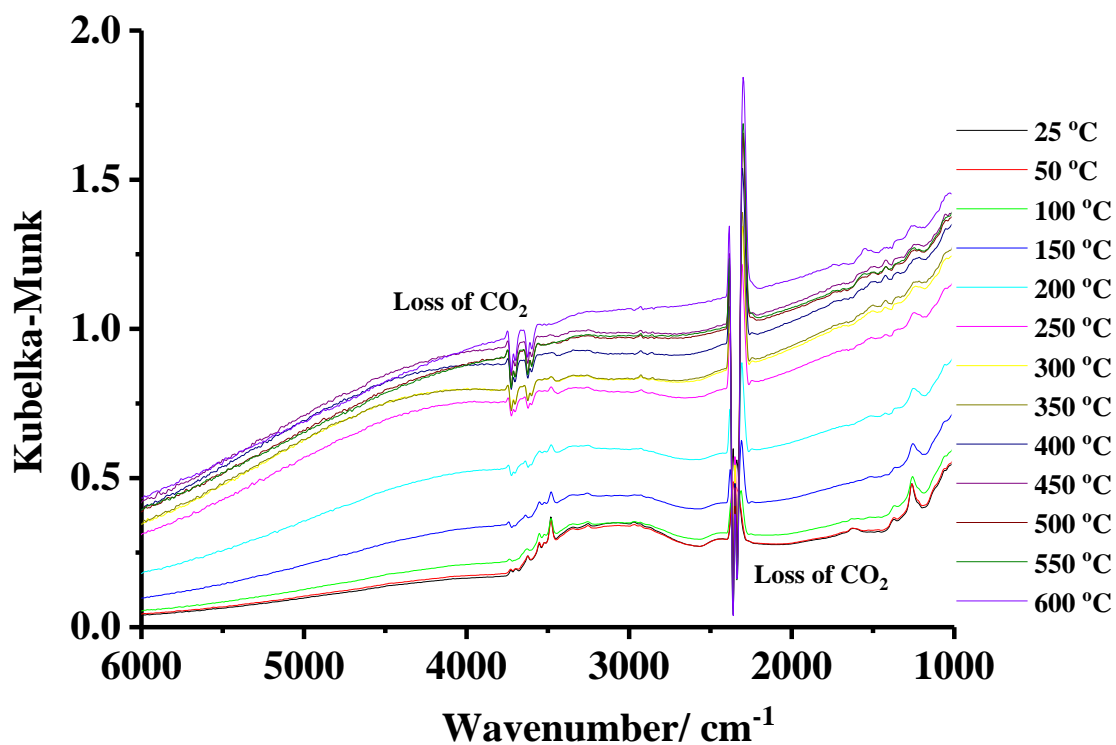
(a)



(b)



(c)



(d)

Figure 5.10. In-situ FTIR spectra (100 co-added scans and averaged scans at 8 cm^{-1} resolution ca. 100 seconds per scanset) collected using the environmental chamber during an experiment in which a spectrum was collected at $25\text{ }^{\circ}\text{C}$ and the temperature ramped at $5\text{ }^{\circ}\text{C min}^{-1}$ and further spectra taken at the temperatures shown. The sample was SnO_2 powder + KBr in the ratio 1:5 calcined at: (a) SnO_2 $400\text{ }^{\circ}\text{C}$ in a static environment of $65\%\text{ N}_2 + 35\%\text{ CH}_4$, (b) SnO_2 $700\text{ }^{\circ}\text{C}$ in a static environment of $60\%\text{ N}_2 + 40\%\text{ CH}_4$, (c) SnO_2 $400\text{ }^{\circ}\text{C}$ in a static environment of $86\%\text{ N}_2 + 14\%\text{ CO}_2$ and (d) SnO_2 $700\text{ }^{\circ}\text{C}$ in a static environment of $80\%\text{ N}_2 + 20\%\text{ CO}_2$.

As can be seen from fig. 5.10, it is clear that N_2 with CO_2 and/or CH_4 do not react at SnO_2 under thermal activation.

5.4 The plasma driven reaction of CO₂, CH₄ and N₂ at Macor/Ti mesh with CeO₂

Figure 5.11 shows spectra collected using the plasma reflectance cell with a gas feed of N₂, CO₂ and CH₄ at a total flow rate of 30 cm³ min⁻¹ and 20 W input power. The reference spectrum was collected under the same conditions but with no plasma and fig. 5.12 compares the spectrum collected after 20 minutes in fig. 5.11 to that collected in analogous experiment using Macor after the same time and under the same experimental conditions.

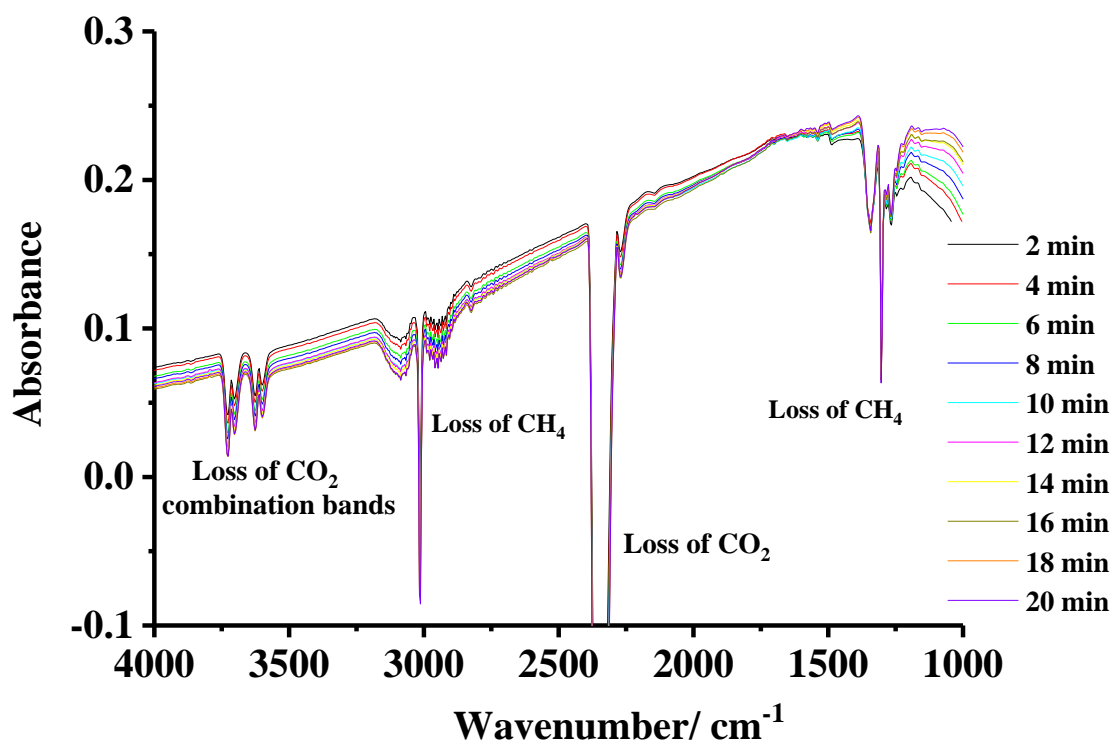


Figure 5.11. In situ FTIR spectra (8cm^{-1} resolution, 100 co-added and averaged scans, 60 seconds per scanset) collected at the times shown on the figure at an input power of 20 W. The gas composition was 20.9% CO₂ + 35.8% CH₄ + 43.3% N₂ and the reference spectrum was that taken with no plasma.

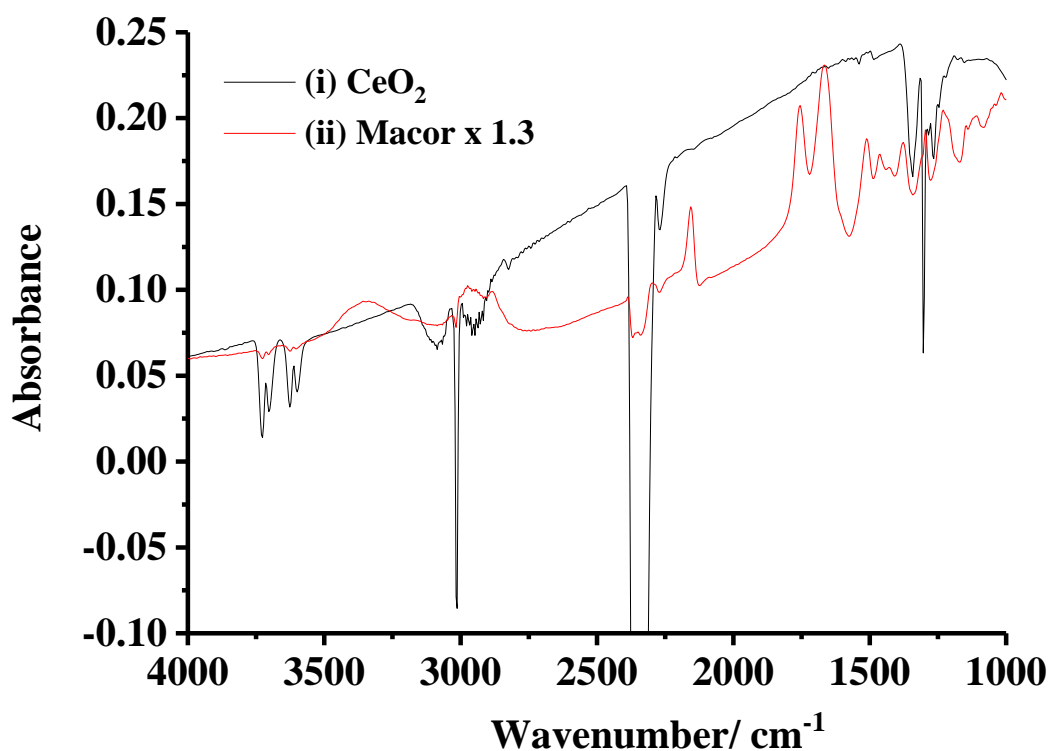
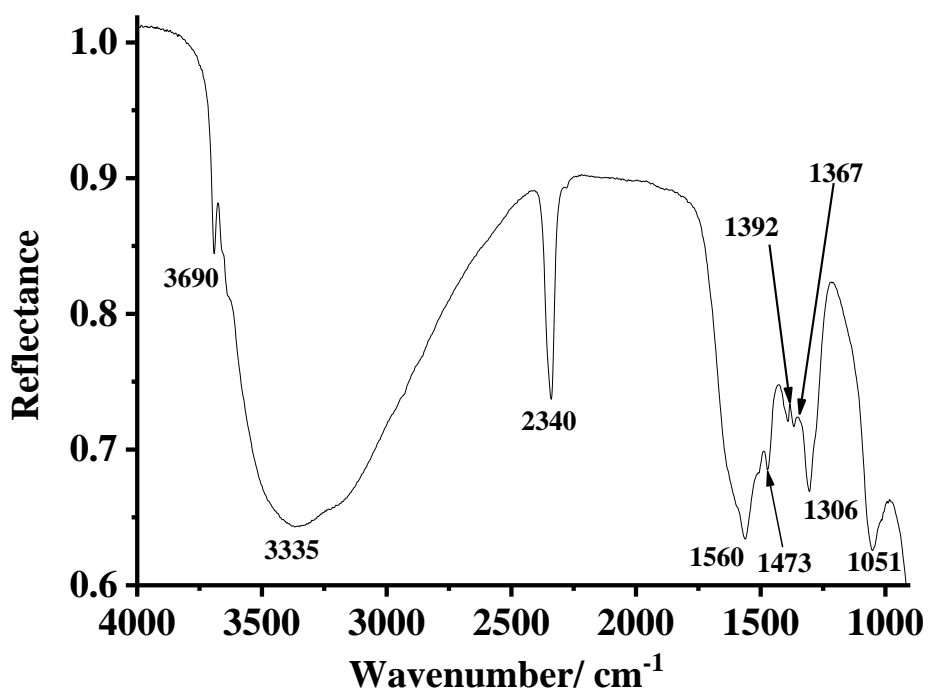


Figure 5.12. In-situ FTIR spectra (8 cm^{-1} resolution, 100 spectra per scan set, and 1 minute per spectrum) collected after 20 minutes operation with plasma as a function of dielectric/catalyst. The gas compositions are: (i) 20.9% CO_2 + 35.8% CH_4 + 43.3% N_2 and (ii) 3 % CO_2 + 9 % CH_4 + 88% N_2 as at a total flow rate of $30\text{ cm}^3\text{ min}^{-1}$ and at an input power of 20 W; the reference spectrum was collected under the same conditions but with no plasma. The spectra of Macor were multiplied by the factor shown in order to facilitate comparison.

From figs. 5.11 and 5.12, it can be seen that the only features observed were due to the loss of CO_2 and CH_4 , and these bands increased in intensity with time. It should be noted that, no conversion of N_2 , CO_2 , and CH_4 was observed at SnO_2 either in plasma reflectance cell, even at higher input power of 24 W. The differences between the data obtained with SnO_2 and CeO_2 on the one hand, and Macor on the other is a key observation, as it shows that these materials exhibited no catalytic activity and hence inhibited that of Macor when employed as coating.

5.5 Blank thermal experiments using CeO₂

Figure 5.13(a) shows the spectra collected at 25 °C during an experiment in which temperature the sample (20 mg of CeO₂ was mixed with 80 mg of spectroscopic grade KBr) was ramped from 25 °C to 600 °C, and sample spectra (S_S) were recorded in reflectance mode collected at regular intervals (referenced to pure KBr, S_R) in a static N₂ atmosphere. Figure 5.13(b) shows all the spectra from the experiment and fig. 5.13(c) compares the spectra collected at 25 °C and 200 °C in fig. 5.13(b) over the spectral region in which the physisorbed CO₂ occurs and both spectra were offset to R_T = 1 at 2340 cm⁻¹.



(a)

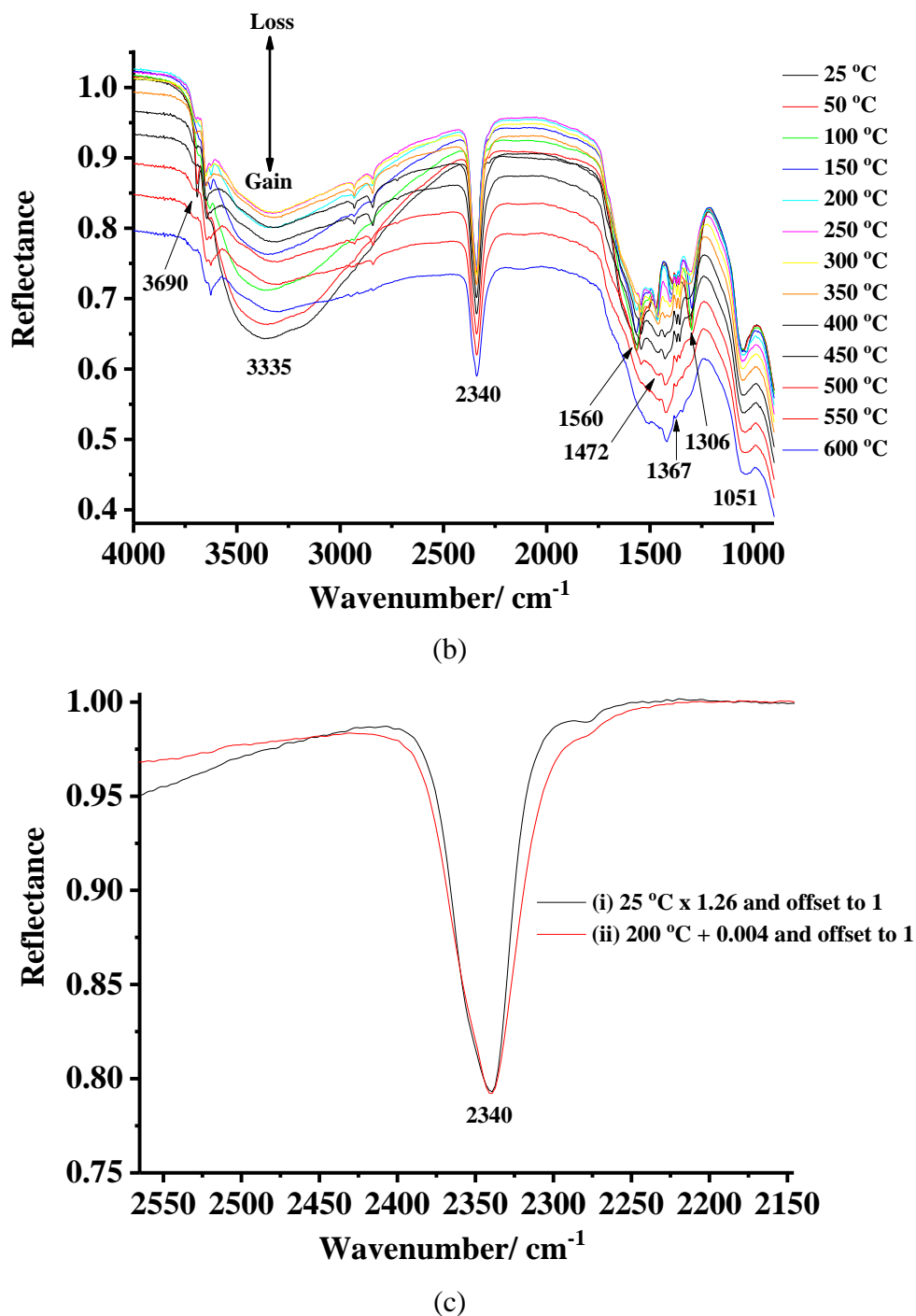


Figure 5.13. Spectra (4 cm^{-1} resolution, 100 co-added and averaged scans, 120 s per scanset) collected as a function of temperature during an experiment in which the temperature of 20 mg CeO_2 + 80 mg KBr was ramped from 25 °C to 600 °C in a static N_2 atmosphere. The spectrum collected at 25 °C using KBr in the same atmosphere was employed as the reference. (a) the spectrum taken at 25 °C, (b) all spectra collected during the experiment and (c) the spectra taken at (i) 25 °C and (ii) 200 °C showing the CO_2 asymmetric stretch region. The spectra were moved up by the absorbances shown in order to facilitate comparison.

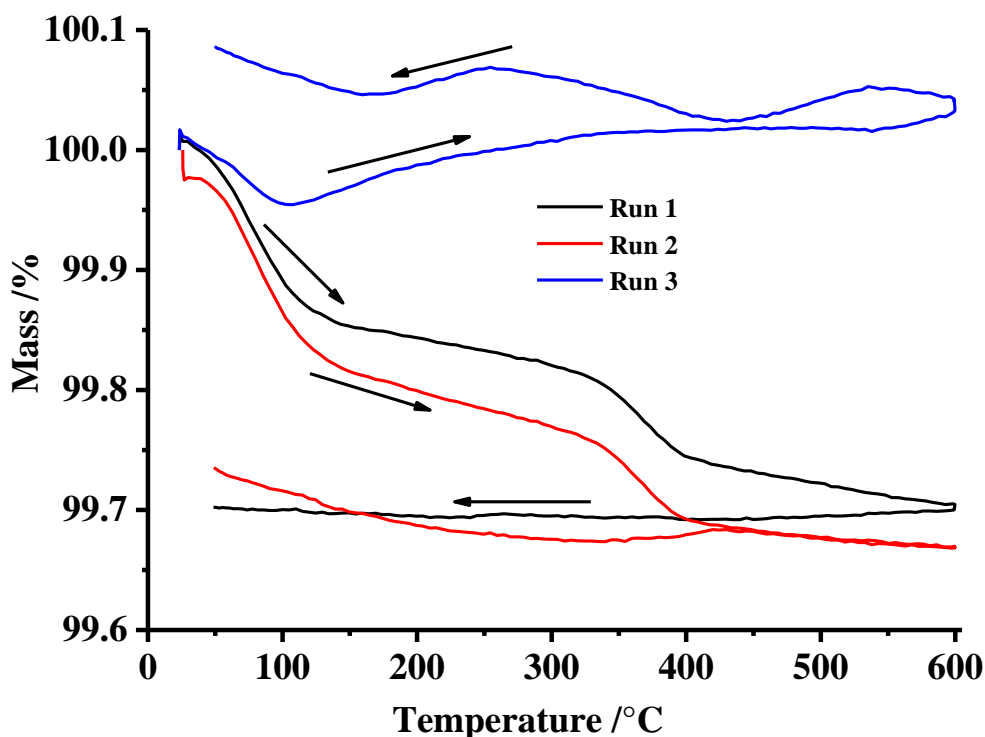
As can be seen from the figs. 5.13, the spectra are dominated by strong absorptions due to hydrogen-bonded Ce-OH groups in between 2250 – 4000 cm^{-1} [11] and various forms of adsorbed carbonate at 900 – 1750 cm^{-1} [12-15]. The sharp feature at 3690 cm^{-1} in fig. 5.13(b) may be attributed to isolated OH [11], i.e. Ce-OH groups not hydrogen bonded and the band at 2340 cm^{-1} may be attributed to the asymmetric stretch mode of physisorbed CO_2 [16,17]. Interestingly, the band at 2340 cm^{-1} was present even up to 600 °C and may indicate that the CO_2 was present in interstitial voids in the CeO_2 [18]. Figure 5.13(c) compares the spectra collected at 25 °C and 200 °C in fig. 5.13(b) over the spectral region in which the physisorbed CO_2 occurs. As can be seen, the asymmetric shape of the CO_2 bands suggests the CO_2 is physisorbed on a number of different sites [19]: the band maxima of the two features were the same and, as expected, the band at 200°C was broader than that at 25 °C suggesting some rotational excitation. The small changes in band shape on heating may suggest some redistribution among surface sites.

In general, the adsorption of CO_2 on CeO_2 has been well-studied, and a summary of the assignments of various features observed in the IR studies is presented in table 5.2. In terms of the temperature at which the various forms of carbonate desorb or convert, Slostowski et. al. [19] divides the adsorbates into weakly adsorbed (hydrogen carbonate and bridged) which can be removed at room temperature by flowing nitrogen over the sample and strongly adsorbed (bidentate, monodentate and polydentate) which require a temperature of up to 500 °C to remove them from the surface. Yoshikawa and co-workers [20] present a somewhat detailed and different picture: with a temperature of 200 °C required for desorption of bicarbonate, 300 °C for monodentate and bidentate carbonate and 450 °C for the polydentate form. Intuitively, however, it may be expected that those forms of carbonate with multiple metal-oxygen bonds (eg. bridged, bidentate and polydentate) would be more strongly bonded to the surface than monodentate carbonate and bicarbonate.

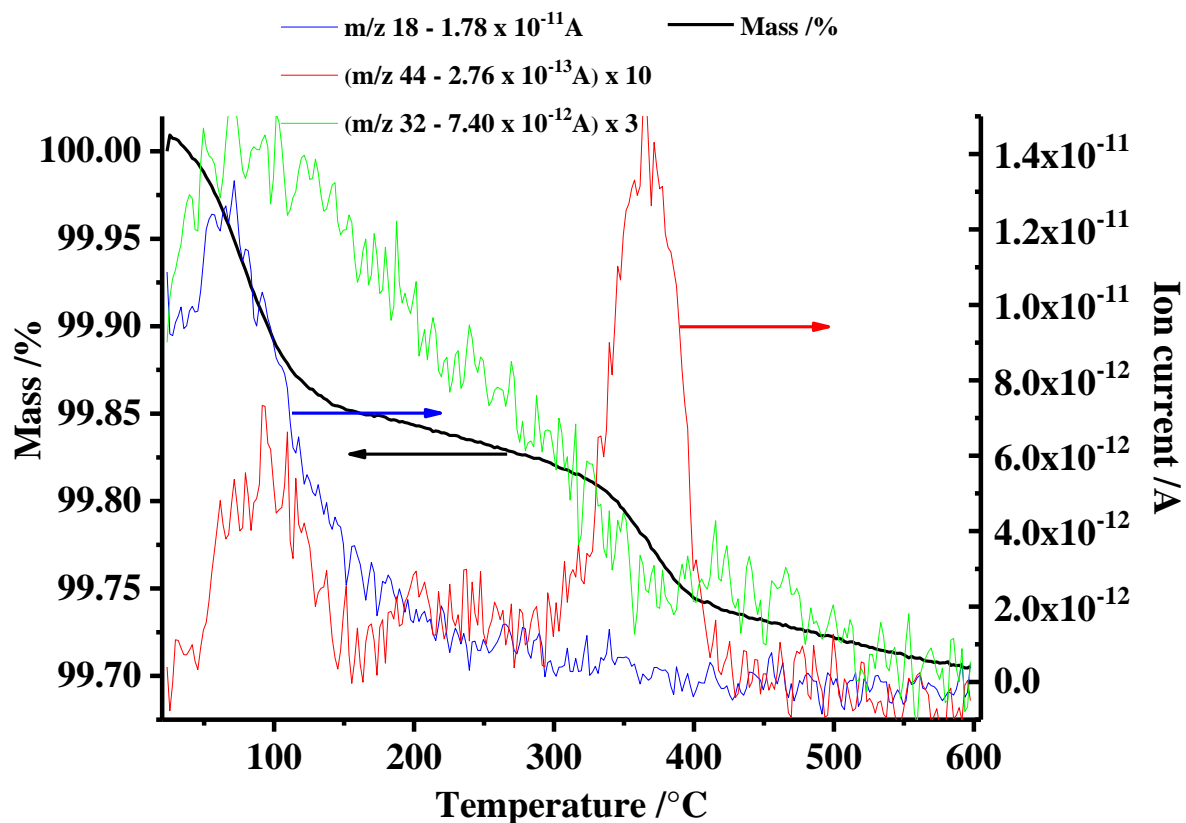
Adsorbed species		References				
		[15]	[12]	[14]	[19]	
Bicarbonate		1600 1398 1215	I 3617 1599 1413 1218 1025 823	II 3617 1613 1391 1218 1045 823	1404 1217	1670 – 1695 1310 – 1338 650 – 970
Monodentate		1465 1353	1504 1351	1507		1454 1348 1062 854
Bridged		1651 1242	1736 1135			1728 1396 1219 1132
Bidentate		1580 1292	1567 1289 1014 856	1570 1287 1011 856		1562 1286 1028 854
Polydentate		- -	1462 1353 1066 854	1476 1367		

Table 5.2. Summary of the assignments of various features observed in the IR studies of CO₂ on CeO₂.

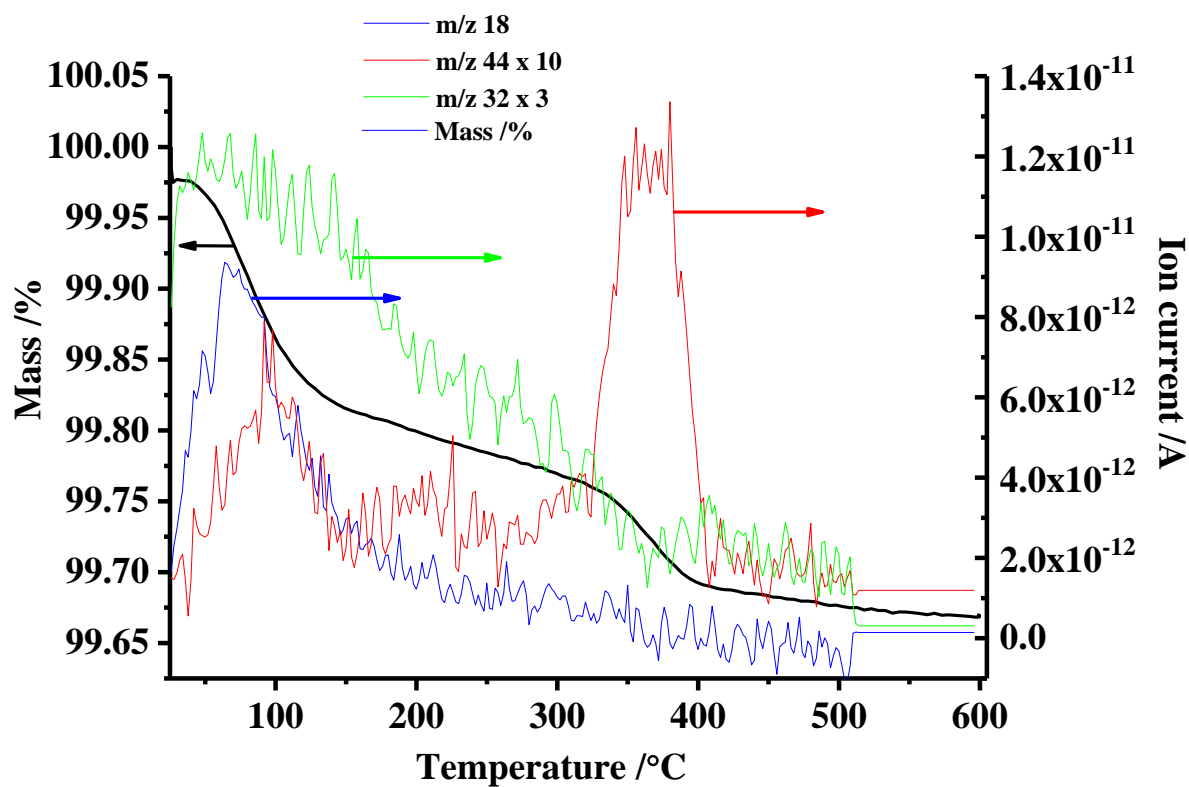
Figure 5.14(a) shows a TGA experiment in which a sample of CeO_2 was heated in N_2 to 600°C , allowed to cool and the change in its mass recorded as a function of temperature and repeated a further two times. Figure 5.14(b) shows the $m/z = 18, 32$ and 44 responses recorded during the first heating of the sample along with the change in mass (note scaling factors). As can be seen from the figures, the sample loses mass over the full temperature range, but most particularly between 25 and 150°C and 300 and 400°C ; there is also a steady evolution of O_2 over the full range, and of water up to ca. 400°C . CO_2 is evolved in two distinct regions, $75 - 150^\circ\text{C}$ and $300 - 400^\circ\text{C}$, the latter in broad agreement with the postulated existence of adsorbed carbonaceous species having various thermal stabilities. Figure 5.14(c) shows the mass change and the $m/z = 18, 32$ and 44 responses recorded during the second heating of the sample (run 2) in fig. 5.14(a): the responses are very similar to those observed during run 1, suggesting that, on being stored overnight in air, CO_2 and water re-adsorbed onto the sample surface. Figure 5.14(d) shows the mass change and the $m/z = 18, 32$ and 44 responses recorded during run 3: as may be seen from the figure, whilst there is no evolution of O_2 or CO_2 , dehydration and/or dehydroxylation of the sample still took place [21], although with about 60% the amount of evolved H_2O . This is associated with a very small mass loss of 0.05% compared with 0.15% for the previous two runs.



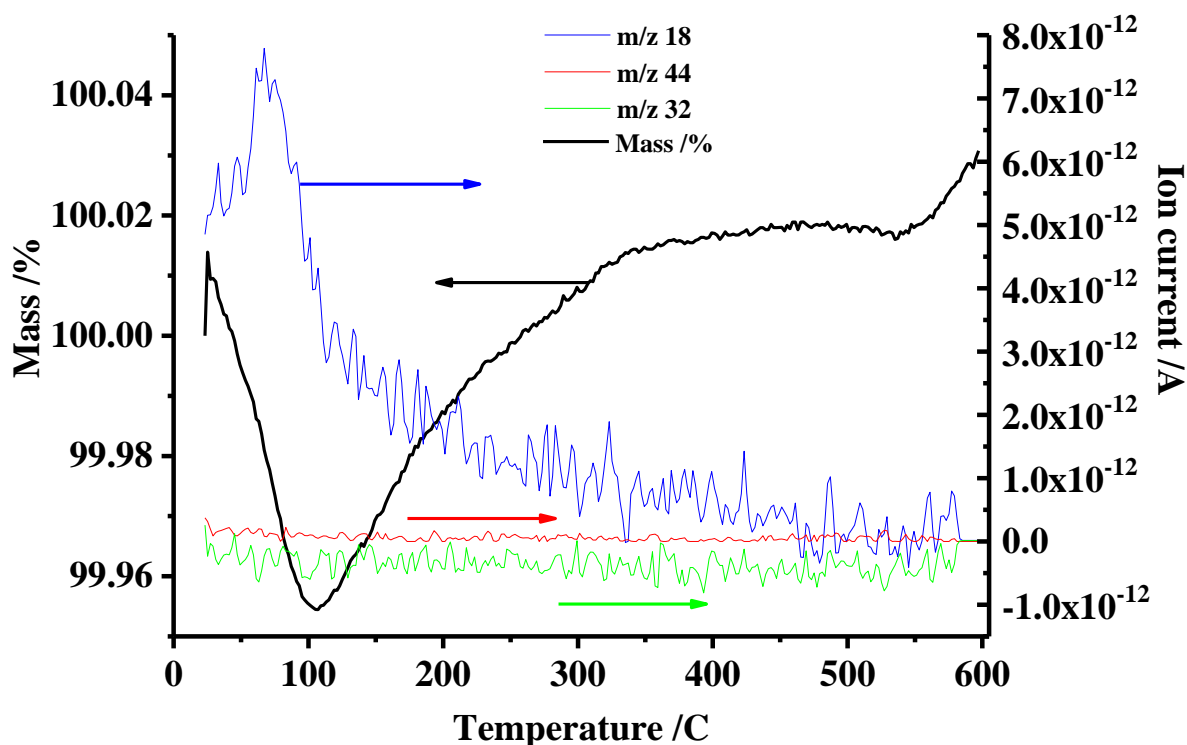
(a)



(b)



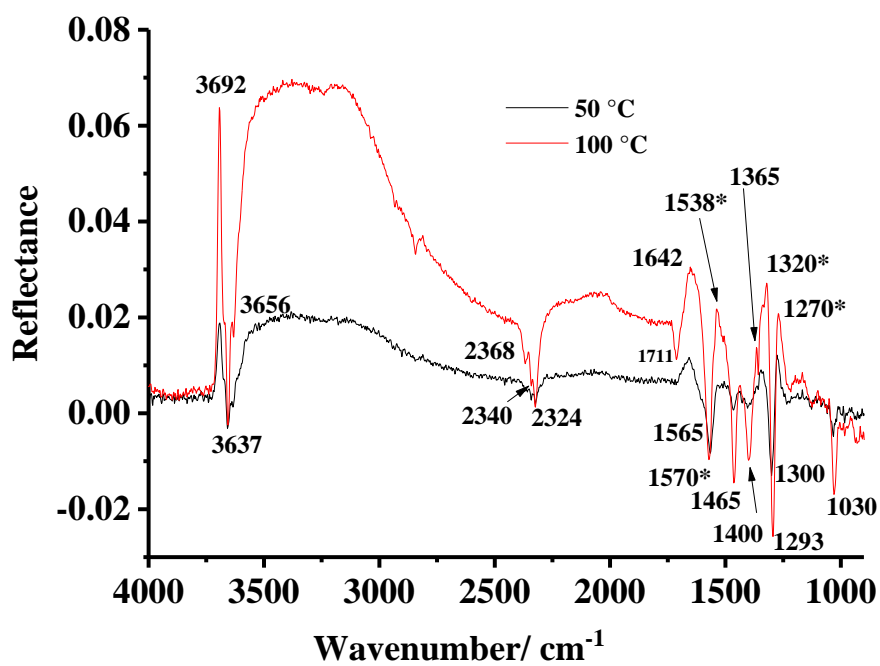
(c)



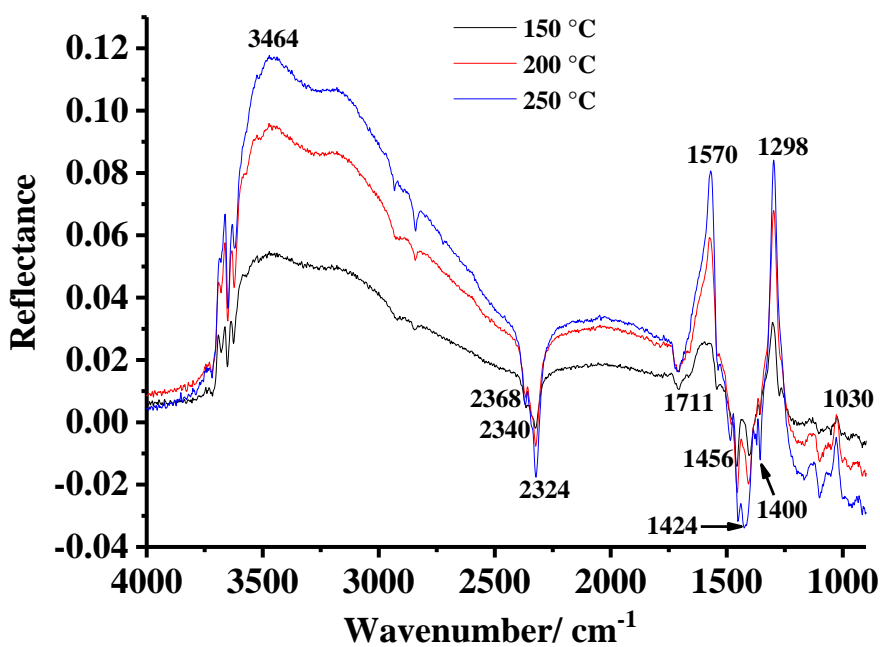
(d)

Figure 5.14. (a) The thermogravimetric response of 55.5 mg of CeO_2 , heated in $40 \text{ cm}^3 \text{ min}^{-1}$ flowing N_2 at heating rate of $5 \text{ }^\circ\text{C min}^{-1}$ from room temperature to $600 \text{ }^\circ\text{C}$ (Run 1). The sample was held at $600 \text{ }^\circ\text{C}$ for 10 minutes and then cooled at $5 \text{ }^\circ\text{C min}^{-1}$ to room temperature. (b) & (c) The $m/z = 18, 32$ and 44 responses recorded during the first and second heating cycles (Runs 1 and 2, respectively) of the sample in (a): the $m/z = 32$ responses are enhanced by a factor of 3 and the $m/z = 44$ responses by a factor of 10. (d) The $m/z = 18, 32$ and 44 responses recorded during the third heating of the sample in (a), Run 3. Run 1 was carried out on day 1 and the sample left in air overnight. Run 2 was carried out on day 2 and the sample left in flowing nitrogen overnight and run 3 carried out the following day.

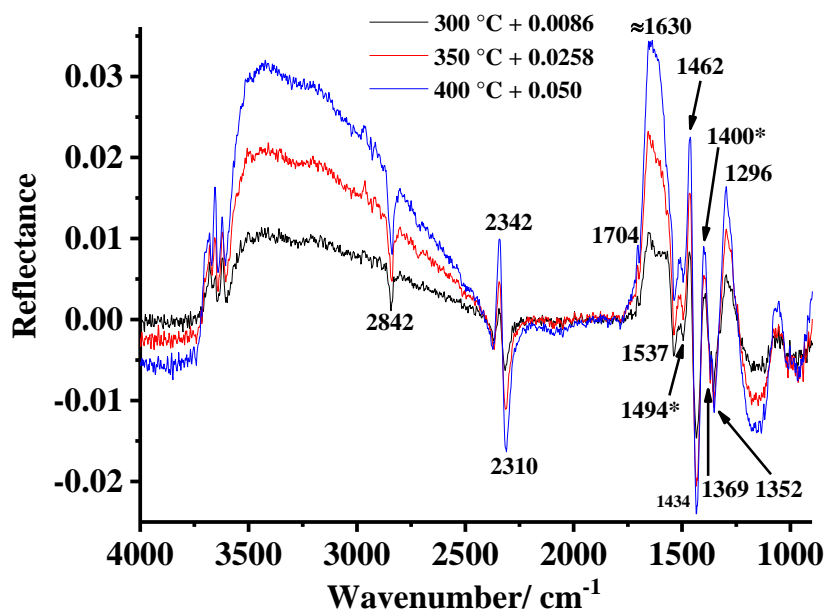
Figures 5.15(a) – (d) show the spectra in fig. 5.13(c) presented as difference spectra reflecting, in broad terms, the temperature ranges identified in the TGA experiment: thus fig. 5.15(a) shows the spectrum collected at $25 \text{ }^\circ\text{C}$ subtracted from those taken at 50 and $100 \text{ }^\circ\text{C}$, fig. 5.15(b) the spectrum taken at $100 \text{ }^\circ\text{C}$ subtracted from those up to $250 \text{ }^\circ\text{C}$, fig. 5.15(c) the spectrum collected at $250 \text{ }^\circ\text{C}$ subtracted from the 350 and $400 \text{ }^\circ\text{C}$ spectra and (d) the spectrum taken at $400 \text{ }^\circ\text{C}$ subtracted from those collected up to $600 \text{ }^\circ\text{C}$.



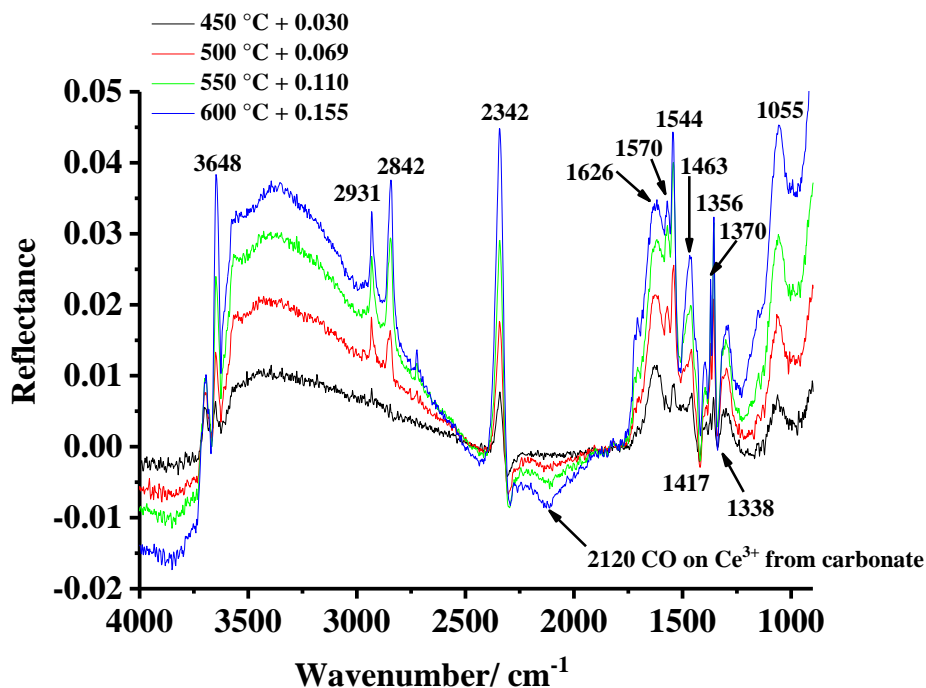
(a)



(b)



(c)



(d)

Figure 5.15. The spectra in fig. 5.13(a): (a) the spectrum taken at 25 °C subtracted from those collected at 50 and 100 °C; (b) the spectrum taken at 100 °C subtracted from those collected up to 250 °C; (c) the spectrum taken at 125 °C subtracted from those collected at 300, 350 and 400 °C, the spectra were moved up by 0.009, 0.025 and 0.050, respectively and (d) the spectrum taken at 400 °C subtracted from those collected up to 600 °C. The spectra collected at 450, 500, 550 and 600 °C were moved up by 0.030, 0.069, 0.110 and 0.155, respectively.

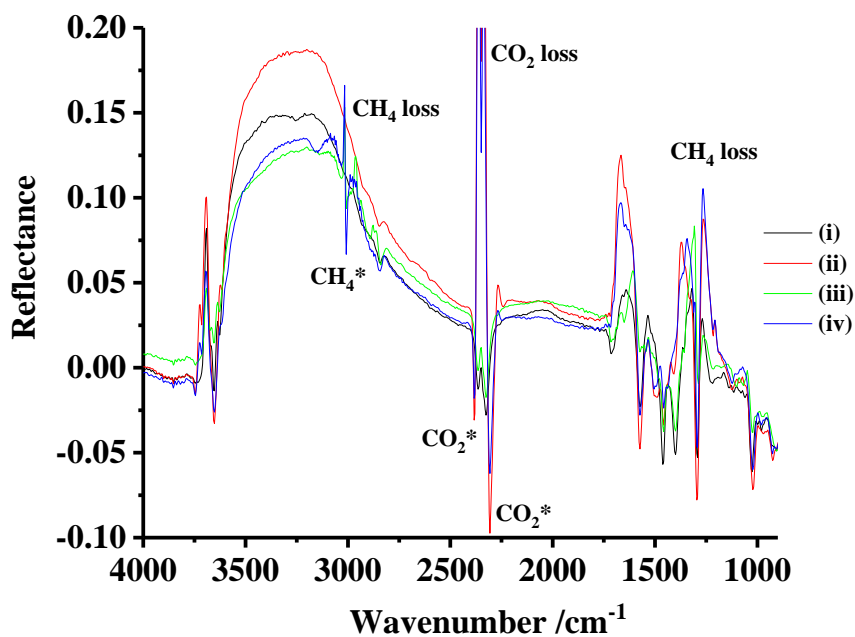
From figs. 5.15(a) – (d) it can be seen that there is a broad loss extending from ca. 2250 to 3750 cm^{-1} accompanied by a band at ca. 1642 cm^{-1} : by analogy to SnO_2 [21], this may be attributed to the loss of hydrogen-bonded Ce-OH groups via the dehydration and possibly dehydroxylation of the CeO_2 . There are also the loss and gain of sharp features above 3500 cm^{-1} due to the redistribution/loss of isolated Ce-OH groups [13]. In figs. 5.15(a) and (b) there are gain features in the region of the asymmetric stretch of physisorbed CO_2 : the absence of corresponding loss features in the same region suggest that there is a conversion of adsorbed carbonate/ bicarbonate species to CO_2 and that these molecules are distributed across different sites. It may also be the case that some of the adsorbed carbonates, e.g. bicarbonates [19], are desorbing as CO_2 . Due to its relatively high frequency, the 1711 cm^{-1} gain feature in figs. 5.15(a) and (b) is most likely due to bridged carbonate (see table 5.2). The peaks at 1570 and 1298 cm^{-1} in the same figures (the 1298 cm^{-1} feature appears at 1293 cm^{-1} in fig. 5.15(a) due to distortion by the loss features either side) may be attributed to bidentate carbonate [12-15]: they are gained up to 100 °C and then lost between 100 and 250 °C.

Over the temperature range between 300 and 400 °C, the physisorbed CO_2 band is bipolar, suggesting the transfer of more loosely bound CO_2 to sites where the CO_2 is more strongly adsorbed. At higher temperatures, there is a marked loss of physisorbed CO_2 , also clear in fig. 5.13(c), presumably due to diffusion out of the voids and desorption into the gas phase: the amount of CO_2 involved is too low for the corresponding gain features due to gas phase CO_2 to be observed. The gain feature at ca. 2120 cm^{-1} in fig. 5.15(d) may be due to CO adsorbed on Ce^{3+} sites [18], the latter produced during the heating process and responsible for the evolution of O_2 (see fig. 5.14(b)).

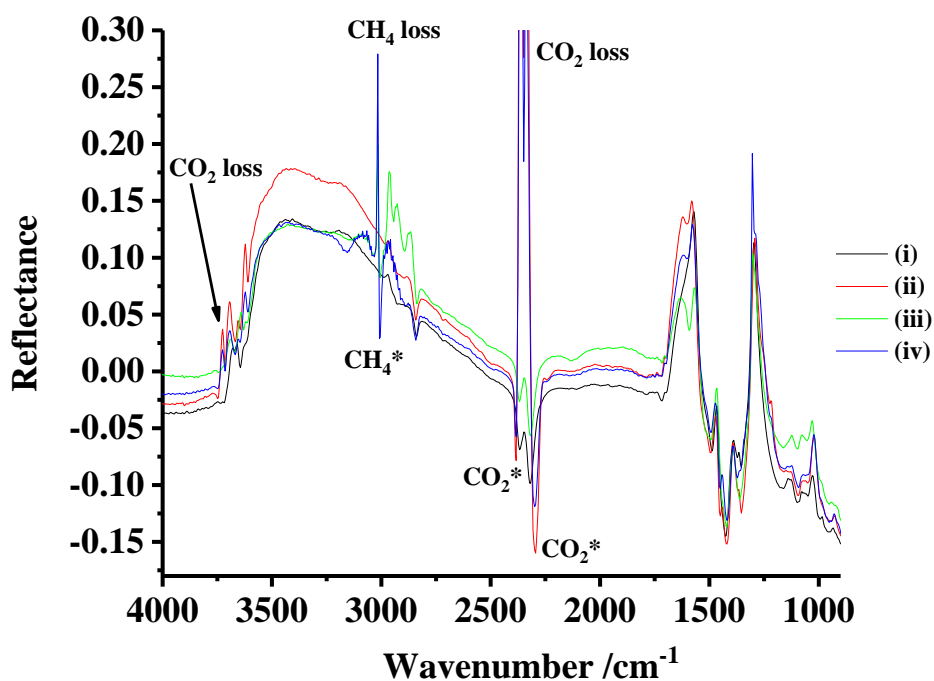
Overall, from figs. 5.15(a) to (d) it is clear that heating the CeO_2 causes a redistribution of the surface carbonate/bicarbonate species, with some apparently diffusing into the voids. Comparing the intensities of the various features below 1800 cm^{-1} in figs. 5.15(a) – (d) to the spectra in fig. 5.13(b), however, shows that the amount of adsorbed species is small. Further, given the very wide variation in the band assignments in table 5.2, it is also clear that assigning the various features below 1800 cm^{-1} in any detail to specific forms of adsorbed carbonate or bicarbonate could be of limited validity.

5.5.1 The thermally driven reaction of CO_2 , CH_4 and N_2 with CeO_2

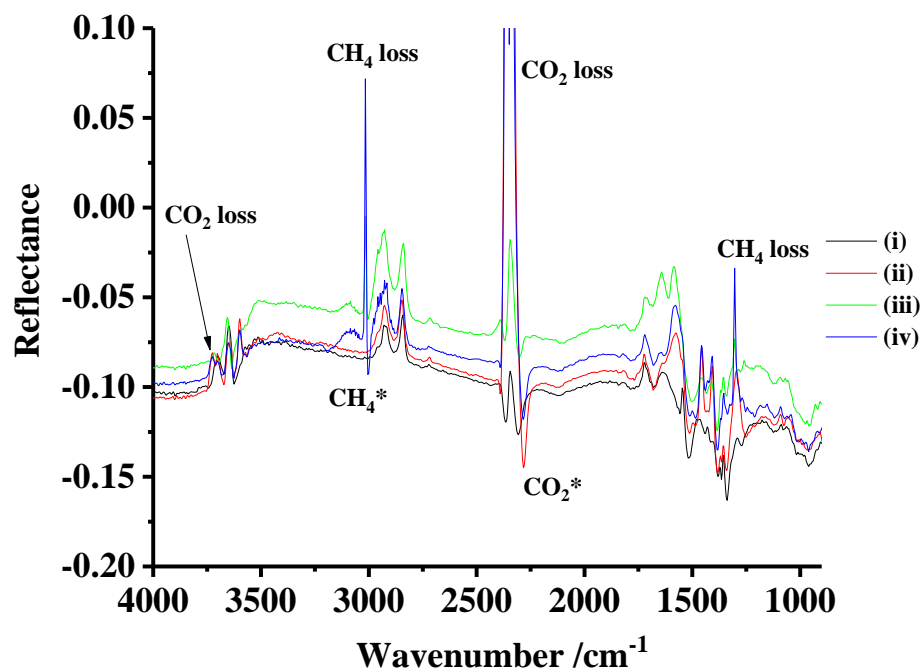
Figures 5.16(a) – (c) show the spectra collected using CeO_2 heated in N_2 at 150, 400 and 600 °C in figs. 5.15(b) – (d) along with the spectra collected in analogous experiments using CeO_2 heated in N_2 and CO_2 and/or CH_4 .



(a)



(b)



(c)

Figure 5.16. The spectra in figs. 5.15(a) – (c) collected at 150 °C, 400 °C and 600 °C. (a) The spectra collected at 25 °C subtracted from those taken at 150 °C, (b) 400 °C – 150 °C and (c) 600 °C – 400 °C. The gas composition are: (i) 100% N₂, (ii), 25.5% CO₂ + 74.5% N₂, (iii) 10.6% CH₄ + 89.4% N₂ and (iv) 12% CO₂ + 38% CH₄ + 50% N₂.

As can be seen from figs. 5.16, all experiments show very similar responses over the spectral range of CO₂ absorption region in figs. 5.15(a) – (d) and as expected, no features were observed at CeO₂ except those due to the loss of CO₂ and/or CH₄ and the gain features of CO₂* or CH₄* respectively when CO₂ and/or CH₄ were added to the system. The band at 2342 cm⁻¹ may be attributed to the asymmetric stretch of physisorbed CO₂ [16,17], however, this feature was somewhat distorted by the loss feature near 2340 and 2360 cm⁻¹ due to the P and R asymmetric stretch (ν_3) bands of CO₂ in the N₂ + CO₂ and N₂ + CO₂ + CH₄ runs. The broad band between ca. 3000 -3600 cm⁻¹ may be due to the loss of hydrogen-bonded O-H from CeO₂ and the sharp feature at 3692 cm⁻¹ in fig 5.16(a) may be attributed to isolated OH [11]. Overall, in all cases, it is clear that, whilst the presence of adsorbed carbonates /bicarbonates inhibits the thermal reaction of at CeO₂, the plasma-driven process is not inhibited at all and more importantly there are no reaction taking place in the plasma-driven reaction.

5.6 Conclusion

The results obtained using coated Macor were somewhat different, with no reaction taking place in plasma-driven experiments on CeO₂ and SnO₂, whereas a number of adsorbed carbonates/bicarbonates were observed in the thermal experiment of CeO₂ and no reaction of SnO₂ on CO₂ and/or CH₄ even with different calcination temperature at all feed gases. The data gained in this work clearly showing that invalidity of catalyst selection for NTP-based on thermal activity and support the catalytic activity of Macor in the plasma-driven conversion of N₂, CO₂ and CH₄ reported in the previous chapters.

5.7 References

1. Harrison, P.G. and A. Guest, *Tin oxide surfaces. Part 17.-An infrared and thermogravimetric analysis of the thermal dehydration of tin(IV) oxide gel*. Journal of the Chemical Society, Faraday Transactions 1: Physical Chemistry in Condensed Phases, 1987. **83**(11): p. 3383-3397.
2. Harrison, P.G. and M.J. Willett, *Tin oxide surfaces. Part 20.-Electrical properties of tin(IV) oxide gel: nature of the surface species controlling the electrical conductance in air as a function of temperature*. Journal of the Chemical Society, Faraday Transactions 1: Physical Chemistry in Condensed Phases, 1989. **85**(8): p. 1921-1932.
3. Rahmelow, K. and W. Hübner, *Infrared Spectroscopy in Aqueous Solution: Difficulties and Accuracy of Water Subtraction*. Applied Spectroscopy, 1997. **51**(2): p. 160-170.
4. Al-Abadleh, H.A. and V.H. Grassian, *FT-IR Study of Water Adsorption on Aluminum Oxide Surfaces*. Langmuir, 2003. **19**(2): p. 341-347.
5. Devlin, J.P., J. Sadlej, and V. Buch, *Infrared Spectra of Large H₂O Clusters: New Understanding of the Elusive Bending Mode of Ice*. The Journal of Physical Chemistry A, 2001. **105**(6): p. 974-983.
6. Maneelok, S., *The relationship between the composition and structure of Ni/Sb-SnO₂ and electrochemical ozone activity*, in *School of Chemical Engineering and Advanced Materials*. 2017, Newcastle University Newcastle University
7. Thornton, E.W. and P.G. Harrison, *Tin oxide surfaces. Part 1.-Surface hydroxyl groups and the chemisorption of carbon dioxide and carbon monoxide on tin(IV)*

- oxide*. Journal of the Chemical Society, Faraday Transactions 1: Physical Chemistry in Condensed Phases, 1975. **71**(0): p. 461-472.
8. Ghiotti, G., A. Chiorino, and F. Boccuzzi, *Infrared study of surface chemistry and electronic effects of different atmospheres on SnO₂*. Sensors and Actuators, 1989. **19**(2): p. 151-157.
 9. Ghiotti, G., A. Chiorino, and W. Xiong Pan, *Surface chemistry and electronic effects of H₂(D₂) on pure SnO₂ and Cr-doped SnO₂*. Sensors and Actuators B: Chemical, 1993. **16**(1): p. 367-371.
 10. Boroumand, F., J.E. Moser, and H. Van Den Bergh, *Quantitative Diffuse Reflectance and Transmittance Infrared Spectroscopy of Nondiluted Powders*. Applied Spectroscopy, 1992. **46**(12): p. 1874-1886.
 11. Zaki, M.I. and N. Sheppard, *An infrared spectroscopic study of the adsorption and mechanism of surface reactions of 2-propanol on ceria*. Journal of Catalysis, 1983. **80**(1): p. 114-122.
 12. Binet, C., M. Daturi, and J.-C. Lavalley, *IR study of polycrystalline ceria properties in oxidised and reduced states*. Catalysis Today, 1999. **50**(2): p. 207-225.
 13. Li, C., Y. Sakata, T. Arai, K. Domen, K.-i. Maruya, and T. Onishi, *Carbon monoxide and carbon dioxide adsorption on cerium oxide studied by Fourier-transform infrared spectroscopy. Part 1.-Formation of carbonate species on dehydroxylated CeO₂, at room temperature*. Journal of the Chemical Society, Faraday Transactions 1: Physical Chemistry in Condensed Phases, 1989. **85**(4): p. 929-943.
 14. Yoshikawa, K., H. Sato, M. Kaneeda, and J.N. Kondo, *Synthesis and analysis of CO₂ adsorbents based on cerium oxide*. Journal of CO₂ Utilization, 2014. **8**: p. 34-38.
 15. Zhao, S.-Y., S.-P. Wang, Y.-J. Zhao, and X.-B. Ma, *An in situ infrared study of dimethyl carbonate synthesis from carbon dioxide and methanol over well-shaped CeO₂*. Chinese Chemical Letters, 2017. **28**(1): p. 65-69.
 16. Morterra, C. and L. Orto, *Surface characterization of zirconium oxide. II. The interaction with carbon dioxide at ambient temperature*. Materials Chemistry and Physics, 1990. **24**(3): p. 247-268.
 17. Ramis, G., G. Busca, and V. Lorenzelli, *Low-temperature CO₂ adsorption on metal oxides: spectroscopic characterization of some weakly adsorbed species*. Materials Chemistry and Physics, 1991. **29**(1): p. 425-435.

18. Zaki, M.I., B. Vielhaber, and H. Knoezinger, *Low-temperature carbon monoxide adsorption and state of molybdena supported on alumina, titania, ceria, and zirconia. An infrared spectroscopic investigation*. The Journal of Physical Chemistry, 1986. **90**(14): p. 3176-3183.
19. Slostowski, C., S. Marre, P. Dagault, O. Babot, T. Toupance, and C. Aymonier, *CeO₂ nanopowders as solid sorbents for efficient CO₂ capture/release processes*. Journal of CO₂ Utilization, 2017. **20**: p. 52-58.
20. Yoshikawa, K., M. Kaneeda, and H. Nakamura, *Development of Novel CeO₂-based CO₂ adsorbent and analysis on its CO₂ adsorption and desorption mechanism*. Energy Procedia, 2017. **114**: p. 2481-2487.
21. Christensen, P.A., P.S. Attidekou, R.G. Egdell, S. Maneelok, and D.A.C. Manning, *An in situ FTIR spectroscopic and thermogravimetric analysis study of the dehydration and dihydroxylation of SnO₂: the contribution of the (100), (110) and (111) facets*. Physical Chemistry Chemical Physics, 2016. **18**(33): p. 22990-22998.

Chapter 6. Conclusions and Future Work

An in-situ non-thermal plasma (NTP) infrared (IR) transmission cell and an in-situ NTP IR reflectance cell were designed, fabricated and commissioned to study the dry reforming of CO_2 and CH_4 in dinitrogen at various potential catalysts. The data so obtained were compared to results obtained from analogous thermally-driven experiments.

The first material employed was Macor, a ceramic consisting of the oxides of Al, Mg and Si: this was chosen to provide benchmark data as it was not expected to be catalytically active, had a reasonable dielectric constant and was thermally stable.

Before progressing to methane and CO_2 , the reduction of CO_2 in the plasma was studied at Macor in the transmission cell. Rotationally-excited CO_2 was produced in the plasma, along with rotationally-excited CO: the latter was produced at conversions and energy efficiencies consistent with the literature. N_2 played an important part in the reduction as, in contrast to the chemistry observed in the absence of N_2 , the CO was produced via electron impact excitation of the N_2 followed by energy transfer to CO_2 . In general, the data obtained with the reflectance cell supported those obtained using the transmission cell when allowance was made for the increased residence time and specific input energies of the former. Two additional bands, at 1150 cm^{-1} and 1210 cm^{-1} were observed only when using the reflectance cell: these could only be due to the Macor and/or the Ti mesh electrode, did not appear to take part in the chemical processes observed and the origin of which remains obscure.

Macor proved to be wholly unexpectedly active for the conversion of methane, CO_2 and N_2 to some important products. The data were extremely interesting not just for the products but also for the possible mechanisms by which they were produced. Thus, the chemistry took place in three reaction zones: in the bulk of the plasma remote from the Macor, at the plasma/Macor interface and at the interface between the plasma and the liquid phase products produced. In addition to rotationally excited CO_2 and CH_4 , HCN and CO were also produced in the bulk of the plasma, the CO due only to the reduction of CO_2 and not influenced by the presence of methane. The HCN and CO were produced constantly and at the same rate at which they were swept out of the plasma region by the gas stream, hence attaining steady-state concentrations within the first minute of turning on the plasma. HCN was produced in

significant concentrations, which is undesirable, but it did show that nitrogen was being fixed. An oily liquid was produced through the reaction of CH_4 , CO_2 and N_2 catalysed by the Macor, a liquid that contained acetamide as well as other products. The presence of acetamide showed that nitrogen had been fixed to give a more complicated molecule than HCN. The chain oxides ketene and C_5O_2 were produced at the plasma/liquid interface catalysed or facilitated by the liquid film. The formation of liquid products has been reported by others but the possible wider significance of this has not hitherto been recognised: it offers a wholly new dimension to plasma catalytic chemistry, one that could transform the technology into a viable option for large scale chemical syntheses through a paradigm shift in plasma catalysis and reactor design.

The composition of the feed gas had a major effect upon product distribution as replacing N_2 by Ar not only inhibited the production of acetamide (as expected) but also stopped the production of the liquid film and chain oxides, strongly suggesting the participation of N_2 in ways other than as a reactant: possibly via the “dark states” of nitrogen (atomic and molecular) acting as energy reservoirs facilitating reactive and dissociative collisions.

The production of the chain oxides by a catalyst consisting of such abundant elements could have major implications for novel chemical synthesis: further, as well as the implication for terrestrial synthesis, the data could have significant implications for the study of the interstellar origins of life and prebiotic chemistry.

CO_2 , CH_4 and N_2 did not react at temperatures up to 600°C . No reaction took place at SnO_2 or CeO_2 in either the plasma or thermal experiments.

In terms of possible future studies, the first step must be to unpick the catalytic activity of Macor by determining what component, or combination of components, produce the carbon chain oxides, acetamide and liquid film, by investigating if and to what extent simpler materials can effect the same chemistry as Macor, eg. Al_2TiO_5 and MgTiO_3 with and without SiO_2 .

The possible role of the liquid film product in the NTP-driven dry-reforming of CO_2 and CH_4 in N_2 should be investigated by modifying the reflectance cell to include well-defined

depressions and troughs to contain static and flowing liquids. The first step should be to employ the liquid product, then the product diluted with suitable, inert solvents to decrease viscosity and then model liquids chosen for their properties including: dielectric constant, conductivity, viscosity and ability to dissolve one or more of the reactant gases (eg. monoethanolamines which are widely employed to trap CO₂).

All future IR studies should be carried out with complementary analytical techniques such as downstream UV Vis and IR analyses and, most especially, GC-MS. GC-MS analysis should be employed to determine and quantify the product distributions allowing conversion and energy efficiencies to be calculated. Coupled with the development of these in-line analytical techniques, the use of isotopically labelled materials, e.g. ¹³CH₄, ¹³C¹⁸O₂, would facilitate the exploration of the possible reaction pathways, identify the origin of the fragments of the more complex organic structures generated during the process and thus allow selective production of the individual NTP components.

It is clear that the interaction of the highly excited and reactive species generated in plasma with solid surfaces (catalysts, dielectrics) remains largely unknown both in terms of the chemistry and the timescale over which such reactions take place: the latter is important as non-thermal plasma is driven by a succession of microdischarges (the amplitude and frequency of which depend strongly on the dielectric material between the electrodes) each with a lifetime of a few tens of nanoseconds. The importance of this is that the lifetime of many of the species formed is only of this magnitude, with the result that decay of the molecular fragments takes place on timescales comparable to the discharges themselves. Hence time-resolved studies using e.g. step-scan FTIR (timescales down to 10s of ns) should be employed to identify intermediates and their lifetimes. Such data would be invaluable with respect to the production of valid, predictive models and hence the elucidation of mechanism and the identification of new and effective catalysts and new reactor designs.

Appendix 1

Example of integrated absorption coefficient calculations for 100% CO at 2002 cm^{-1} to 2225 cm^{-1} using 1 cm pathlength cell analysed by Origin.

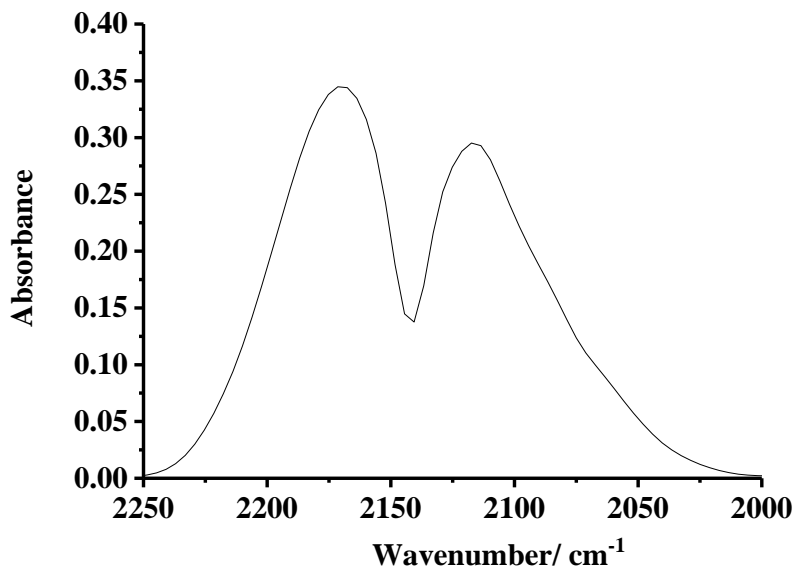


Figure 1. The typical spectrum of 100% CO in a 1 cm pathlength transmission cell with no plasma and 100% N_2 feed gas as the reference.

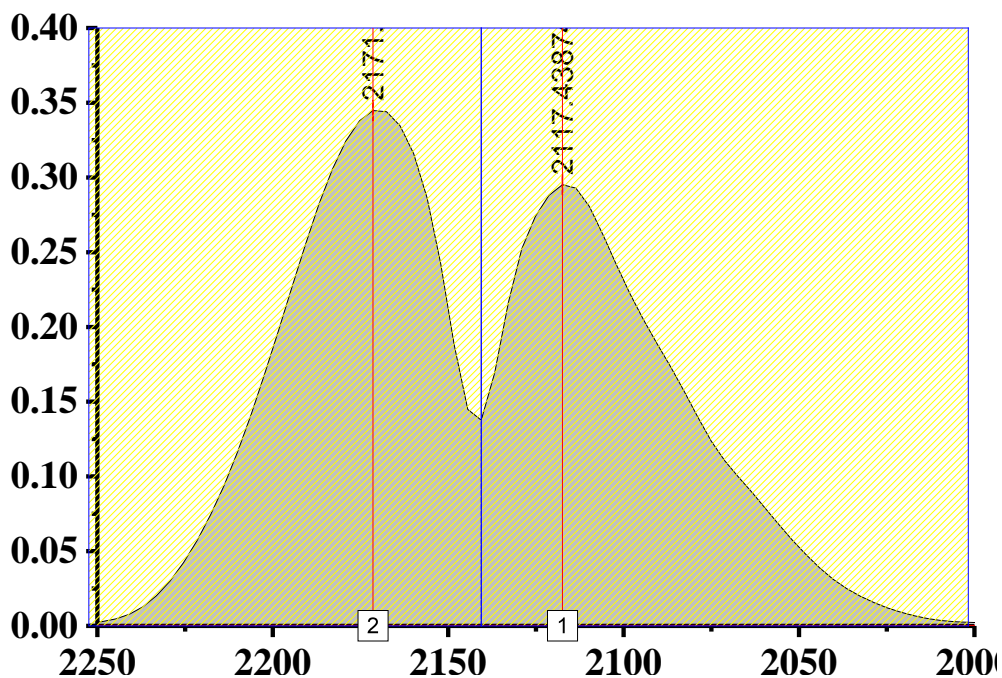


Figure 2. The integrated area of CO peaks in fig 1. analysed using Origin.

Appendix 1

Area	Integrated Area	FWHM	Center	Height
1	14.5	54.93	2117.43	0.27
2	14.8	50.92	2171.43	0.31

Table 2. Results gained from the Origin for fig. 2.

Total integrated area = 29.3 cm⁻¹

$$A = \epsilon c L$$

$$\epsilon = A / c L$$

$$\epsilon = 29.3 \text{ cm}^{-1} / (0.00004171 \text{ mol cm}^{-3} \times 1 \text{ cm})$$

$$\epsilon = 702469 \text{ mol}^{-1} \text{ cm}$$

$$\epsilon = 7.0 \times 10^5 \text{ mol}^{-1} \text{ cm}$$

Appendix 2

Example of integrated absorption coefficient calculations for 100% CO₂ at 3491 cm⁻¹ to 3768 cm⁻¹ using 1 cm pathlength cell analysed by Origin.

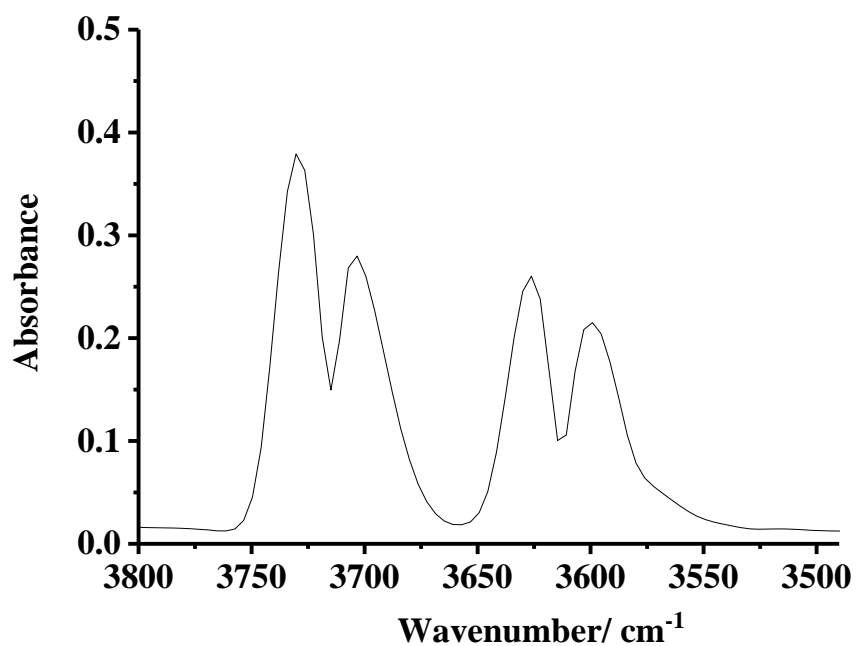


Figure 3. The typical spectrum of 100% CO₂ in a 1 cm pathlength transmission cell with no plasma and 100% N₂ feed gas as the reference.

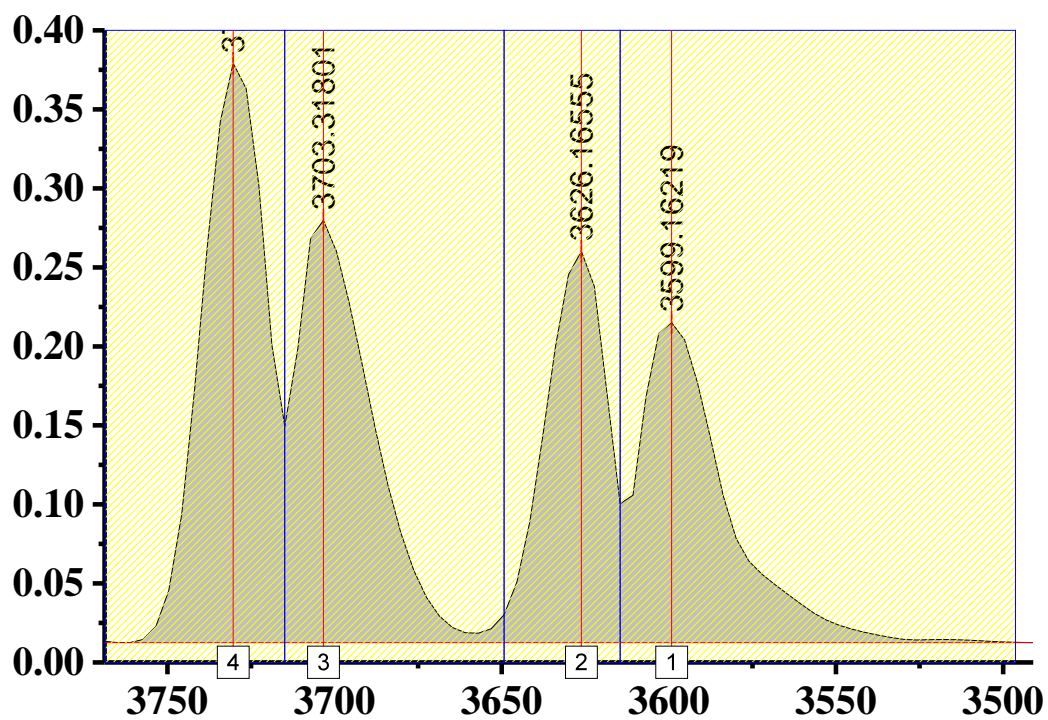


Figure 4. The integrated area of CO₂ peaks in fig 3. analysed using Origin.

Appendix 2

Area	Integrated Area	FWHM	Center	Height
1	6.2	25.64	3599.16	0.20
2	5.6	21.61	3626.16	0.24
3	7.2	23.41	3703.31	0.26
4	8.2	22.52	3730.32	0.36

Table 1. Results gained from the Origin for fig. 4.

Total integrated area = 27.2 cm⁻¹

$$A = \epsilon c L$$

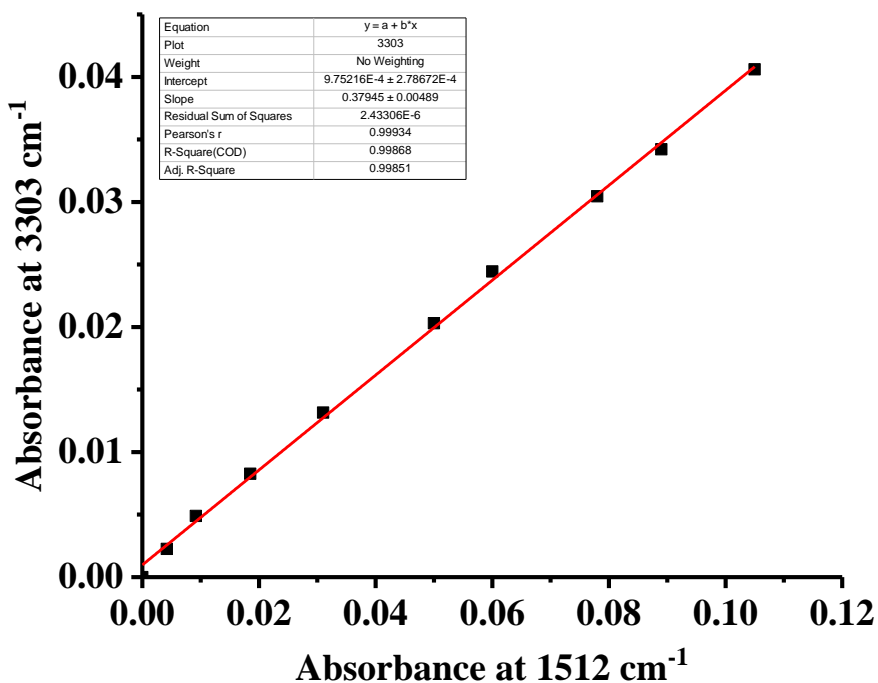
$$\epsilon = A / c L$$

$$\epsilon = 27.2 \text{ cm}^{-1} / (0.00004171 \text{ mol cm}^{-3} \times 1 \text{ cm})$$

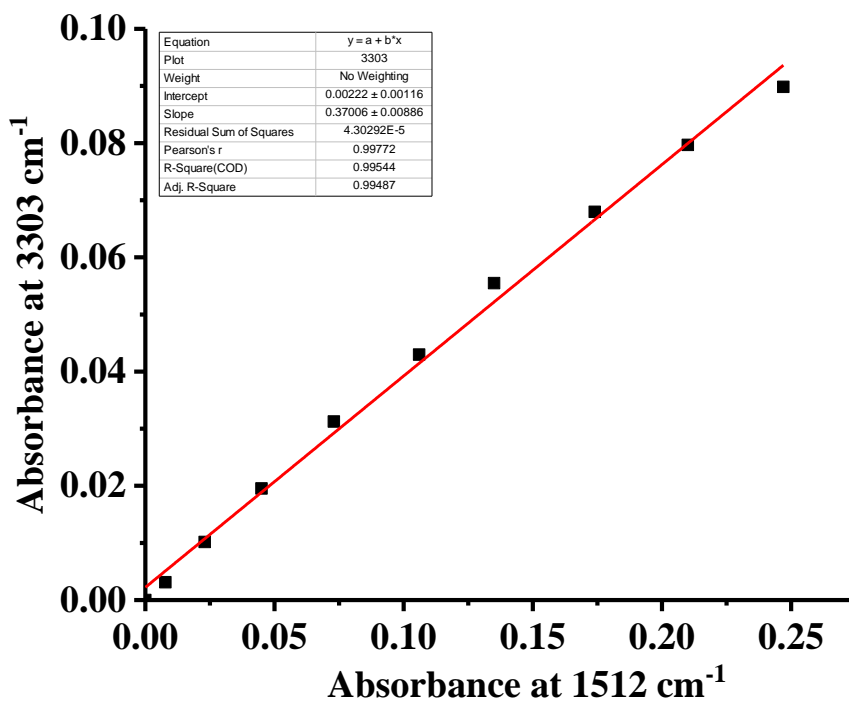
$$\epsilon = 652121 \text{ mol}^{-1} \text{ cm}$$

$$\epsilon = 6.5 \times 10^5 \text{ mol}^{-1} \text{ cm}$$

Appendix 3

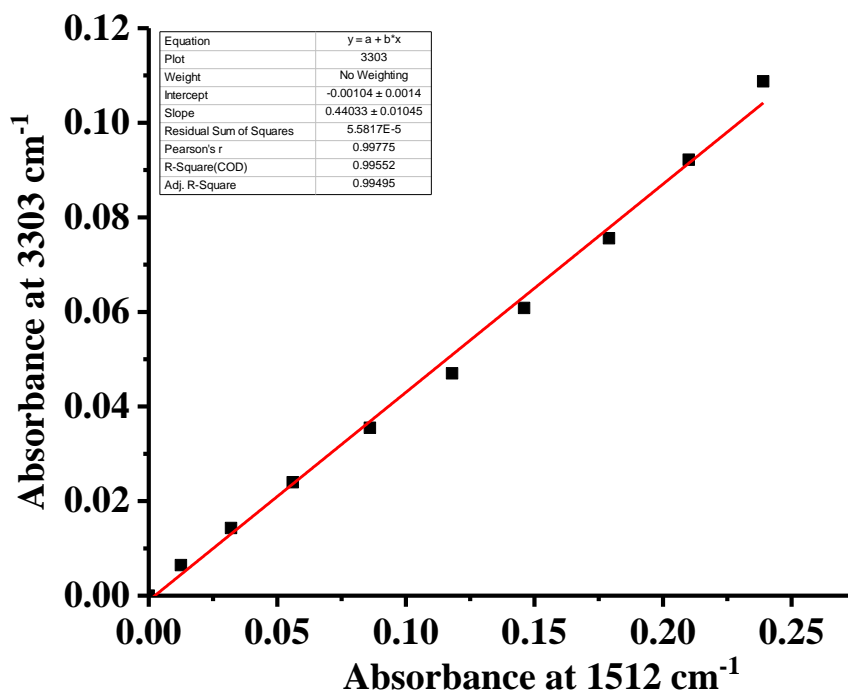


(a)



(b)

Appendix 3



(c)

Figure 5. Plots of the absorbance of the 3303 cm^{-1} band vs the absorbance at 1512 cm^{-1} for the experiment in fig. 4.10 and the analogous experiments carried out at input powers of (a) 20 W (b) 24 W and (c) 28 W. (Corresponding to rows 1(a), 3(a) and 5(a) in table 4.1).

Appendix 4

Example of integrated absorption coefficient calculations for 100% CH₄ at 1149 cm⁻¹ to 1400 cm⁻¹ using 1 cm pathlength cell analysed by Origin.

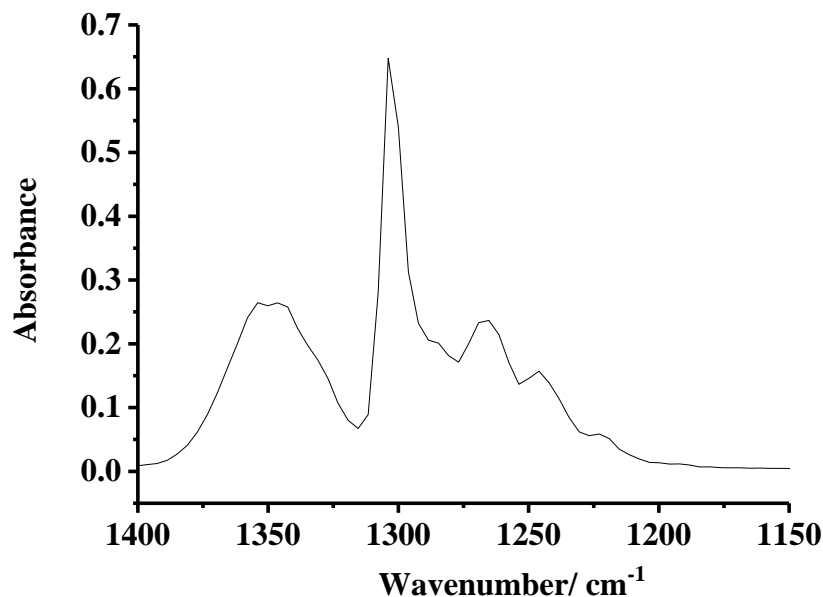


Figure 6. The typical spectrum of 100% CH₄ in a 1 cm pathlength transmission cell with no plasma and 100% N₂ feed gas as the reference.

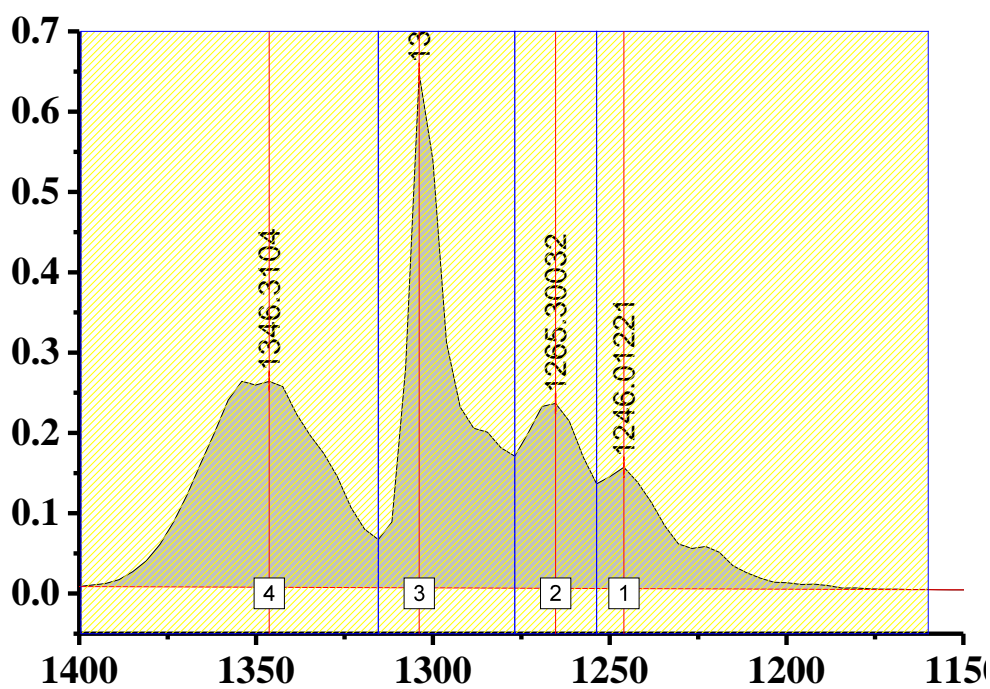


Figure 7. The integrated area of CH₄ peaks in fig 6. analysed using Origin.

Appendix 4

Area	Integrated Area	FWHM	Center	Height
1	3.9	15.9	1246.0	0.15
2	4.6	19.2	1265.3	0.23
3	10.7	10.8	1303.8	0.64
4	11.0	42.1	1346.3	0.25

Table 3. Results gained from the Origin for fig. 7.

Total integrated area = 30.2 cm⁻¹

$$A = \epsilon c L$$

$$\epsilon = A / c L$$

$$\epsilon = 30.2 \text{ cm}^{-1} / (0.00004171 \text{ mol cm}^{-3} \times 1 \text{ cm})$$

$$\epsilon = 724046 \text{ mol}^{-1} \text{ cm}$$

$$\epsilon = 7.2 \times 10^5 \text{ mol}^{-1} \text{ cm}$$